Physics of Single and Two-Phase Flows in Bifurcating Vessels

Thesis

Submitted in partial fulfillment of the requirements for the degree of

Doctor of Philosophy

by

Nagargoje Mahesh Shahadeo

(Roll No.166107014)

Supervisor:

Dr. Raghvendra Gupta

Department of Chemical Engineering

Indian Institute of Technology Guwahati

Guwahati, India

August, 2021

Dedication

To my parents.

Acknowledgments

First and foremost, I want to thank my thesis adviser, Dr. Raghvendra Gupta, for giving me the opportunity to pursue doctoral research in his lab and for his constant support and guidance throughout this endeavor. I also want to thank Prof. Dipankar Bandyopadhyay, Dr. Nageswara Rao Peela, and Dr. Dipankar Narayan Basu for their commitment to serving on my doctoral committee and their invaluable feedback. I am thankful to Prof. Anugrah Singh, head of chemical engineering, for his valuable inputs and support during my research work. I am also thankful to all my academic and non-academic teachers who shaped my ideas, thinking, and actions. I feel proud for having curious lab mates like Deepak Mishra, Roushni Kumari, P. Premsagar, Mudrika Singhal, and V. Ashwini. I learnt a lot of things from Deepak during tea-break discussions. I thank the Ministry of Education, the Government of India for the fellowship support during my Ph.D. work.

I have received much encouragement and affection from my extended family and friends during these years. They have been very kind and understanding during my stay at IIT Guwahati. I am deeply grateful to my mother, brother, and wife for their constant support and love. Finally, I must confess that this thesis work has been a humble offering of thanks and praise to motherland India and the great people of this land. Before 2016, I was not aware of the rich culture and people of Northeast India. I feel fortunate to stay here for around five years and learned a lot about woman empowerment and patriotism from the people of Assam.

Abstract

Bifurcating vessels are ubiquitous in cardiovascular and pulmonary systems, microfluidics, and several biomedical applications. The flow is distributed in the daughter vessels, and the streamlines become curved at the bifurcations. As a result, the flow becomes complex at the bifurcations. In this work, the steady and pulsatile flow of blood, assuming it to be a Newtonian fluid, is modeled in idealized symmetric and asymmetric bifurcations. The effect of different geometric parameters such as bifurcation angles, mother to daughter vessel ratio, area change near the bifurcation on the flow behavior is investigated computationally. In particular, the effect of these parameters on instantaneous and time-averaged wall shear stress, oscillatory shear index, and relative residence time, the potential biomarkers for atherosclerosis development, is presented. The results show that the shear rate can become significantly low in certain regions, especially around the bifurcation. Therefore, the fluid is also modeled as a shear-thinning fluid, and the results are compared with those obtained, assuming the fluid to be Newtonian. Further, the effect of pulse frequency on flow behavior is investigated in a patient-specific geometry available in the open literature.

In several cases, such as during movement of gas emboli, in gas embolotherapy, in mechanical ventilation, and in microfluidic applications, gas-liquid flow is encountered in bifurcating geometries. The dynamics of bubbles in symmetric and asymmetric bifurcations is investigated using the volume of fluid method in a planar, two-dimensional computational domain. The effect of bifurcation angle, Reynolds, and capillary numbers on the bubble is investigated. Bubble dynamics is also investigated experimentally in a symmetric bifurcation geometry. Results show two different regimes: splitting and non-splitting, depending on the flow and geometric parameters. A qualitative comparison between the experimental data and two-dimensional simulation is made.

Executive summary

Bifurcations are a common occurrence in a number of biomedical, physiological, and process engineering applications. Two very common examples are human vascular and respiratory systems. In both the systems, fluid flow occurs continuously and the disease development, diagnosis, and treatment require a good understanding of flow behavior along with other biological and biochemical factors.

Atherosclerosis (arterial disease) is a significant cause of mortality worldwide and occurs due to the deposition of fatty material on the inner wall of the artery. The accumulation of fat causes a stenosis i.e. reduction in the cross-section of the vessel. Hemodynamics plays a vital role in the localization of arterial disease in the areas of arterial bifurcation and curved vessels, especially in the carotid sinus. Atherosclerosis is generally correlated with low wall shear stress (WSS). WSS value < 0.4 Pa is regarded as a risk factor for atherosclerosis. The influence of complex flow at the carotid bifurcation on atherogenesis has been studied numerically and experimentally in the last four decades for steady and pulsatile flow. The flow separation occurs on the outer wall of daughter vessel just after the bifurcation, resulting in the backflow and reduced wall shear stress (WSS) on the outer wall. Further, secondary flow or Dean vortices are observed due to the curvature of streamlines at the bifurcation. The flow behavior and wall shear stress strongly depends on the geometrical parameters such as bifurcation angle i.e. the angle between the axes of mother and each daughter vessel, the ratio of the diameter of mother and daughter vessels, boundary conditions at the inlet and exit, change in vessel cross-section.

The gas-liquid flow problem is encountered in a number of biomedical applications. Two such applications are gas embolotherapy and mechanical ventilation. Gas embolotherapy is a potential cancer treatment in which intra-arterial blood supply to cancer tumor is cut off using perfluorocarbon (PFC) gas bubbles. In many respiratory diseases, including Coronavirus disease 2019 (COVID19), the lungs of the patients can get severely affected, and sometimes external mechanical ventilation is required to supply the air to the liquid-filled lungs. The air enters the liquid in the form of gas bubbles, and high wall shear stress around the bubble may potentially cause damage to the airways. Again, the bubble dynamics at the bifurcation depend on bifurcation geometry and flow parameters such as capillary and Bond number.

Therefore, this thesis aims to develop a comprehensive understanding of the flow of liquid and gas-liquid in symmetric and asymmetric bifurcating vessels over a wide range of geometric and flow parameters.

In the cardiovascular system, the bifurcations are often asymmetric, flow is pulsatile, and blood shows complex rheology. First, single-phase flow in a bifurcating vessel having mother and daughter vessels of the same diameter is considered. The effect of bifurcation angle on flow dynamics for steady and pulsatile flow in symmetric and asymmetric bifurcations is studied for Newtonian and shear thinning fluid following the Carreau model. During steady flow in asymmetric bifurcations, the flow distribution in daughter vessels is observed to be asymmetric with a higher flow rate in the daughter vessel having the smaller bifurcation angle. In pulsatile flow, the flow divides in the two daughter vessels equally in symmetric bifurcations, and the flow distribution is time-dependent during a cardiac cycle in asymmetric bifurcations. The flow pattern changes significantly during a cardiac cycle. The secondary flow caused by the curvature of streamlines at the bifurcation is observed to be stronger at the start of the diastole despite a reduction in the flow rate. The flow is separated at the outer wall of the bifurcation and causes a significant reduction in time-averaged wall shear stress, a biomarker to assess the possibility of atherosclerotic plaque development. While no significant difference is observed in the results obtained for Newtonian and non-Newtonian fluids at high shear rates e.g. during systole, significant differences are observed when the shear rate is low, during diastole, or in the separation region. The velocity profile for the non-Newtonian fluid is observed to be flatter than that for a Newtonian fluid. Further oscillatory shearing index, relative residence time, the parameters used as biomarkers are plotted.

One of the very important and critical arterial bifurcations in the human vascular system is carotid artery bifurcation. Atherosclerosis and resulting stenosis in the carotid artery may cause a stroke. Each carotid artery bifurcates in internal and external carotid arteries that supply blood to the brain and face and neck, respectively. Generally, a widening in the internal carotid artery, known as carotid sinus, exists at the bifurcation. The location and size of the sinus can vary in different people and the change in sinus size and location can affect the hemodynamics. An idealized geometry having similar dimensions as those in a typical carotid artery bifurcation is considered. The carotid sinus is modeled as having an ellipsoidal shape. The effect of its size and location on

the flow behavior and wall shear stress is investigated, assuming the blood follows Newtonian behavior. The results show the shear rate to be low at the bifurcation and in the sinus. Since blood behaves as a shear-thinning fluid at low shear rates, the simulations also assume blood is a non-Newtonian fluid. The sinus away from bifurcation and larger diameter have bigger recirculation regions and lower wall shear stress. Therefore, a person with sinus away from bifurcation and larger sinus diameter are more susceptible to plaque formation. The profile of velocity in the main flow, secondary flow as well as the commonly established hemodynamic parameters such as time-averaged wall shear stress (TAWSS), oscillatory shear index (OSI), relative residence time (RRT), and secondary flow are analyzed in the sinus region and compared. Larger sinuses contribute to backflow, which causes a significant difference in hemodynamic parameters between the Newtonian and non-Newtonian flow.

Further, flow behavior in a patient-specific carotid artery geometry obtained from the literature is studied. The effect of three inlet waveforms with varying pulsatile frequency on hemodynamics is analyzed. With an increase in the cardiac cycle frequency, the size of flow separation in the sinus region is observed to reduce. A smaller region of low wall shear stress is observed in the case of a high frequency of blood flow in comparison with those in low-frequency cases. Similarly, the higher pulsatile frequency causes a decrease in the values of an oscillatory shearing index (OSI) and relative residence time (RRT).

The flow of bubbles and droplets in confined geometries is a common phenomenon that occurs in a wide range of applications such as microfluidics, medicine and food, and cosmetics amongst others. Various geometrical configurations have been employed to generate and split the bubbles, for example, T-shaped bifurcations, Y-shaped bifurcations, and combinations of both configurations. With a motivation to understand the bubble dynamics during gas embolotherapy and in pulmonary airways, CFD simulations in planar, two-dimensional bifurcations have been performed using the volume of fluid (VOF) method to capture the interface between the two phases. Two different scenarios are considered. In scenario one, CFD simulations are performed using blood as the liquid and perfluorocarbon (PFC) as the gas phase for two different values of capillary numbers. The effect of bifurcation angle on the bubble splitting is investigated in symmetric and asymmetric bifurcating geometries. While the bubble splits at the higher capillary

number in all the cases, no splitting occurs at the lower value of the capillary number in symmetric bifurcation having a large bifurcation angle and in asymmetric bifurcation geometries considered.

In the second scenario, CFD simulations are performed for gas-liquid flow in an asymmetric bifurcation, and the effect of Bond and capillary numbers on pressure gradient is analyzed. The bubble split does not occur, and the bubble moves in the daughter vessel having a smaller bifurcation angle. The stresses, both normal and shear, and their gradients are observed to be high in the vicinity of the bubble. The pressure gradient, a parameter correlated with the cell damage, is observed to be the highest at the bifurcation and is observed to increase with a decrease in capillary number.

Finally, the bubble dynamics in three Newtonian liquids of varying viscosities for various bubble lengths (l_b/d_m = 2-9) is investigated experimentally at a symmetric bifurcation. A PDMS channel is fabricated in-house using a 3D-printed mold. The effect of liquid flow rate at a fixed gas flow rate on bubble size, splitting flow dynamics, and bubble neck dynamics is investigated. The bubbles forms at a T-junction and the length of the bubble increases with an increase in ratio of gas to liquid flow rate for each fluid. As in CFD simulations, both splitting and non-splitting behavior is observed in experiments too. The non-splitting behavior is observed at low capillary numbers and/or for shorter bubbles. The rate of neck thinning is observed to be constant. A qualitative comparison is made between the bubble break-up and neck thinning between the results obtained from experiments and planar, two-dimensional CFD simulations.

Research publications

Journal Publications:

1. **Nagargoje, M.,** & Gupta, R. (2020). Effect of asymmetry on the flow behavior in an idealized arterial bifurcation. *Computer Methods in Biomechanics and Biomedical Engineering*, *23*(6), 232-247.
2. **Nagargoje, M.,** & Gupta, R. (2020). Effect of sinus size and position on hemodynamics during pulsatile flow in a carotid artery bifurcation. *Computer Methods and Programs in Biomedicine*, *192*, 105440.
3. **Nagargoje MS,** Mishra D, Gupta R, 2021. Pulsatile flow dynamics in symmetric and asymmetric bifurcating vessels. *Physics of Fluids*, 33(7), 071904.

Journal Publications (to be submitted):

4. **Nagargoje MS,** Gupta R, 2021. Effect of pulse rate on hemodynamics in a carotid artery bifurcation (*under review*).
5. **Nagargoje MS,** Gupta R, 2021. Bubble propagation in an asymmetric airway bifurcation *(under review)*.
6. **Nagargoje MS,** Gupta R, 2020. Numerical simulations of the blood flow dynamics in an idealized carotid artery bifurcation for varying sinus and stenosis sizes *(under review).*
7. **Nagargoje MS,** Gupta R, 2021. Role of CFD in the diagnosis and treatment of cardiovascular diseases (CVDs) (*under preparation*).
8. **Nagargoje MS,** Gupta R, 2021. Splitting dynamics of bubble transport in an asymmetric bifurcation (*under preparation*).
9. **Nagargoje MS,** Gupta R, 2021. Experimental investigations on the bubble dynamics in a bifurcating vessel (*under preparation*).

Conference proceedings:

1. **Nagargoje MS,** Gupta R, 2021. Numerical and experimental hemodynamic study in an in-vitro 3D printed patient-specific carotid artery bifurcation. *26th Congress of European Society of Biomechanics Conference, Milan, Italy, 2021.*
2. **Nagargoje MS**, Gupta R, 2020. Numerical simulation of bubble transport and splitting dynamics for varying bifurcation angle. *14th International Conference on CFD in Oil & Gas, Metallurgical and Process Industries SINTEF, Trondheim, Norway, October 12–14, 2020.*
3. **Nagargoje M**, Gupta R, 2018. Effect of sinus shape and position on pulsatile blood flow in carotid artery bifurcation. *4th International Conference on Fluid Mechanics & Fluid Power, IIT Bombay, Dec. 2018.*
4. **Nagargoje M**, Gupta R, 2017. Numerical modeling of blood flow in bifurcations. *Complex Fluids, IIT Madras, Dec. 2017.*

Contents

List of figures

List of Tables

List of Symbols

Greek letters

α, β	Bifurcation angles of daughter vessels with mother vessel (degrees)
α_G	Volume fraction of gas phase
$\dot{\gamma}$	Shear rate (s^{-1})
δ	Film thickness (m)
$\delta(\boldsymbol{r})$	Dirac delta function
κ	Kappa
λ	Relaxation time (s)
μ	Dynamic viscosity (Pa. s)
μ_∞	Apparent viscosity at infinite shear rate (Pa. s)
μ_0	Apparent viscosity at zero shear rate (Pa. s)
ρ	Density (kg/m^3)
$\boldsymbol{\tau}$	Stress tensor (Pa)
τ_w	Wall shear stress (Pa)

Roman Letters

d, d_m	Diameter of mother vessel (m)
Bo	Bond number
Re	Reynolds number
Ca	Capillary number
Q_L	Liquid flow rate (m^3/s)
Q_G	Gas flow rate (m^3/s)
u	Velocity vector (m/s)
g	Acceleration due to gravity (m/s^2)
k	Flow consistency index
n	Power law index
p	Sinus position non-dimensinalized with radius of CCA

w	Sinus size non-dimensinalized with radius of CCA
$\hat{\mathbf{n}}$	Unit vector normal to the interface
$\boldsymbol{r_{int}}$	Position vector of the interface (m)
$\boldsymbol{r}$	Position vector (m)
t	Time (s)
d_n	Neck thickness of bubble (m)
U_B	Bubble velocity (m/s)

Abbreviations

CVDs	Cardiovascular diseases
CFD	Computational fluid dynamics
WSS	Wall shear stress
OSI	Oscillatory shear index
RRT	Relative residence time
CCA	Common carotid artery
ECA	External carotid artery
ICA	Internal carotid artery
CT	Computer tomography
CTA	Computed tomography angiography
MRI	Magnetic resonance imaging
RBCs	Red blood cells
PFC	Perfluorocarbon

Chapter 1 Introduction

Flow bifurcation occurs in several biological applications such as blood flow in arteries, airflow in the pulmonary system, and microfluidic devices developed for biological applications. The cardiovascular and airways networks are complex and consist of various geometric variations such as bifurcations, curvature, change in the lumen or cross-sectional area, and non-planarity. The flow behavior at the bifurcations can have significant implications on cardiovascular disease development and progression (Caro et al., 1971b; Chen and Lu, 2006; Ku et al., 1985; Nguyen et al., 2008), gas embolism (Li et al., 2021), embolotherapy (Bull, 2005), gas exchange in diseased pulmonary airways (Grotberg, 1994; Huh et al., 2007), and droplet-based microfluidics (Ma et al., 2021; Wang et al., 2019; Ziyi et al., 2019).

Single-phase flow in a bifurcation

Cardiovascular diseases (CVDs) are the leading cause of death globally. An estimated 17.7 million people died from CVDs in 2015, representing 31% of all global deaths. Of these deaths, an estimated 7.4 million were due to coronary heart disease, and 6.7 million were due to stroke, according to the world health organization (WHO) (WHO, 2019). In India, heart disease and stroke are the major causes of death, contributing more than 80% to all CVDs. CVD death rate of 272 per 100,000 population in India is higher than the global average of 235 per 100,000 people (Prabhakaran et al., 2018, 2016). The deaths due to CVDs are not only related to lifestyle and diet but also to ethnicity and culture (Anand et al., 2020). Low and middle-income countries face the highest mortality rate due to CVDs. The deaths due to stroke in the northeast region are much higher as compared to other parts of India.

Cardiovascular diseases are related to compromised blood flow in various body organs, and the formation of these diseases is called atherosclerosis. Atherosclerosis occurs due to fat accumulation on the inner arterial walls. The accumulation of fat causes a reduction in the cross-sectional area of the vessel and is known as stenosis. The stenosis may compromise the blood supply to various body organs, which can lead to a life-threatening situation. Fat deposition is observed frequently at the arterial bifurcations and curved regions of the vascular vessels. A theory relating to atherosclerosis and dynamics of blood flow was proposed based on the pressure

difference between the inner and outer walls of curvature in curved vessels (Texon, 1957). The inner wall of curvature (outer wall in case of bifurcation) has a lower pressure than that of the outer wall, and the transverse pressure difference across the vessel pulls the endothelium into the lumen. However, this theory was not very successful as the transverse pressure gradient is very small and would not cause any significant change in pressure in the transverse direction. Subsequently, a theory correlating atherosclerosis with low wall shear stress emerged and is now widely accepted in the medical community (Caro et al., 1971a). According to some researchers, cholesterol is synthesized in the arterial walls and diffuses into the lumen (Caro et al., 1971b). While this cholesterol is washed away in the region of high wall shear stress, it gets deposited on the arterial wall in the regions of low wall shear stress, such as flow separation and recirculation zones. According to another hypothesis, transport of nutrients and waste products between the blood and vessel walls depends on the wall shear stress, and its transport is low in the regions having slow or stagnant flow and low wall shear stress. Several studies have confirmed that the plaques tend to occur in the region of low velocity, low wall shear stress (WSS) (Caro et al., 1971a; Malek et al., 1999; Zarins et al., 1983). However, for pulsatile blood flow, the time-varying parameters need to be considered and defined as an oscillatory shear index (OSI) and relative residence time (RRT). The high oscillatory shear index (OSI) (Ku et al., 1985; Perktold et al., 1991; Perktold and Hilbert, 1986; Perktold and Resch, 1990), and high particle residence time (Araim et al., 2001; Glagov et al., 1988) regions are the indicator of atherosclerosis formation.

Carotid arteries supply oxygen-rich blood to the head, brain, and face. They are located on each side of the neck. The human carotid artery consists of the common carotid artery (CCA) that bifurcates into the external carotid artery (ECA) and internal carotid artery (ICA), as shown in Fig.1.1. The dilated region in the internal carotid artery is called the carotid sinus. At the carotid Sinus, where the flow is disturbed, endothelial cells are observed to show atherosclerosis-prone characteristics driven by activation of NF-kB transcription factor which leads to the entry of monocytes. On the other hand, in the region of unidirectional laminar flow, atherosclerosis protective behaviour of endothelial cells is observed which is driven by transcription factors KLF2 and KLF4. The carotid artery geometry is more homogenous in youth, while there can be significant variation in older subjects. The interrelationship between vascular geometry, local hemodynamics, and atherosclerosis is very complex in older people (Thomas et al., 2005a). An angiogram study of various patients showed the anatomical differences between the carotid

geometries of men and women (Schulz and Rothwell, 2001). CFD analysis of various patient-specific models of carotid arteries showed variation in disturbed flow quantified as the surface area occupied by low WSS or high Oscillatory Shear Index (OSI) (Lee et al., 2008). The analysis of CT angiography images of patients showed that the carotid artery anatomy and geometry are closely associated with the risk of developing atherosclerosis (Gregg et al., 2018a; Phan et al., 2012). The presence of carotid sinus increases the recirculation zones and lowers the WSS, which increases the risk of stroke (Compagne et al., 2019; Gallo et al., 2018). The larger size of the sinus increases recirculation, OSI value, and increases the OSI region, which could be a risk factor for atherosclerosis (Kuan et al., 2015; Perktold and Resch, 1990; Saho and Onishi, 2017; D. R. Wells et al., 1996).

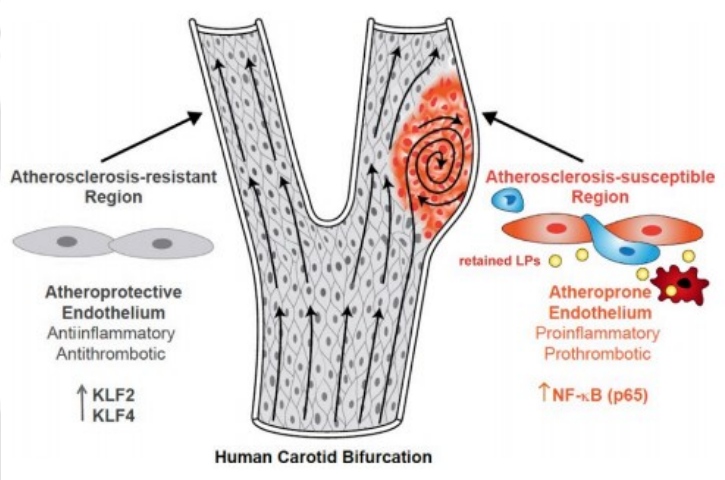

Figure 1.1 Flow patterns in the carotid artery bifurcation showing backflow in the carotid sinus, adapted from (Tabas et al., 2015).

The angle between each daughter vessel with respect to the mother vessel is called a bifurcation angle. The bifurcation angle plays an important role in hemodynamics at the arterial bifurcation and is a crucial factor in formulating intervention strategies in the stenting of coronary arteries (Zhang and Dou, 2015). The WSS value and its relation to atherosclerosis change with the bifurcation angle. A computed tomography (CT) study on various patients with symptoms of headache found that the internal carotid artery angle is wider for patients with stroke than healthy patients (Noh and Kang, 2019). Perktold et al. (1991) analyzed the effect of the bifurcation angle in a carotid artery. They showed that the complex flow at the bifurcation is affected by the angle variation (Perktold et al., 1991). WSS peaks exist on the inner side of bifurcation at the entry point

of the daughter vessel, and these peaks drop as the bifurcation angle increases (Arjmandi-Tash et al., 2011; Chaichana et al., 2011).

The higher angled vessels and larger sinuses generate a circulation which leads to a low shear rate. The rheology of blood plays a vital role in the low shear rate region due to its complex nature. The blood behaves as a non-Newtonian fluid at low shear regions (Roberston and Owens, 2009). At low shear rates, aggregation of red blood cells (RBCs) into cylinder-like long structures, known as rouleaux formation, occurs, which causes an increase in apparent viscosity of blood (DiCarlo et al., 2019; Roberston and Owens, 2009), as shown in Fig. 1.2. In many investigations on flow in large arteries, blood was modeled as a Newtonian fluid by considering higher shear rate values (Ku, 1997; Wootton and Ku, 1999). The non-Newtonian nature of blood might need to be revisited in larger arteries, especially in the region of recirculation. Due to recirculation, the local shear rate values change and there is a need to analyze the non-Newtonian behavior. The influence of the non-Newtonian properties of blood on hemodynamics in a bifurcation is a crucial parameter. A recent study shows the importance of non-Newtonian modeling of blood in the highly stenosed vessel (Mendieta et al., 2020).

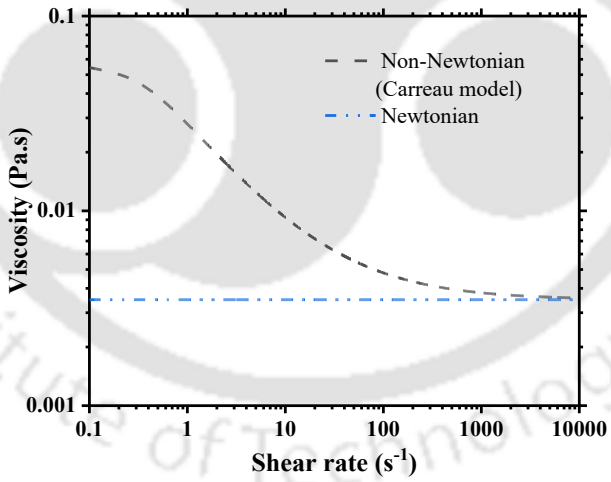

Figure 1.2 Apparent viscosity as a function of shear rate for Newtonian and non-Newtonian (Carreau) model.

The sinus size, position, and bifurcation angles are unique to each person. While the sinus is generally located immediately after the bifurcation, the dilation starts slightly away from the bifurcation in the stenosed ICA. The unique geometry of each person's carotid artery has different

flow features and the possibility of atherosclerosis. Therefore, it is necessary to study the effect of sinus size, position, and bifurcation angles on hemodynamics in a carotid artery bifurcation.

Two-phase flow in a bifurcation

The gas-liquid flow problem in medicine is encountered during gas embolism, gas embolotherapy, mechanical ventilation, and different microfluidic applications. Air embolism is a blockage of blood supply due to air bubbles in the blood, as shown in Fig. 1.3. An embolism has severe side effects, but it can be used to starve unwanted tumors. Gas embolotherapy is a potential cancer treatment in which intra-arterial blood supply to cancer tumors is cut off using gas bubbles (Bull, 2007). In this treatment, the perfluorocarbon (PFC) microdroplets (~6 μm in diameter) are passed through the arteries and selectively vaporized at the desired tumor location using high-intensity ultrasound to occlude the vessels. Due to the occlusion of capillaries, the tumor gets starved because of a shortage of blood supply. For effective treatment, a large number of these bubbles should pass through tumor-affected vessels. Most of the literature studies used symmetric bifurcation, but in-vivo, the arterial network is very complex and asymmetric. For precise and effective embolotherapy, a comprehensive understanding of bubble dynamics at the bifurcation is necessary.

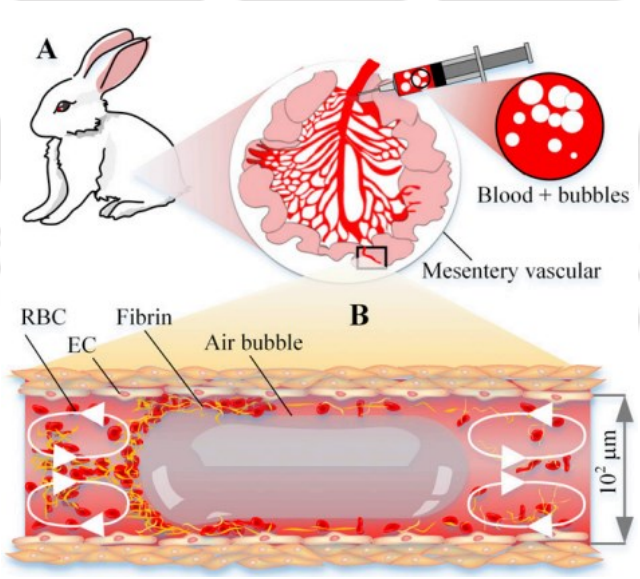

Figure 1.3 Schematic of air embolization and flow patterns around the bubble, adapted from (Li et al., 2021).

Another application of gas-liquid flow in medicine occurred during surfactant therapy (Grotberg, 1994), ventilation during viral pneumonia (Ruuskanen et al., 2011), chronic obstructive pulmonary disease (Pauwels and Rabe, 2004), and COVID19 (Gibson et al., 2020). COVID19 and pneumonia affect respiratory systems and leads to acute respiratory distress syndrome, which needs oxygen supply by a mechanical ventilator. During mechanical ventilation, the oxygen enters the small airways bifurcation (bronchioles) in the form of microbubbles, as shown in Fig. 1.4. These microbubbles exert hydrodynamic stresses on the airway walls, which may enhance the existing lung injuries by damaging the pulmonary epithelium. The hydrodynamic stresses caused by the motion of a bubble depend on the flow velocity, surface tension, viscosity, buoyancy effect, bubble diameter, and airway bifurcation diameter (Chen et al., 2014; Munir and Xu, 2020). Past studies suggested shear stress, pressure, shear stress gradient, and pressure gradient to be potentially injurious to the epithelial cells. Correlating the simulation results with the experimental data, they suggested that the steep pressure gradients near the bubble front or nose are the most likely cause of cellular damage (Bilek et al., 2003; Kay et al., 2004).

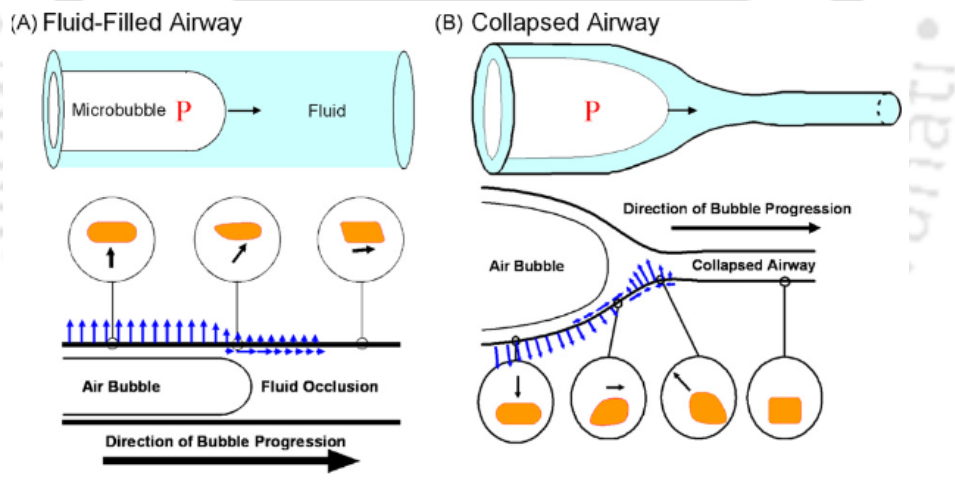

Figure 1.4 Air bubbles propagating through the small fluid-filled and collapsed airways, adapted from (Ghadiali and Gaver, 2008).

Most of the previous studies are limited to bubble propagation and splitting into straight and symmetric airway bifurcations. A recent study analyzed the effect of asymmetric airway bifurcation on hydrodynamic stresses for the constant bubble size and bifurcation angle computationally (Munir and Xu, 2020). In airway bifurcation, the bifurcation size and angle may have an asymmetry. It is necessary to study the bubble hydrodynamics for asymmetric bifurcations.

Chapter 2 Objectives

This thesis aims to develop a comprehensive understanding of flow of liquid and gas-liquid in symmetric and asymmetric bifurcating vessels for application in cardiovascular and pulmonary disease development and management. The specific objectives of the thesis are outlined below:

Single phase flow

- To understand the effect of bifurcation angle on the flow behavior in symmetric and asymmetric bifurcation for steady and pulsatile flow.
- To investigate the effect of sinus size and position in an idealized carotid artery bifurcation on the hemodynamic parameters for pulsatile flow of Newtonian and non-Newtonian liquids.
- To model the flow behavior in a patient-specific carotid artery bifurcation and understand the effect of pulse frequency on the hemodynamic parameters.

Gas-liquid flow

- To understand the effect of bifurcation angle, capillary and Bond numbers on bubble splitting dynamics in symmetric and asymmetric bifurcation using two-dimensional computational fluid dynamic simulations.
- To study the bubble splitting dynamics in a symmetric bifurcation in liquids of different viscosities using flow visualization.

Thesis organization

This thesis is divided in eight chapters. Chapter 1 discusses the motivation of the work whereas this chapter, Chapter 2, describes the objectives of the thesis. The literature relevant to each problem is discussed in each chapter. Chapters 3-5 presents the studies on flow of blood in bifurcating vessels whereas Chapters 6 and 7 describes gas-liquid flow in bifurcating vessels. Finally, main conclusions of the work and recommendation for the future work are presented in Chapter 8. Figure 2.1 shows a schematic of the thesis.

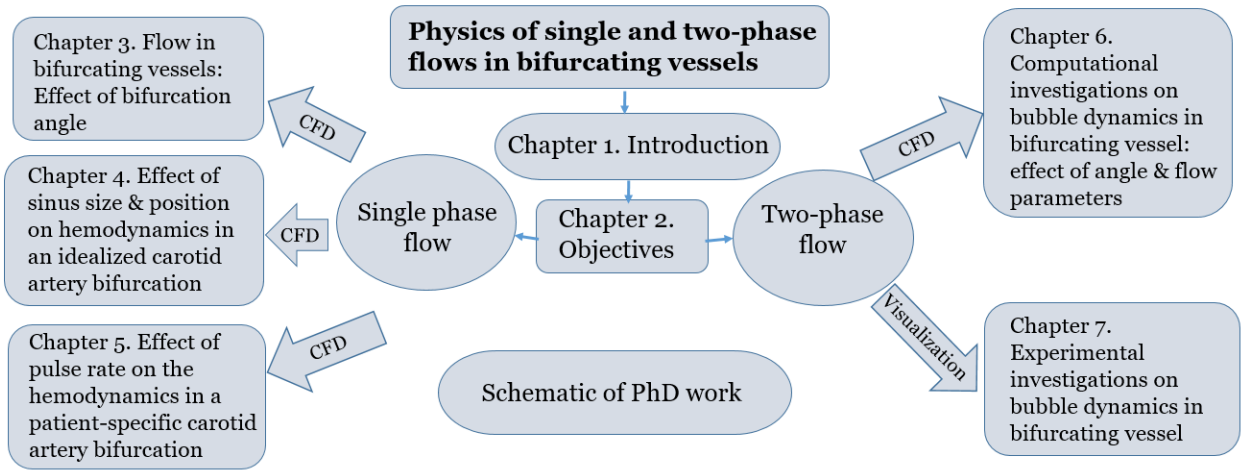

Figure 2.1 Schematic of flow chart for Ph.D. thesis objectives.

In chapter 3, steady as well as pulsatile flow in an idealised arterial bifurcation having equal diameters of mother and daughter vessels is considered. The effect of variation in bifurcation angle on the flow behavior in general and wall shear stress in particular is investigated in symmetric as well as asymmetric bifurcations using computational fluid dynamics (CFD) simulations. Further, the parameters characterising the secondary flow such as vorticity and helicity are presented and the parameters characterising oscillatory nature of wall shear stress such as time-averaged wall shear stress, oscillatory shear index (OSI) and relative residence time (RRT) are analysed.

In chapter 4, an idealised carotid artery bifurcation is considered and the carotid sinus, a dilation in the internal carotid artery is considered. The effect of the position and size of carotid sinus on the flow behavior is investigated on the flow behavior using transient CFD simulations assuming blood to be a Newtonian as well as non-Newtonian liquid. The results are compared in detail in order to understand the circumstances under which the non-Newtonian model must be employed.

In chapter 5, transient CFD simulations have been performed in a patient-specific carotid artery bifurcation geometry obtained from literature. Three different waveforms of different frequencies are considered to understand the effect of pulse frequency on flow behavior and wall shear stress.

In chapter 6, CFD simulations in planar, two-dimensional bifurcations have been performed using volume of fluid (VOF) method to capture the interface between the two phases. Two different scenarios are considered. In scenario one, CFD simulations are performed using blood as the liquid and perfluorocarbon (PFC) as the gas phase for two different values of capillary numbers. The

effect of bifurcation angle on the bubble splitting is investigated in symmetric and asymmetric bifurcating geometries. In the second scenario, CFD simulations are performed for gas-liquid flow in an asymmetric bifurcation and the effect of Bond and capillary numbers on pressure gradient is analysed.

In chapter 7, the bubble dynamics in three Newtonian liquids of varying viscosities for various bubble lengths (l_b/d_m = 2-9) is investigated experimentally at a symmetric bifurcation. A PDMS channel is fabricated in-house using a 3D printed mould. The effect of liquid flow rate at a fixed gas flow rate on bubble size, splitting flow dynamics, and bubble neck dynamics is investigated. A qualitative comparison is made between the bubble break-up and neck thinning between the results obtained from experiments and planar, two-dimensional CFD simulations.

Finally, in chapter 8, the main conclusions of the studies performed in this thesis are summarised and the recommendations have been made for future work.

Chapter 3 Flow in Bifurcating Vessels: Effect of Bifurcation Angle

This chapter describes the effect of bifurcation angle on flow dynamics for steady as well as pulsatile flow in symmetric and asymmetric bifurcations for Newtonian and shear-thinning fluids.

3.1 Introduction

Atherosclerosis or arterial disease is a significant cause of mortality worldwide. It occurs due to the deposition of fatty material on the arterial wall. The accumulation of fat causes a reduction in the cross-sectional area of the vessel and is known as stenosis. Blood flow dynamics or hemodynamics plays a vital role in fat deposition and consequently in the development of arterial disease. Fat deposition is observed frequently at the arterial bifurcations and curved regions of the vascular vessels. Low wall shear stress regions have been linked to atherosclerosis formation and is now widely accepted in the medicine community (Caro et al., 1971a). Transport of nutrients and waste products between the blood and vessel walls depends on the wall shear stress and is low in the regions having slow or stagnant flow and low wall shear stress. Several studies have confirmed that the plaques tend to occur in the regions of low velocity, low wall shear stress (WSS) (Caro et al., 1971a; Malek et al., 1999; Zarins et al., 1983), high oscillatory shear index (OSI) (Ku et al., 1985; Perktold et al., 1991; Perktold and Hilbert, 1986; Perktold and Resch, 1990), and high particle residence time (Araim et al., 2001; Glagov et al., 1988).

At a bifurcation, the mother vessel bifurcates into two daughter vessels, each forming an angle, termed as bifurcation angle, with the mother vessel. The flow and wall shear stress at the bifurcation is affected by different geometrical factors such as the ratio of the diameters of mother and daughter vessels, bifurcation angles, and planarity/ non-planarity of daughter vessels (Chen and Lu, 2006, 2004). In a bifurcating vessel, the flow is generally separated near the outer wall of bifurcation, which causes the recirculation and reduces wall shear stress (WSS) on the outer wall (Chandran et al., 2007). The bifurcation angle is a crucial factor in formulating an intervention strategy in the stenting of coronary arteries (Zhang and Dou, 2015). The wider bifurcation angle causes an increase in backflow, which leads to a decrease in the WSS (Chaichana et al., 2011; Nguyen et al., 2008; Perktold and Resch, 1990). A recent study on planar bifurcation indicates that at a particular flow rate, there exists a critical bifurcation angle above which the vessel is prone to plaque formation (Otero-Cacho et al., 2018). A computed tomography (CT) study on 128 patients with symptoms of headache found that the internal carotid artery angle was wider for patients with

stroke than those for healthy patients (Noh and Kang, 2019). Recently, computed tomography angiography (CTA) study on thirty young patients showed that the patients having wider bifurcation angle had a higher risk of ischemic stroke (Apaydin and Cetinoglu, 2021). There existed an asymmetry in the bifurcation angle at carotid bifurcation in stroke patients, the higher angle between an internal carotid artery (ICA) and common carotid artery (CCA) as compared to that between an external carotid artery (ECA) and CCA.

In a bifurcating vessel, the flow divides in the two daughter vessels and passes through a curved section present at the bifurcation. As a result, the curvature effect also plays an important role in bifurcations. Flow through curved vessels was first studied in 1902 with the experiments of the flow of water in the curved pipe (Williams et al., 1902). They observed the shift in primary velocity towards the outer wall of curvature. Eustice (1910) proposed the presence of secondary flow in a coiled pipe (Eustice, 1911, 1910). Dean (1927) observed secondary flow i.e. flow in the plane normal to the streamwise direction in curved channels (Dean, 1928, 1927). To maintain the balance between centrifugal force and pressure gradient, faster moving fluid must move along the larger radius of curvature paths than that of slower moving fluid (Soh and Berger, 1984). The fluid experience a centrifugal force directed away from the center of curvature. Recently, few studies investigated the secondary flow structures in rigid and flexible curved vessels using numerical and particle image velocimetry (PIV) experiments (Cox et al., 2019; Najjari et al., 2019; Seetharaman et al., 2021). The work by Cox et al. (2019) was extended for analyzing the WSS on the curved artery wall (Cox et al., 2019). The number of secondary vortices in a curved vessel depends on the Reynolds number and the ratio of vessel radius, and the radius of curvature.

Blood exhibits complex rheological behavior. While it behaves as a Newtonian fluid at high shear rates, it shows shear thinning behavior at a low shear rate. At low shear rates, the erythrocytes or red blood cells (RBCs) aggregate, forming cylinder-like long structures, known as rouleaux, and cause an increase in the blood viscosity (Roberston and Owens, 2009). With an increase in the shear rate, the aggregates gradually break up, resulting in a decrease in the viscosity and finally reaching an asymptotic value of ~3.5 centipoises. In a straight vessel, the velocity gradient and shear rate change from zero at the center to a maximum value on the channel wall. In a bifurcating vessel, there are large variations in the shear rates in different regions. Especially, the shear is low in the region where the flow is separated from the wall. As a result, it is important to consider the non-Newtonian behavior in the modeling of blood flow in bifurcating vessels.

Chen and Lu (2004) investigated flow in a symmetric, non-planar bifurcating vessel for steady and pulsatile flow of blood and compared the flow behavior for Newtonian and non-Newtonian fluids (Chen and Lu, 2006, 2004). Chaichana et al. (2011) investigated the flow behavior in the left coronary artery for symmetric bifurcation. The bifurcation angle varied from 7.5° to 60° (Chaichana et al., 2011). To the best of the author's knowledge, there is no study that investigates the blood flow in an asymmetric bifurcation for a non-Newtonian fluid.

In the present work, numerically the steady and pulsatile flow of blood is studied in symmetric and asymmetric bifurcating vessels assuming the blood to be a Newtonian fluid as well as a non-Newtonian fluid following the Carreau model (Cho and Kensey, 1991). The effect of bifurcation angle on primary, secondary flow, and wall shear stress (WSS) is investigated for steady flow. In pulsatile flow, for symmetric bifurcations, the flow field, secondary flow, wall shear stress, vorticity, and helicity are studied by varying the bifurcation angle for three bifurcation angles 30°, 45°, and 60°. For asymmetric bifurcation, the flow field in three different combinations of bifurcation angles 15°-60°, 30°-60°, and 45°-60° is investigated. Further, the time-averaged wall shear stress (TAWSS), oscillatory shear index (OSI), and relative residence time (RRT), the parameters suggested in the literature as biomarkers, are presented for symmetric as well as asymmetric bifurcations.

3.2 Computational methodology

3.2.1 Computational domain

The diameters *(d)* of the mother and daughter vessels are assumed to be 8 mm each, the length of the mother vessel is 3*d,* and that of each daughter vessel is 8*d* following Chen and Lu (2004, 2006). The schematic of the bifurcating vessel is plotted in xz coordinate system, as shown in Fig. 3.1(a). Velocity components are defined using global coordinate system defined in the Fig. 3.1(a). The bifurcation angles (α, β) are varied symmetrically ($\alpha = \beta$) and asymmetrically ($\alpha \neq \beta$). The origin of the coordinate system lies at the end of mother vessel i. e. 3 mm from the inlet and it is shown by red cross symbol in Fig. 3.1(a). The values of the angles are given in Table 3.1 for both cases.

Table 3.1 Various bifurcation angle combinations used in the present study

Sr. No.	Case	Angle
1	Symmetric	$\alpha = \beta = 15°$
2	Symmetric	$\alpha = \beta = 30°$
3	Symmetric	$\alpha = \beta = 45°$
4	Symmetric	$\alpha = \beta = 60°$
5	Asymmetric	$\alpha = 15°, \beta = 30°$
6	Asymmetric	$\alpha = 15°, \beta = 45°$
7	Asymmetric	$\alpha = 15°, \beta = 60°$
8	Asymmetric	$\alpha = 30°, \beta = 45°$
9	Asymmetric	$\alpha = 30°, \beta = 60°$
10	Asymmetric	$\alpha = 45°, \beta = 60°$

3.2.2 Governing equations

Pulsatile, incompressible, laminar flow of blood in planar three-dimensional idealized arterial bifurcation is considered. The channel walls are assumed to be smooth and rigid. The mass and momentum conservation equations can be written as given by Eqs. (3.1) and (3.2), respectively.

Continuity equation:

$$\nabla . \boldsymbol{u} = 0 \tag{3.1}$$

Momentum conservation equation:

$$\rho \left(\frac{\partial \boldsymbol{u}}{\partial t} + (\boldsymbol{u}.\boldsymbol{\nabla})\boldsymbol{u} \right) = -\boldsymbol{\nabla} P + \boldsymbol{\nabla}.\boldsymbol{\tau} \tag{3.2}$$

where ρ is the density of the fluid, $\boldsymbol{u}$ is the fluid velocity vector, and P is the pressure. $\boldsymbol{\tau}$ is the stress tensor and is represented by Eq. (3.3).

$$\boldsymbol{\tau} = \mu(\dot{\gamma})\, \boldsymbol{D} \tag{3.3}$$

μ represents the viscosity or apparent viscosity of the fluid, and $\boldsymbol{D}$ is the shear rate tensor. For a Newtonian fluid, μ is a constant, whereas for a non-Newtonian fluid, μ is a function of $\boldsymbol{D}$. The shear rate tensor is represented by Eq. (3.4).

$$\boldsymbol{D} = \frac{1}{2} (\nabla \boldsymbol{u} + \nabla \boldsymbol{u}^T) \tag{3.4}$$

$\dot{\gamma}$ is the magnitude of shear rate tensor $\boldsymbol{D}$ given by Eq. (3.5).

$$\dot{\gamma} = \sqrt{\frac{1}{2}\boldsymbol{D}:\boldsymbol{D}} \tag{3.5}$$

3.2.3 Rheological model

The apparent viscosity of blood depends on the shear rate. Carreau Model, given by Eq. (3.6), is used to represent the shear dependence of blood viscosity.

$$\mu = \mu_\infty + (\mu_0 - \mu_\infty)[1 + (\lambda\dot{\gamma})^2]^{\frac{n-1}{2}} \tag{3.6}$$

μ_0 is the viscosity at zero shear rate, μ_∞ is the viscosity as shear rate approaches to high values and the fluid shows Newtonian behavior, λ is the relaxation time (s) and its value is empirically determined, $\dot{\gamma}$ is the shear rate (s^{-1}), and n is the power-law index (Cho and Kensey, 1991). The parameters used for Carreau model are summarized in Table 3.2.

3.2.4 Boundary conditions

3.2.4.1 Inlet

Steady flow

At the inlet of the mother vessel, a constant velocity of 0.149 m s^{-1} (Re = 360) normal to the inlet plane having a parabolic profile corresponding to fully developed laminar flow in a pipe is imposed.

Pulsatile flow

The flow in large arteries is pulsatile in nature. The pulse rate in a healthy human being is 72 per minute in resting conditions and becomes significantly higher during exercise conditions (Hall and Guyton, 2011). A pulse rate of 120 beats per minute is considered in this work. This results in a cycle time period of 0.5 s, as shown in Fig. 3.1(b). The Womersley number $= \sqrt{\frac{R^2\omega\rho}{\mu}}$ (R=0.004 m, ρ=1060 kg/m^3, μ=0.0035) (Womersley, 1957), corresponding to this frequency for the Newtonian fluid is 3.1. In each cycle, the left ventricle pumps blood to the circulatory system during systole and is filled with blood during the period of diastole. The period of systole is typically 40% of the cardiac cycle and increases with an increase in the pulse rate. During the systolic period, the flow rate increases and then decreases while the flow is relatively steady in the systemic circulation

during the period of diastole. The flow is therefore assumed to be sinusoidal during the period of systole and steady during the period of diastole. At the inlet boundary, a time-dependent boundary condition given by Eq. (3.7) is specified.

$$u_{inlet}(t) = \begin{cases} 0.5\,sin[4\pi t + 0.218], & 0.5n < t \leq 0.5n + 0.218 \\ 0.1, & 0.5n + 0.218 < t \leq 0.5(n+1) \end{cases} \quad (3.7)$$

3.2.4.2 Outlet

The pressure at the two outlet boundaries is assumed to be the same, and uniform pressure (gauge) of 0 Pa is specified at the outlet boundaries for steady as well as pulsatile flow.

3.2.4.3 Walls

The vessel walls are assumed to be rigid. A no-slip boundary condition is specified on the channel walls.

Table 3.2 Parameters of the rheological models used in the present CFD simulations.

Viscosity model	Parameters
Newtonian	μ = 0.0035 Pa.s
Carreau (non-Newtonian)	μ_0 = 0.056 Pa.s
(Cho, Y. I., Kensey, 1991)	μ_∞ = 0.0035 Pa.s
	λ = 3.131 s
	n = 0.3568

3.2.5 Numerical schemes

The governing equations are solved using a commercial computational fluid dynamics (CFD) software package ANSYS Fluent (Fluent, 2019), which uses a finite volume method to discretize the system of equations. The pressure-based solver, which sequentially solves non-linear mass and momentum conservation equations, is used. A first-order implicit time marching scheme is used for the discretization of the unsteady term. A second-order upwind scheme is used to discretize the advection term (Barth and Jaspersen, 1989).

Following the suggestions of Nguyen et al. (Nguyen et al., 2008), a time step of 0.005 s is used for the unsteady simulations so that the results are independent of the time step used. The time-

dependent simulations are run for five cycles or a flow time of 2.5 s. The solution convergence criteria are set such that residuals are below 10^{-4} at each time step.

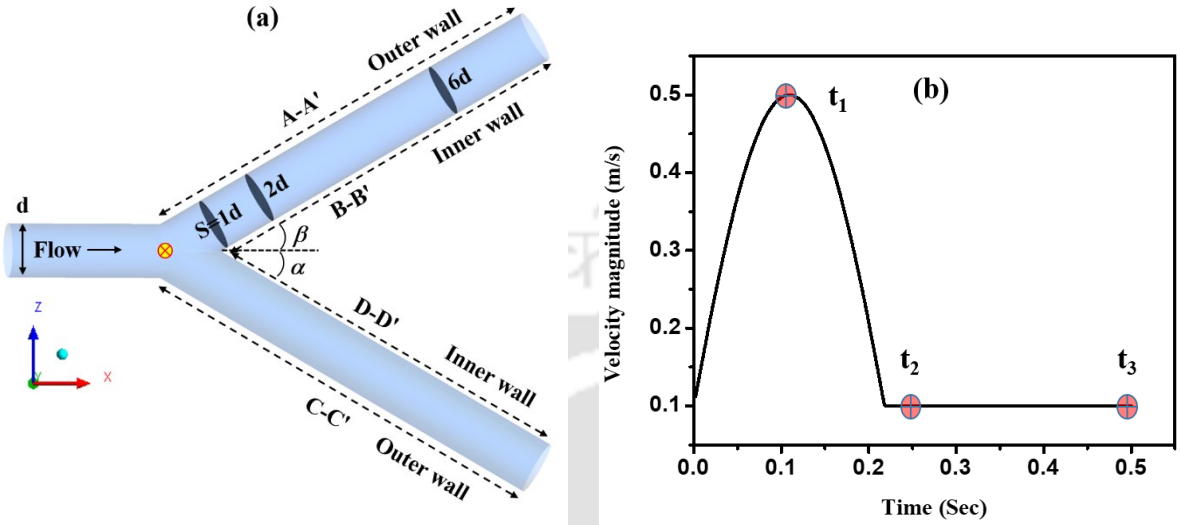

Figure 3.1 (a) Schematic of the bifurcation geometry having mother and daughter vessels of diameter *d*, red cross symbol shows origin (b) Time-varying velocity imposed on the inlet boundary in a cardiac cycle (t_1 = peak systole, t_2 = beginning of diastole, t_3 = end of diastole).

3.3 Results and discussion

3.3.1 Steady flow

A computational grid consisting of tetrahedral elements with five layers of inflation (prism elements) on the channel walls, as shown in Fig. 3.2(a), has been used for the steady simulations. The grid is refined at the bifurcation to capture the large gradients. A grid independence study has been carried out to establish the accuracy of the solution. It is found that the solution becomes independent for the grid having 0.36 million cells. So, the final grid comprises 0.36 million elements.

The Validation of the simulations has been done with the results of Lu et al. (2002) and carotid artery experimental results of Gijsen et al. (1999). Fig. 3.2(b) shows the comparison of axial velocity profile obtained in a carotid artery at Re = 270 with that obtained experimentally by Gijsen et al. (1999). Fig. 3.3 shows the comparison of secondary flow streamlines at different cross-sections in the daughter vessel (radii 8mm & Re = 200) at various locations obtained by Lu et al. (2002) and the present CFD simulations. There is a good qualitative agreement between the two cases.

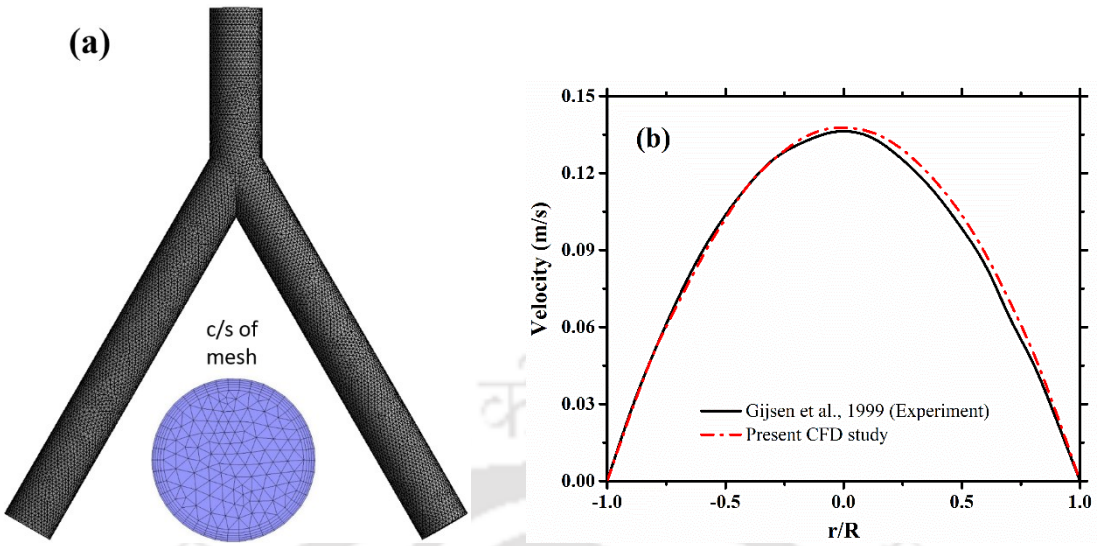

Figure 3.2 (a) Mesh with five layer of inflation (b) Comparison of axial velocity across pipe diameter (diameter 8mm) at the end of mother vessel (16 mm from inlet) with experimental results of Gijsen et al. 1999 at Re = 270.

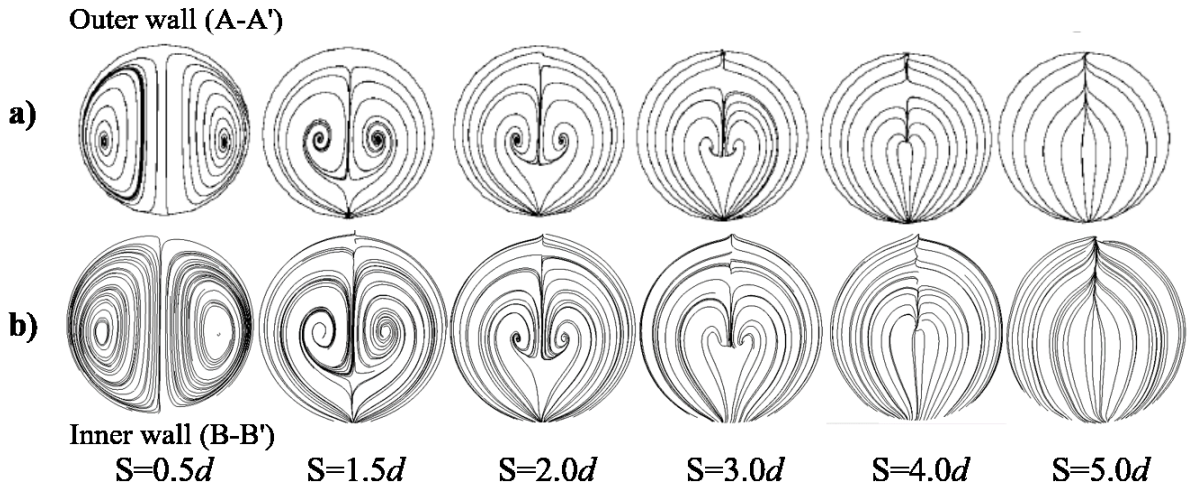

Figure 3.3 Comparison of the secondary vortices obtained in the daughter vessel in a bifurcating channel having vessel radii 8mm, Reynolds number 200 (a) Lu et al., 2002 (b) Present CFD study.

3.3.1.1 Symmetric Bifurcation (α=β)

In the symmetric bifurcation, the angle between the two daughter vessels is equal. Fig. 3.4 shows the typical flow features at the symmetric bifurcation having bifurcation angles of 45° each for a mother vessel Reynolds number of 360. The streamlines follow a helical path at the bifurcation, and the flow has recirculating patterns along the streamwise as well as transverse directions. In the streamwise direction, the flow separates from the outer channel wall at the bifurcation and

reattaches downstream. Consequently, a recirculation along the axial direction is formed near the outer wall.

Furthermore, similar to the Dean vortices observed in the curved channels, secondary vortices occur in the transverse direction. Due to the flow separation, the area available for the forward flow reduces in the daughter vessel near the bifurcation. The decrease in the area causes an increase in the velocity near the inner wall of bifurcation. The streamlines are symmetric about the bifurcation plane passing through the center of the channels. The pressure distribution superimposed on surface streamlines in the bifurcation plane is shown in Fig. 3.4(b). As the flow is laminar and fully developed in the mother vessel, the pressure decreases linearly in it. Lower pressure is observed at the junction of the mother and daughter vessel at the outer walls. The pressure increases downstream of the intersection and causes the flow to separate from the exterior wall. Consequently, the flow coming out of the mother vessel moves straight first and divides in the two daughter vessels when it approaches the inner wall. The pressure at the junction of the inner wall is observed to be maximum. As the flow turns, the pressure near the inner wall increases to balance the centrifugal force (Matsumoto et al., 2016).

Fig. 3.5 shows the evolution of the axial velocity profile on the bifurcation plane in the daughter vessel as the flow moves downstream of the bifurcation. The velocity profiles are plotted at locations having different values of S, representing the distance of the line from the bifurcation point, as shown in Fig. 3.1, ranging from 0 to 8*d*. The non-dimensional radius (*r/R*) shown on the y-axis varies from -0.5 to 0.5 and corresponds to the outer and inner walls, respectively. The velocity profiles are plotted for four different bifurcation angles 15°, 30°, 45°, and 60°.

Negative x-velocity near the bifurcation, for example at S=1*d* for all the bifurcation angles, is because of the flow separation in the outer wall region. The active area available for the downstream flow is reduced because of the flow separation, and the downstream flow is shifted towards the inner wall.

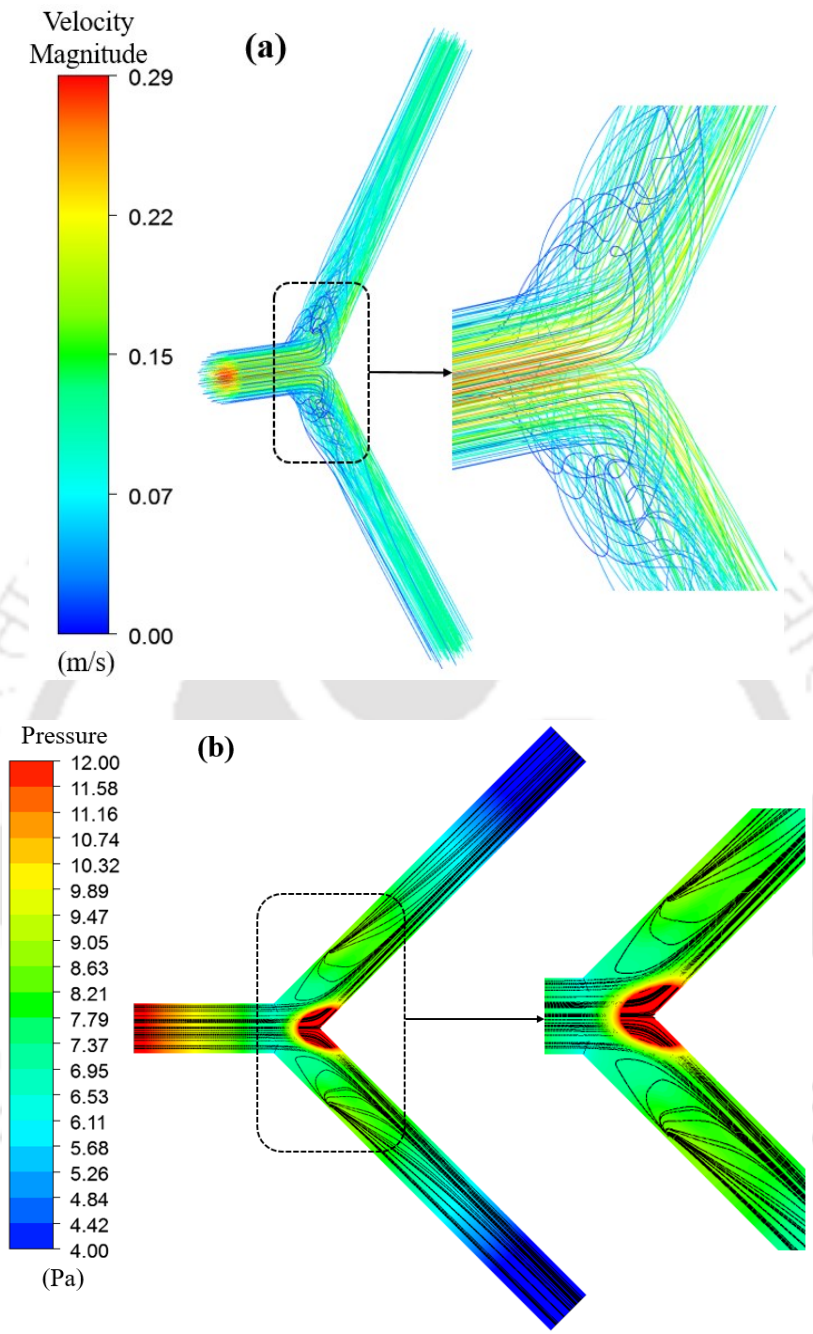

Figure 3.4 Streamlines and pressure contours superimposed on surface streamlines in symmetric bifurcating channel ($\alpha = \beta = 45^{O}$) at r=0 of xz plane colored by velocity magnitude having circular cross-section of radius 8mm, flow Re = 360 (a) Streamlines (b) Pressure contour.

Consequently, the location of maximum velocity in the downstream flow is shifted towards the inner wall. A reduction in the magnitude of the x-component of velocity with an increase in the bifurcation angle is observed. This is because of the decrease in the x-component of velocity with an increase in the bifurcation angle. As the flow moves downstream in the daughter vessel, the

velocity profile approaches again towards a symmetric parabolic velocity profile corresponding to the fully-developed laminar flow in a channel. For a higher bifurcation angle, the vessel length required to obtain a symmetric velocity profile is less than that required for the daughter vessel having a lower bifurcation angle.

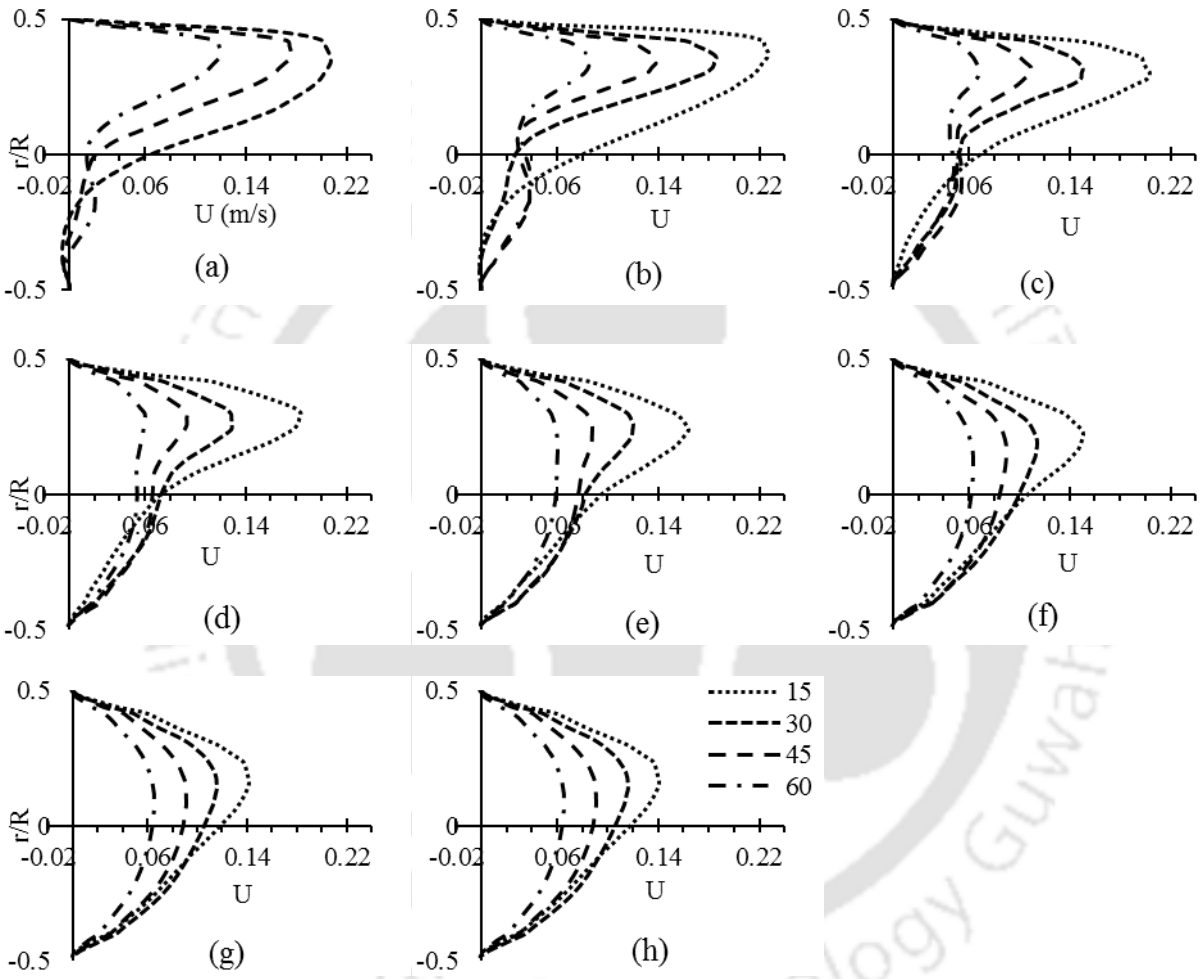

Figure 3.5 Profile of x-velocity on a line segment passing through x-z plane at different bifurcation angle (α=β =15^{O}, 30^{O},45^{O},60^{O}) and at a distance of (a) S=1d (b) S=2d (c) S=3d (d) S=4d (e) S=5d (f) S=6d (g) S=7d (h) S=8d.

As mentioned earlier, the flow turns at the bifurcations, and secondary flow is observed near the bifurcation. The surface streamlines at six different planes normal to the axis in the daughter vessel show the secondary motion along with the contours of velocity magnitude in Fig. 3.6. Again, it can be observed from the figure that the velocity magnitude is maximum near the inner wall (left) for all the angles, and the location of maximum velocity shifts towards the channel axis on moving

away from the bifurcation. A pair of the secondary vortices are generated on the plane normal to the axis of the daughter vessel right after the mother vessel. The center of vortices moves from the vessel wall towards the axis on moving downstream of the bifurcation. Further downstream, the secondary flow disappears, as can be seen in Figs. 3.6(a) and 3.6(b). There is a noticeable effect of the bifurcation angle on the secondary flow. With an increase in the bifurcation angle, the secondary flow or Dean vortices take more length downstream of the channel to get merged. In past studies, a similar kind of secondary flow vortices has been shown for steady and pulsatile flow through arterial bifurcation for non-Newtonian fluid (Chen and Lu, 2006, 2004). Similarly, Dean vortices were observed for multiple bifurcations of the lung model for constant and symmetric bifurcation angle (Evegren et al., 2010; Guha et al., 2016; Guha and Pradhan, 2017). The primary flow and secondary vortices are symmetric about the bifurcation plane for all the cases.

The wall shear stress (WSS) depends on the flow behavior in the vessel. In Fig. 3.7, the wall shear stress is plotted on the inner and outer walls at the bifurcation plane for four different bifurcation angles ($\alpha = \beta$ =15°, 30°, 45°, 60°) for the symmetric bifurcation. The lines on the outer wall are named AA' and CC', whereas those on the inner wall are named as BB' and DD' in the two daughter vessels. The magnitude of wall shear stress normalized by that for Poiseuille flow (corresponding to the flow rate in the mother vessel, 0.52 Pa) is plotted. The magnitude of WSS on the outer wall (~0.05 Pa) at the bifurcation is one order of magnitude lower than that at the inner wall (~1-2 Pa). However, away from the bifurcation, WSS approaches the same value (~0.25 Pa) on both the walls as the boundary layer redevelops in the channel. In the case of a higher angle, the WSS value approaches the value for fully-developed flow in a shorter distance as compared with that in the daughter vessel having a smaller angle, as shown in Fig. 3.7(a).

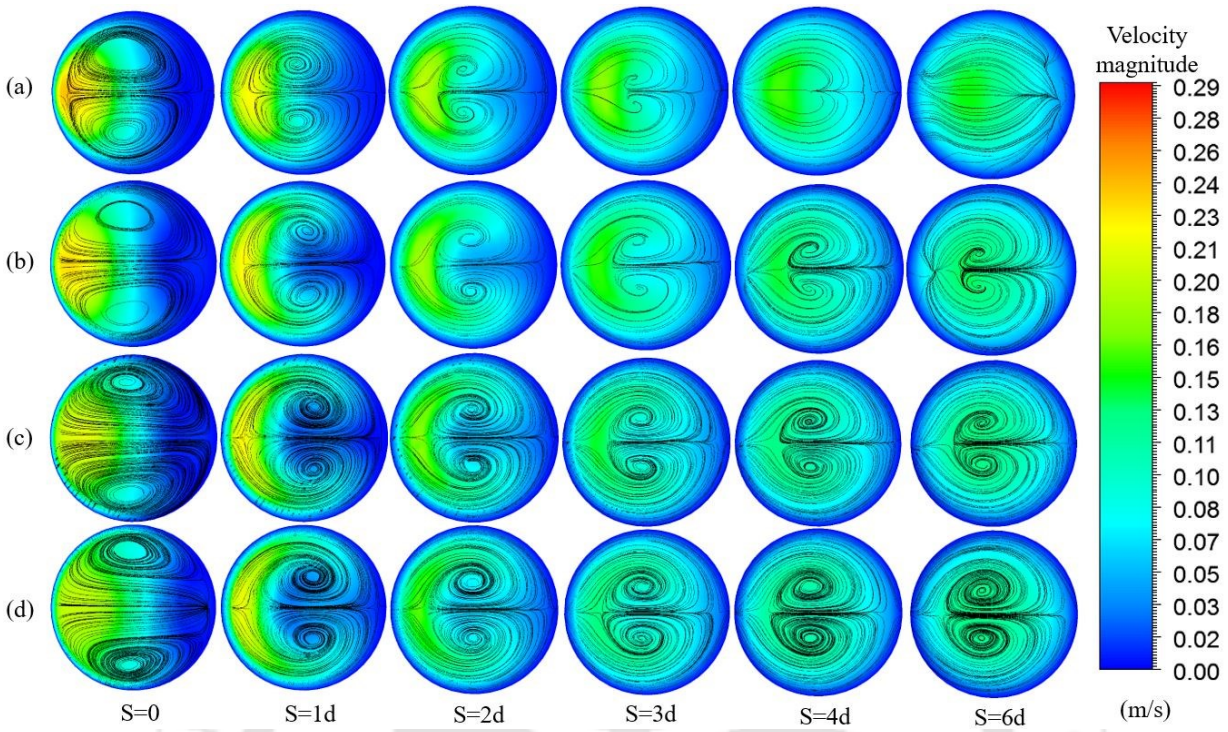

Figure 3.6 Streamlines superimposed on the velocity magnitude contour on a plane normal to the axis of daughter vessel on six planes at a distance of 0-6d from the point of bifurcation (right side of Fig.: outer wall of bifurcation, left side: inner wall of bifurcation). (a) $\alpha = \beta = 15^{O}$ (b) $\alpha = \beta = 30^{O}$ (c) $\alpha = \beta = 45^{O}$ (d) $\alpha = \beta = 60^{O}$.

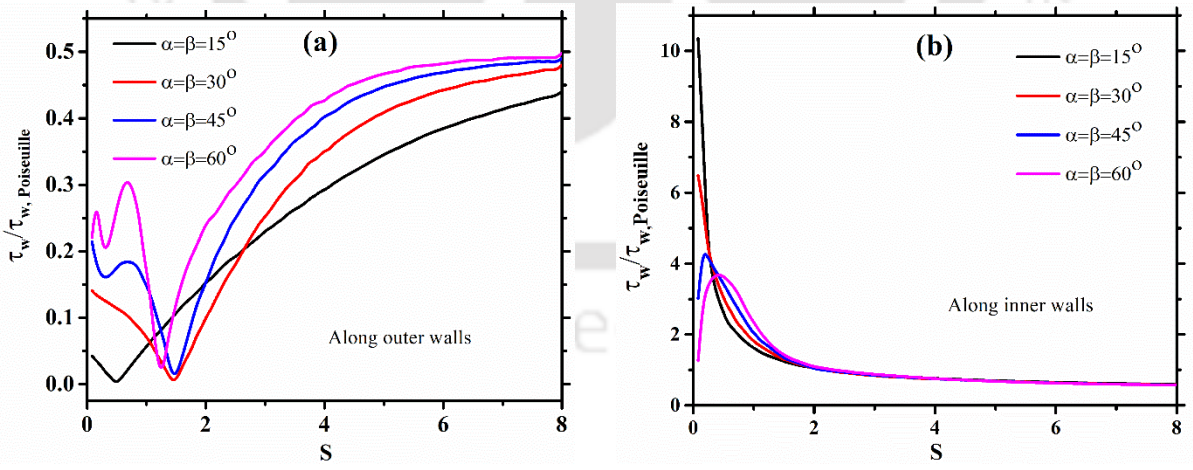

Figure 3.7 WSS along the daughter vessels for symmetric case (a) CC' (outer wall) (b) DD' (inner wall), respectively for different bifurcation angles in a channel of diameter 8 mm and flow Reynolds number 360.

As seen earlier, the flow velocity near the inner wall is increased near the bifurcation. This explains the high WSS on the inner wall. The velocity magnitude in the recirculation near the outer wall is low, causing low WSS on the outer wall. The point at which the WSS is zero also represents the point on the exterior wall at which the velocity and shear stress change direction, and this point represents the length of the recirculation zone. The recirculation zone is minimal for the 15° angle, whereas those for the three larger angles are almost equal. Fig. 3.8 (a) shows the effect of bifurcation angle on maximum WSS on daughter vessels. With an increase in the angle, the maximum value of WSS decreases, which is in agreement with the literature (Arjmandi-Tash et al., 2011; Chaichana et al., 2011; Perktold et al., 1991). The effect of the bifurcation angle on the pressure drop in the daughter vessel, i.e., the pressure difference between the entry and exit planes, is shown in Fig. 3.8 (b). The pressure drop in the daughter vessel increases with an increase in the bifurcation angle.

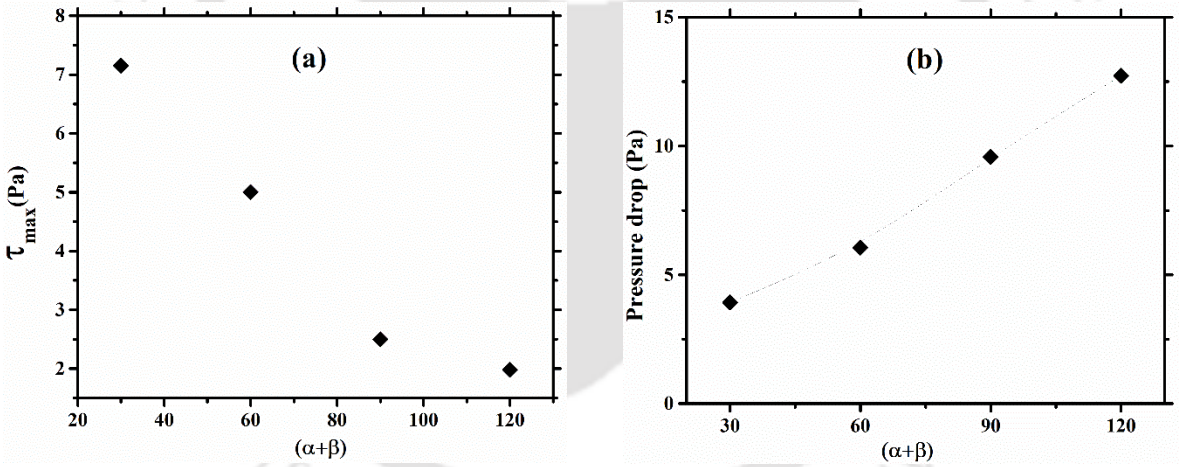

Figure 3.8 Effect of symmetric bifurcation angle ($\alpha + \beta$) on (a) the maximum wall shear stress on daughter vessels (b) pressure drop at the bifurcation.

3.3.1.2 Asymmetric bifurcation (α≠β)

As given in Table 3.1, the effect of bifurcation asymmetry on the flow behavior is investigated by choosing two different bifurcation angles, i.e., $\alpha \neq \beta$. Fig. 3.9 (a) and (b) show the streamlines colored by velocity magnitude and pressure contours superimposed on surface streamlines at the bifurcation plane, respectively, in an asymmetric channel having $\alpha = 15^{O}$ and $\beta = 60^{O}$. From the streamlines, it is clear that the flow is bifurcated asymmetrically in the two daughter vessels with

higher velocity in the daughter vessel having a smaller angle. The vortices are observed to be stronger in the daughter vessel, having a larger bifurcation angle. The pressure decreases monotonically in the axial direction in the mother vessel and is uniform radially except near the bifurcation. Near the bifurcation, the pressure is observed to vary radially, with high pressure towards the daughter vessel having a smaller angle and lower pressure towards the vessel having a larger angle. This results in a small transverse velocity component causing the flow to turn slightly towards the daughter vessel having a larger angle. When the fluid stream hits the intersection points of the inner walls of the two daughter vessels, it gets diverted in the two daughter vessels. As the intersection point is located away from the axis of the mother vessel towards the daughter vessel having a larger angle, a larger part of the flow enters in the daughter vessel having a smaller angle. The pressure drop in the daughter vessel having a larger angle is significantly higher than that in the daughter vessel having a lower angle.

In Fig. 3.10 (a) and (b), the flow fraction in the daughter vessel having a larger angle is plotted as a function of the angle ratio. For the symmetric bifurcation, i.e. an angle ratio of 1, the flow fraction in each vessel is 0.5. As can be deduced from Table 3.1, the angle ratio varies from 1.33 (α=45^O, β =60^O) to 4.0 (α=15^O and β =60^O) in the asymmetric cases simulated. Note that the angle ratio has the same value of 2 for two cases α=15^O, β =30^O and α=30^O, β =60^O. With an increase in the angle ratio, the flow fraction in the daughter vessel has larger angle decreases. For an angle ratio of 1.5, 44% of the flow goes in the daughter vessel having a higher angle. The flow fraction in the daughter vessel decreases to 40.5% and 35.5% for the angle ratios of two and three, respectively. Finally, at an angle ratio of 4, the flow fraction decreases to 32%.

In all results presented in Fig. 3.11-3.13, the profile of x- component of velocity for different asymmetric bifurcating vessels for the cases given in Table 3.1 is shown at various locations in the daughter vessels. The x – component of velocity is the component parallel to mother vessel. These axial velocity profiles across channel diameter of daughter vessel at different locations downstream are consistent with observations obtained in the numerical studies for constant bifurcation angle (Chen and Lu, 2006, 2004; Lu et al., 2002).

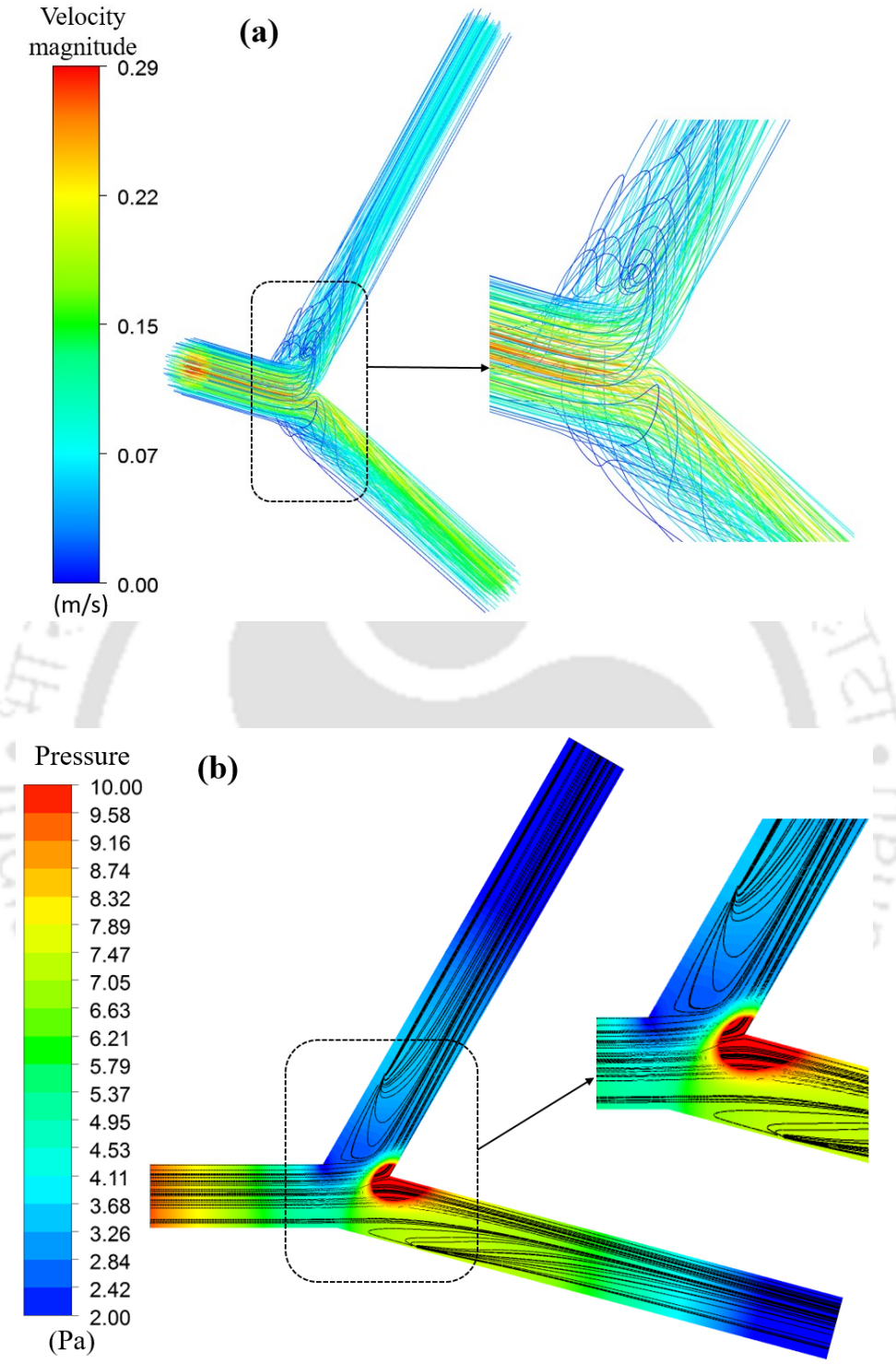

Figure 3.9 Streamlines and pressure contours superimposed on surface streamlines in the asymmetric bifurcating channel ($\alpha = 15^{O}$, $\beta = 60^{O}$) colored by velocity magnitude having a circular cross-section of radius 8mm, flow Re=360 (a) Streamlines (b) Pressure contour.

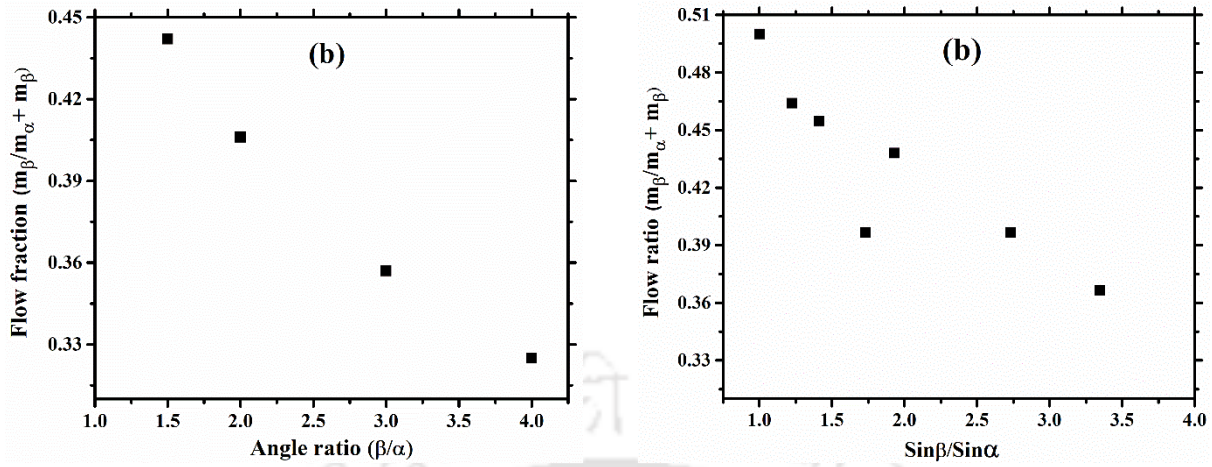

Figure 3.10 (a) Effect of angle ratio on flow fraction in daughter vessels (b) Effect of Sine of angle ratio on flow fraction in daughter vessels at Re = 360.

Figure 3.11 shows the results for the three cases having bifurcation angles of $\alpha = 15°$ and $\beta = 30°$, 45°, and 60° in the daughter vessel. The daughter vessel having a larger angle shows a decrease in the maximum x-component of velocity, and the area swept by recirculation increases with an increase in angle, as can be seen from Fig. 3.11 (a). The disturbed or skewed velocity profile at bifurcation regains its symmetric shape downstream of the daughter vessel. The length required to get a symmetric velocity profile downstream of the daughter vessel depends on the bifurcation angle. The skewed flow at the bifurcation tries to regain its symmetric velocity profile across the vessel diameter towards the outlet of the daughter vessel. The asymmetry in the profile at the outlet is less in the case of a larger angle as compared to the smaller ones. As shown in Fig. 3.11(f), the velocity profile for the daughter vessel having angle *(β=60°)* becomes symmetric at the distance *8d* while lower angles vessels still have asymmetric velocity profile across the diameter of the channel. The asymmetry is more for lower angle vessels as compared with for higher angled ones at a particular position on the daughter vessel.

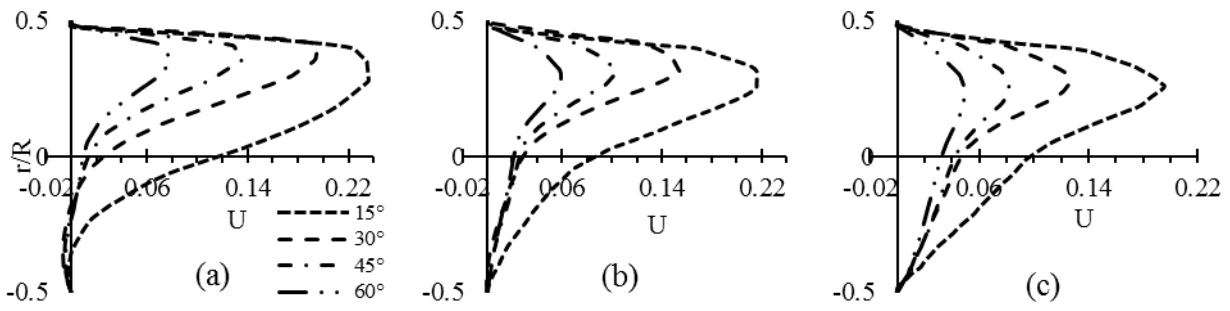

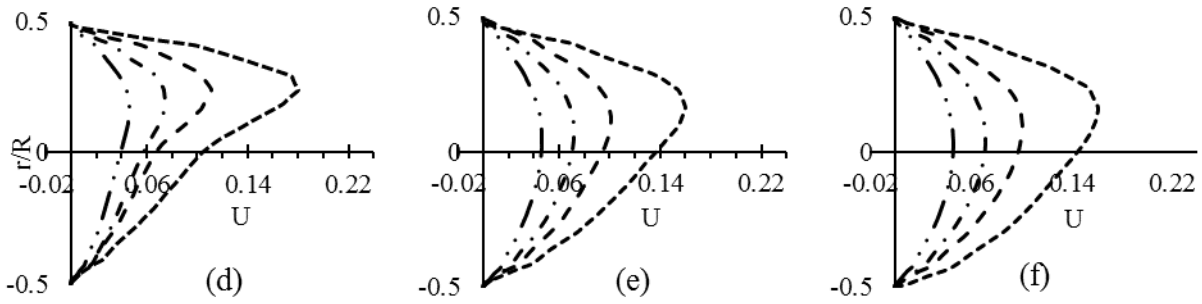

Figure 3.11 Profile of x-velocity on a line segment passing through x-z plane for (α = 15^{O}, β = 30^{O},45^{O},60^{O}) and at a distance of (a) S = 1.5d (b) S = 2.5d (c) S = 3.5d (d) S = 4.5d (e) S = 7d (f) S = 8d.

The value of the total bifurcation angle *(α+β)* has a direct effect on the flow at the outer wall of bifurcation. As the total angle increases, two axial velocity peaks are observed, one at the outer side of the bifurcation wall and maximum one at the inner side, as shown in Fig. 3.12 (a, b, c). The two axial velocity peaks started at an angle of 90°, as shown in Fig. 3.12 (b). This flow behavior occurs due to a wider angle. Similar flow profiles are observed for higher α = 45^{O}, β = 60^{O} case, as shown in Fig. 3.13. Maximum velocity values decrease with an increase in the total bifurcation angle.

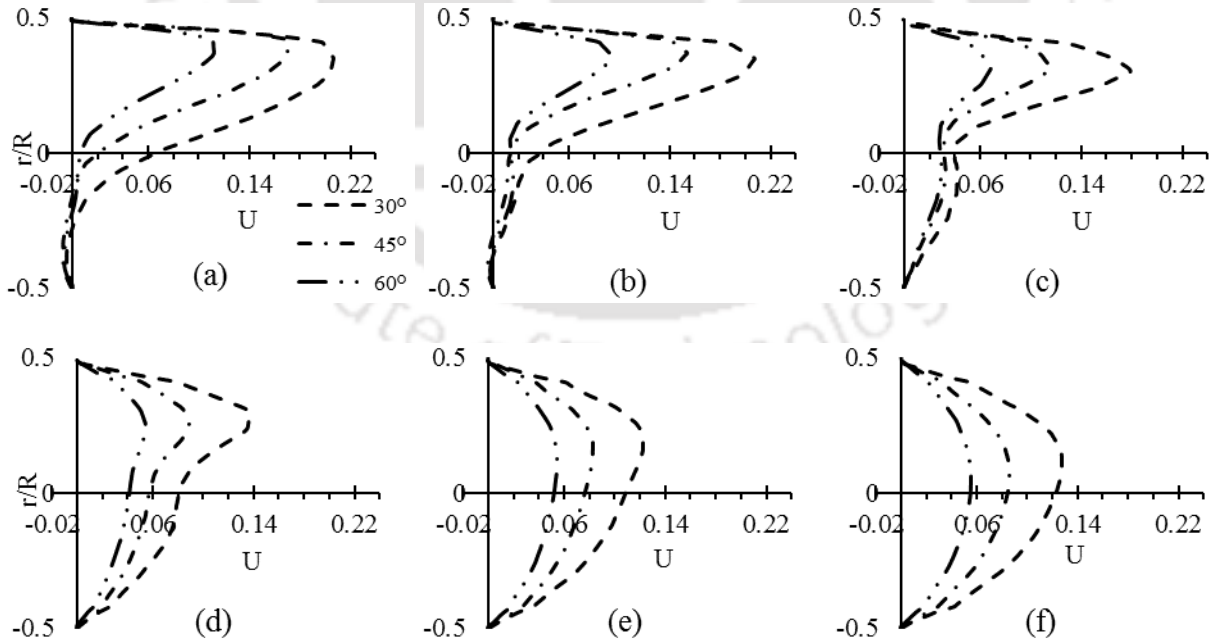

Figure 3.12 Profile of x-velocity on a line segment passing through x-z plane (α = 30^{O}, β = 45^{O} and 60^{O}) and at a distance of (a) S = 1d (b) S = 1.5d (c) S = 2.5d (d) S = 4d (e) S = 6d (f) S = 8d.

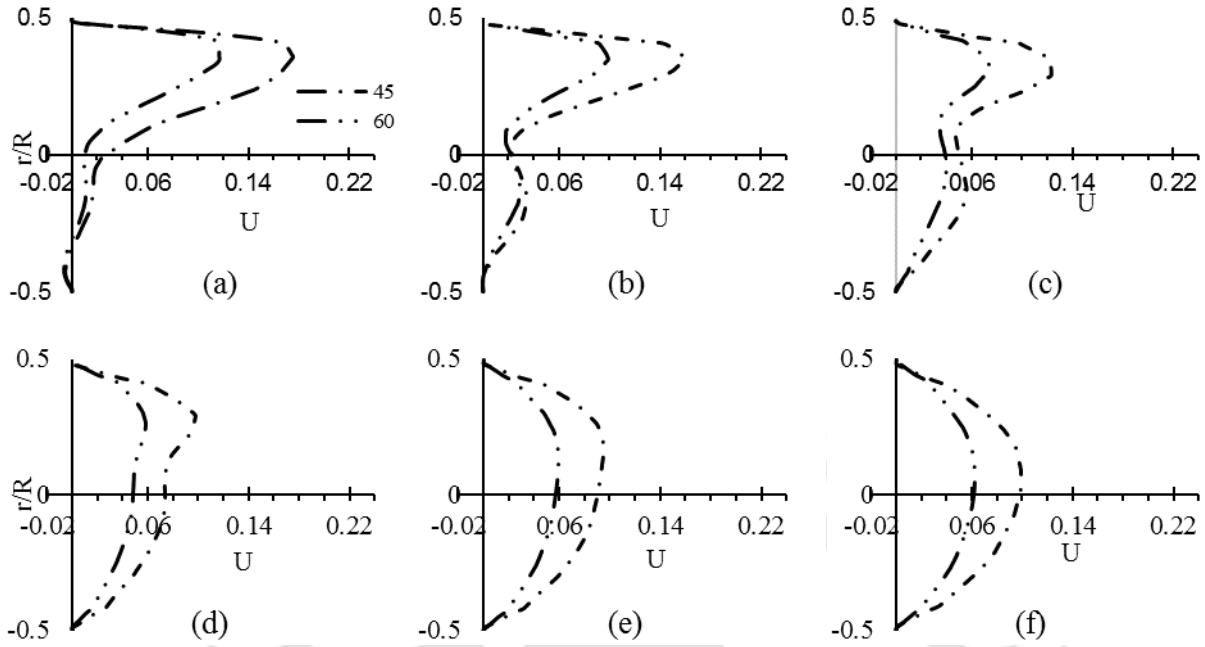

Figure 3.13 Profile of x-velocity on a line segment passing through x-z plane (α = 45^{O}, β = 60^{O}) and at a distance of (a) S = 1*d* (b) S = 1.5*d* (c) S = 2.5*d* (d) S = 4*d* (e) S = 6*d* (f) S = 8*d*.

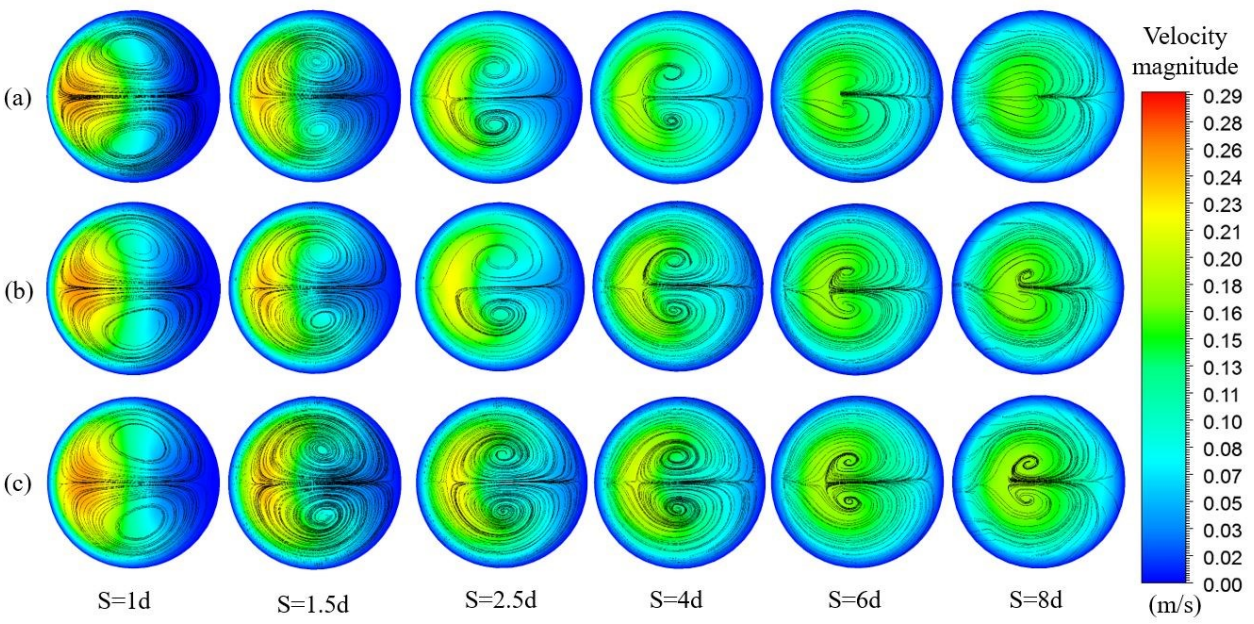

Figure 3.14 Streamlines superimposed on the velocity magnitude contour on a plane normal to the axis of daughter vessel on six planes at a distance of 0-8d from the point of bifurcation in the daughter vessel having larger angle. (1-6) (a) α = 15^{O}, β = 30^{O} (b) α = 15^{O}, β = 45^{O} (c) α = 15^{O}, β = 60^{O}.

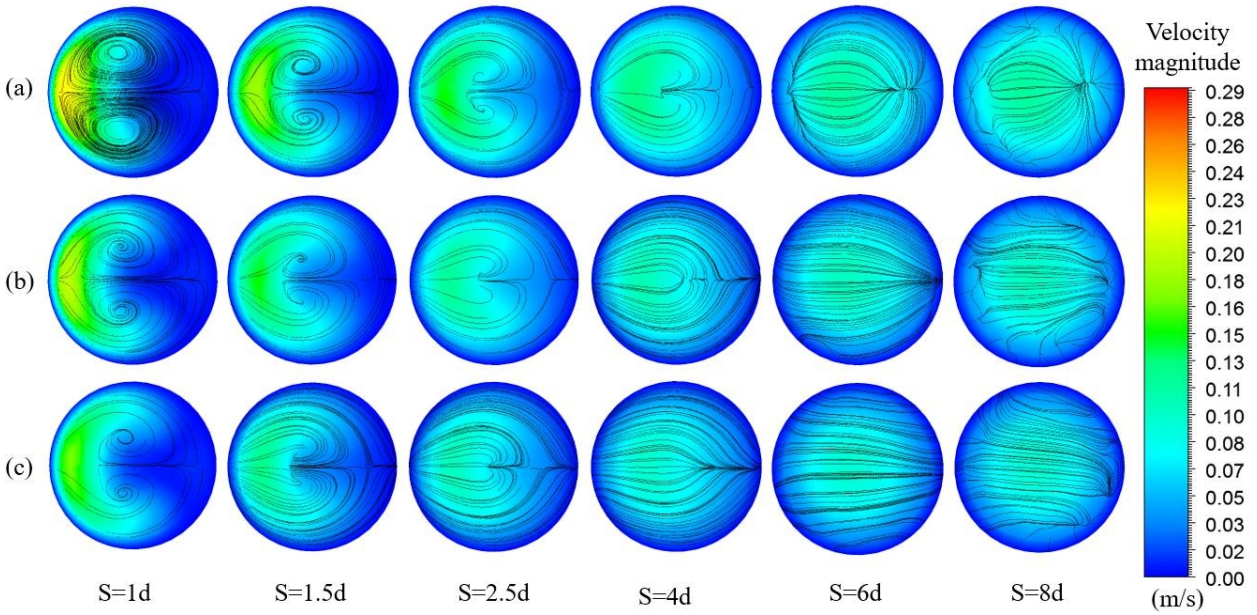

Figure 3.15 Streamlines superimposed on the velocity magnitude contour on a plane normal to the axis of daughter vessel on six planes at a distance of 0-8d from the point of bifurcation in the daughter vessel having smaller angle. (1-6) (a) $\alpha = 15^{O}$, $\beta = 30^{O}$ (b) $\alpha = 15^{O}$, $\beta = 45^{O}$ (c) $\alpha = 15^{O}$, $\beta = 60^{O}$.

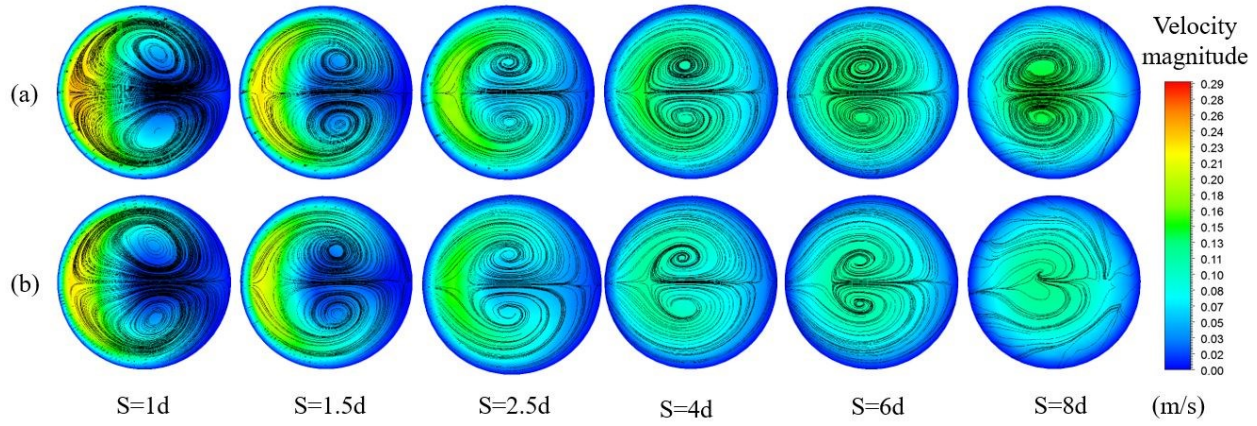

Figure 3.16 Streamlines (superimposed on the velocity magnitude contour) on a plane normal to the axis of the daughter vessel on six planes at a distance of 0-6d from the point of bifurcation. (1-6) (a) $\alpha = 45^{O}$ (b) $\beta = 60^{O}$.

In Figs. 3.14 and 3.15, the streamlines have been plotted in the daughter vessel having a smaller angle 15^{O}, and the larger angle is varied to 30^{O}, 45^{O}, and 60^{O}. In Fig. 3.14, the results are shown for the daughter vessel having a smaller angle. In Fig. 3.16, the nature of secondary vortices is similar in the small-angle daughter vessel in all three cases, except that it takes longer for the vortices to die out in a vessel having a smaller angle. Fig. 3.15 shows the secondary flow for the

daughter vessel having a larger angle. As observed earlier, an increase in the angle causes the velocity magnitude (and x-component of velocity) to decrease in the daughter vessel having a larger angle. As the flow moves downstream, the location of maximum velocity is shifted from the inner wall (towards the left) to the center of the vessel. The center of the secondary vortex is observed to be close to the inner wall for all three cases. Surprisingly, the secondary vortices die out quickly in the daughter vessel having a larger angle. This could possibly be because of the high-velocity magnitude when the angle is smaller.

Fig. 3.16 shows the secondary streamlines in the two daughter vessels for the case having bifurcation angles of 45^{O} and 60^{O}. Unlike previous cases, the center of the secondary vortex is observed to be away from the inner wall. As seen in Fig. 3.16, the eddies die out quickly in the daughter vessel having a larger angle.

Fig. 3.17 shows the wall shear stress distribution on the inner and outer walls at the bifurcation plane for all 6 cases of asymmetric bifurcation. For all 6 cases, the shear stress on both the outer walls (AA', CC') is very low when compared with that on the inner walls, and no significant effect of the change in the angle is observed on the WSS on the outer walls. For Figs. 3.17(a), (b) and (c), the bifurcation angle for one daughter vessel is fixed at 15°, whereas the angle for the other vessel has been varied to 30°, 45°, and 60°, respectively. An increase in the ratio of the bifurcation angles (β/α) decreases the wall shear stress (WSS) on the higher angled vessel, which results in an increase in WSS difference between respective daughter vessels. WSS is higher on the inner wall with a higher angle (BB') near the bifurcation. However, away from the bifurcation, the opposite behavior is observed, i.e., WSS is higher on the inner wall with a lower angle (DD'). Similar behavior is also observed for the cases shown in Figs. 3.17(d) and (e) for which the lower bifurcation angle was 30°, and the higher angle was varied to 45° and 60°. For the last two cases shown in Fig. 3.17(e) and (f), the WSS trend on the two inner walls is different from all other cases in that the WSS first increases and then decreases near the bifurcation. The total bifurcation angle is the same in Figs. 3.17(c) and (d) having the two angles at 15°, 60°, and 30°, 45°. WSS is higher for the case is shown in Fig. 3.17(c), having a larger angle for one daughter vessel.

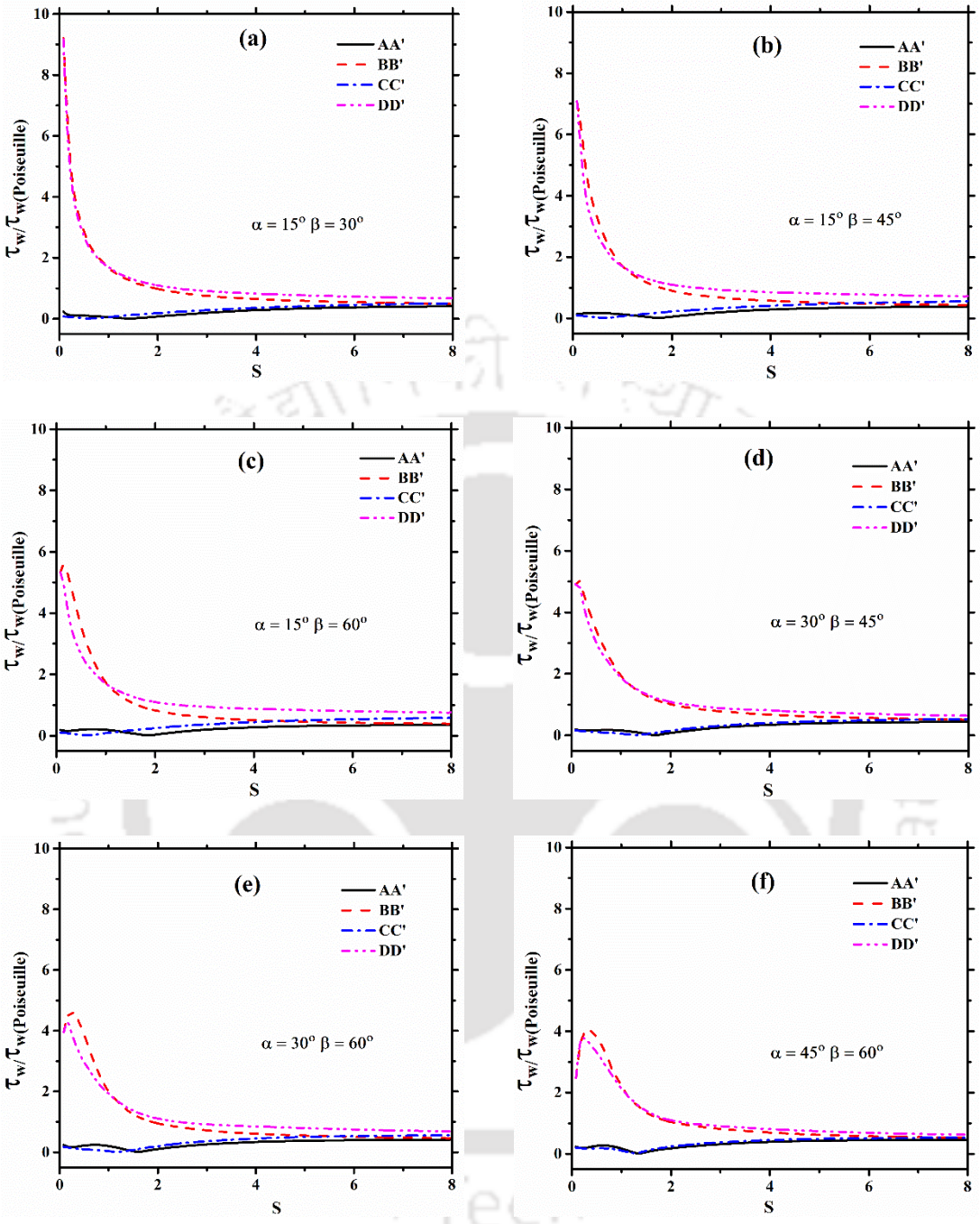

Figure 3.17 WSS along daughter walls on the vessels for asymmetric cases (a) $\alpha = 15$, $\beta = 30^{O}$ (b) $\alpha = 15^{O}$, $\beta = 45^{O}$ (c) $\alpha = 15^{O}$, $\beta = 60^{O}$ (d) $\alpha = 30^{O}$, $\beta = 45^{O}$ (e) $\alpha = 30^{O}$, $\beta = 60^{O}$ (f) $\alpha = 45^{O}$, $\beta = 60^{O}$.

3.3.2 Pulsatile flow

The simulations have been performed for symmetric and asymmetric bifurcations, as summarised in Table 3.1. The results of the last cycle, when the flow has become fully periodic, are presented.

Section 3.3.2.1 discusses the results for the symmetric bifurcation, whereas section 3.3.2.2 discusses the results for asymmetric bifurcation.

A grid independence study has been performed using four different mesh sizes containing 0.022, 0.087, 0.182, and 0.382 million elements. The density of blood is assumed to be 1060 kg/m^3 in all the simulations. The profile of dimensionless x-component of velocity obtained using four different meshes is plotted in Fig. 3.18(a) at a line located on the bifurcation plane in the daughter vessel at a distance of $2d$ from the bifurcation. The difference between the velocity values for the two finest meshes (0.182 and 0.382 million elements) is less than 1%. Hence, the mesh consisting of 0.182 million computational elements is used for subsequent simulations. All the simulations are performed on a computer with an i5-6500 processor and 16 GB RAM, using four processors in parallel. The time taken to achieve a converged solution for five cardiac cycles of period 2.5 s and a time step size of $\Delta t = 0.005$ s is about 24 hours. It typically took 200 iterations per time step to achieve the desired convergence at each time step.

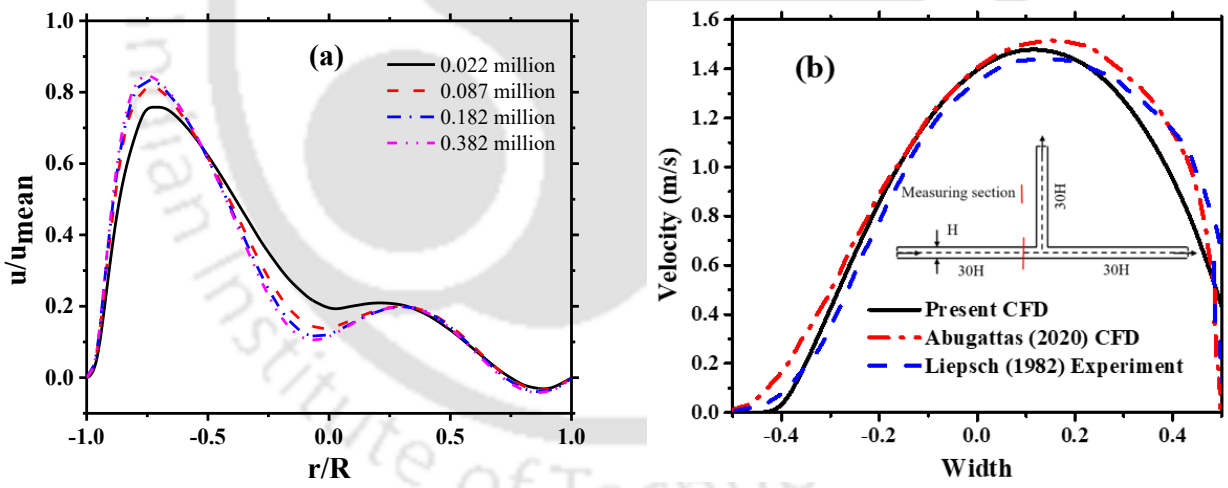

Figure 3.18 (a) Dimensionless axial velocity comparison across the radius of daughter vessel at location S = 1d for $\alpha = \beta = 30^O$ bifurcation using various mesh densities (b) Validation of current CFD results with the experimental data of Liepsch et al. (1999) and Numerical data of Abugattas et al. (2020) at the T bifurcation for Newtonian fluid flow at Re = 496.

To establish the veracity of the CFD simulations, simulations are performed for a Newtonian fluid (water) in a T bifurcation and compared with the experimental (Liepsch et al., 1982) and numerical data (Abugattas et al., 2020) available in the literature for T bifurcation. The geometry used

consists of the main branch that splits into two daughter vessels separated by bifurcation angle 90°. The width of the vessel is H, and the length is 30H for mother and daughter vessels. The simulations are performed in a 2D computational domain in both cases. Fig. 3.18(b) shows the comparison of velocity profile on a line in the middle plane 0.0005 m from the bifurcation, as shown by a red line, obtained from our CFD simulations with the literature data. The parabolic velocity is imposed at the inlet (Re = 496). The results are in good agreement with the literature data.

3.3.2.1 Symmetric Bifurcation ($\alpha = \beta$)

As the flow is transient, the flow field changes with time. The results are presented at three time instants shown as t_1 (peak systole), t_2 (start of diastole), and t_3 (end of diastole) in Fig. 3.1(b). The velocity changes continuously with time during systole, whereas it has a constant value during diastole. Figure 3.19(a) shows the velocity vectors colored by velocity magnitude at eight different cross-sectional planes for bifurcation angle $\alpha = \beta = 30^{o}$ for Newtonian and non-Newtonian fluid at the end of diastole and represents the typical flow behavior at a symmetric bifurcation. The first plane is at a distance of d from the bifurcation, and the subsequent planes are a distance d apart. At the bifurcation, the flow is divided in the two daughter vessels symmetrically. As the flow streamlines turn at the bifurcation, the fluid particles experience a centrifugal force forcing them towards the inner wall of the bifurcation in each daughter vessel. Due to the rise in pressure on the outer walls of the daughter vessel, flow separation occurs on the outer wall, and a recirculation zone is established. The enlarged view of the velocity vectors on the first and second planes clearly shows the reversed flow in the daughter vessel. As the area available for the forward flow reduces, the velocity near the inner wall increases. As the daughter vessels are straight, the flow again starts developing in the downstream direction. It may be noted that the velocity at the axis of daughter vessel for the Newtonian fluid is higher than that for the non-Newtonian fluid, as observed by comparing the velocity values at the outlet of the daughter vessel for the two cases. Shear-thinning behavior can be attributed to the flattening in the velocity profile at the center of the pipe. The analytical solution for laminar, fully-developed flow in a circular vessel for a constant flow rate also shows that the velocity on the vessel axis is more in the case of a Newtonian fluid than that for shear-thinning fluid.

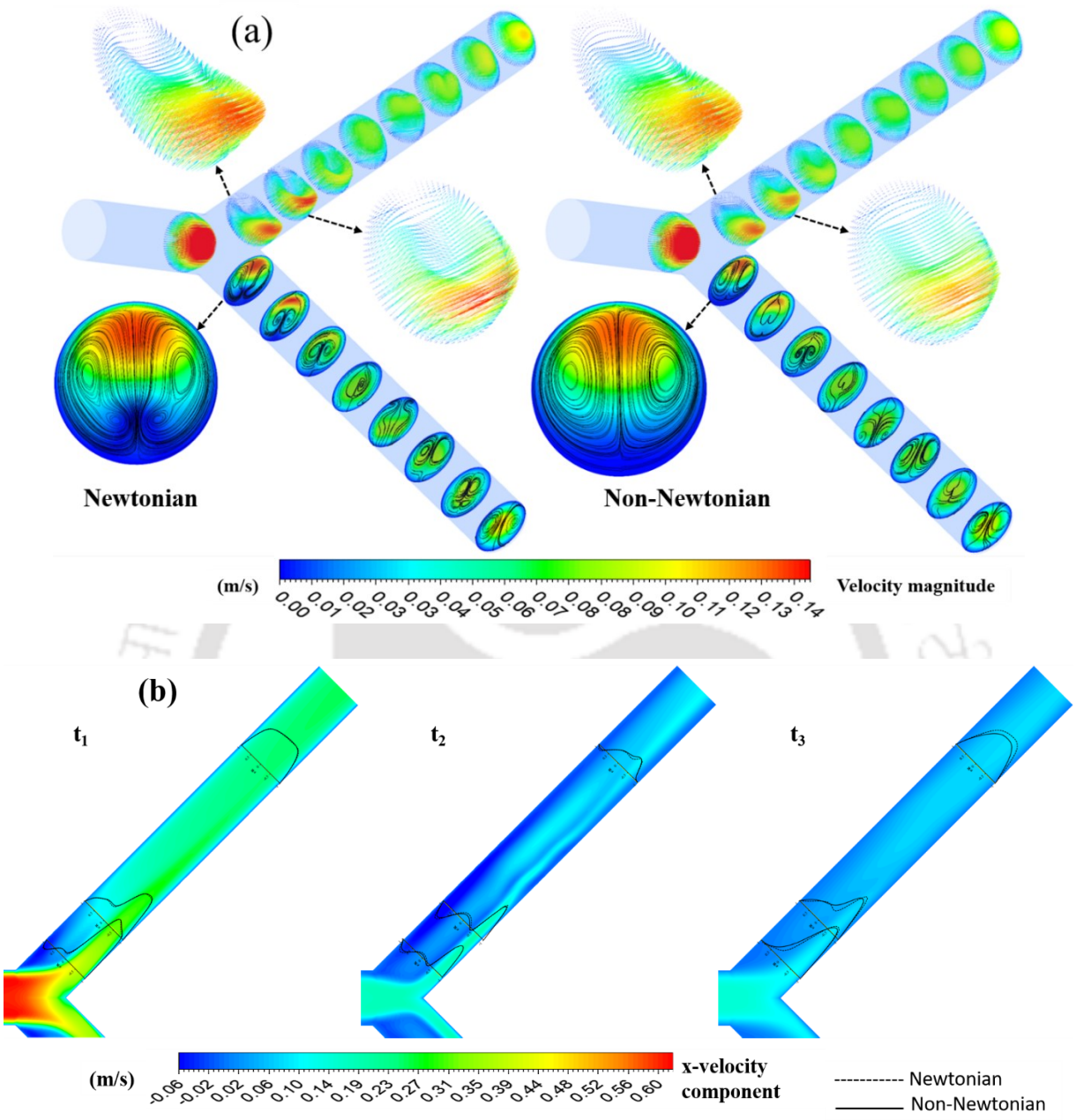

Figure 3.19 Velocity vectors and secondary flow streamlines for Newtonian and non-Newtonian (Carreau model) flow of blood at selected cross-sectional planes at the end of diastole for symmetric bifurcation angle $\alpha = \beta = 30^{O}$. (b) Contours of x-component of velocity (u) on the bifurcation plane at times t_1 (peak systole), t_2 (start of diastole) and t_3 (end of diastole) for $\alpha = \beta = 45^{O}$.

The streamlines on the cross-sectional planes show the secondary flow in the other daughter vessel.

Two symmetric Dean vortices are observed at a distance of S = 1d from the bifurcation in each

case. For the Newtonian fluid, each vortex is observed to further divide into two vortices in the core region. In comparison, only two symmetric vortices are seen for the non-Newtonian fluid.

Fig. 3.19(b) shows the contours of x-component (parallel to the axis of mother vessel) of velocity on the bifurcation plane in a daughter vessel for $\alpha = \beta = 45°$ at times t_1 (peak systole), t_2 (start of diastole) and t_3 (end of diastole). Figures 3.20, 3.21, and 3.22 show the profiles of x-component of velocity (u) on the bifurcation plane in the daughter vessel for Newtonian and non-Newtonian fluids at times t_1, t_2, and t_3, respectively. The profiles have been plotted on a line normal to the axis of daughter vessel. The velocity profiles have been plotted for the three bifurcation angles ($\alpha = \beta$ = 30°, 45°, 60°) at three locations- at distances d, $2d$ and $6d$ from the bifurcation. The non-dimensional radius (r/R) varies from -1 (inner wall) to 1 (outer wall).

As shown in Fig. 3.19b and 3.20, flow separation, indicated by negative values of u, is observed near the outer wall of bifurcation at S = d at t_1 for all three bifurcation angles. As the flow is symmetric, it is equally divided between the two daughter vessels, and the flow rate is the same in each daughter vessel. A decrease observed in the value of u with an increase in the bifurcation angle is because u is proportional to $\sim\cos\alpha$. Only minor differences are observed between the velocity profiles for Newtonian and the non-Newtonian fluids in all the cases at t_1. In the separation region, u is zero on the inner wall (r/R = -1) and then increases on moving towards the outer wall, reaches a peak and then starts decreasing and reaches a value of zero and then becomes negative before again becoming zero on the outer wall. The zero value of u (except when on the wall) represents the center of the recirculation region at which the flow direction reverses, and the negative value represents the backflow. Several inflection points i.e. the points at which the profile curvature changes the sign, are observed in the velocity profile. For example, for bifurcation angle 45°, at location S = d, there are four inflection points. On moving from the inner wall towards the outer wall, the first inflection point corresponds to the maximum in the forward flow; the second inflection point indicates the boundary between the forward and recirculating fluid; third and fourth inflection points represent the maximum in the forward and reverse flow in the recirculation zone, respectively. The flat velocity profile at peak systole is similar to that obtained using Womersley solution for laminar, Newtonian, fully-developed, and pulsatile flow in a channel (Womersley, 1955).

(I)

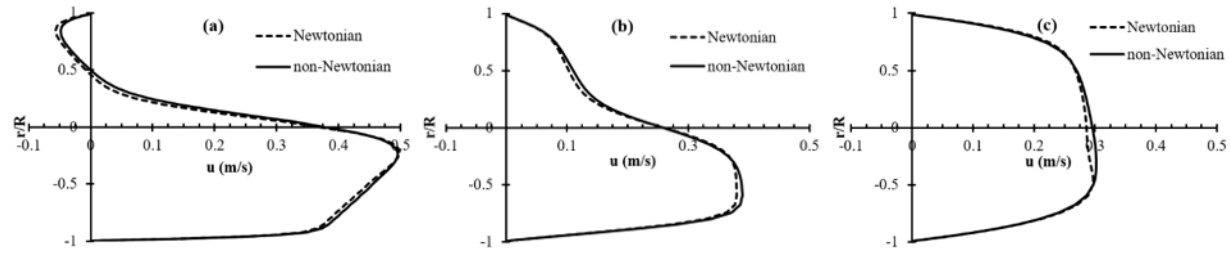

(II)

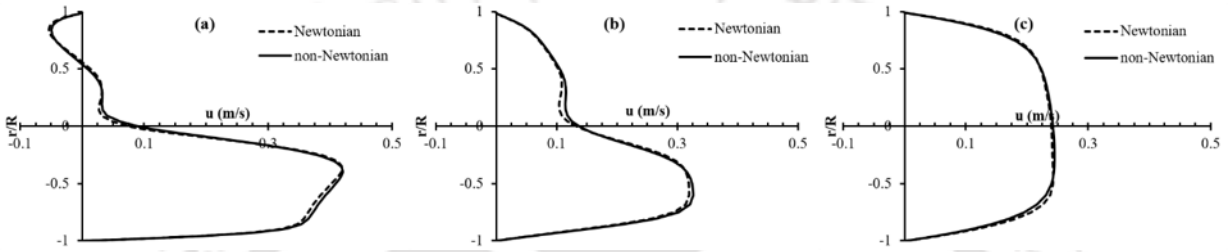

(III)

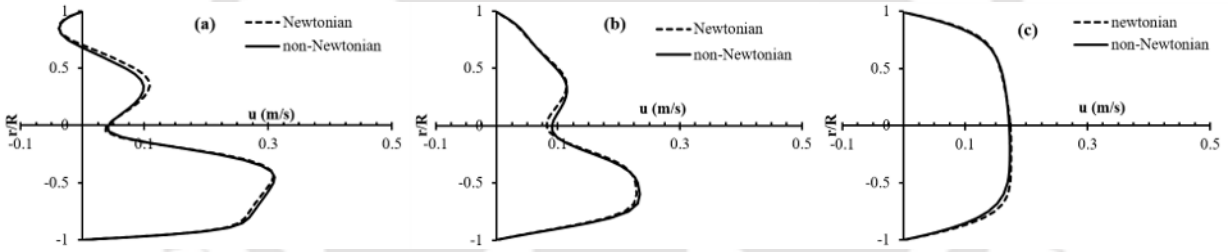

Figure 3.20 Profiles of x-component of velocity (u) in the daughter vessel on the bifurcation plane at (a) S = d (b) S = 2d (c) S = 6d during t_1 (peak systole) for (I) $\alpha = \beta = 30°$, (II) $\alpha = \beta = 45°$, (III) $\alpha = \beta = 60°$.

Figure 3.21 shows the profiles of u at time t_2 (the beginning of the diastole) at the same locations as shown in Fig. 3.20. The velocity magnitude is reduced relative to those observed in Fig. 3.20 due to the reduced flow rate during diastole, as shown in Fig. 3.1(b). The extent and size of the recirculation zone is increased significantly at the beginning of diastole as compared to that during the peak systole. At t_1, the negative value of u is observed only at S = d, whereas at t_2 it is observed at all three locations for all the three bifurcation angles. During this period, the differences between the velocity values for Newtonian and non-Newtonian fluids are relatively more when compared with those during the peak systole. This can be attributed to the relatively low shear rates during this period. The velocity profile for the forward flow is sharper during this period than that during

the peak systole. This observation is again consistent with the Womersley solution (Ritman and Zamir, 2012).

(I)

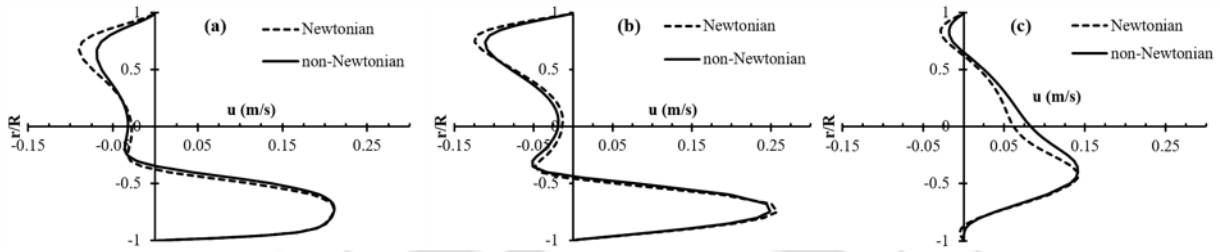

(II)

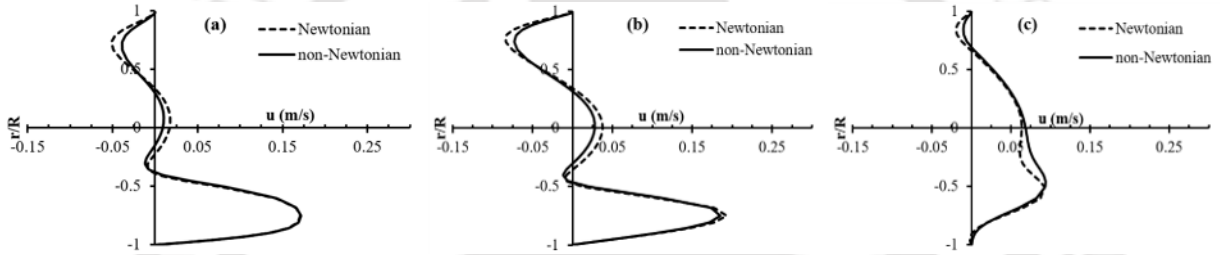

(III)

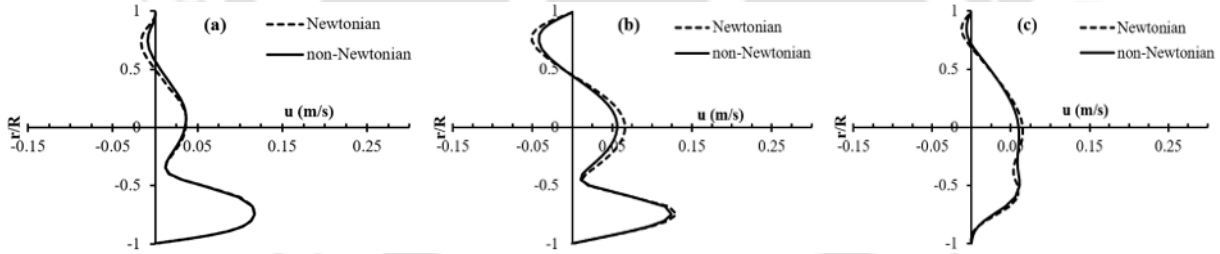

Figure 3.21 Profiles of *x*-component of velocity (u) in the daughter vessel on the bifurcation plane at (a) S = d (b) S = $2d$ (c) S = $6d$ during t_2 (beginning of diastole) for (I) $\alpha = \beta = 30°$, (II) $\alpha = \beta = 45°$, (III) $\alpha = \beta = 60°$.

Figure 3.22 shows the profiles of u at time t_3 (the end of the diastole) for the three bifurcation angles. At the end of the diastole, the backflow is negligible and observed only at the location S = d and absent on all the other locations for all the three bifurcation angles. The maximum velocity is less than that observed at the start of diastole, which results in a reduction in shear rate. The low shear rate results in the difference in the velocity profiles for the Newtonian and non-Newtonian fluids. The magnitude of velocity is observed to be higher for the Newtonian fluid.

(I)

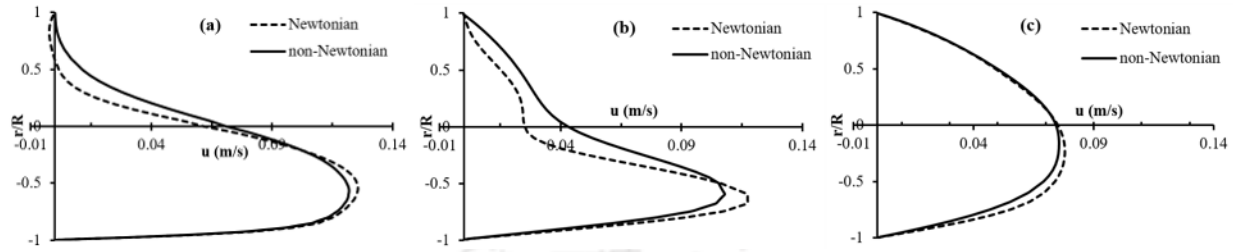

(II)

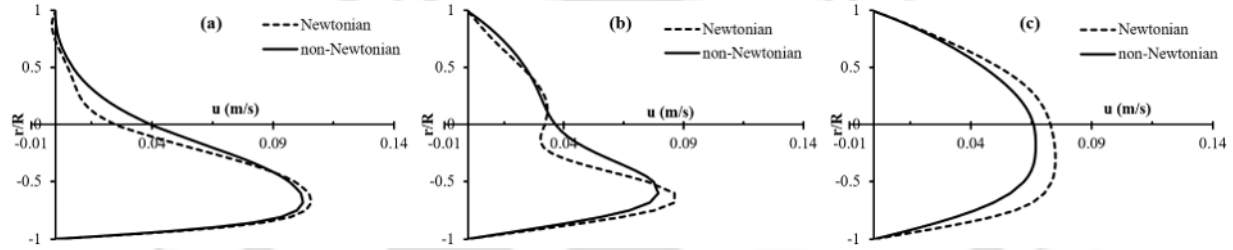

(III)

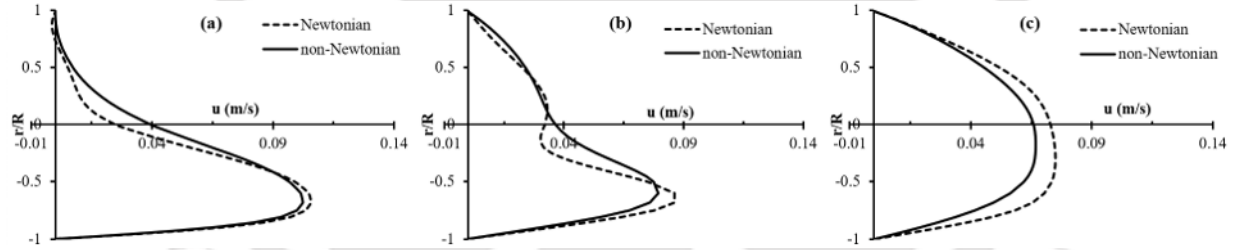

Figure 3.22 Profiles of x-component of velocity (u) in the daughter vessel on the bifurcation plane at (a) S = d (b) S = 2d (c) S = 6d during t_3 (end of diastole) for (I) $\alpha = \beta = 30°$, (II) $\alpha = \beta = 45°$, (III) $\alpha = \beta = 60°$.

As shown in Fig. 3.19, significant secondary flow is present at the cross-sectional plane in the daughter vessel. To understand the evolution of secondary flow with time and location, the contours and vectors of secondary flow at S = d, 2d, 6d for the symmetric bifurcation angle ($\alpha = \beta = 45°$) at times t_1, t_2 and t_3 are shown in Fig. 3.23.

At peak systole, the secondary vortices are located near the outer wall and move towards the inner wall downstream. In the cross-sectional plane located at S = d, the liquid is directed from the outer to an inner wall on the centerline and returns back to the outer wall from the near-wall region. On moving away from the outer wall the flow expands, and the velocity magnitude decreases. When the flow returns via the wall resulting in higher velocity magnitude in the near-wall region. The

center of the vortex can be easily identified by the zero velocity in the middle of the vortex. On moving downstream, the vortex size becomes bigger, but the magnitude of secondary velocity reduces. The secondary flow dies down on moving further downstream in the daughter vessel as there is no curvature in the vessel after the bifurcation.

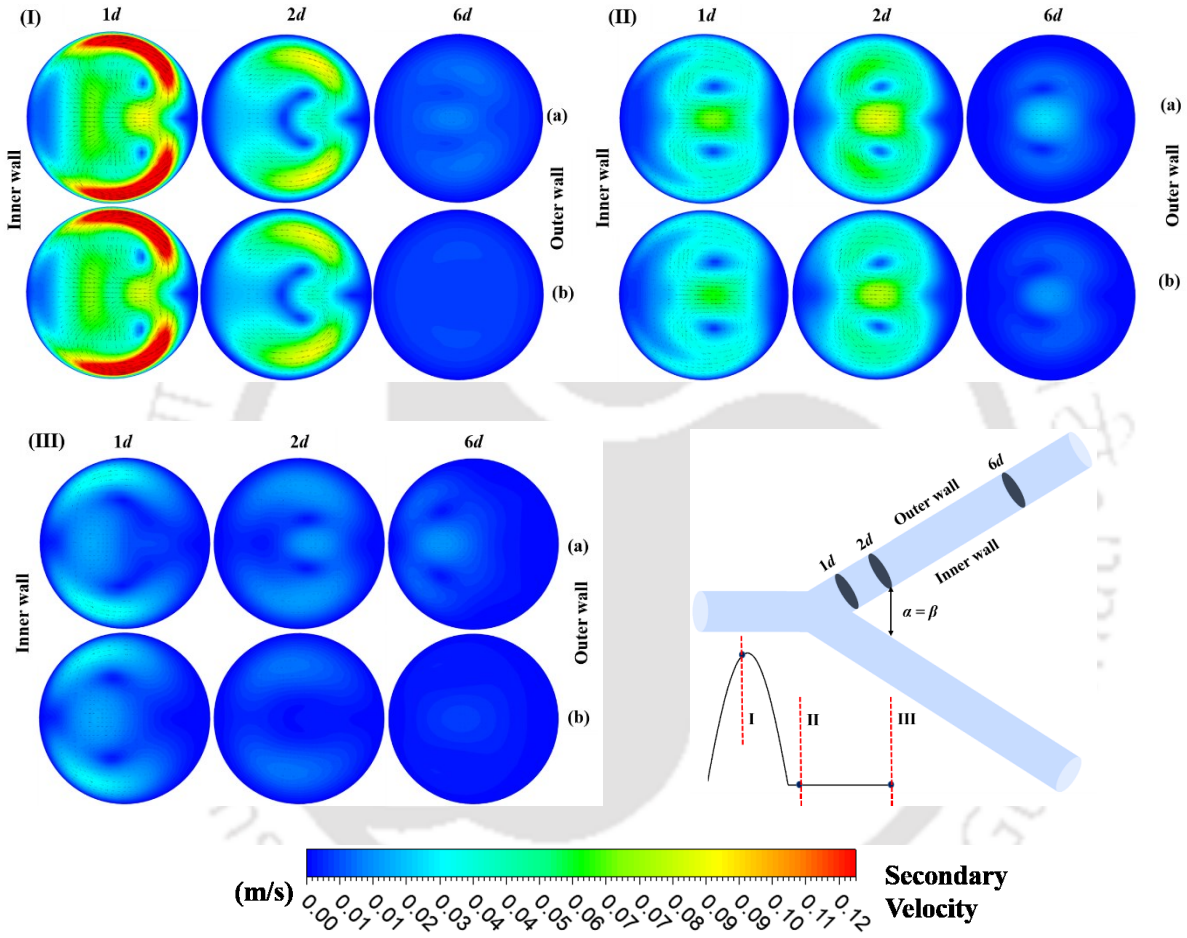

Figure 3.23 Contours and streamlines of secondary velocity on the cross-sectional planes in the daughter vessel for (a) Newtonian and (b) non-Newtonian fluids at S = *d*, 2*d*, 6*d* for symmetric bifurcation angle $\alpha = \beta = 45°$ (I) at peak systole, (II) at the beginning of diastole, (III) at the end of diastole.

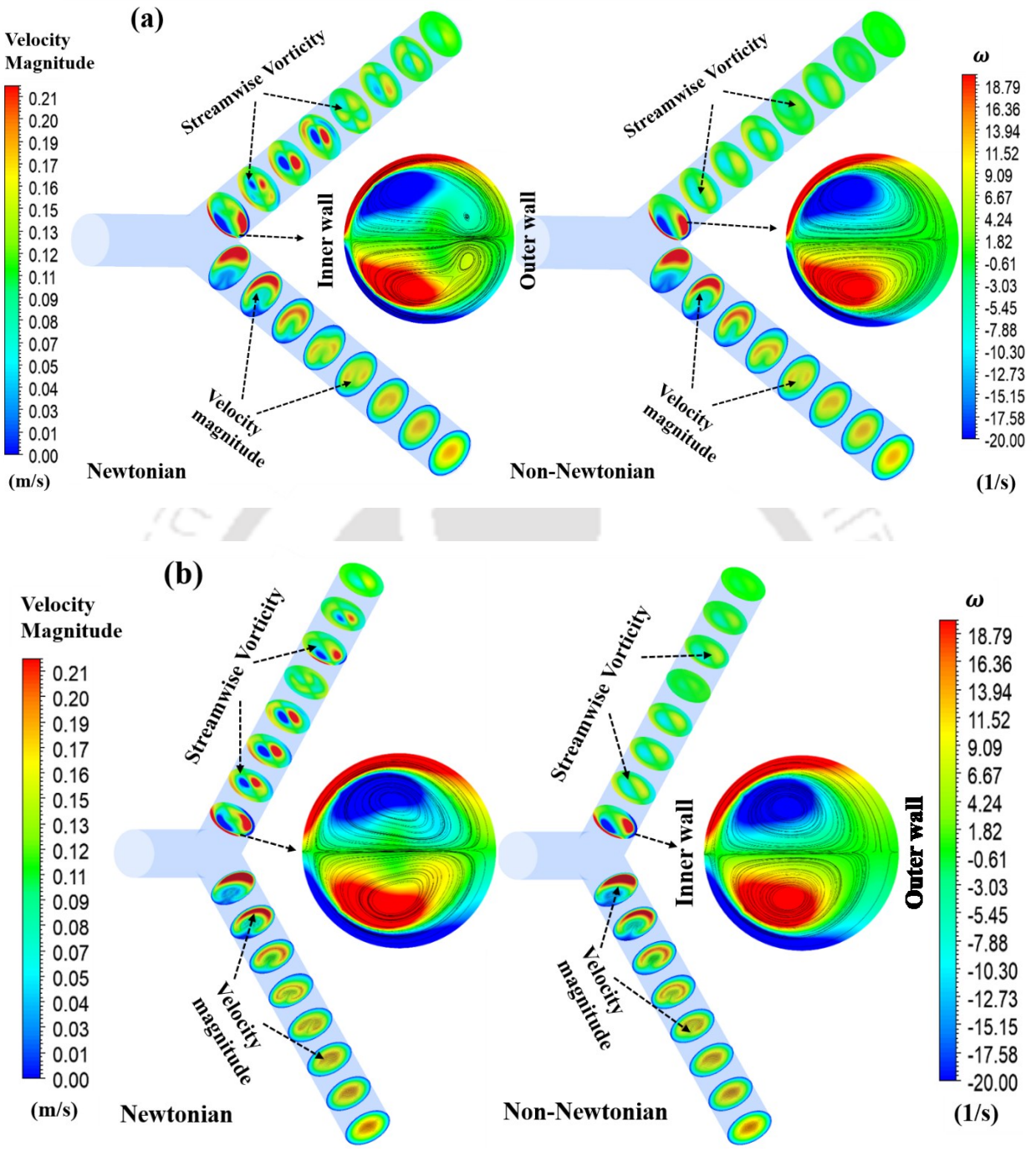

Figure 3.24 Comparison of time-averaged velocity magnitude over one cardiac cycle for Newtonian and non-Newtonian blood flow, and streamwise vorticity (ω) at selected cross-sectional planes for (a) $\alpha = \beta = 30°$, (b) $\alpha = \beta = 60°$.

At the beginning of diastole, the vortices move towards the center of the vessel, and the magnitude of secondary velocity at S = d is of the same order as the primary flow at that instant. However, the secondary flow appears to die down with time, as can be seen from the contours of secondary

velocity. From the images, there appears to be very little difference in the secondary flow for Newtonian and non-Newtonian fluids.

The secondary vortices can further be characterized using vorticity. Figure 3.24 shows the contours of streamwise vorticity (ω) and velocity magnitude on different cross-sectional planes in the daughter vessel for Newtonian and non-Newtonian fluids. The streamwise vorticity in the daughter vessel is the component of vorticity parallel to the axis of the daughter vessel and characterizes the secondary vortices in the cross-sectional plane. Two vortices symmetric with respect to the bifurcation plane are observed on the first plane. The magnitude of vorticity is the same in the two vortices, but the sign is different as the vortices are counter-rotating. The magnitude of vorticity is high in the boundary layer region near the wall and decreases away from it, as can be seen by red or blue colors on the wall. Further, the high magnitude of streamwise vorticity in the core region corresponds to the two vortices.

The magnitude of vorticity is high near the inner wall, both in the boundary layer as well as core regions. The magnitude of vorticity decreases downstream of the bifurcation in the daughter vessel. There are some minor differences in the vorticity distribution for the Newtonian and non-Newtonian fluids. The size of vortices is observed to be slightly bigger for the Newtonian fluid. Further, the secondary vortex is observed to be dividing into two vortices for the Newtonian fluid for a smaller bifurcation angle, but the size and of this vortex is relatively small. For the larger bifurcation angle, the center of the vortex is shifted away from the wall. The boundary layer thickness is observed to be greater for the larger bifurcation angle, as shown in Fig. 3.24(b).

The primary flow in the streamwise direction combined with the secondary flow gives rise to the helical motion of fluid particles, which can be characterized using helicity. Helicity is defined as the dot product of vorticity and velocity, as given by Eq. (3.8).

$$H = (\boldsymbol{\nabla} \times \boldsymbol{u}).\boldsymbol{u} \tag{3.8}$$

Figure 3.25 shows the contours of helicity at the end of diastole for the Newtonian and non-Newtonian fluids on various cross-sectional planes in the daughter vessel for 30° and 60° bifurcation angles. At the bifurcation, the helicity is higher near the inner wall. However, the region having higher angle suggest greater helicity shifts towards the center downstream of the bifurcation.

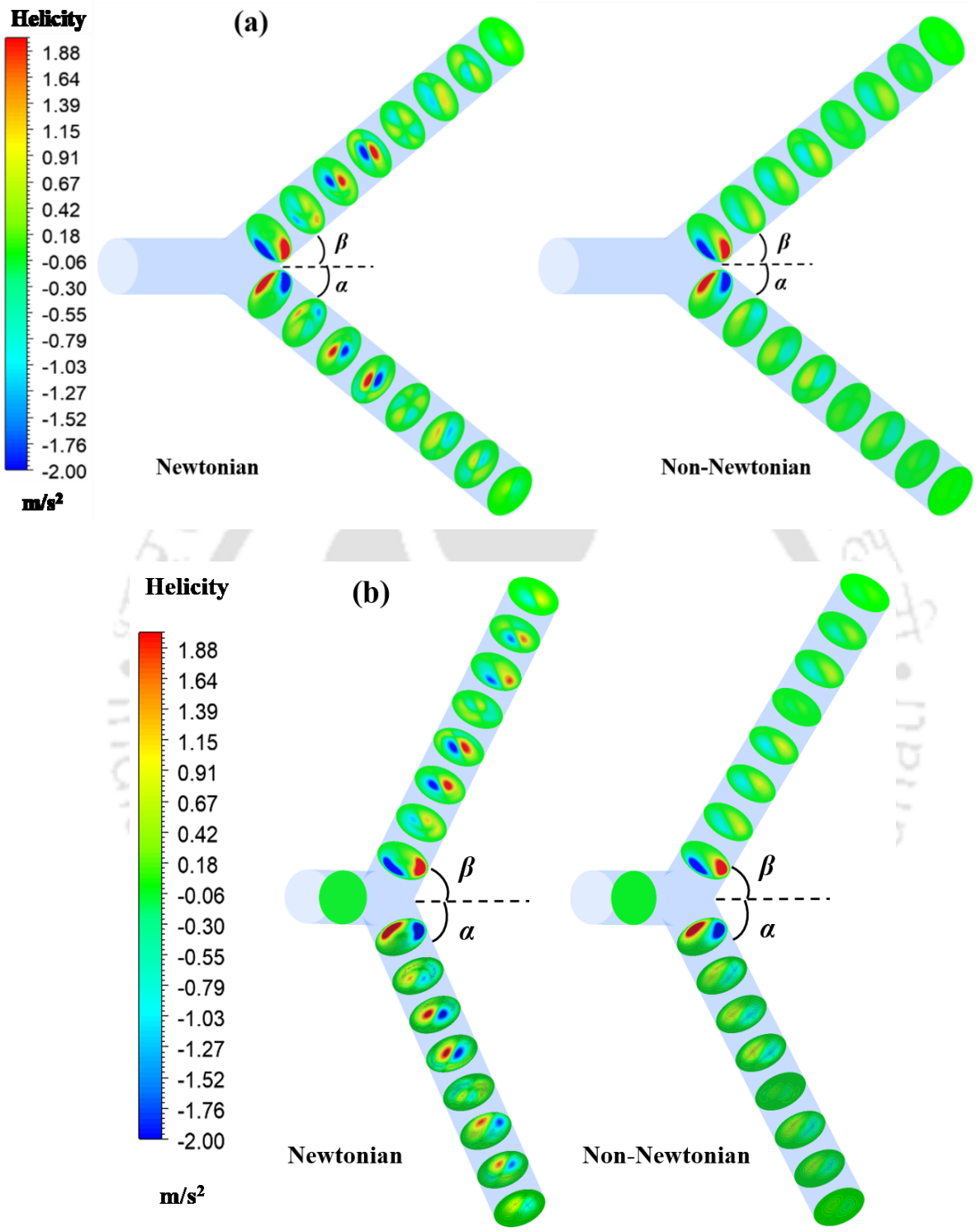

Figure 3.25 Comparison of helicity for Newtonian and non-Newtonian fluid at the end of diastole, showing helical strength at selected cross-sectional planes for (a) $\alpha = \beta = 30°$, (b) $\alpha = \beta = 60°$.

It can be observed that the helicity dies down faster downstream of bifurcation for the non-Newtonian fluid as compared with that for the Newtonian fluid. The increase in the angle causes increased helicity. It can be confirmed by comparing the distance up to which helicity is strong for both the Newtonian and non-Newtonian fluid. In the lower angled case (Fig. 3.25a), helicity lasts for a shorter distance downstream, while in a higher bifurcation angled vessel (Fig. 3.25b), it lasts for a longer distance. The results are similar to the streamwise vorticity patterns discussed in the previous section.

Hemodynamic parameters analysis

The solution of the conservation equations provides velocity and pressure field from which other parameters of interest can be calculated. In arterial flow, the wall shear is an important parameter and can be used as a biomarker. In a pulsatile flow, WSS varies with time, and different parameters are defined in the literature to represent mean WSS and its oscillating behavior. Some of these are time-averaged wall shear stress (TAWSS), oscillatory shear index (OSI) (Ku et al., 1985) and relative residence time (RRT) (Himburg et al., 2004; Soulis et al., 2011).

TAWSS is defined as the time average of the magnitude of wall shear stress over a periodic cycle as given by Eq. (3.9).

$$TAWSS = \frac{1}{T}\int_0^T |\tau_w| dt \tag{3.9}$$

Where T is the period of one cardiac cycle and τ_w is the shear stress on the vessel wall. Distributions of time-averaged wall shear stress (TAWSS) along the inner and outer walls in the bifurcation plane of the daughter vessels are shown in Fig. 3.26 for the three bifurcation angles. The TAWSS on the outer wall (AA') is lower than that on the inner walls for all three bifurcation angles. The TAWSS peaks are observed on the inner wall near the bifurcation, and its value decreases with an increase in bifurcation angle. This corresponds to the high velocity near the inner wall observed in Figs. 3.19-3.22. In contrast, no significant change is observed in TAWSS on the outer wall (BB'). Low WSS is observed for higher bifurcation angle in the past studies (Chaichana et al., 2011; Perktold and Resch, 1990), and our results are in agreement with them. The TAWSS results show a significant difference between Newtonian and non-Newtonian fluid due to the shear-thinning effect. The TAWSS profile shows a minor difference in values for Newtonian and non-Newtonian fluid for S < 1 but shows a significant difference for S > 1. The TAWSS values

for the Newtonian fluid are slightly lower than those for the non-Newtonian fluid, and this observation is in agreement with the past studies (Chen and Lu, 2006; R. Wells et al., 1996).

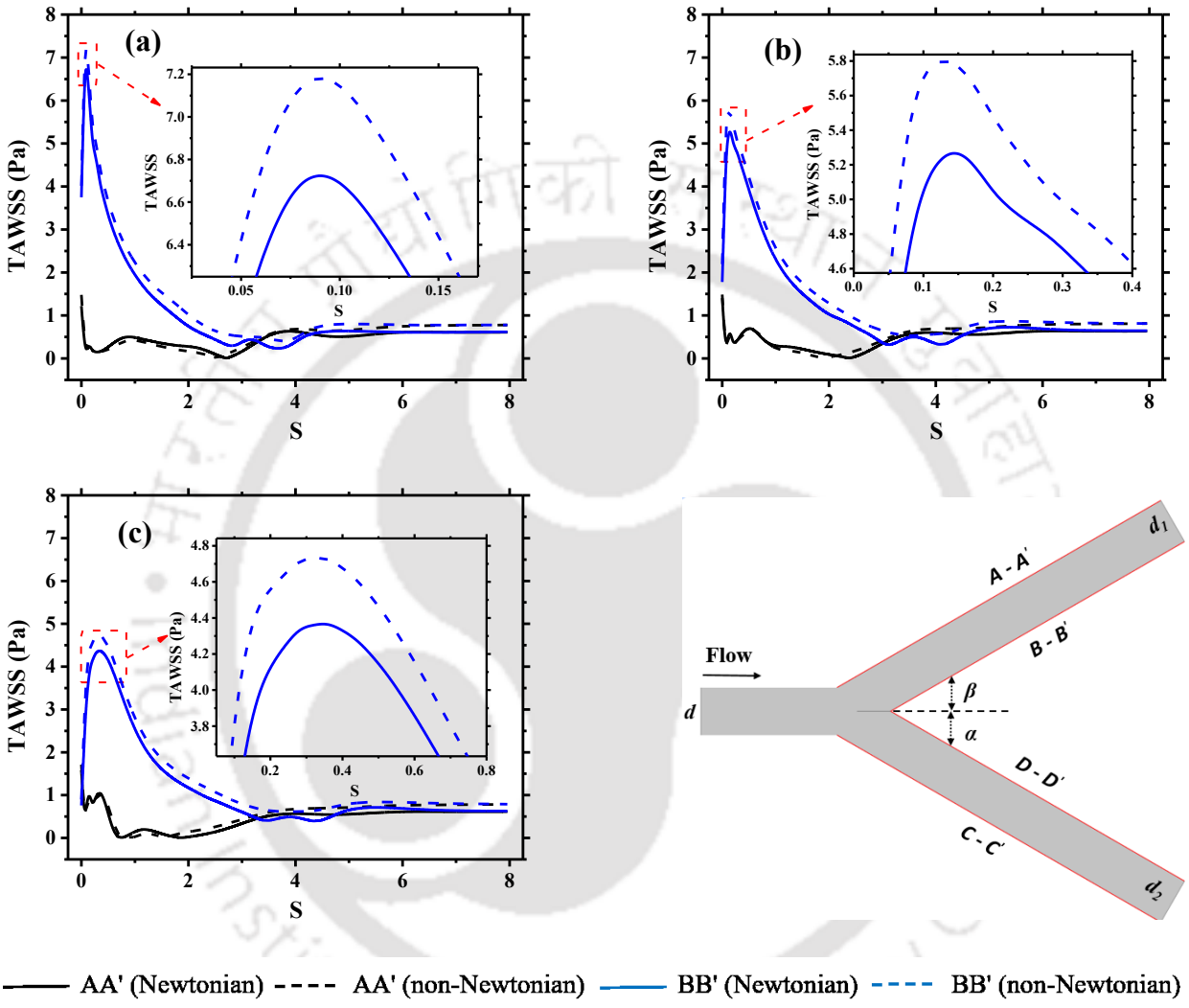

Figure 3.26 TAWSS profile along outer (AA') and inner (BB') walls on the bifurcation plane of daughter vessel for (a) $\alpha = \beta = 30°$, (b) $\alpha = \beta = 45°$, (c) $\alpha = \beta = 60°$.

Another important parameter to characterize wall shear stress for pulsatile flow is oscillatory shear index (OSI) defined by Eq. (3.10).

$$OSI = \frac{1}{2}\left[1 - \frac{\left|\int_0^T \tau_w dt\right|}{\int_0^T |\tau_w| dt}\right] \tag{3.10}$$

If the wall shear stress is only positive or only negative throughout the cycle, the value of OSI is zero. However, if the wall shear stress changes signs during the cycle, it has a non-zero value. The OSI value is maximum (= 0.5) when the shear stress is positive and negative for equal durations in a cycle. Figure 3.25 shows the OSI along the inner and outer walls of daughter vessels for two bifurcation angles. The value of the OSI is zero on the inner wall as the direction of flow is downstream, and the sign of WSS remains the same during the cycle. On the outer wall, the value of OSI is non-zero in some locations near the bifurcation. These are the regions at which the flow changes sign. Due to the change in flow rate during a cycle, the size of the separation region and the location at which flow separation starts and ends change in a cycle. The profiles of OSI for the Newtonian and non-Newtonian fluids are slightly different for both smaller (Fig. 3.27(a)) and higher (Fig. 3.27(b)) bifurcation angles, indicating the difference in the size and location of flow separation.

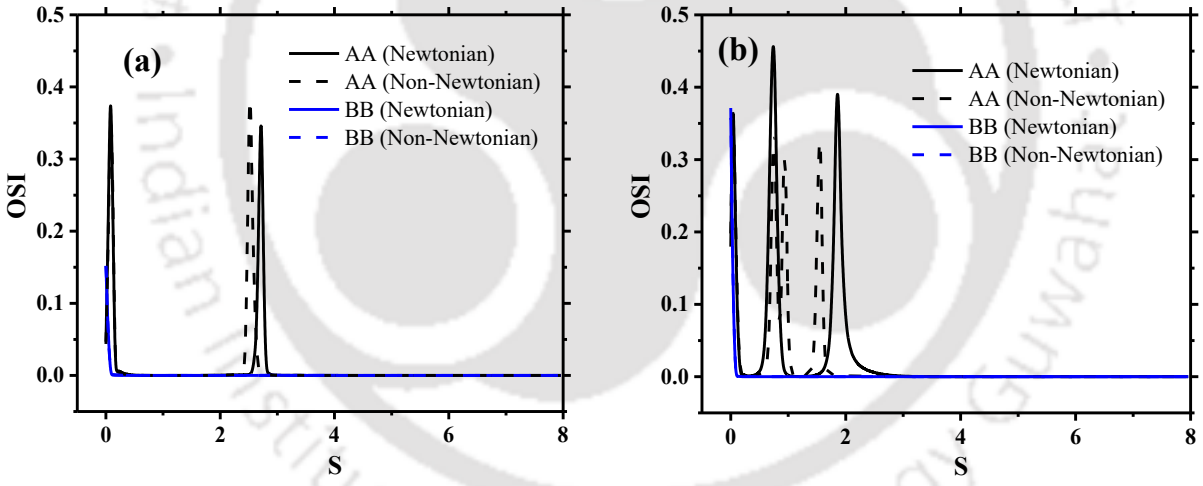

Figure 3.27 OSI profile along inner and outer walls in the mid-plane of daughter vessel for various bifurcation angles (a) $\alpha = \beta = 30°$, (b) $\alpha = \beta = 60°$.

While OSI can identify the regions having backflow, it does not provide any information regarding the magnitude of shear stress which is an important parameter for atherosclerosis development. Another parameter has been proposed based on the concept of relative residence time (Himburg et al., 2004). The fluid that do not adhere to the vessel wall move in the fluid continuously and have zero residence time. Relative residence time or RRT, given by Eq. (3.11), refers to the residence time of the fluid near the wall.

$$RRT = \frac{1}{(1-2\ OSI)\ TAWSS} \tag{3.11}$$

RRT is inversely proportional to the value of time-averaged wall shear stress and is recommended as a robust indicator of low and oscillating wall shear stress (Lee et al., 2009).

Figure 3.28 shows the distribution of RRT along the inner and outer walls of daughter vessels on the bifurcation plane for two bifurcation angles. A peak in RRT is observed at the location where the flow reattaches the vessel wall. These peaks correspond to the regions where the value of OSI is close to 0.5. As with OSI, the value of peaks of RRT and their locations are different for Newtonian and non-Newtonian fluids.

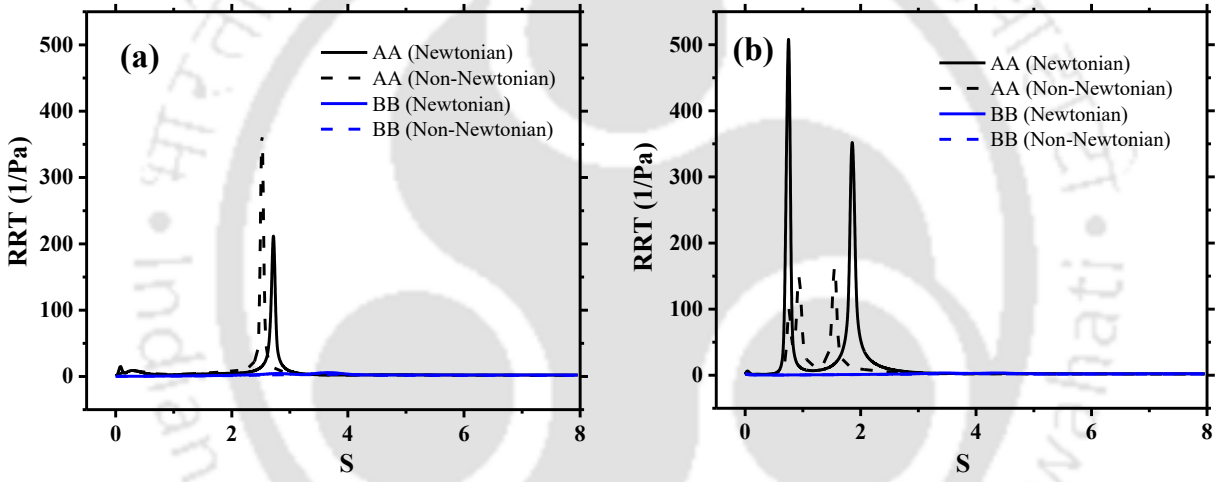

Figure 3.28 RRT profile along inner and outer walls in the mid-plane of daughter vessel for various bifurcation angles (a) $\alpha = \beta = 30°$, (b) $\alpha = \beta = 60°$.

3.3.2.2 Asymmetric bifurcation ($\alpha \neq \beta$)

For asymmetric bifurcation, flow behavior for three different combinations of bifurcation angles 15°-60°, 30°-60°, and 45°-60° is studied. Typical velocity distribution in an asymmetric bifurcation can be observed from Fig. 3.29(a), which shows the velocity vectors during diastole for Newtonian and non-Newtonian fluids on eight cross-sectional planes in the daughter vessel for asymmetric bifurcation having $\alpha = 15^{O}$, $\beta = 60^{O}$. More flow passes through the daughter vessel, having a lower angle, as is evident from the magnitude of velocity in the two cases. No or very little backflow is observed in the daughter vessel having a lower angle, whereas there is higher backflow in the daughter vessel having a higher angle. This is because of the larger curvature of

the higher angled daughter vessel. As the flow proceeds towards the outlet in the daughter vessel, the velocity profile approaches towards a fully-developed profile in both the daughter vessels. However, the length required to achieve a fully-developed profile in the daughter vessel having a higher angle is more even though it has a lower flow rate and hence lower flow Reynolds number. This is because of the flow separation in the higher angled daughter vessel.

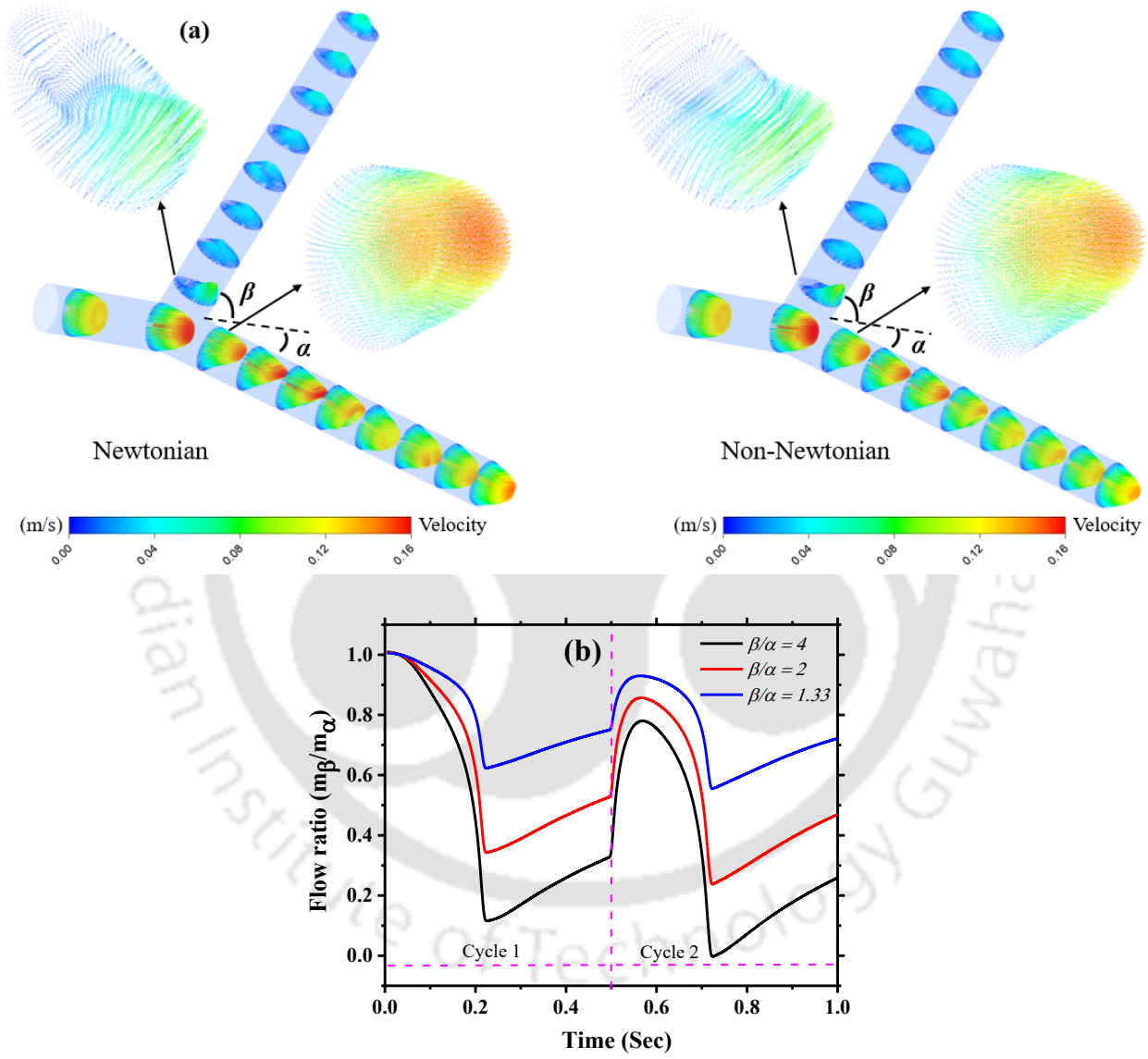

Figure 3.29 (a) Comparison of velocity vectors and secondary flow streamlines for Newtonian and non-Newtonian (Carreau model) blood flow at selected cross-sectional planes at the end of diastole, showing the three-dimensional flow field for asymmetric bifurcation angle $\alpha = 15^{O}$, $\beta = 60^{O}$ (b) ratio of mass flow rate distribution in daughter vessels with time in a cardiac cycle for varying bifurcation angle ratios.

Interestingly, the flow distribution in the two daughter vessels changes with time during the pulsatile flow. To represent the flow distribution in the daughter vessels, a flow ratio is defined as the ratio of flow rates in the larger angle vessel to the smaller angle vessel. Figure 3.29(b) shows the variation of the flow ratio in the two daughter vessels with time for the three cases for the first two cycles. While there are some differences in the first and second cycle, the flow is periodic after the first cycle. The value of flow ratio one at time equal to zero is just a reflection of the initial condition. During the Systole, the ratio of mass flow increases first and then decreases until the beginning of diastole. During diastole, the ratio increases with time. The distribution of flow in the two daughter vessels depends on the flow resistance in the two vessels. The flow resistance depends on the flow pattern e.g. degree of skewness in the flow, flow separation. The flow pattern depends upon the flow Reynolds number in the vessel, which is a function of flow rate. Therefore, time-dependent flow distribution in the two daughter vessels has been observed. With a decrease in the angle ratio, the flow ratio approaches towards one and would become one for a symmetric bifurcation.

Figures 3.30, 3.31, and 3.32 show the profiles of u on the mid-plane of arterial bifurcation for Newtonian and non-Newtonian fluids for the three asymmetric cases given in Table 3.1. The velocity profiles are plotted by taking the average over one cardiac cycle at various non-dimensional distances (S) from the bifurcation.

Figure 3.30 shows the profiles of time-averaged x – component of velocity in the two daughter vessels having $\alpha = 15°$, $\beta = 60°$. The velocity is higher in the daughter vessel, having a lower angle (15°) than that having a higher angle (60°) and is positive at all locations. The u value is higher in the lower angled daughter vessel because more liquid goes in the lower angled vessel. The velocity is negative near the outer wall, and the flow gets separated in the lower angled vessel also. However, a larger negative value of u is observed in the daughter vessel having a higher bifurcation angle (60°) at the location S = d. The velocity profile is asymmetric in both the daughter vessels. Interestingly, the profile of time-averaged velocity becomes sharper on moving downstream of bifurcation. While there are small differences between the velocity profiles for the Newtonian and non-Newtonian fluids in the daughter vessel having smaller angles (15°), the differences are significant in the daughter vessel having a higher bifurcation angle (60°).

(I)

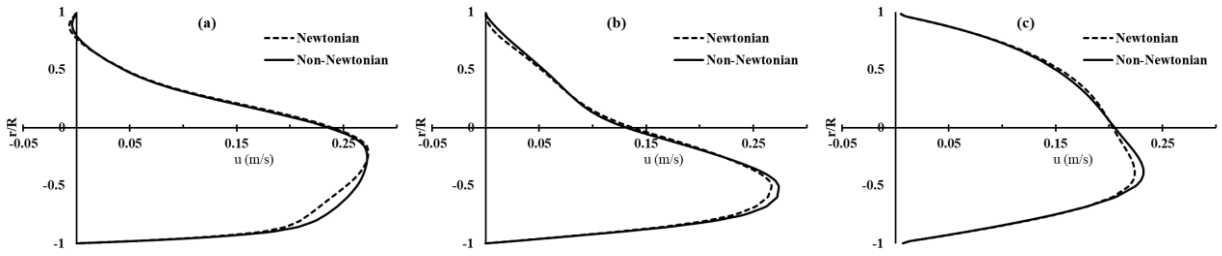

(II)

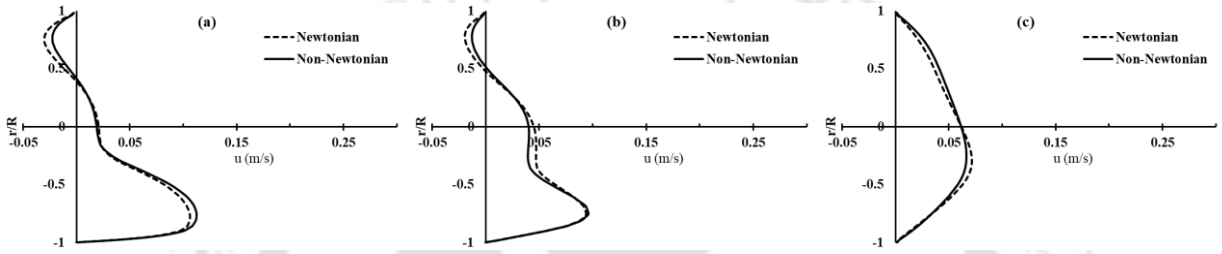

Figure 3.30 Profiles of *x*-component of time-averaged velocity over one cardiac cycle along the daughter vessel in the mid-plane of bifurcation for various location (S), (a) S = 1*d* (b) S = 2*d* (c) S = 6*d* at asymmetric bifurcation angle $\alpha = 15°$, $\beta = 60°$ ($\beta/\alpha = 4$) (I) $\alpha = 15°$, (II) $\beta = 60°$.

In their experimental and computational studies for steady flow in a carotid artery bifurcation, Lower velocity gradients at the divider wall (inner wall of bifurcation) and higher velocity gradients at the non-divider wall (outer wall of bifurcation) for non-Newtonian fluid when compared with those for a Newtonian fluid (Gijsen et al., 1999). They also noted that no flow separation was observed for the non-Newtonian fluid. Similar behavior can be seen for the time-averaged velocity in our CFD simulations. Further, the relatively flatter velocity profile for the shear-thinning fluid observed in our CFD simulations is in agreement with the CFD simulations of Chen and Lu (2002, 2004), who studied numerically steady and pulsatile flow for Newtonian and shear-thinning fluids in a non-planar bifurcation (Chen and Lu, 2006, 2004).

The profiles of time-averaged *x*–component of velocity at three different locations on the bifurcation plane for the geometry having $\alpha = 30°$ and 45° are shown in Figs. 3.31 and 3.32, respectively. The larger angle is the same ($\beta = 60°$) for both cases. The velocity in the higher angled daughter vessel ($\beta = 60°$) increases, whereas that in the lower angled vessel decreases with a decrease in angle ratio.

(I)

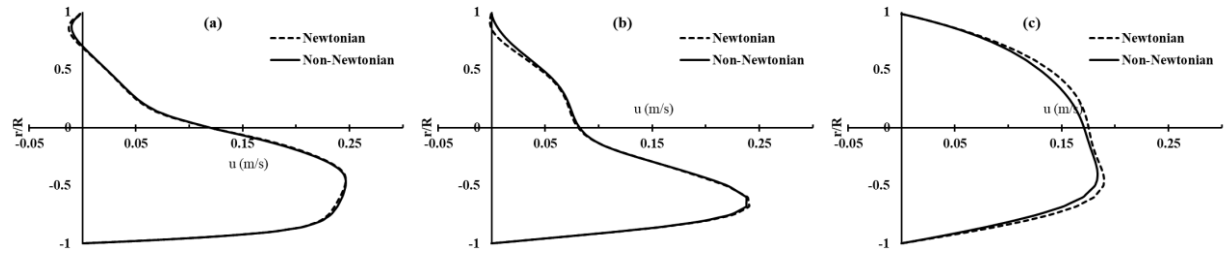

(II)

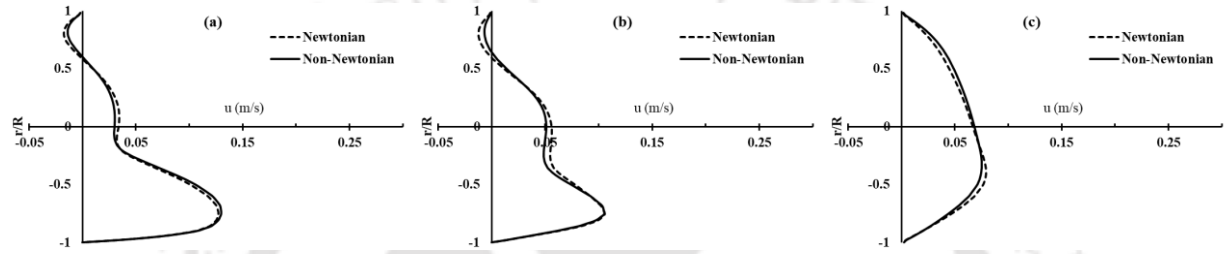

Figure 3.31 Profiles of x-component of time-averaged velocity over one cardiac cycle along the daughter vessel in the mid-plane of bifurcation for various location (S), (a) S = 1*d* (b) S = 2*d* (c) S = 6*d* at asymmetric bifurcation angle $\alpha = 30°$, $\beta = 60°$ ($\beta/\alpha = 2$) (I) $\alpha = 30°$, (II) $\beta = 60°$.

(I)

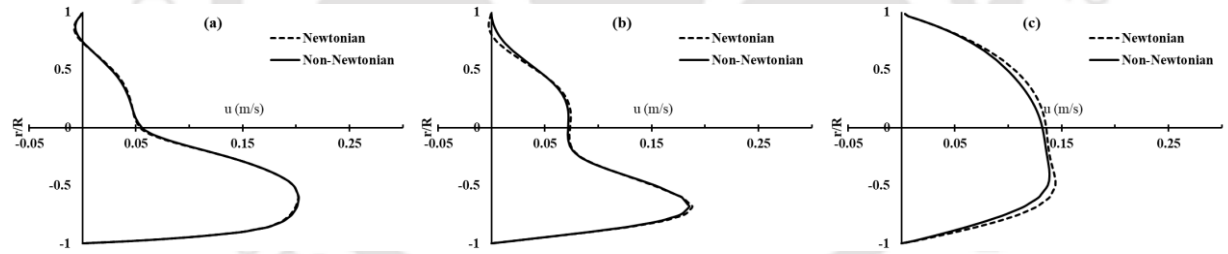

(II)

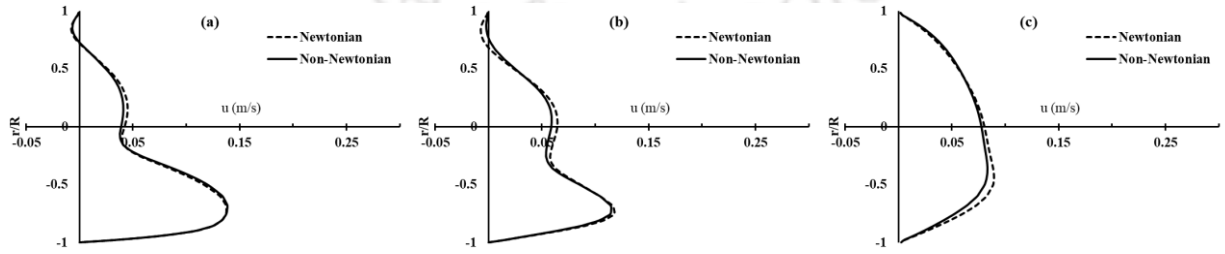

Figure 3.32 Profiles of x-component of time-averaged velocity over one cardiac cycle along the daughter vessel in the mid-plane of bifurcation for various location (S), (a) S = 1*d* (b) S = 2*d* (c) S = 6*d* at asymmetric bifurcation angle $\alpha = 45°$, $\beta = 60°$ ($\beta/\alpha = 1.33$) (I) $\alpha = 45°$, (II) $\beta = 60°$.

Backflow in the 60° daughter vessel is observed to reduce with an increase in the value of α. A significant difference in the velocity profiles is observed between the Newtonian and shear-thinning fluids.

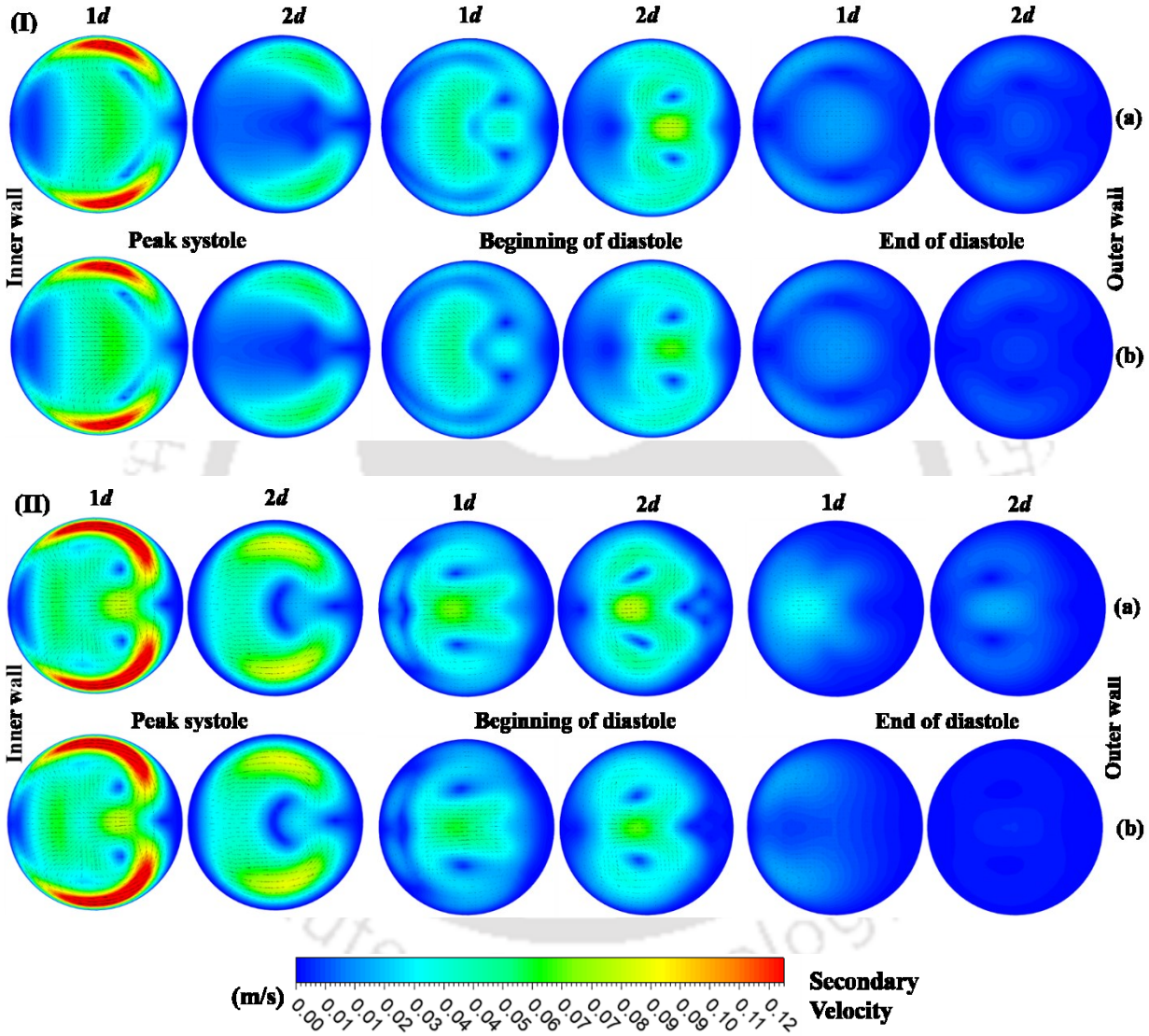

Figure 3.33 Contours and streamlines of secondary velocity on the cross-sectional planes in the daughter vessel for (a) Newtonian and (b) non-Newtonian fluids at S = d, $2d$ at t_1, t_2 and t_3 for (I) α = 15° (II) β = 60°.

The contours and vectors of secondary flow at different cross-sections for the case having $\alpha = 15°$, β = 60° for the Newtonian and non-Newtonian fluids flow are shown in Fig. 3.33. In the lower angled vessel, the center of the vortices is relatively far from the bifurcation plane at S = d and

move closer to the plane at the beginning of diastole. The secondary flow is observed to be stronger in the higher angled vessel due to the large radius of curvature of the streamlines. Almost no difference is observed in the secondary flow for the Newtonian and non-Newtonian fluids.

Figure 3.34 shows contours of streamwise vorticity (ω) on the cross-sectional planes in the daughter vessels for the Newtonian and non-Newtonian fluids at the end of diastole. The streamwise vorticity is observed to last for a longer distance downstream of bifurcation in the lower angle daughter vessel than that in the higher angle daughter vessel. The secondary flow depends on the Dean number ($De = Re\sqrt{\frac{R}{R_C}}$). Note that the flow rate and, therefore the Dean number in the lower angled daughter vessel is higher. A comparison of streamwise vorticity and secondary flow between Newtonian and non-Newtonian cases confirms the existence of higher streamwise vorticity for the Newtonian case. For the higher angle between daughter vessels, the streamwise vorticity is relatively higher downstream of the bifurcation.

Figure 3.35 shows the contours of helicity at various cross-sections in the daughter vessel for Newtonian and non-Newtonian fluids. As for the streamwise vorticity, helicity is observed to be higher in the lower angle daughter vessel in an asymmetric bifurcation, and the helical motion is present all the way to the vessel exit in the lower angle daughter vessel. As observed for the symmetric bifurcation, the helical motion is stronger for the Newtonian fluid than that for the non-Newtonian fluid. The increase in the total bifurcation angle causes increased helicity, as shown in Fig. 3.35(b).

Figure 3.36 shows the distribution of TAWSS on the inner and outer walls on the bifurcation plane for Newtonian and non-Newtonian fluids for all three asymmetric cases. The TAWSS on the outer wall near the bifurcation is significantly lower than that on the inner walls. The TAWSS on the inner wall is high at the carina (bifurcation point on the inner wall) of bifurcation due to the high-velocity gradient.

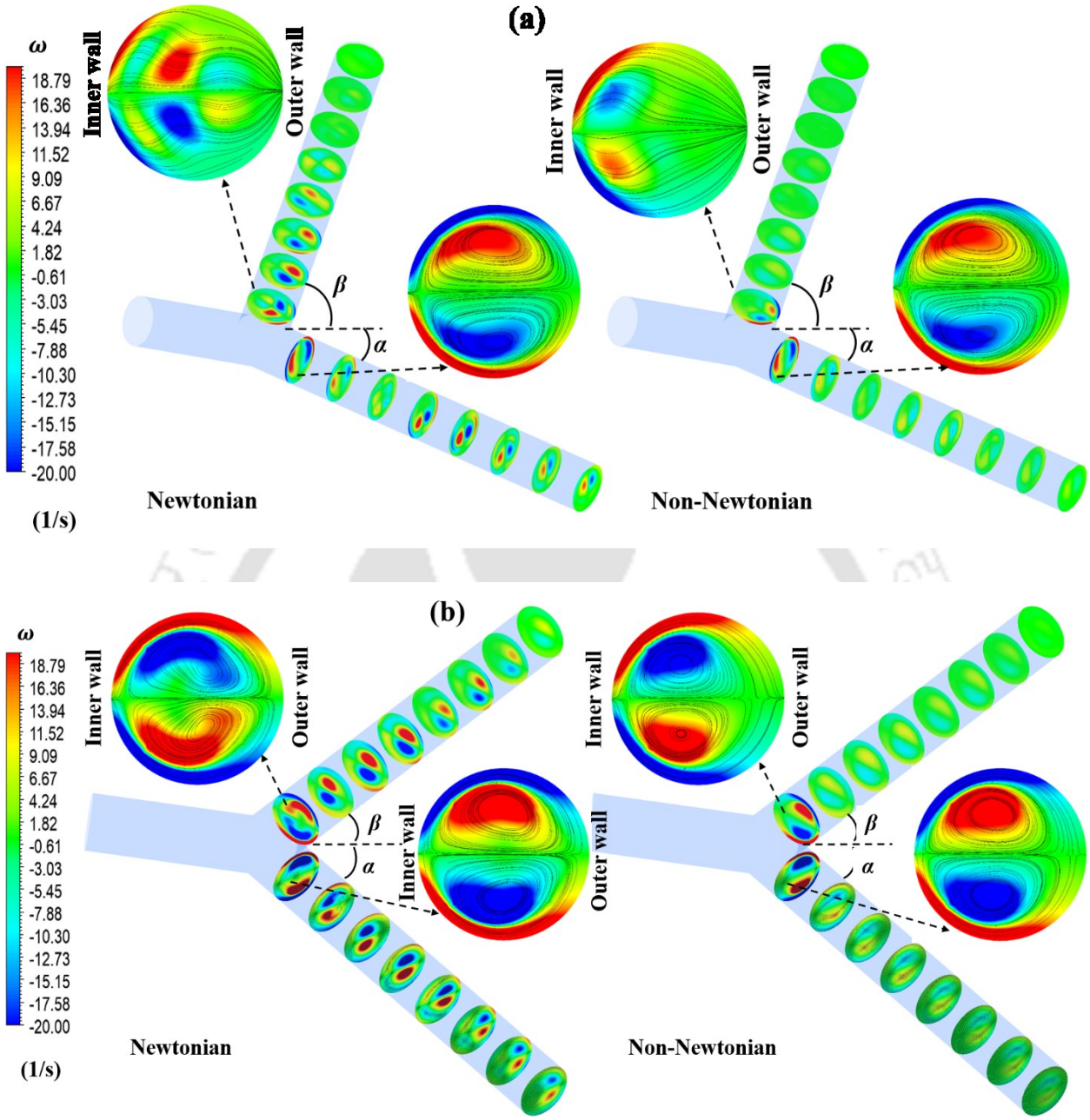

Figure 3.34 Comparison of streamwise vorticity (ω) for Newtonian and non-Newtonian fluid at the end of diastole, showing vortices strength at selected cross-sectional planes for (a) $\alpha = 15°$, $\beta = 60°$, (b) $\alpha = 45°$, $\beta = 60°$.

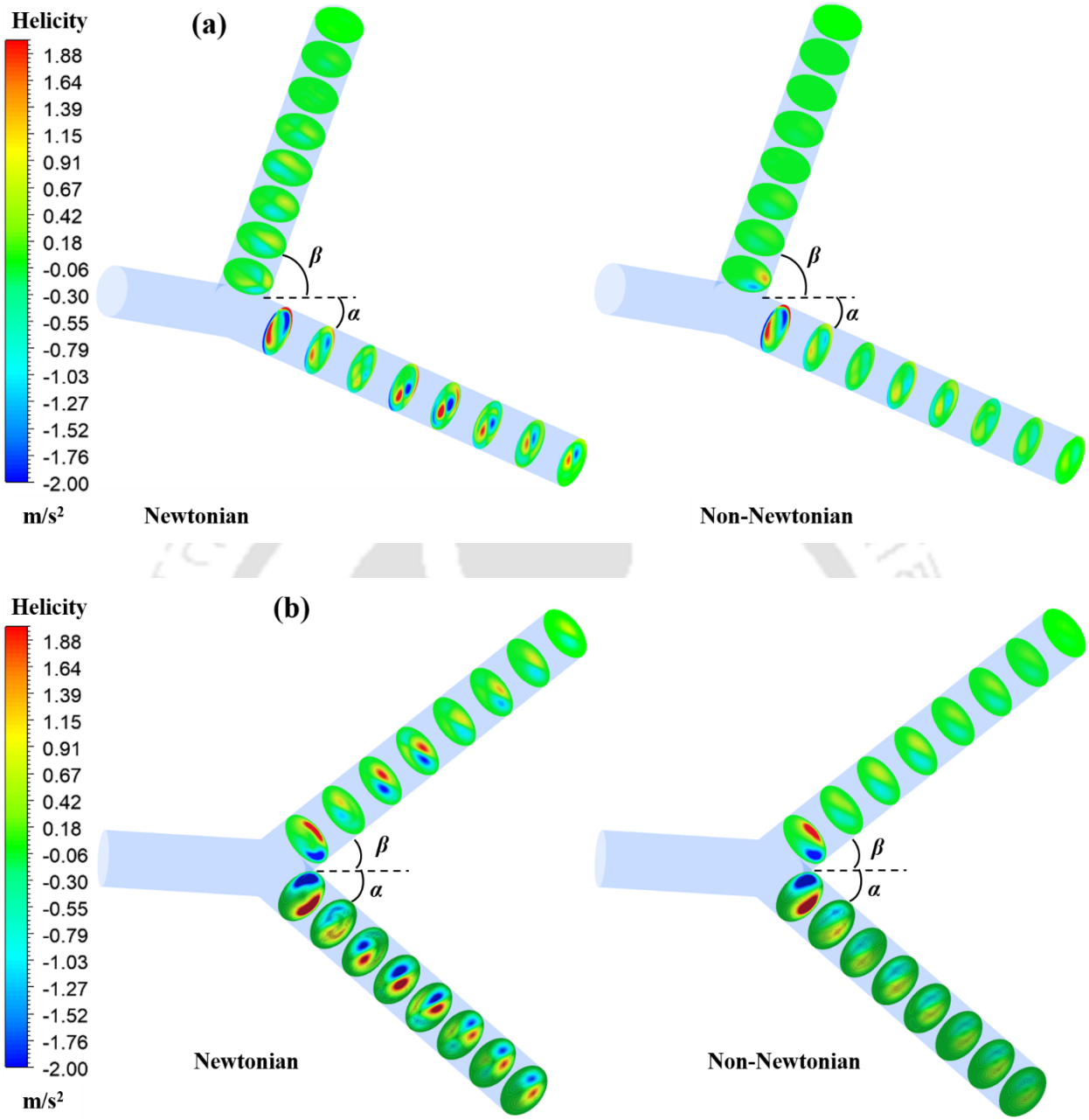

Figure 3.35 Comparison of helicity for Newtonian and non-Newtonian fluid at the end of diastole, showing helical strength at selected cross-sectional planes for (a) $\alpha = 15°$, $\beta = 60°$, (b) $\alpha = 45°$, $\beta = 60°$.

The flow rate and the velocity in the smaller angle daughter vessel is more than that in the larger angle daughter vessel. Therefore, WSS for fully-developed flow would be higher in the smaller angle daughter vessel, as can be observed downstream of the bifurcation on the inner and outer

walls. The WSS is higher on the walls CC' and DD' than on the AA' and BB', respectively downstream of

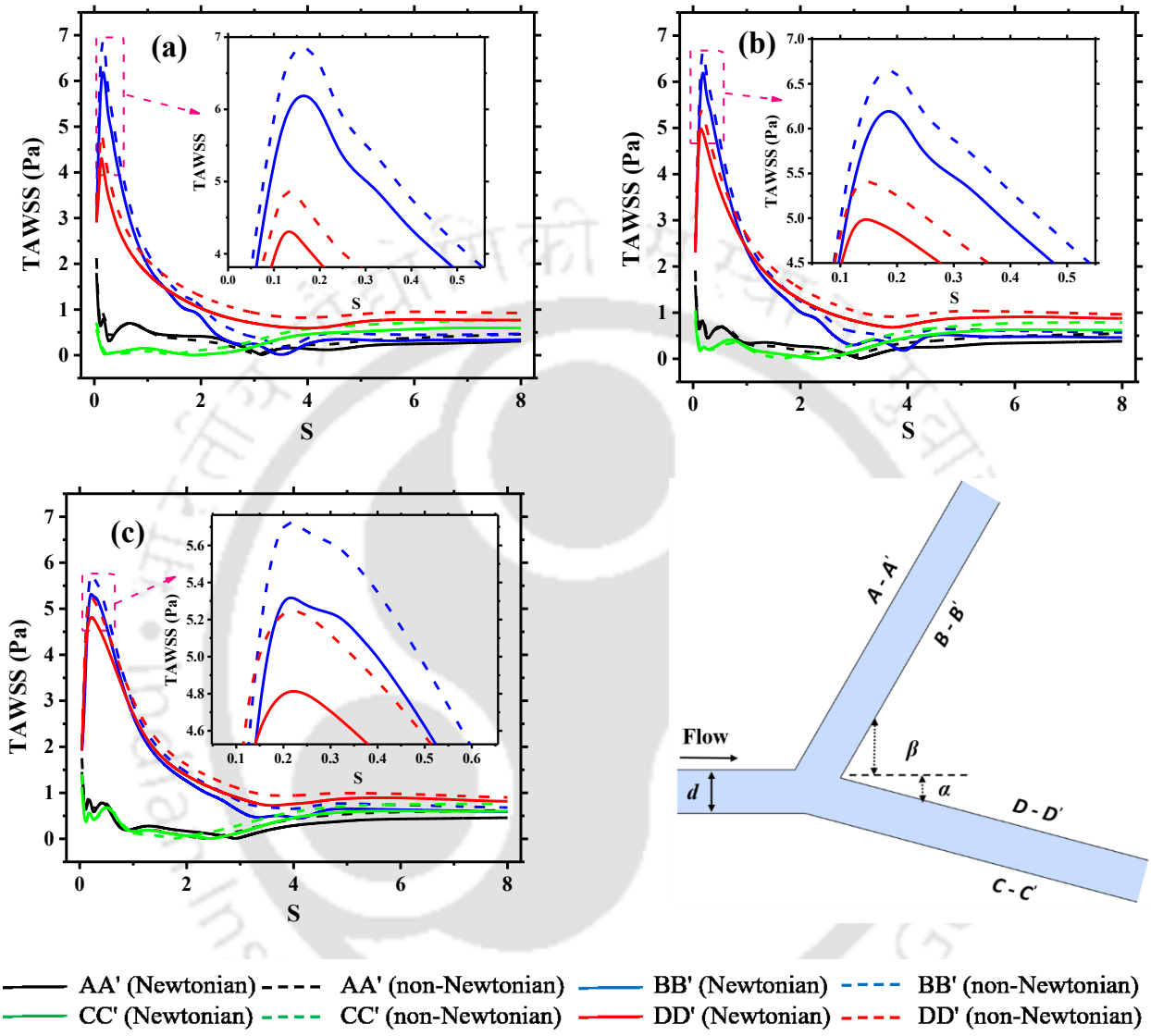

Figure 3.36 TAWSS profile along inner and outer walls in the bifurcation plane for (a) $\alpha = 15°$, $\beta = 60°$, (b) $\alpha = 30°$, $\beta = 60°$, (c) $\alpha = 45°$, $\beta = 60°$.

the bifurcation (S > 3). However, the opposite behavior is observed, and TAWSS on the lower angled vessel is less than that on, the higher angled vessel. This is because of the skewed flow in the higher angled vessel. Some differences in the TAWSS are observed for Newtonian and non-Newtonian fluids, which corresponds to the difference in the flow profile and the TAWSS for the Newtonian fluid is smaller than that for non-Newtonian fluid. While the TAWSS on the outer wall remains below 1 Pa for all three cases, the peak TAWSS on the inner wall decreases with a decrease

in the angle ratio (β/α). The results for Newtonian and non-Newtonian shear stress are in agreement with the past experiments and simulations (Araim et al., 2001; Chen and Lu, 2006; Gijsen et al., 1999).

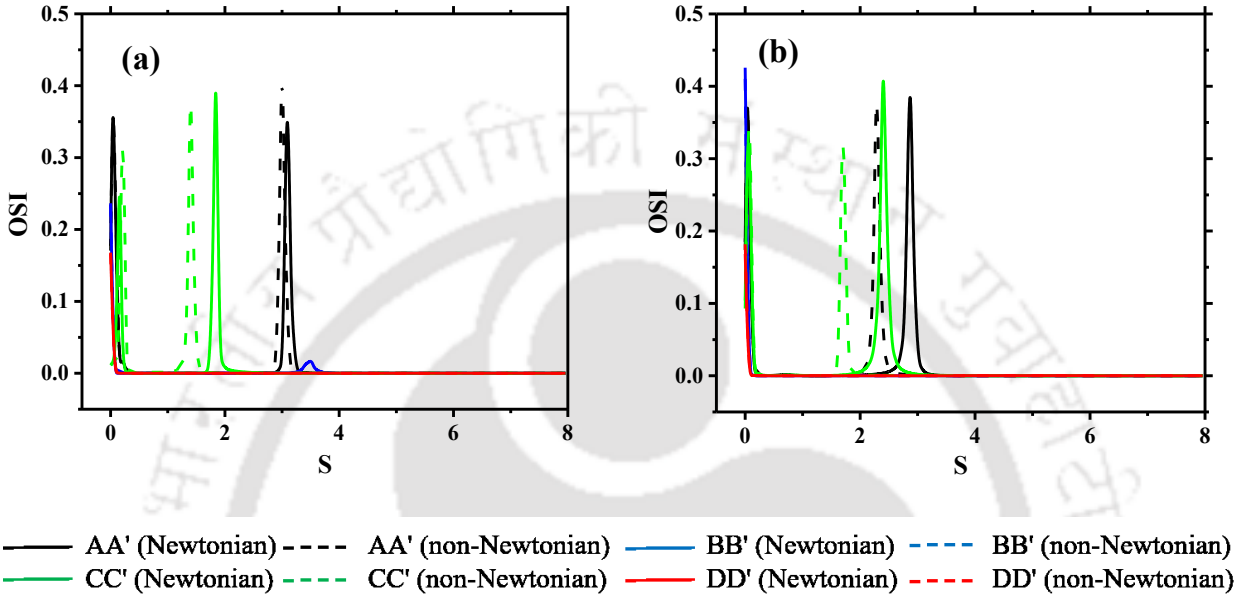

Figure 3.37 OSI profile along inner and outer walls in the bifurcation plane for (a) $\alpha = 15°$, $\beta = 60°$, (b) $\alpha = 45°$, $\beta = 60°$.

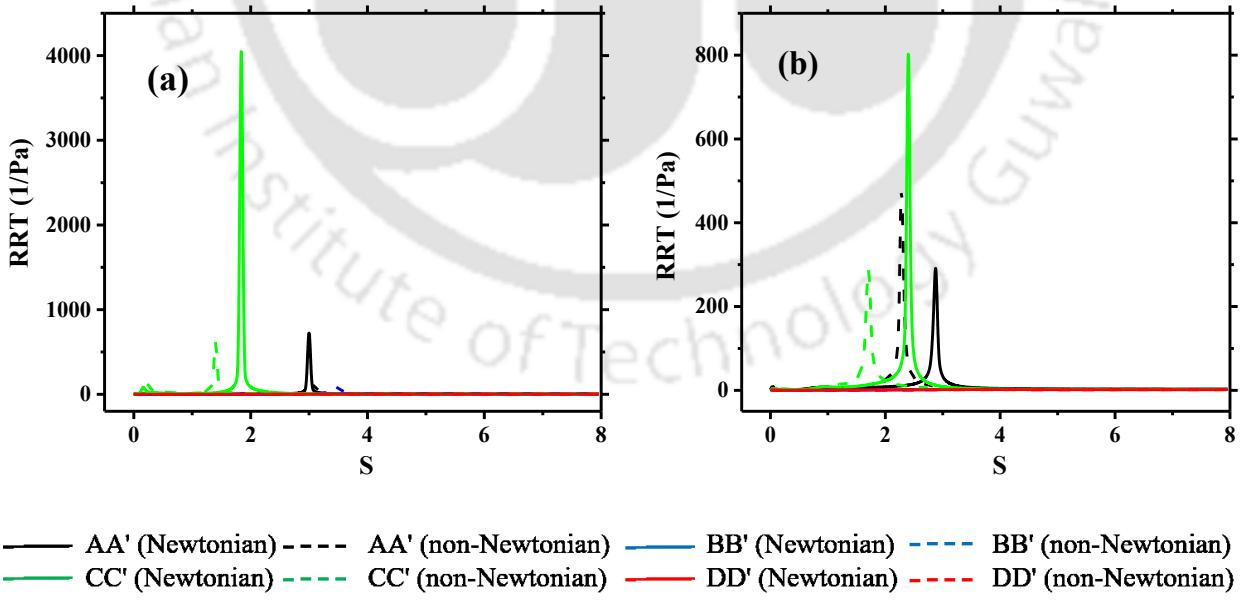

Figure 3.38 RRT profile along inner and outer walls in the bifurcation plane for (a) $\alpha = 15°$, $\beta = 60°$, (b) $\alpha = 45°$, $\beta = 60°$.

Figures 3.37 and 3.38 show the OSI and RRT, respectively, on the inner and outer walls at the bifurcation plane. As for symmetric bifurcations, OSI and RRT are zero everywhere on the inner walls and have non-zero values on the outer wall. The location of peaks in OSI and RRT are different for Newtonian and non-Newtonian fluids on both the daughter vessels. Low WSS and high OSI, and therefore high RRT, are generally related to the high possibility of atherosclerotic plaque development.

3.4 Conclusions

The steady and pulsatile flow of blood in symmetric and asymmetric bifurcating vessels assuming the blood to be a Newtonian fluid as well as a non-Newtonian fluid following the Carreau model (Cho and Kensey, 1991) is studied.

- During steady flow in asymmetric bifurcations, the flow distribution in daughter vessels is observed to be asymmetric with higher flow rate in the daughter vessel having the smaller bifurcation angle.
- While the flow divides equally between the two daughter vessels in the symmetric bifurcation, the flow in the lower angled vessel is higher in the asymmetric bifurcation, and the ratio of flow in the daughter vessels varies with time during a cardiac cycle.
- Secondary flow caused by the curvature of the streamlines is observed near the bifurcation. The secondary flow combined with the primary flow gives rise to the helical motion of the fluid in all the cases.
- Flow separation occurs at the outer wall of bifurcation, and the wall shear stress on the wall (WSS), which can be used as a biomarker, is observed to be low on the outer wall of bifurcation.
- In an asymmetric bifurcation, WSS is observed to be lower on the lower angled wall near the bifurcation and higher away from the bifurcation.
- Significant differences are observed between the results for Newtonian and non-Newtonian fluids when the shear rate is low i.e. during the period of diastole and in the flow separation region on the outer wall.
- The velocity profiles for the non-Newtonian fluid are observed to be relatively flatter than those for Newtonian fluids.

Chapter 4 Effect of Sinus Size and Position on Flow Behavior in an Idealized Carotid Artery Bifurcation

In Chapter 3, steady and pulsatile flow in a bifurcating geometry having mother and daughter vessels of the same diameters is investigated. In this chapter, an idealized geometry having similar dimensions as those in the carotid artery bifurcation is considered. Further, in the carotid sinus, a widening in the internal carotid artery is considered, and the effect of its size and location on the flow behavior and wall shear stress is investigated, assuming blood to follow a Newtonian and three different non-Newtonian models.

4.1 Introduction

Atherosclerosis is a significant cause of mortality worldwide and occurs due to the deposition of fatty material on the walls of arteries. This accumulation of fat causes a reduction in the lumen, i. e. cross-section of the vascular vessel, and is termed stenosis. The stenosis creates turbulence in the fluid which has been explored in past studies (Johari et al., 2019; Li et al., 2015; Wang et al., 2015). Atherosclerosis generally occurs at the bends and arterial bifurcations (Caro et al., 1971a; Debakey et al., 1985; Moradicheghamahi et al., 2019a; Zarins et al., 1983). Hemodynamics plays a vital role in the localization of atherosclerosis in the areas of arterial bifurcation and curved vessels. Atherosclerosis can be treated using the deployment of stents. The use of stents on hemodynamics in carotid and curved coronary artery has been investigated in past studies (Johari et al., 2020; Kabinejadian et al., 2015; Wei et al., 2019).

Carotid arteries, two in number, are located in the neck, each on the left and right sides. Each carotid artery bifurcates in internal and external carotid arteries that supply blood to the brain and face and neck, respectively. The carotid sinus or bulb, the widening of the internal carotid artery at the bifurcation, consists of baroreceptors that monitor blood pressure. At the carotid artery bifurcation, the flow is observed to skew towards the inner wall of the bifurcation, and flow separation occurs near the outer wall of the bifurcation in the daughter vessels (Chandran et al., 2007). This causes recirculation and a reduction in wall shear stress (WSS) on the outer wall, especially for higher bifurcation angles. The regions having large curvature and planar vessels are more vulnerable to atherosclerosis (Zhang et al., 2012). Past studies on the hemodynamics at

carotid artery bifurcation show that plaque formation and, therefore, stenosis tends to occur in the region of flow separation, low velocity, and low wall shear stress (WSS) (Debakey et al., 1985; Gallo et al., 2018; Ku et al., 1985; Ku and Giddens, 1983; Malek et al., 1999). These may result in carotid artery atherosclerosis and may lead to stroke.

Several hemodynamic studies suggest that wall shear stress is an important marker for the occurrence of stenosis. The flow of blood in large arteries is pulsatile in nature, and consequently the velocity in the arteries and shear stress on the arterial walls also varies with time. Several parameters derived from the transient wall shear stress have been defined in the literature to identify the probable sites of atherosclerosis. Two such parameters are oscillatory shear index (OSI) and relative residence time (RRT). The oscillatory shear index is an indicator of whether the shear stress is aligned with the time-averaged wall shear stress (TAWSS) throughout the cycle and can identify the regions of flow reversal. The Hemodynamics study in patient-specific models showed a direct relation between tortuosity and low WSS or high OSI (Lee et al., 2008). Relative residence time is the time spent by the fluid locally near the artery wall (Himburg et al., 2004). High OSI (Ku et al., 1985; Perktold and Hilbert, 1986) and high RRT (Araim et al., 2001; Glagov et al., 1988) indicate the location of fat accumulation sites.

The carotid artery geometry can have significant variation based on country, sex, age, and pathological conditions. Stroke is common in older people due to changes in carotid artery geometry with age, especially the bifurcation angle and increased curvature (Thomas et al., 2005a). Computed Tomography Angiography (CTA) studies reveal that men are more susceptible to plaque formation in the internal carotid artery (ICA) (Choi et al., 2015). In contrast, the chances of plaque formation in women are more in the external carotid artery (ECA) (Compagne et al., 2019). Another imaging study shows the sinus inflow area, sinus volume, bifurcation angle as having a positive correlation with the plaque volume (Gregg et al., 2018b). The sinus on the internal carotid artery is prone to atherosclerosis, causing fibromuscular dysplasia, or a carotid web caused ischemic stroke (Choi et al., 2015; Joux et al., 2014). Hemodynamic studies using CFD confirm that the presence of carotid sinus lowers the WSS due to backflow and increases the risk of atherosclerosis (Compagne et al., 2019; Ku et al., 1985). Similarly, the hemodynamics studies in dilated aorta have been analyzed for entry size, variable aortic neck angles, and patient-specific aorta dilation (Keramati et al., 2020; Yeow and Leo, 2016; Zhu et al., 2021).

Blood is a complex fluid. High shear rates show Newtonian behavior, i.e. a linear relationship between shear stress and shear rate. However, at low shear rates, aggregation of red blood cells (RBCs) into cylinder-like long structures, known as rouleaux, is observed causing the apparent viscosity of blood to increase (DiCarlo et al., 2019; Roberston and Owens, 2009). Literature studies show that the Newtonian model may show a significant difference, especially in stenotic vessels, between WSS values when compared with those obtained using non-Newtonian models due to the inability to capture shear-thinning behavior (Chen and Lu, 2004; Huh et al., 2015). Shear rate is low near the outer wall of arterial bifurcations. At the larger sinuses, these values are even lower. Therefore, it is imperative to assess if non-Newtonian models are required to model flow in carotid artery bifurcation. With this motivation, the need to model non-Newtonian Behavior in an idealized geometry of carotid artery bifurcation is assessed. The results obtained are compared with those obtained assuming blood to be a Newtonian fluid. Three different non-Newtonian models, namely Carreau, Herschel-Bulkley, and Power Law model, are considered. The hemodynamics study in an idealized carotid artery geometry has been investigated by considering three different non-dimensionless sinus sizes (w = 2.00, 2.50, 3.00) and sinus positions (p = 2.50, 3.75, 5.00) for Newtonian and non-Newtonian fluids.

4.2 Computational methodology

4.2.1 Bifurcation model

The geometry considered in Chapter 3 has the diameters of the mother and daughter vessels to be equal. However, the diameters of mother and daughter vessels are different in an arterial bifurcation. In this chapter, an idealized geometry of carotid artery bifurcation has been considered. The carotid artery model dimensions have been taken from the literature (Nguyen et al., 2008). The diameter of the CCA is 8 mm and has a length of 41 mm. The ECA has a diameter of 4.62 mm and a length of 47 mm, and ICA has a diameter of 5.55 mm, and a length of 47 mm. An ellipsoid represented the ICA sinus with a major axis of 22 mm, and a minor axis of 8, 10, and 12 mm for three different cases. The sinus has the same axis as the ICA, and its center is located 20, 15, and 10 mm from the bifurcation point, as shown in Fig. 4.1 (a). The geometry of the carotid artery changes with age. The average bifurcation angle ($\alpha+\beta$) is 48.5^{o} in young people (age 20-28 years) and 63.6^{o} in older people (age 50-70 years) (Thomas et al., 2005b). In the present study, the symmetric bifurcation angle ($\alpha+\beta$) between ICA and ECA is 50^{o}.

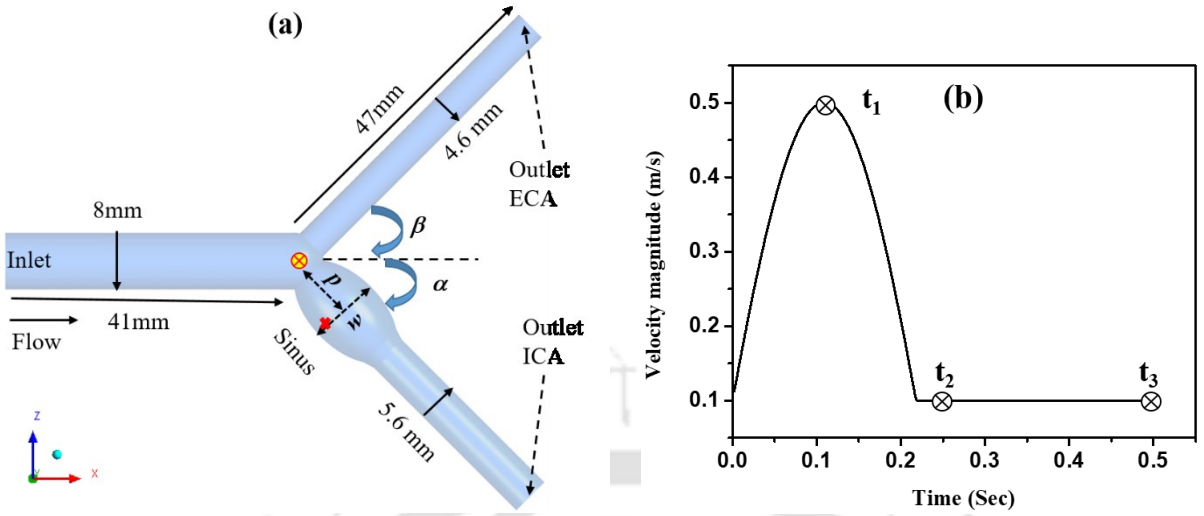

Figure 4.1 (a) Schematic of the carotid artery bifurcation model used in the present study which exists in xz plane and origin shown by red cross symbol. The x – componenet of velocity aligned with mother vessel (b) Pulsatile flow profile imposed at the inlet of the common carotid artery.

4.2.2 Rheological models

The governing equations and boundary conditions for single-phase flow are discussed in Sections 3.2.2 and 3.2.4, respectively. In this chapter, three different non-Newtonian models are considered and are described in this section.

The rheological behavior of blood depends on the shear rate. In healthy arteries, the shear rate varies from 1 to 1200 s^{-1} and depends on the time instant during a cardiac cycle and location in the vascular system (Roberston and Owens, 2009). Shear-dependent models such as power law, Herschel-Bulkley, and Carreau are used to model the shear-thinning behavior of blood. The power-law model can be expressed in the following form given by Eq. (4.1)

$$\mu = k\dot{\gamma}^{n-1} \tag{4.1}$$

where k, n are flow consistency index and power law index, respectively (Hussain et al., 1999). Depending upon the value of n, the model denotes shear thinning ($n < 1$) or shear thickening ($n > 1$) behavior of the fluid.

The Herschel-Bulkley model shows yield stress behavior in addition to shear dependent viscosity, as is clear from Eq. (4.2):

$$\mu = k'\dot{\gamma}^{n'-1} + \frac{\tau_0}{\dot{\gamma}} \tag{4.2}$$

where k' is the consistency index, τ_0 is the yield stress (Pa), $\dot{\gamma}$ is the shear rate (s^{-1}), and n' is the power-law index (Valencia et al., 2006).

The third model considered in blood flow modeling is the Carreau model, similar to the Power-law model, and expressed in the form given by Eq. (4.3)

$$\mu = \mu_\infty + (\mu_0 - \mu_\infty)[1 + (\lambda\dot{\gamma})^2]^{\frac{n^*-1}{2}} \quad (4.3)$$

Where μ_0 is the viscosity at zero shear rate, μ_∞ is the viscosity at an infinite shear rate, λ is the relaxation time, $\dot{\gamma}$ is the shear rate, and n^* is the power-law index (Cho, Y. I., Kensey, 1991). The parameters used for each viscosity model are summarized in Table 4.1.

Fig. 4.2(a) shows the apparent viscosity as a function of the shear rate obtained from the three rheological models. Experiments have shown that the apparent viscosity of blood is shear-dependent at low shear rates but is constant at the higher values of shear rate. The apparent viscosity obtained from power law and Herschel-Bulkley models decreases continuously with increasing shear rate and therefore, these models do not capture the blood rheology accurately at a high shear rate. This limitation is overcome by the Carreau model, in which the apparent viscosity is constant at low and high values of shear rates but varies at the intermediate values of shear rates. The discretization schemes and solver settings are the same as discussed in Section 3.2.5.

Table 4.1 Parameters of the viscosity models used in the CFD simulations

Viscosity model	Parameters
Newtonian	μ = 0.0035 Pa s
Power law (Hussain et al., 1999)	k = 0.01467
	n = 0.7755
Herschel - Bulkley (Valencia et al., 2006)	τ_0 = 0.0175 Pa
	n' = 0.8601
	k' = 0.0089721 kg s^{n-2} m^{-1}
Carreau (Cho, Y. I., Kensey, 1991)	μ_0 = 0.056 Pa s
	μ_∞ = 0.0035 Pa s
	λ = 3.131 (s)
	n^* = 0.3568

4.2.3 Mesh independence study and validation

A mesh independence study is carried out with three different mesh densities having 0.3, 0.45, and 0.6 million mesh elements. The five layers of prism elements are used near the wall to capture the high-velocity gradient near the wall accurately. The comparison of axial velocity for various mesh densities is shown in Fig. 4.2(a). The difference between the velocity profile at a bifurcation between 0.4 and 0.6 million elements was less than 2%.

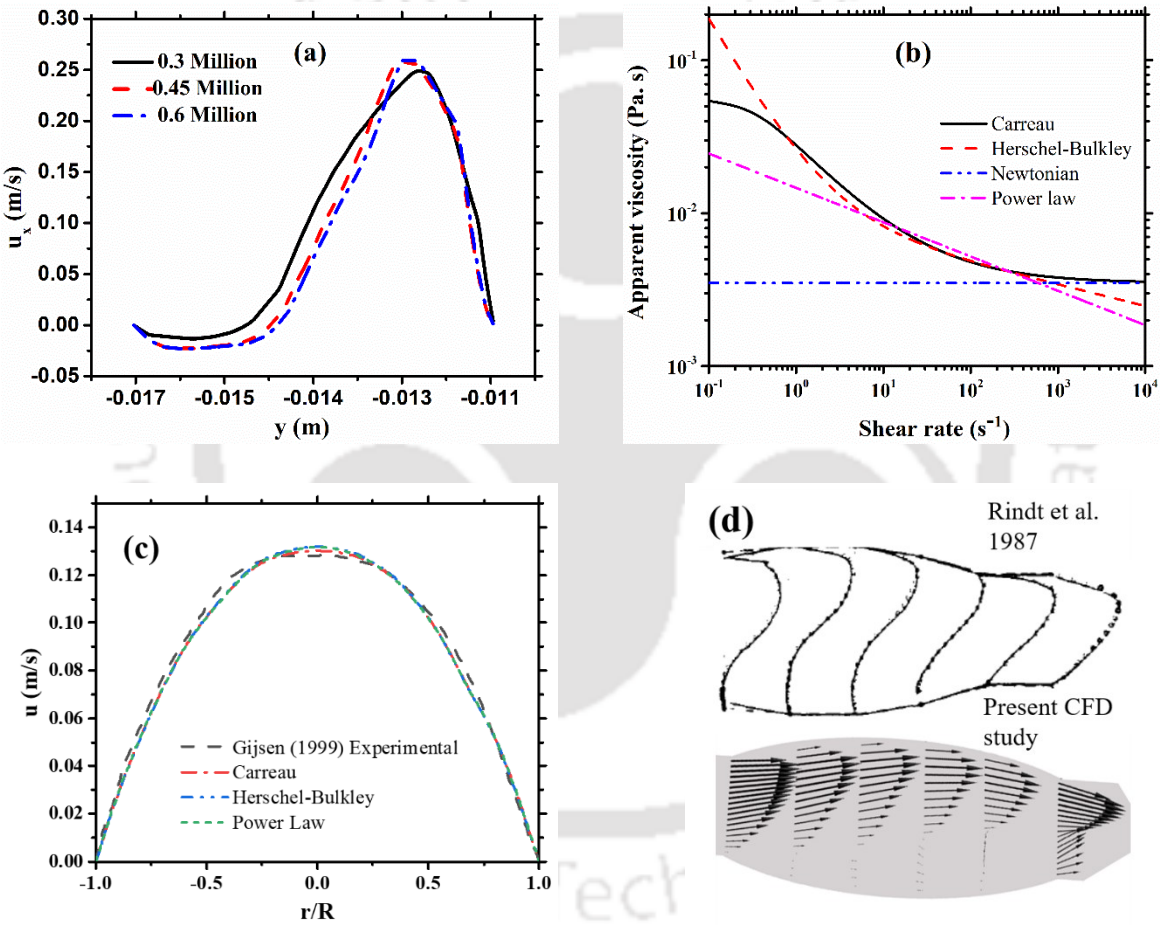

Figure 4.2 (a) Grid independence study: comparison of x-component of velocity at line 1 for steady flow (Re = 360) at various mesh density 0.3, 0.45 and 0.6 million. (b) Apparent viscosity as a function of shear rate for various rheological models (c) Comparison of axial velocity profile in mother vessel at a distance of 40 mm from inlet obtained from CFD simulations using three non-Newtonian models for steady flow at Re = 270 with experimental data of Gijsen et al. (Gijsen et al., 1999) (d) Comparison of velocity vectors at a various position on mid-plane of the carotid sinus with the experiments of Rindt et al. (1987) at Re=640.

Fig. 4.2(b) shows the apparent viscosity as a function of the shear rate obtained from the three rheological models. The shear rate in the carotid arteries varies from 1-1200 s^{-1} and respective apparent viscosity of blood varies from 0.0035-0.01 pa.s. Experiments have shown that the apparent viscosity of blood is shear-dependent at intermediate shear rates but is constant at the higher values of shear rate. Gijsen *et al.* (1999) prepared a potassium thiocyanate (KSCN) solution (KSCN, 71% by weight in water) exhibiting similar rheological behavior as that of the blood and obtained local velocity data employing laser Doppler anemometry (Gijsen et al., 1999). The results obtained from CFD simulations are compared with the results of Gijsen *et al.* (2009) for validation purposes. Figure 4.2(c) shows the profile of axial velocity in the mother vessel at a distance of 40 mm from the inlet obtained from CFD simulations for Newtonian and non-Newtonian models at *Re* = 270 in the mother vessel. The velocity profiles for both the models obtained from CFD are in good agreement with experimental data. The velocity profile for non-Newtonian models is flattened at the centre of channel due to the presence of low shear gradient. At low shear rates the viscosity of shear-thinning fluids increases which causes more resistance to flow. Due to higher viscosity at the center of vessel the non-Newtonian flow shows lower velocity values than that of Newtonian flow.

The Validation of the simulations has been done with the experimental results of the carotid artery bifurcation model (Rindt et al., 1987). Rindt et al. (1987) obtained axial velocity vectors using laser Doppler anemometry (LDA) experiments for steady flow at the mid-plane of daughter vessels (radii 8mm & Re=640) at various locations in the sinus (Rindt et al., 1987). In the present work, the carotid geometry is not exactly same as Rindt et al. (1987). Therefore, the quantitative comparison is not possible due to varying geometric configuration, but qualitatively compared to understand the velocity profiles. As shown in Fig. 4.2(d), there is a good qualitative agreement between the results obtained by Rindt et al. (1987) and current CFD simulations.

4.3 Results and discussion

4.3.1 Newtonian fluid

CFD simulations have been performed for six different cases – three for different sinus locations (p) and three for different sinus widths (w) on ICA. The change in sinus position is denoted by 'p', which is sinus position from bifurcation normalized by the radius of CCA (r_c), and its values are varied as p = 2.5, 3.75, and 5 (at fixed sinus width 'w' = 2.0). The change in sinus size is denoted

by '*w*', which is sinus minor axis normalized by the radius of CCA (r_c), and its values are varied as *w* = 2.0, 2.5, and 3.0 (at fix sinus position '*p*' = 5). The effect of these parameters on WSS, velocity profiles, and secondary flow (Dean vortices) have been investigated. Simulations have been run up to 5s (10 cardiac cycles) for each case, and results are shown for the last cycle unless stated otherwise. The results are independent of the period beyond the second cycle at a certain time instance in a cycle.

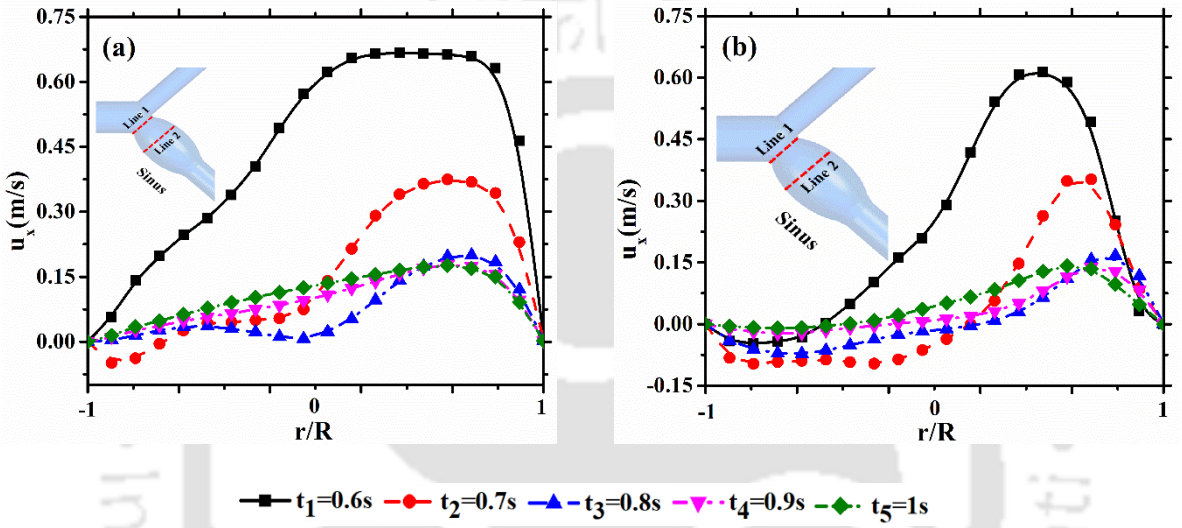

Figure 4.3 Axial velocity profiles at different time instants in second cardiac cycle for sinus width (*w*) = 2 (a) at sinus entrance (line 1) (b) in the sinus (line 2) (r/R = -1 belongs to outer wall, and r/R = 1 belongs to inner wall).

In order to present the flow field in the sinus, four different axial locations in the sinus are chosen. At these locations, velocity profiles and WSS have been plotted. The axial velocity has been plotted across diameter in the bifurcation plane in ICA. The first line, Line 1, is 9 mm away from the point of bifurcation (red cross symbol in Fig. 4.1a). The spacing between two consecutive lines is 5.5 mm. Figures 4.3(a) and 4.3(b) show the profiles of x-component of velocity for five different time instants in the second cardiac cycle on lines 1 and 2, respectively. The velocity profile at line 1 is observed to be flatter than that at line 2. The maximum negative velocity occurs just after the peak velocity, as shown in Fig. 4.3 for both line 1 and line 2. The sudden area change occurs from sinus entrance to middle of sinus, which causes flow separation. The negative velocity or recirculation is found more at line 2, which is located in the sinus, than at line 1.

4.3.1.1 Varying sinus position (p)

In this section, the effect of the distance of sinus from the bifurcation on WSS and secondary flow, the flow that occurs in a plane normal to the streamwise direction due to curvature (Dean, 1927), has been discussed. The velocity streamlines at the beginning of diastole (t_2) are shown in Fig. 4.4 for different sinus positions (p). There appears to be significant recirculation in the sinus in all three cases. Fig. 4.5 shows velocity vectors superimposed over the axial velocity contours in the sinus for three different time instants peak systole (t_1), beginning of diastole (t_2), and end of diastole (t_3). Separated flow and recirculation region can be identified by the negative x-component of velocity (dark blue color). The magnitude of velocity decreases, and the size of the region having backflow increases from time t_1 to t_2 and t_3.

The comparison of WSS magnitude contours for different sinus positions is shown in Fig. 4.6 for different time instants in one cardiac cycle. Comparing the values at a particular time instant for different sinus positions (p) shows that the WSS value decreases as the sinus moves away from the bifurcation for time instants t = 4.05 and 4.15 s. However, there is no clear trend in the shear stress at other time instants.

Figure 4.7 shows the contours of the x-component of velocity (u_x) and streamlines showing secondary flow on a plane normal to the flow direction at four different locations in the sinus. Plane 1 to plane 4 in the sinus, and each plane is equidistant from one another. The contours of u_x show the locations in the plane where the flow is reversed. It can be seen that the reverse flow occurs close to the outer wall near the bifurcation plane. The backflow is observed primarily on planes 2 and 3 located in the sinus. The reverse flow increases with an increase in the sinus distance from the bifurcation. The sinus away from bifurcation causes more backflow, especially in the middle region of the sinus. Due to backflow, the WSS values decrease and which is the probable cause of atherosclerosis initiation and progression.

Figure 4.8 shows the WSS distribution along the outer and inner walls of the internal carotid artery. The mass flow distribution in the two daughter vessels remains unchanged with the change in sinus location. The ratio of flow fraction between ICA and ECA is 0.6:0.4 during the entire cycle. WSS at the outer wall of ICA is lower than the inner walls at each time instant in the cardiac cycle, as shown in Fig. 4.8. Fig. 4.8 (b, d) shows the comparison of the effect of p on WSS value on the inner wall of ICA, the WSS value is lower for p = 5 and 3.75 compared with that for p = 2.5 for

the entire cardiac cycle. Peaks in WSS are observed at the end of the sinus. When the flow exits the sinus, the cross-sectional area decreases, and the velocity gradient near the wall is increased, leading to a sudden increase in WSS. The location of these peaks, along with ICA length, changes with a change in sinus position. Fig. 4.8 (a, c) shows the comparison WSS value comparison for different p values on the outer wall of ICA. While the variation of WSS along the downstream direction on the outer wall is the same as that on the inner wall, there is little effect of sinus location on WSS at the outer wall. However, the magnitude of WSS is smaller than that for the inner wall.

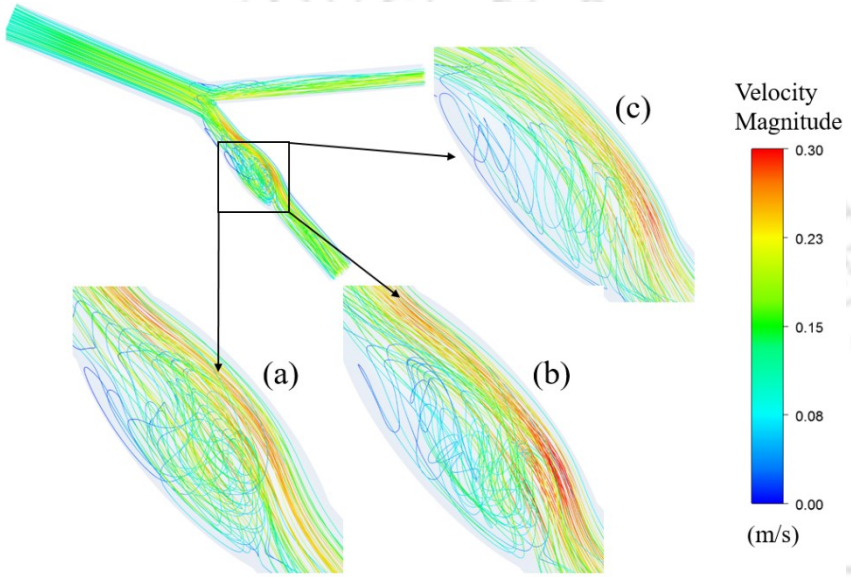

Figure 4.4 3D streamlines at the bifurcation plane (xz plane) for different sinus positions at time t_2 (a) $p = 5$ (b) $p = 3.75$ (c) $p = 2.5$ at fix value of $w = 2.00$.

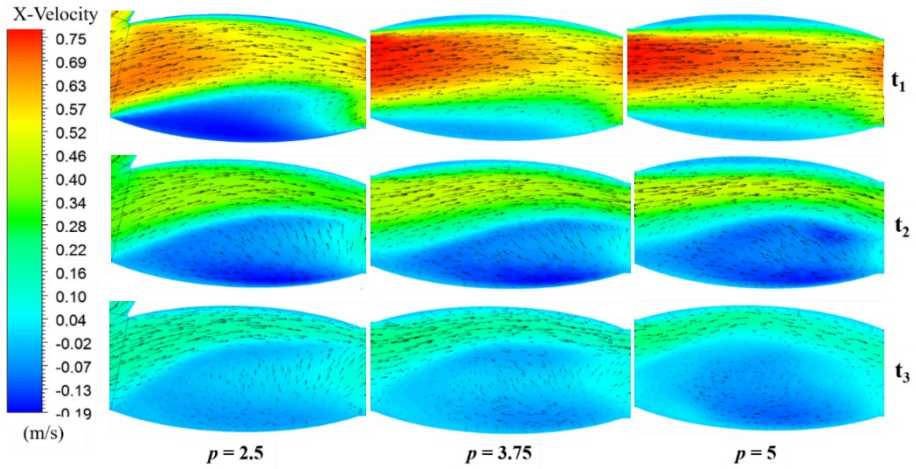

Figure 4.5 Contours of x-component of velocity superimposed over velocity vector at carotid sinus for different sinus positions (p) at fix value of $w = 2.00$ during beginning of diastole (t_2).

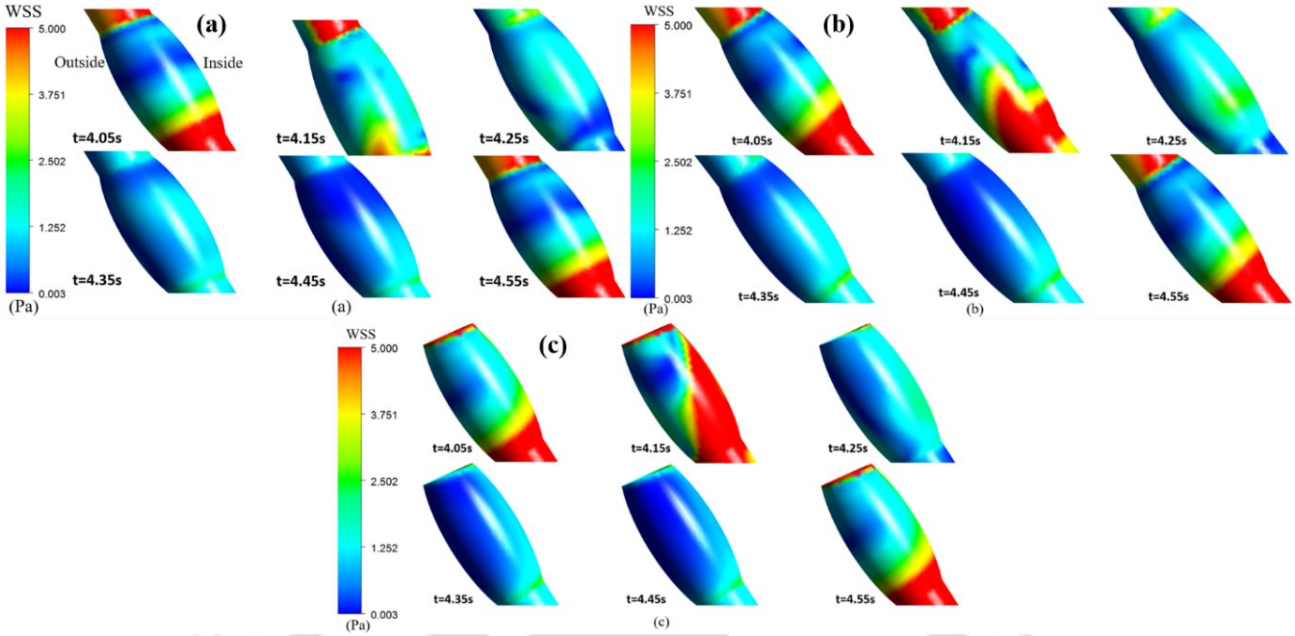

Figure 4.6 WSS magnitude on sinus at different time instants for second last cardiac cycle (a) Sinus position (a) $p = 5$ (b) $p = 3.75$ (c) $p = 2.5$ at fix value of $w = 2.00$.

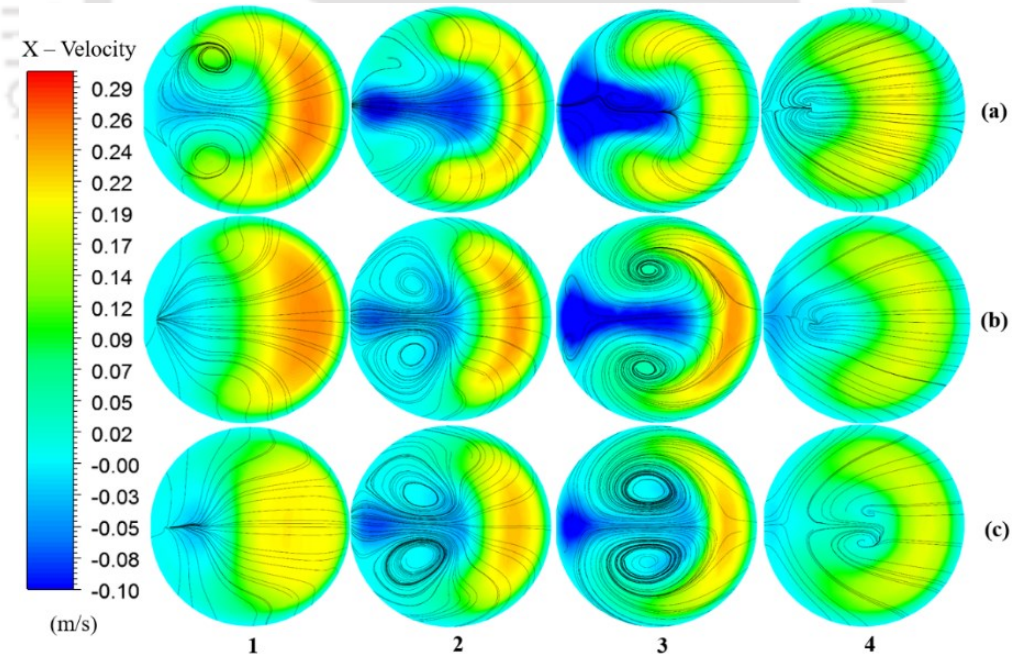

Figure 4.7 Contours of x - component of velocity superimposed on surface streamlines on the sinus cross-section from plane 1-4 at time t_2 (a) $p = 5$ (b) $p = 3.75$ (c) $p = 2.5$ at fix value of $w = 2.00$. The outer wall is towards the left in the figure.

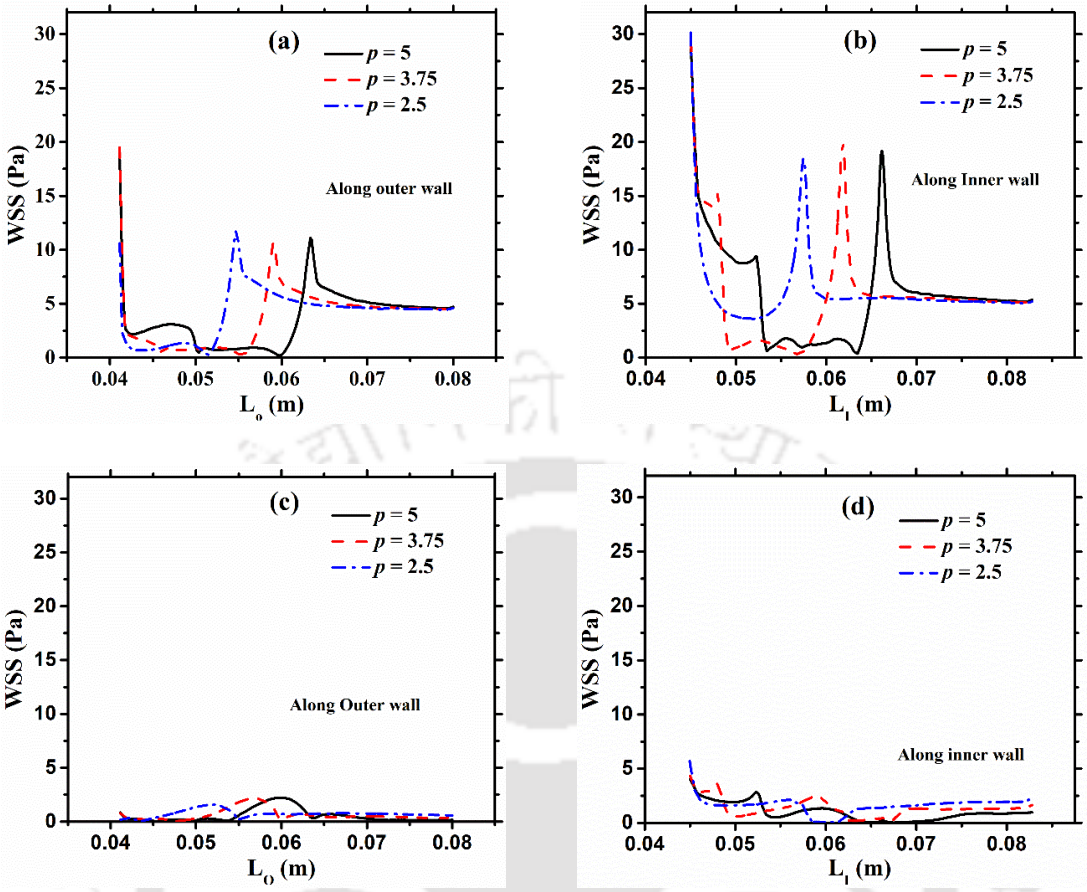

Figure 4.8 WSS along the inner and outer wall of ICA for different sinus positions at various time instances during the cardiac cycle (a) & (b) at peak systole (t_1), (c) & (d) at the beginning of diastole (t_2).

4.3.1.2 Various sinus size (w)

This section describes the effect of sinus size (length along diameter) on flow behavior and WSS. Simulations are performed for three different sinus sizes (w) of 2.0, 2.5, and 3.0 for the constant sinus position of $p = 5$. The sinus sizes are ratio of length of major axis to mother vessel diameter. As the sinus size increases, the expansion ratio from ICA to sinus increases, which results in a smaller velocity in the sinus. Surface streamlines are shown in Fig. 4.9 for the different sinus sizes (w). While the recirculation exists only at the outer wall for $w = 2.0$, the recirculation is observed near the inner and outer walls for the two bigger sinuses. As a result, a large fraction of the sinus cross-section is covered by the recirculating flow in the bigger sinuses, and only a smaller area is available for the streamwise flow. Consequently, the maximum velocity is highest in the largest sinus.

The comparison of WSS magnitude contours for different sinus sizes is shown in Fig. 4.10 at different time instants during one cycle. While it is difficult to predict a consistent trend of WSS with the change in sinus size at all-time instants on the entire sinus, on average bigger sinus shows a low WSS value compared with that for the smaller one.

Figure 4.11 shows the contours of the x-component of velocity (u_x) and streamlines showing secondary flow on a plane normal to the flow direction at four different locations in the sinus. The reverse flow increases with an increase in sinus size. With an increase in the sinus size, the area available for the flow in the downstream direction decreases. Interestingly, in the bigger sinuses, the downstream flow is observed to have secondary flow (see streamlines for planes 2 and 3 for w = 2.5 and 3.0). Further, in the bigger sinuses, backflow is observed at inner as well as outer walls. In the larger sinuses, this backflow is observed even at the exit of the sinus (plane 4), and the backflow is not limited to the bifurcation plane. The bigger sinuses are more susceptible to atherosclerosis due to their low WSS value.

Figure 4.12 shows WSS on the inner and outer walls of the internal carotid artery at different time instants. On the inner wall, the WSS is lower for two bigger sinuses (at sinus) than the smallest one (w = 2.0), which is caused by the presence of recirculations on the inner wall in the bigger sinuses. As observed in Fig. 4.10 in section 5.3.1, there is a peak in WSS at the sinus exit. The peak is prominent at the time instant when the flow rate is higher. As the WSS is lower for larger sinus diameter (w), they are more prone to atherosclerosis. The larger sinus diameter shows high OSI (Saho and Onishi, 2017), but it lacks the information of the secondary flow pattern in the sinus, which gives more insight into recirculation. Higher OSI values or low WSS values are an indicator of atherosclerosis, so that the results are in good agreement with literature findings (Ku et al., 1985; Perktold and Resch, 1990; Saho and Onishi, 2017). The CFD results obtained in the present study found that a low WSS value occurs at the larger carotid sinus. The low WSS value reflects the probability of the formation of atherosclerosis. The value of WSS is lowest for a larger sinus diameter.

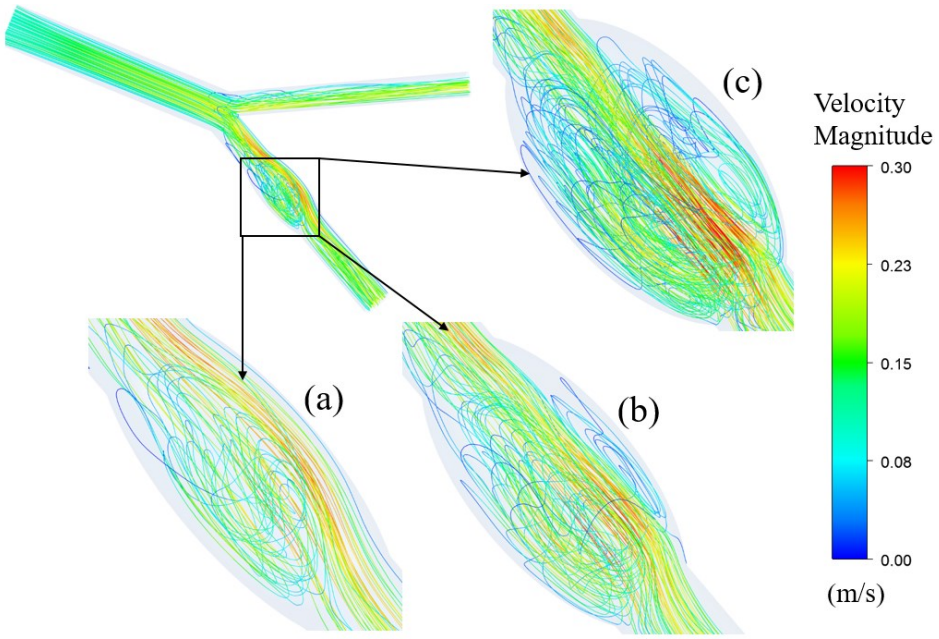

Figure 4.9 Three-dimensional velocity streamlines for different sinus sizes (w) during beginning of diastole (t_2) (a) w = 2.0 (b) w = 2.5 (c) w = 3.0 for the constant sinus position of p = 5.

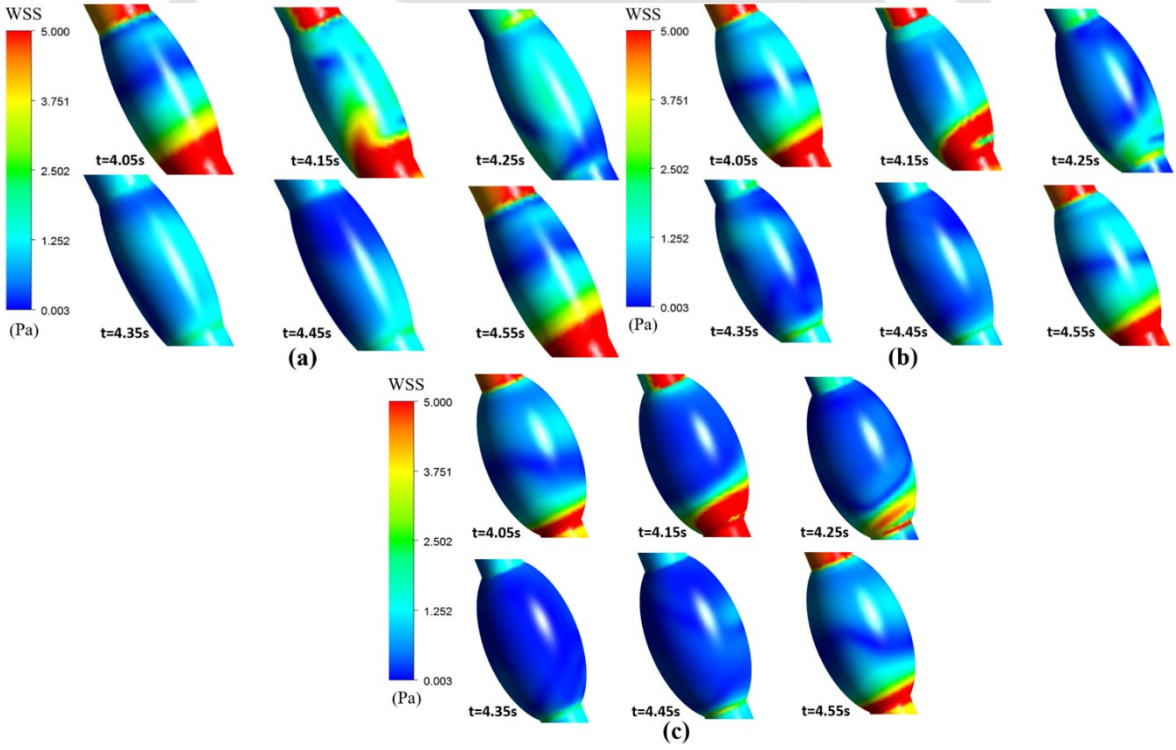

Figure 4.10 WSS magnitude on sinus at different time instants for the second last cardiac cycle (a) w = 2.0 (b) w = 2.5 (c) w = 3.0 for the constant sinus position of p = 5.

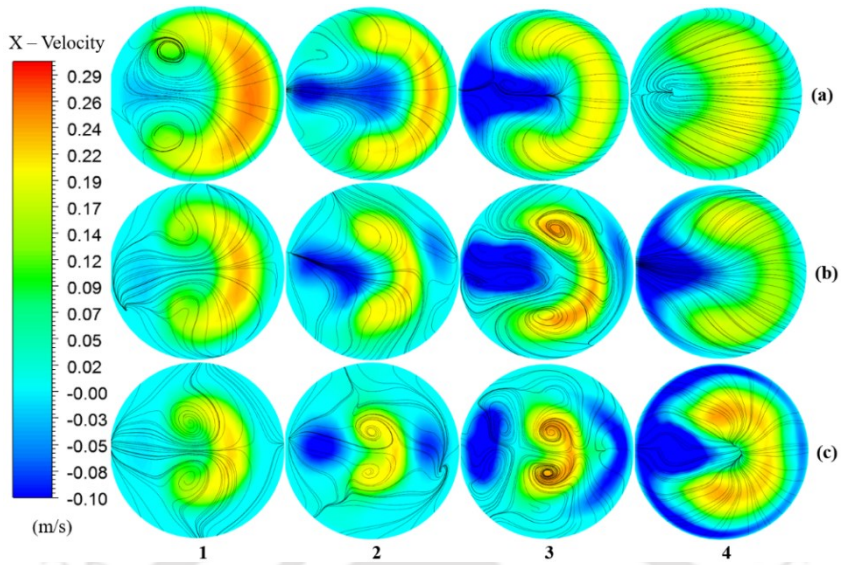

Figure 4.11 Contours of x - component of velocity superimposed on velocity streamlines on the sinus cross-section from plane 1 - 4 at beginning of diastole (t_2) (a) $w = 2.0$ (b) $w = 2.5$ (c) $w = 3.0$ for the constant sinus position of $p = 5$.

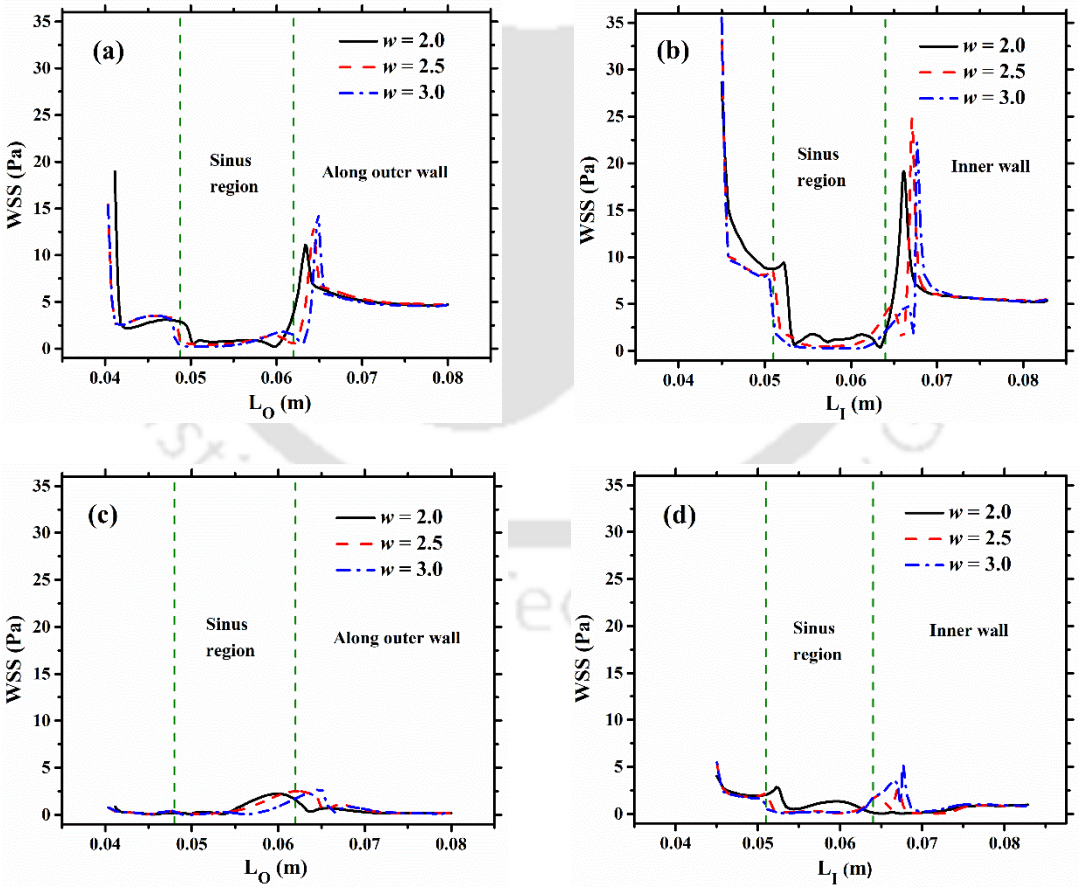

Figure 4.12 WSS along the inner and outer wall of ICA for different sinus sizes at various time instances during cardiac cycle (a) & (b) at peak systole (t_1), (c) & (d) at beginning of diastole (t_2).

4.3.2 Non-Newtonian fluids

The previous section observed a significant backflow in larger sinuses, assuming blood to be a Newtonian fluid. The shear rate is low in this region. As blood behaves as a non-Newtonian fluid, understanding non-Newtonian fluid behavior in a larger sinus needs to be investigated. This section compares three non-Newtonian fluid models, power law, Carreau, and Herschel-Bulkley, with the Newtonian fluid for varying sinus size (w).

CFD simulations are performed for three different sinus sizes, w = 2.0, 2.5, and 3.0. The effect of sinus width on WSS, velocity profiles, and secondary flow (Dean, 1927) using different rheological models has been investigated. Simulations have been run for five cardiac cycles (2.5s) for each case, and the results shown are for the last cycle.

Figs. 4.13(a) and (b) show the variation of apparent viscosity and shear rate, respectively, during a cardiac cycle at a single point near the outer wall of bifurcation, as shown by the red symbol in Fig. 4.1(a). While the trend of change in apparent viscosity is similar for all three non-Newtonian models, there exist some differences in the magnitude of apparent viscosity obtained from the three non-Newtonian models. It is apparent that the WSS obtained from the Herschel-Bulkley model is higher when compared with the value obtained from other models throughout the cardiac cycle. It can be seen from Fig. 4.13 that the apparent viscosity varies opposite to the shear rate. The viscosity is higher when the shear rate is low and vice-versa (Roberston and Owens, 2009).

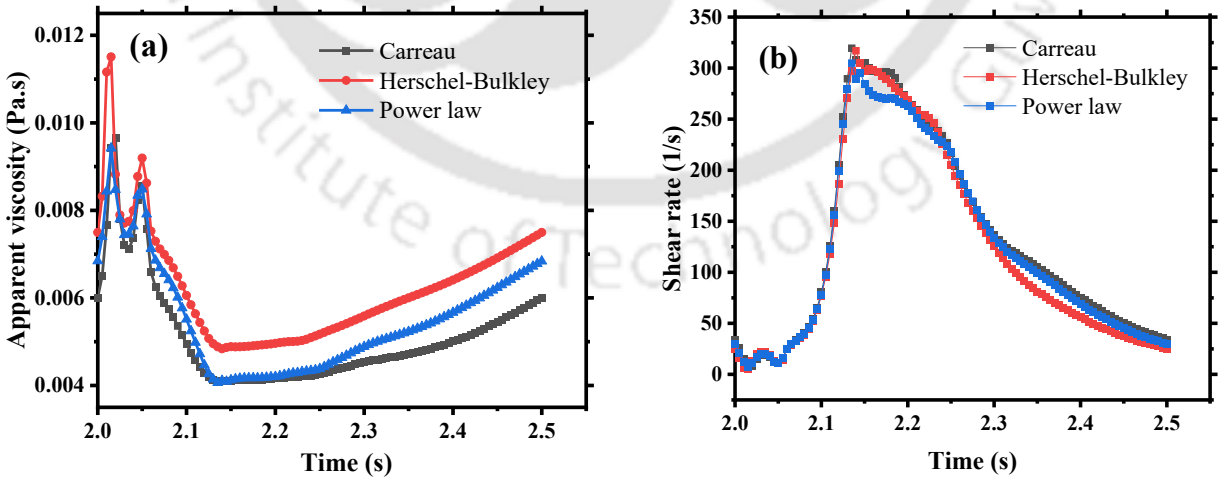

Figure 4.13 (a) Apparent viscosity and (b) shear rate obtained from the three rheological models at a point near (red cross symbol shown in Fig. 1a) the outer wall of the sinus (w = 3.0) during a cardiac cycle.

Figs. 4.14(a) and 4.14(b) show the contour plots of apparent viscosity obtained from the three rheological models at peak systole and end of diastole, respectively. The apparent viscosity for the non-Newtonian models varies spatially and temporally according to the local shear rate. In the developing and fully-developed regions where the flow is unidirectional, in the mother vessel and downstream of the daughter vessel, the apparent viscosity in the non-Newtonian models is high in the middle of the vessel as the shear rate is low in the region. The shear rate is quite high near the wall, which results in low apparent viscosity because of the shear-thinning behavior of the fluid. In fact, the apparent viscosity near the wall appears to be almost the same for all the cases except in the sinus, where flow separation occurs. In the sinus region, flow expands, velocity decreases, and flow separation occurs. As a result, the shear is low and apparent viscosity is high. In the Herschel-Bulkley model, the region occupied by high apparent viscosity is higher when compared with those obtained from power law and Carreau models.

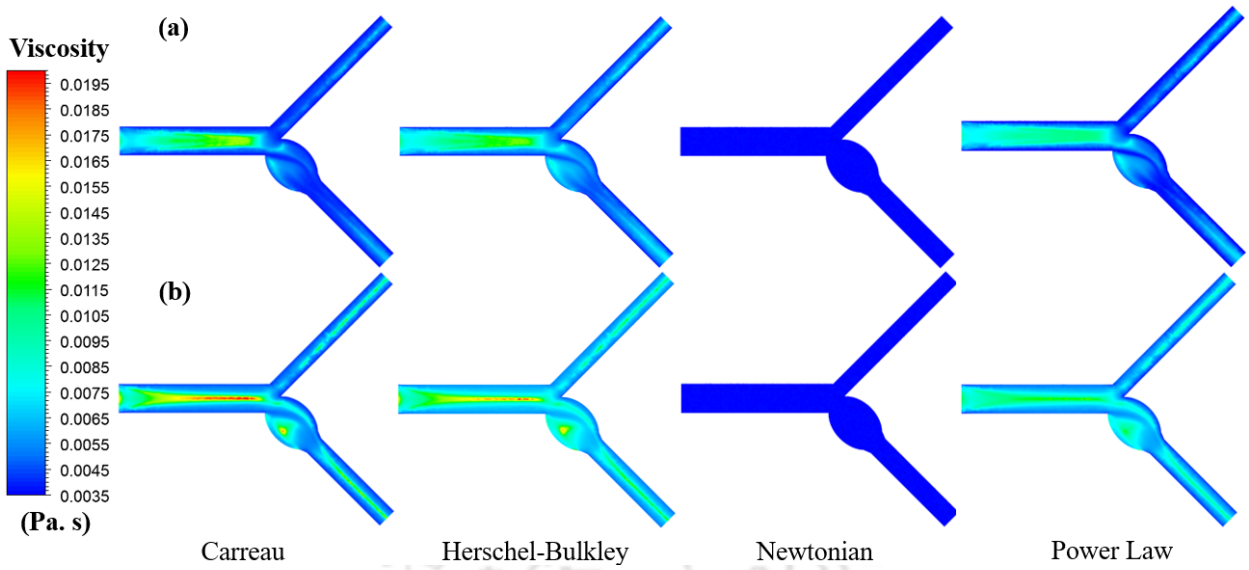

Figure 4.14 Contour of apparent viscosity obtained from the three rheological models at a mid-plane of idealized carotid artery bifurcation ($w = 3.0$). (a) At peak systole, (b) at the end of diastole.

Figures. 4.15 and 4.16 show the comparison of the x – component of velocity across sinus diameter for different rheological models for sinus width (w) of 2.0 and 3.0. The velocity profiles are shown at the entrance (Fig. 4.15, 4.16 (a), (d)), middle (Fig. 4.15, 4.16 (b), (e)), and exit of the sinus (Fig. 4.15, 4.16 (c), (f)). During systole, the Reynolds number is relatively high (Re = 1212), and the boundary layer becomes much thinner, as is evident from steep velocity gradients near the wall as

shown in Fig. 4.15, 4.16 (a, b, and c). The velocity profiles at peak systole are almost the same for Newtonian and non-Newtonian models for all cases of sinus width. The maximum velocity observed in the sinus decreases with an increase in sinus width (w), as seen in Fig. 4.15 and 4.16. The velocity profile in the middle of the sinus shows more recirculation, as shown in Fig. 4.15 and 4.16 (b). Due to recirculation, the shear rate is low in these regions, especially at the outer wall (from r/R = -1 to -0.5).

For the non-Newtonian models, the blood viscosity increases at the low shear rate, resulting in the difference in Newtonian and non-Newtonian velocity profiles. The maximum velocity at all locations decreases with the increase in the sinus size. In the previous section, it is observed that larger sinuses cause a decrease in WSS for Newtonian blood flow.

The distribution of time-averaged wall shear stress (TAWSS) on the carotid sinus wall is shown in Figs. 4.17, and 4.18 for w = 2.0, and 3.0 respectively. TAWSS is lower at the outer wall of the sinus than that at the inner wall for all the cases. A large area on the outer wall has WSS ~0.4 Pa or less and is therefore prone to plaque formation, as suggested in the literature (Ku et al., 1985; Ku and Giddens, 1983; Perktold and Hilbert, 1986). For the smaller sinus (w = 2.0), the low TAWSS region is limited to the outer wall of bifurcation. There is no remarkable difference in TAWSS between Carreau, Herschel-Bulkley, and Power-law models. However, the Herschel-Bulkley model shows a higher value of TAWSS in the region shown by black dotted lines. The difference between Herschel-Bulkley and Newtonian models is very little in the region of interest (dotted circles) for all three cases. For larger sinus, the region of low TAWSS extends to the top and bottom of the sinus wall, as shown in Figs. 4.18. The area-averaged TAWSS values over larger sinus (w = 3.0) wall obtained from Carreau, Herschel-Bulkley, Newtonian, and Power-law models are 140.2, 142.6, 135.0, and 134.8 Pa, respectively. The Herschel-Bulkley and Carreau models show that WSS values are slightly higher than those obtained from Newtonian and Power-law models. The same trend is observed for smaller sinuses.

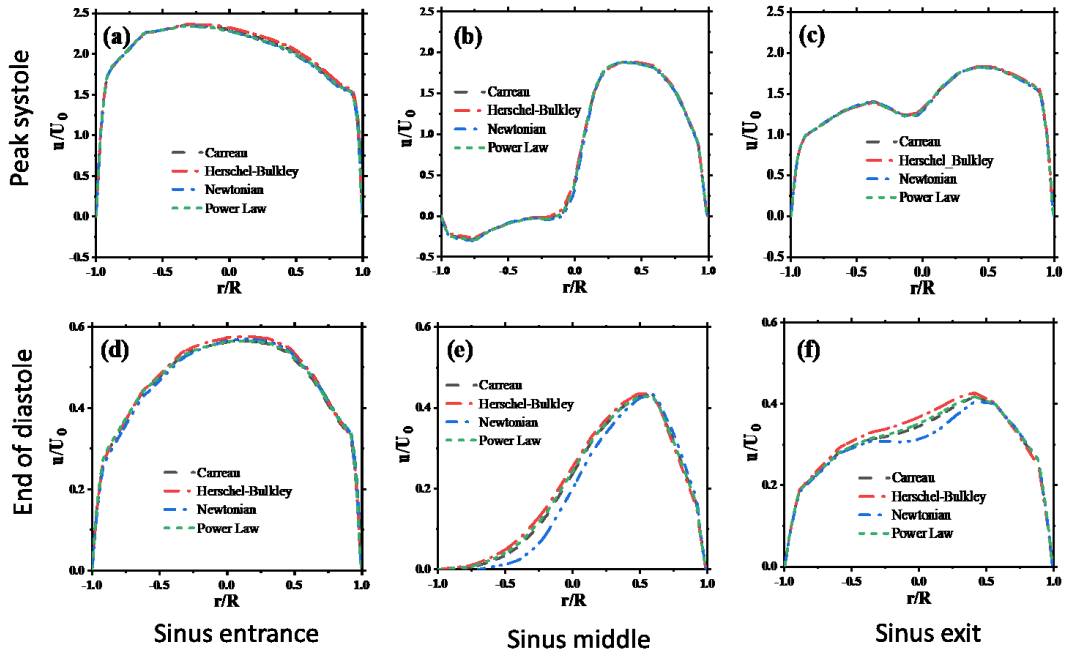

Figure 4.15 The dimensionless x-velocity profile across sinus cross-section at different rheological models for sinus size (w) = 2. (a)-(c): at peak systole, (d-f): at the end of diastole. (a), (d) sinus entrance (b), (e) sinus middle (c), (f) sinus exit.

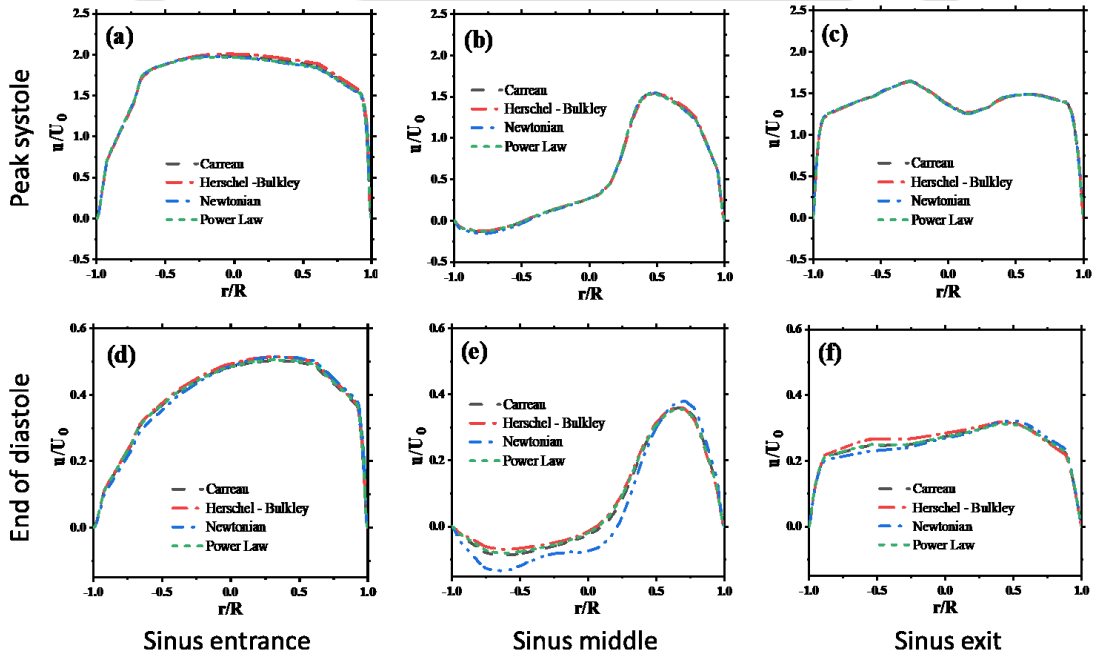

Figure 4.16 The dimensionless x-velocity profile across sinus cross-section at different rheological models for sinus size (w) = 3. (a)-(c): at peak systole (t_1), (d-f): at the end of diastole (t_2). (a), (d) sinus entrance (b), (e) sinus middle (c), (f) sinus exit.

OSI represents an index that describes the shear stress acting in directions other than the direction of the temporal mean shear stress during a cardiac cycle. The distribution of OSI is presented in Figs. 4.19, and 4.20 for different sinus sizes. The zero value of OSI corresponds to no changes in the sign of WSS. In contrast, the OSI value of 0.5 corresponds to the equally positive and negative values of WSS in a cycle at a point (Ku et al., 1985). There is no remarkable difference in OSI value between Carreau, Herschel-Bulkley, and Power-law models. The area occupied by higher OSI increases with an increase in sinus size, as shown in Figs. 4.20.

Figures 4.21, 4.22 present the RRT contours for various models for $w = 2.0$, and 3.0, respectively. The results showed that the outer wall of the sinus has high RRT values, a pattern observed for all non-Newtonian models. A minor difference with RRT values for non-Newtonian models is observed. However, the region occupied by a higher RRT value is larger in the Newtonian case, in the region shown by the black line in Fig. 4.21. A similar pattern is observed for larger sinuses, as shown in Fig. 4.22. For larger sinuses, the high RRT region expanded to the top and bottom walls, which is limited to the middle of the sinus in smaller sinus cases.

Fig. 4.23 shows time-averaged 3D streamlines for three different sinus sizes using Newtonian and non-Newtonian (Carreau) rheological models. An increase in sinus size increases the area occupied by recirculation for both Newtonian and Carreau models, which is almost the same in Newtonian and non-Newtonian cases. A Newtonian model shows a slightly bigger recirculation zone than that for the Carreau model, which is consistent with the past study of particle image velocimetry experiments in stenosed carotid artery phantom (DiCarlo et al., 2019). The increased recirculation in a Newtonian model for all three sinus sizes is probably due to the absence of shear-thinning behavior.

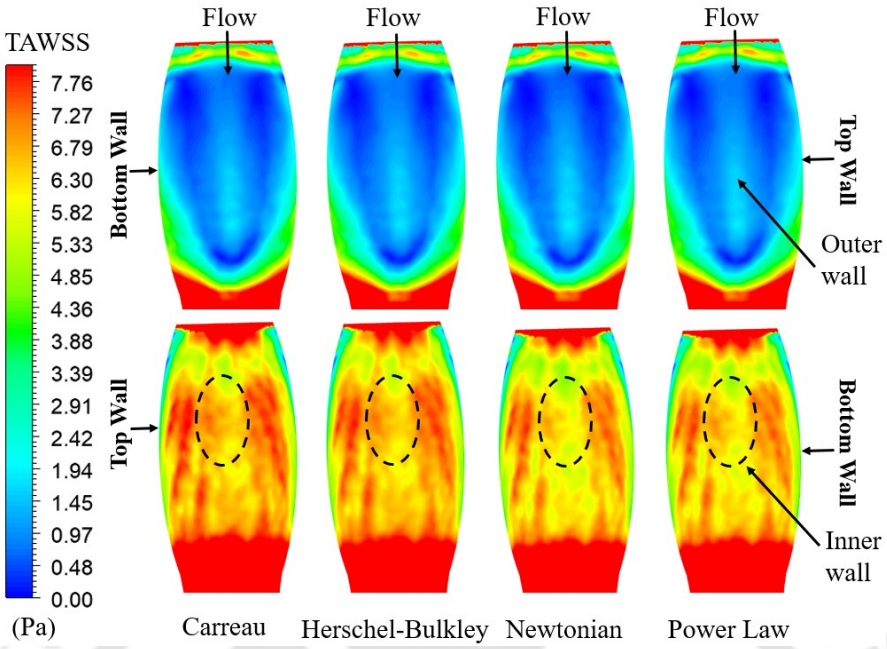

Figure 4.17 Comparison of time-averaged wall shear stress (TAWSS) contours at the inner and outer wall of sinus size (w) = 2 for the three rheological models (area of interests are shown by dotted elliptical lines).

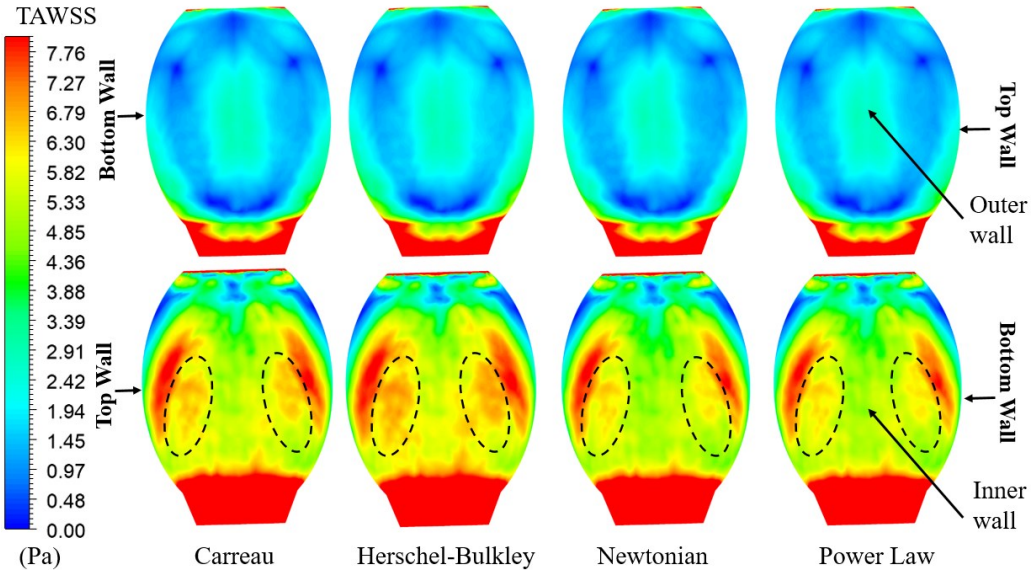

Figure 4.18 Comparison of TAWSS contours at the inner and outer wall of sinus size (w) = 3 for the three rheological models (area of interests are shown by dotted elliptical lines).

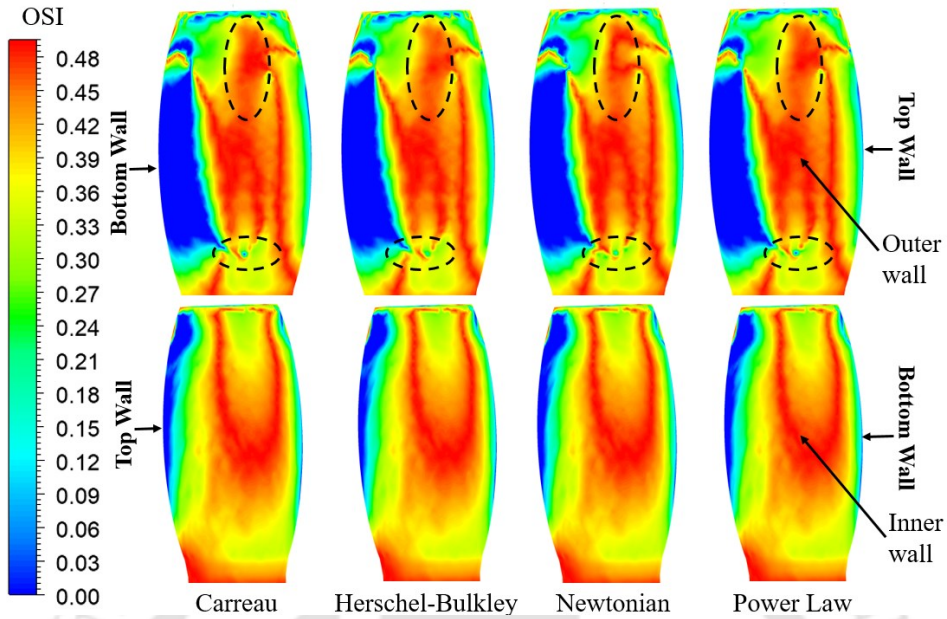

Figure 4.19 OSI contours on the sinus inner and outer wall at sinus size (w) = 2 for the three rheological models (area of interests are shown by black dotted lines).

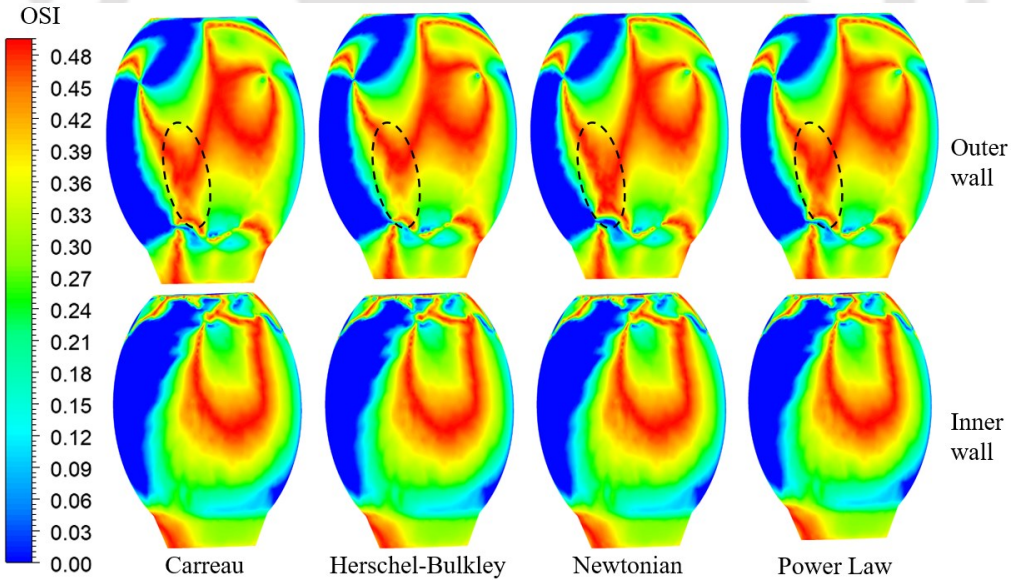

Figure 4.20 OSI contours on the sinus inner and outer wall at sinus size (w) = 3 for the three rheological models (area of interests are shown by black dotted lines).

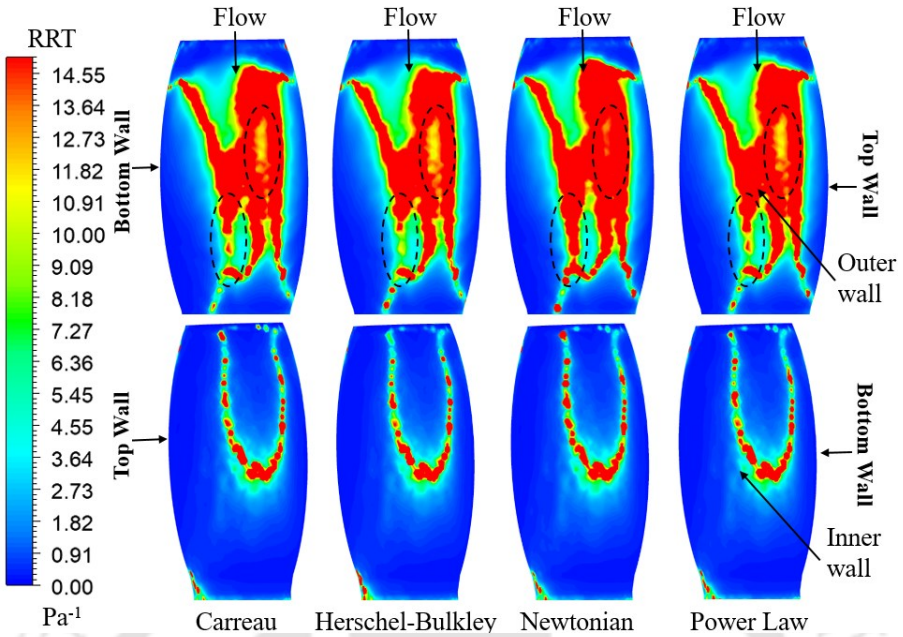

Figure 4.21 RRT contours on the sinus inner and outer wall at sinus size (w) = 2 for various rheological models (area of interests are shown by black dotted lines).

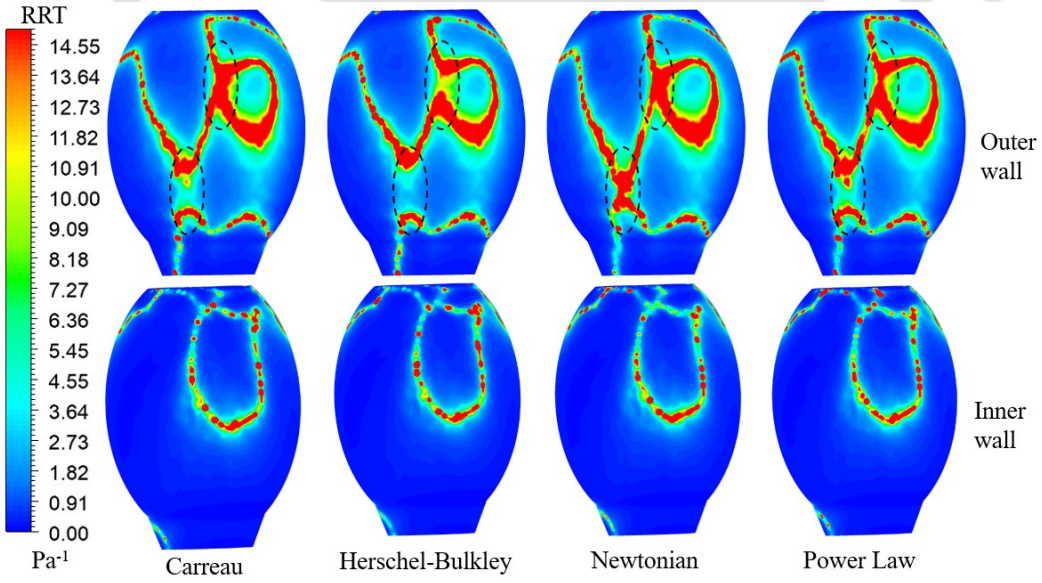

Figure 4.22 RRT contours on the sinus inner and outer wall at sinus size (w) = 3 for various rheological models (area of interests are shown by black dotted lines).

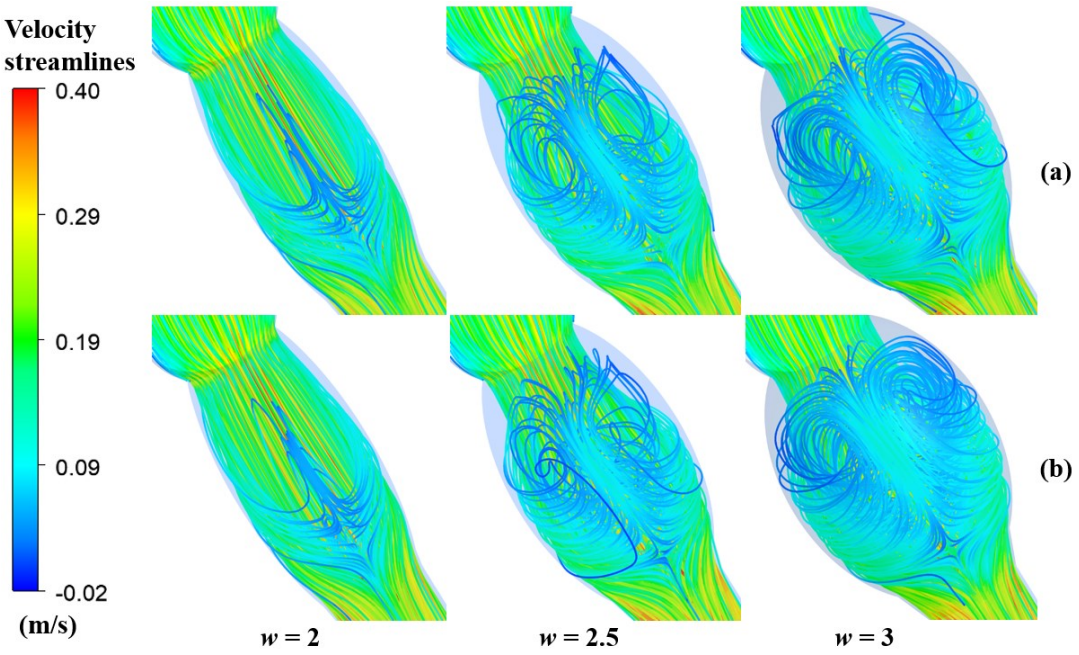

Figure 4.23 Time-averaged three-dimensional streamlines for (a) non - Newtonian (Carreau) (b) Newtonian models at sinus size (w) =2.0, 2.5, 3.0.

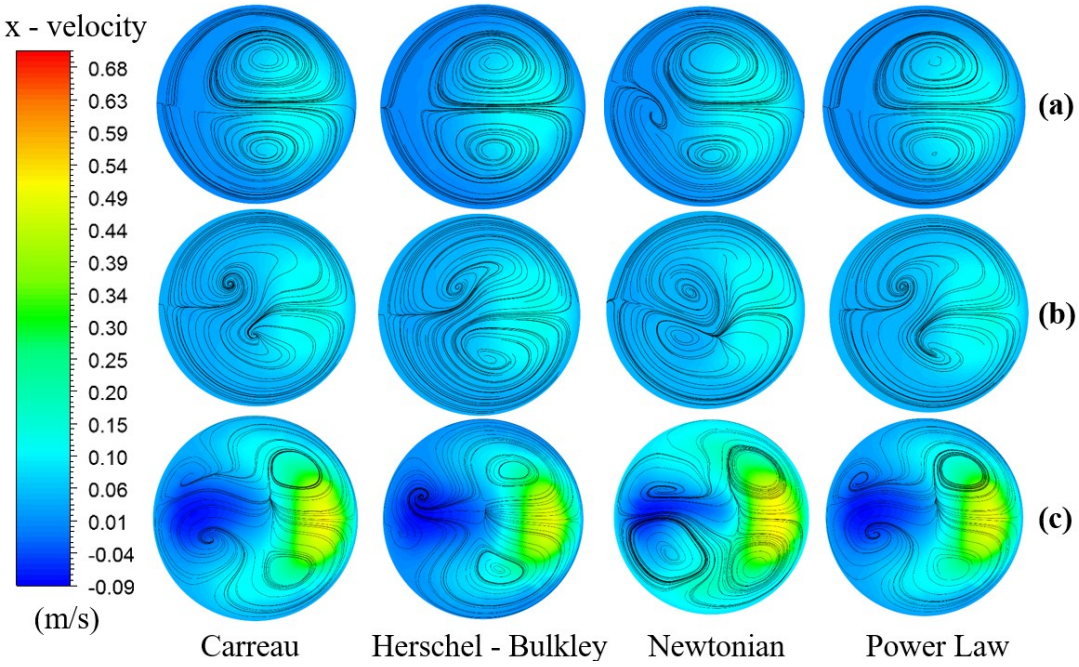

Figure 4.24 Secondary flow streamlines superimposed on x - velocity contours for various rheological models in varying sinus size during the beginning of diastole (t_2) at middle of sinus (w) (a) w = 2.0, (b) w = 2.5, (c) w = 3.0.

The influence of sinus size and non-newtonian behavior on hemodynamics and the secondary flow patterns superposed on contours of x - velocity is analyzed. The x - velocity contours and secondary flow streamlines in the sinus middle planes are shown in Fig. 4.24 for different sinus sizes at the end of the diastole. At peak systole, there is no difference in secondary flow for various non-Newtonian models and the Newtonian model, so they are not shown here. The x - velocity contours shown that the profile is skewed towards the inner wall in the middle of the sinus at the end of the diastole. Secondary motion is observed as the fluid enters into the curved daughter vessels, which is the result of interplay between centrifugal and pressure gradient forces (Dean, 1927). At the end of diastole, there exists an additional vortex in the case of the Newtonian model, and is not seen in non-Newtonian models. For larger sinus size (w = 3.0), the secondary flow is prominent for the Newtonian case as compared to non-Newtonian models. At the end of diastole, the secondary flow is stronger for the Newtonian case as compared to non-Newtonian. The size of the secondary vortex is significant in the Newtonian case, which is smaller for non-Newtonian models. The number of vortices is more in the case of the Newtonian model, in the middle of the larger sinus.

Fig. 4.25 shows the time-averaged secondary velocity over one cardiac cycle for the Newtonian and Carreu model at various cross-sections on the internal carotid artery. The calculation of secondary velocity has been discussed in the previous chapter. The comparison shows the secondary velocity to be similar for the Newtonian and Carreau fluid models for both cases. An increase in sinus size shows larger secondary vortices in the middle of the sinus. The secondary flow is much higher at the end of the larger sinus as compared to that in the smaller sinus. The strength of secondary flow decreases as the flow travels to the outlet of internal carotid artery bifurcation.

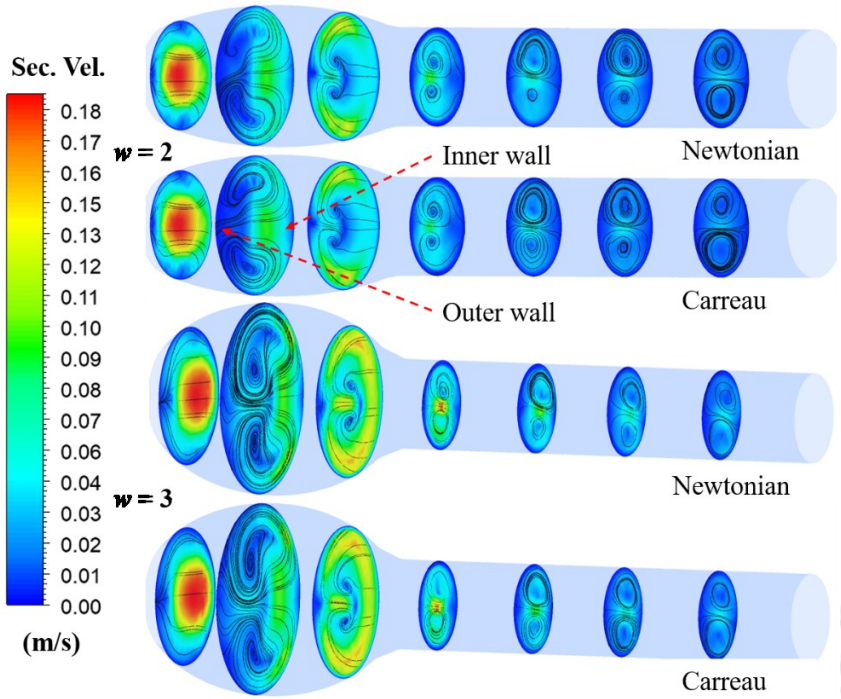

Figure 4.25 Contours and streamlines of time-averaged secondary velocity over one cardiac cycle for Newtonian and non-Newtonian blood flow on the cross-sectional planes in the internal carotid artery (ICA) for varying sinus size (*w*).

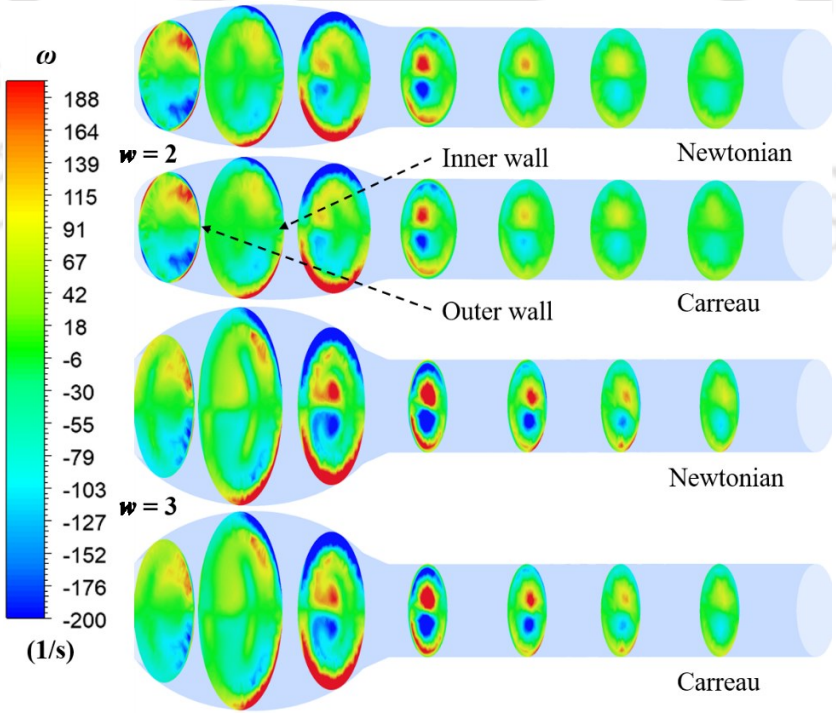

Figure 4.26 Comparison of time-averaged streamwise vorticity (ω) over one cardiac cycle for Newtonian and non-Newtonian blood flow on the various cross-sectional planes in the ICA.

Fig. 4.26 shows the time-averaged streamwise vorticity (ω) over one cardiac cycle for Newtonian and non-Newtonian fluids (Carreu) at various cross-sections in the internal carotid artery. The streamwise vorticity contours show the minor difference for Newtonian and non-Newtonian fluid. Two vortices symmetric about the bifurcation plane are observed on each cross-sectional plane. The magnitude is the same in the two vortices, but the sign is the opposite due to counter-rotation. The magnitude of vorticity is higher in the near-wall region and decreases away from the wall. The region occupied by higher vorticity increases with an increase in the sinus size. The significant vorticity is present in the larger sinus for a longer distance downstream, which is absent in the smaller sinus.

Fig. 4.27(a) shows the representation of the carotid artery model on an XY plane. The length of the carotid model starts at CCA (X = 0) and ends at the exit of ICA and ECA (X = 0.08 m). The TAWSS is shown in Fig 4.27(b) along the outer and inner walls of the carotid model. The TAWSS is constant in CCA, and a sudden decrease in value is observed at the bifurcation and sinus exit. The TAWSS along the outer wall is lower than that at the inner wall. A minimum WSS is observed in the entire sinus region (X = 0.04 – 0.05), especially at the outer sinus wall.

Figures 4.28 and 4.29 show the value of WSS_x along the length (L) of the mid-plane of inner and outer walls of sinuses, during peak systole and end of diastole, for different sinus sizes. As the mean velocity reaches a maximum and the viscous boundary layer becomes much thinner at peak systole, the magnitudes of WSS_x profiles are much higher at peak systole when compared with that at the end of diastole. The shear stress is negative on the outer wall near the sinus entrance for all the cases, whereas it is always positive on the inner wall. Two peaks are observed in WSS_x along the length of the sinus wall. The first peak occurs at the bifurcation point, where L/d is 0, and the second peak is observed at the end of the sinus, which is present between L/d 3 and 4. WSS_x decreases rapidly downstream from the entrance of the bifurcation. This decrease is sharper on the outer wall. The WSS_x value decreases to its minimum in the sinus. The second peak appears due to a sudden change in the cross-section of the channel leading to a higher velocity gradient. The WSS_x value at the second peak increases with the sinus size. The largest sinus size shows the highest value of WSS_x at the end of the sinus caused due to the increase in contraction ratio.

There exists a significant difference in WSS_x of the non-Newtonian and Newtonian models due to the shear-thinning effect, especially during diastole when the velocity and shear stresses are lower.

The Newtonian model shows a lower value of WSS_x throughout the sinus as compared with that for non-Newtonian models. In the non-Newtonian models, the Herschel–Bulkley model gives higher values of WSS_x. With the increase in sinus size, the length occupied by recirculation is increased, which is shown by negative WSS_x values.

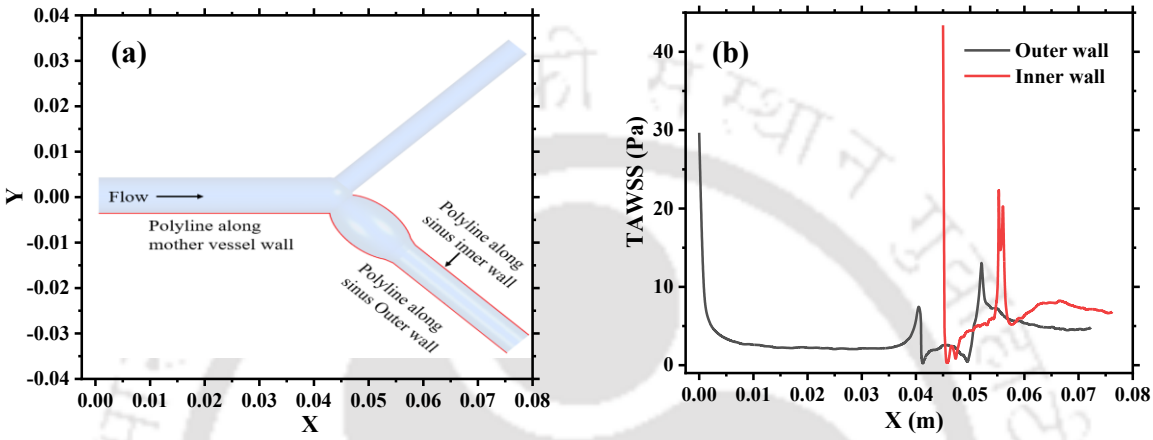

Figure 4.27 (a) Representation of carotid model in XY scale (b) Time-averaged wall shear stress (TAWSS) profile along polylines of mother vessel and daughter vessel (ICA) models at sinus size $w = 2.5$ for the Newtonian model.

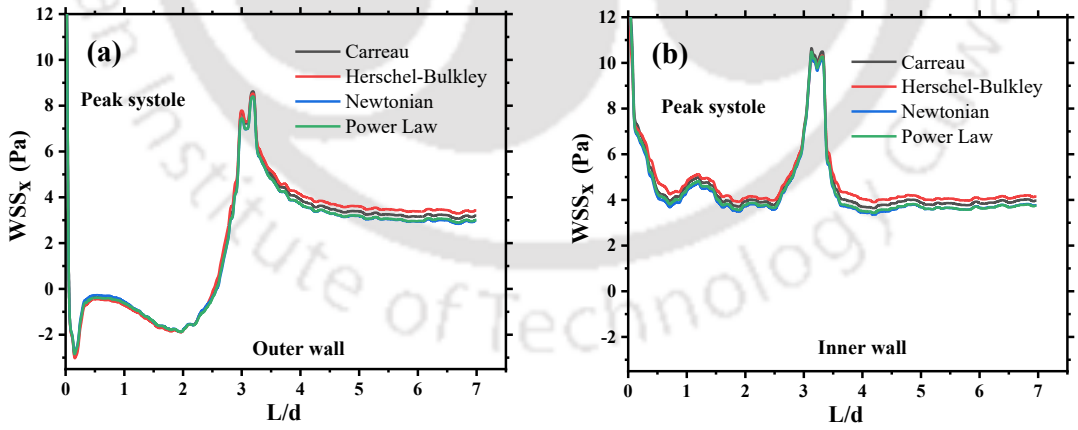

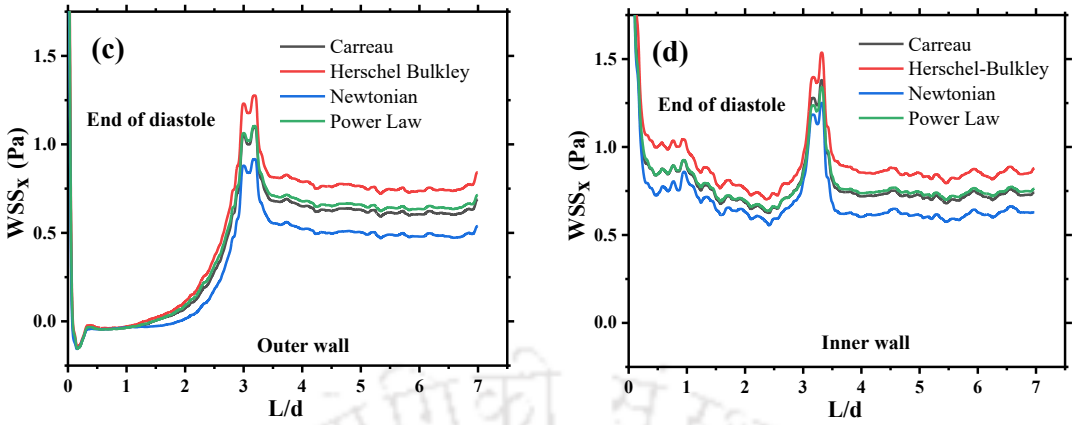

Figure 4.28 Wall shear stress (WSS) profile along walls of ICA for different rheological models at sinus size w = 2.0. (a), (b) Peak systole; (c), (d) End of diastole. Left Fig. (a, c): outer walls, right Fig. (b, d): Inner walls

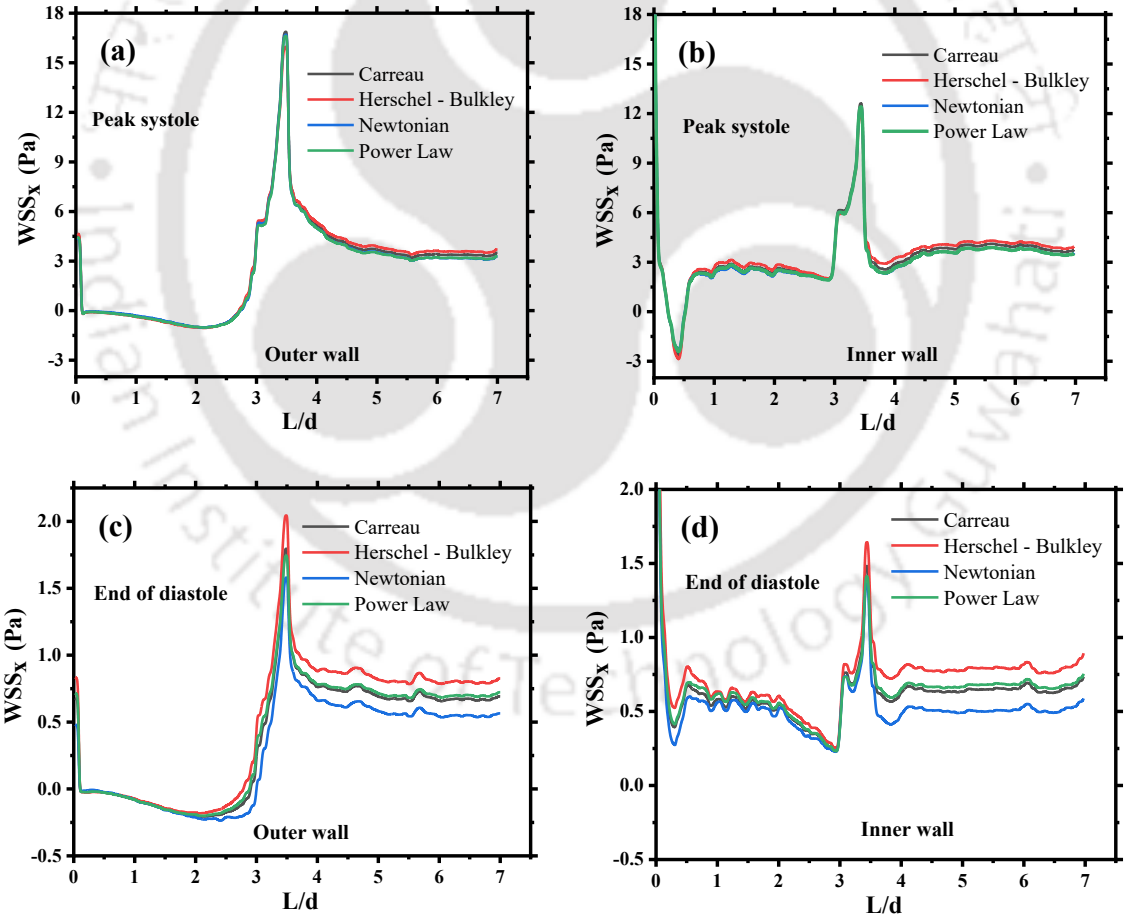

Figure 4.29 Wall shear stress (WSS) profile along walls of ICA for different rheological models at sinus size w = 3.0. (a), (b) Peak systole; (c), (d) End of diastole. Left Fig. (a, c): outer walls, right Fig. (b, d): Inner walls

4.4 Conclusions

The pulsatile flow of blood in an idealized carotid artery bifurcation assuming the blood to be a Newtonian fluid as well as three non-Newtonian models is studied. The emphasis is given to flow in a carotid sinus by varying the sinus size and position.

- A larger sinus size and its position further away from the bifurcation creates a more backflow, low WSS and is more vulnerable to atherosclerosis initiation and progression.
- Four different rheological models - Newtonian, Carreau, Herschel-Bulkley, and power law are used to model the rheology of blood, and results shows a variation in flow parameters in the sinus region.
- The effect of sinus size on the flow behavior and in particular on the wall shear stress is investigated. A comparison of time-averaged wall shear stress, oscillatory shear index, and relative residence time is made for the three sinus sizes for all the rheological models studied. The hemodynamic parameters show a possibility of atherosclerosis initiation on larger sinus size.
- The flow behavior obtained during the systole period is the same using all the rheological models. However, the difference in flow behavior is observed during the diastole period.
- The difference is more prominent in the sinus region where the flow expands, and shear stress and rate of strain have low values. An increase in sinus size results in flow expansion and larger regions having backflow and low wall shear stress.
- The strength of secondary flow and streamwise vorticity increases with an increase in sinus size. The larger sinus shows a presence of streamwise vorticity for a longer distance along the internal carotid artery.

Chapter 5 The Effect of Pulse Rate on Hemodynamics in a Carotid Artery Bifurcation

In this chapter, flow behavior in a carotid artery geometry obtained from the literature and the effect of pulse rate variation on the flow behavior is investigated.

5.1 Introduction

In Chapters 3 and 4, flow behavior in the idealized models of arterial bifurcations has been studied. The mother and daughter vessels are considered to be straight. However, the mother and daughter vessels are generally not straight, and their diameters are not uniform throughout actual arterial bifurcations. Further, the bifurcation geometries and the flow conditions vary from patient to patient. In fact, the pulse rate varies for the same person during different activities, for example, between rest and exercise conditions. Therefore, in recent years, the focus has been to model flow in patient-based arterial bifurcations (Bijari et al., 2014; Bit et al., 2017; Malvè et al., 2012; Morbiducci et al., 2016). The patient-specific geometries of the carotid artery model can be reconstructed from the data obtained from different imaging techniques such as magnetic resonance imaging (MRI), magnetic resonance angiography (MRA), and computed tomography angiography (CT). On the other hand, ultrasound Doppler and phase-contrast MR (PC-MR) imaging are used to get the velocity profile measurements.

The medical image-based carotid artery models have been used for hemodynamic analysis in carotid artery bifurcation, and a methodology was proposed for geometry construction from medical image data (Antiga et al., 2008; Steinman, 2002). In few recent studies (Gharahi et al., 2016; Mendieta et al., 2020), Newtonian and non-Newtonian flow in healthy and diseased carotid artery bifurcation is investigated using patient-based inlet and outlet boundary conditions. The comparison of Newtonian and non-Newtonian fluid in diseased carotid artery models proposed the necessity of considering non-Newtonian behavior in stenosed arteries.

As mentioned earlier, the pulse rate can vary in the same person depending on the state of activity. This raises the question regarding the use of various pulse rate and their effect on the flow behavior in the carotid artery bifurcation. One cardiac cycle consists of systole and diastole, and systole contributes 30-40% of the time period in a cardiac cycle. However, with an increase in the

heartbeat, the systole percent in the cardiac cycle increases (Hall and Guyton, 2011). The peak blood velocity in the common carotid artery is increased by 73.1% during exercise and is recovered to the resting level within three minutes. In comparison, heart rate remains high even after five minutes of exercise (He et al., 1995). During these 3 minutes of the gap, the heart rate is high, but the blood velocity is close to the rest case. Some recent studies used the variation in the inlet waveform for ideal geometries (Huang et al., 2021; Song et al., 2021). Few studies (Xiang et al., 2014; Younis et al., 2003) investigated the combined effect of pulse amplitude and frequency on flow behavior. In order to understand the effect of pulse frequency on the flow behavior, carotid artery bifurcation for three different pulse rates while keeping the pulse amplitude constant has been explored.

In this chapter, flow behavior in a patient-specific carotid artery model is analyzed computationally with an aim to understand the effect of pulse rate on wall shear stress, OSI, RRT, and other relevant flow parameters.

5.2 Methods and materials

5.2.1 Geometry

Figure 5.1 shows the realistic carotid bifurcation model used in the present simulations (Grabcad, 2019; Moradicheghamahi et al., 2019b). The carotid artery consists of the common carotid artery (CCA) that bifurcates into the external carotid artery (ECA) and internal carotid artery (ICA) bifurcation, which supplies blood to the face and brain, respectively. The diameter of CCA inlet, ICA, and ECA outlets are 6.27, 4.32, and 3.02 mm, respectively. The sinus appears at ICA, which is more vulnerable to atherosclerosis formation.

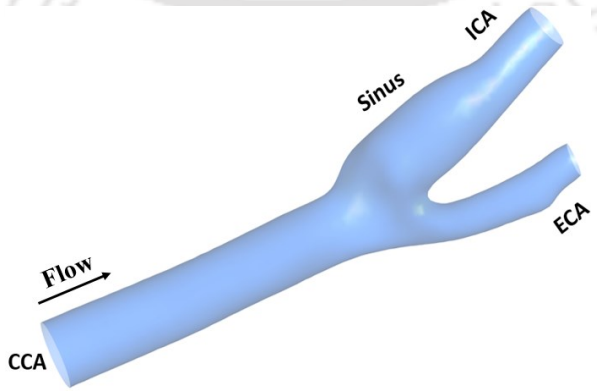

Figure 5.1 Patient-specific carotid artery model used in the present study.

5.2.2 Governing equations

Pulsatile, incompressible, laminar flow of blood in three-dimensional patient-specific carotid artery bifurcation is considered. The channel walls are assumed to be smooth and rigid. The mass and momentum conservation equations are solved as given in Chapters 3 and 4. The non-Newtonian behavior is modeled using the Carreau model given in Chapters 3 and 4.

5.2.3 Boundary conditions

Time-varying velocity is specified at the inlet boundary, as shown in Fig. 5.2. The frequency or time period of the cardiac cycle changes according to human activities, age, and cardiovascular health. In each cycle, the left ventricle pumps blood to the circulatory system during systole and is filled with blood during the period of diastole. During the systolic period, the flow rate increases and then decreases while the flow is relatively steady during the period of diastole. The flow is therefore assumed to be sinusoidal waves during the period of systole and steady during the period of diastole. In normal conditions, it is around a frequency of 1.2, and it increases to ≥ 2 during an intense workout. Three different waveforms have been considered by changing the frequency of the cardiac cycle without changing the amplitude (Gijsen et al., 1999; Sinnott et al., 2006; Sousa et al., 2014), as shown in Fig. 5.2. At the outlet boundary, the gauge pressure of 0 Pa is specified, assuming the pressure downstream of the two arteries to be the same. A no-slip boundary condition is specified at the wall.

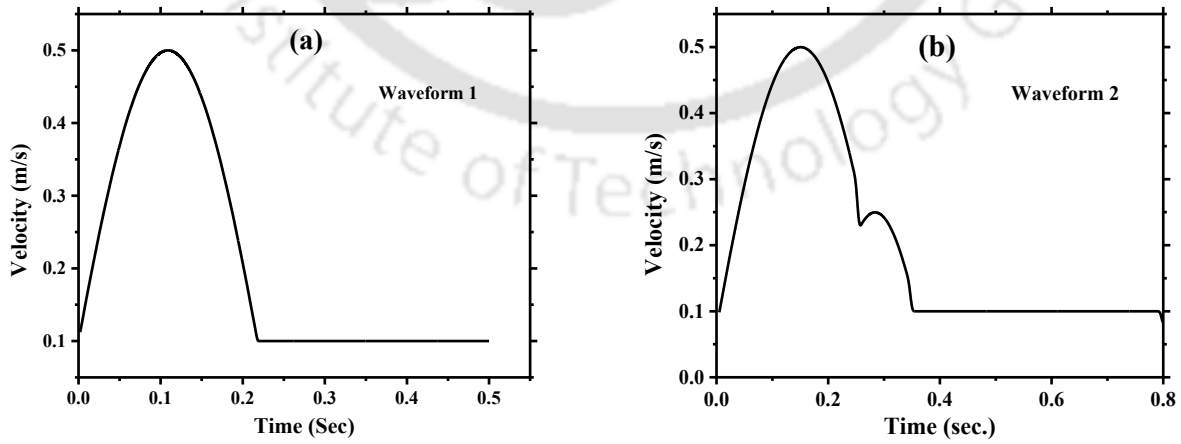

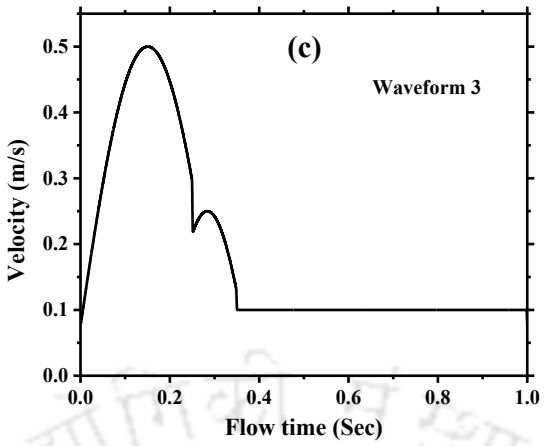

Figure 5.2 Three different waveforms as an inlet boundary condition at CCA for patient-specific carotid artery bifurcation CFD simulations (a) waveform 1 (Sinott et al. 2006) (b) waveform 2 (Sousa et al., 2014) (c) waveform 3 (Gijsen et al. 1999).

5.2.4 Mesh independence study

The grid independence study has been performed using four different mesh densities containing 0.2, 0.3, 0.45, and 0.6 million elements. The value of pressure and wall shear stress is compared at a point (red dot) in the middle of the sinus using various mesh densities, as shown in Fig. 5.3.

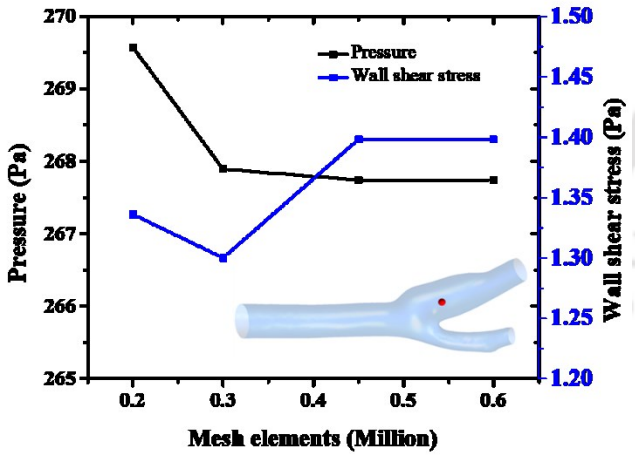

Figure 5.3 Mesh independence study showing the variation of pressure and WSS with varying mesh density.

The difference between the pressure and WSS for the two finest meshes (0.45 and 0.6 million elements) is less than 0.5%. Hence, the mesh consisting of 0.45 million computational elements is used for subsequent simulations. The minimum and maximum sizes of mesh elements are 0.27

and 0.5 mm, respectively. At the bifurcation and in the sinus, the refined mesh is used to capture the complex flow patterns. All the simulations are performed on a computer with an i5-6500 processor and 16 GB RAM, using four processors in parallel. The time is taken to achieve a converged solution for five cardiac cycles of period 2.5 s, and a time step size of Δt = 0.001 s is about 20 hours.

5.3 Results and discussion

Fig. 5.4 shows the three-dimensional time-averaged velocity streamlines and axial velocity contours (over five cardiac cycles) for various inlet waveforms in the patient-specific carotid artery bifurcation. The time period of a single cardiac cycle for each waveform is 0.5, 0.8, and 1 s for waveforms 1, 2, and 3, respectively. As the heartbeats increase, the frequency of pulsatile flow increases. With the increase in the frequency of the cardiac cycle, the size of flow separation in the sinus region reduces. The lowest frequency inlet waveform shows the larger region of flow separation and backflow shown by streamlines in Fig. 5.4(I). The outer region of the sinus shows a backflow and flow separation. The time-averaged axial velocity profiles at various cross-sections clearly show the size of the recirculation region, as shown in Fig. 5.4(II). The size of the backflow region is larger in lower frequency cases as compared to that in higher frequency. The maximum velocity at the bifurcation also reduces by reducing the pulse rate. Lower velocities during decreased pulse rate may be caused due to lower frequency of driving pressure. The flow separation and backflow leads to low WSS, which is the marker of atherosclerosis formation.

Fig. 5.5 shows the TAWSS distribution on the wall for the three inlet waveforms. While similar distributions of TAWSS are observed for the three waveforms, there are some minor differences in the magnitude of TAWSS in specific regions. The difference is noticeable near the bifurcation, both the external and carotid arteries. The high frequency (waveform 1) of blood flow shows a smaller region of low TAWSS and higher values in comparison with that in low frequency (waveform 2, 3) blood flow. With the increase in frequency, the TAWSS values increases, and the region occupied by lower TAWSS decreases. Therefore, a higher frequency of blood flow, which occurs during exercise conditions, can be considered as an atherosclerosis protective measure. On the other hand, during the lower frequency blood flow observed a larger region of low TAWSS. According to past studies, lower values are linked with the possibility of atherosclerosis formation (Caro et al., 1971a; Malek et al., 1999).

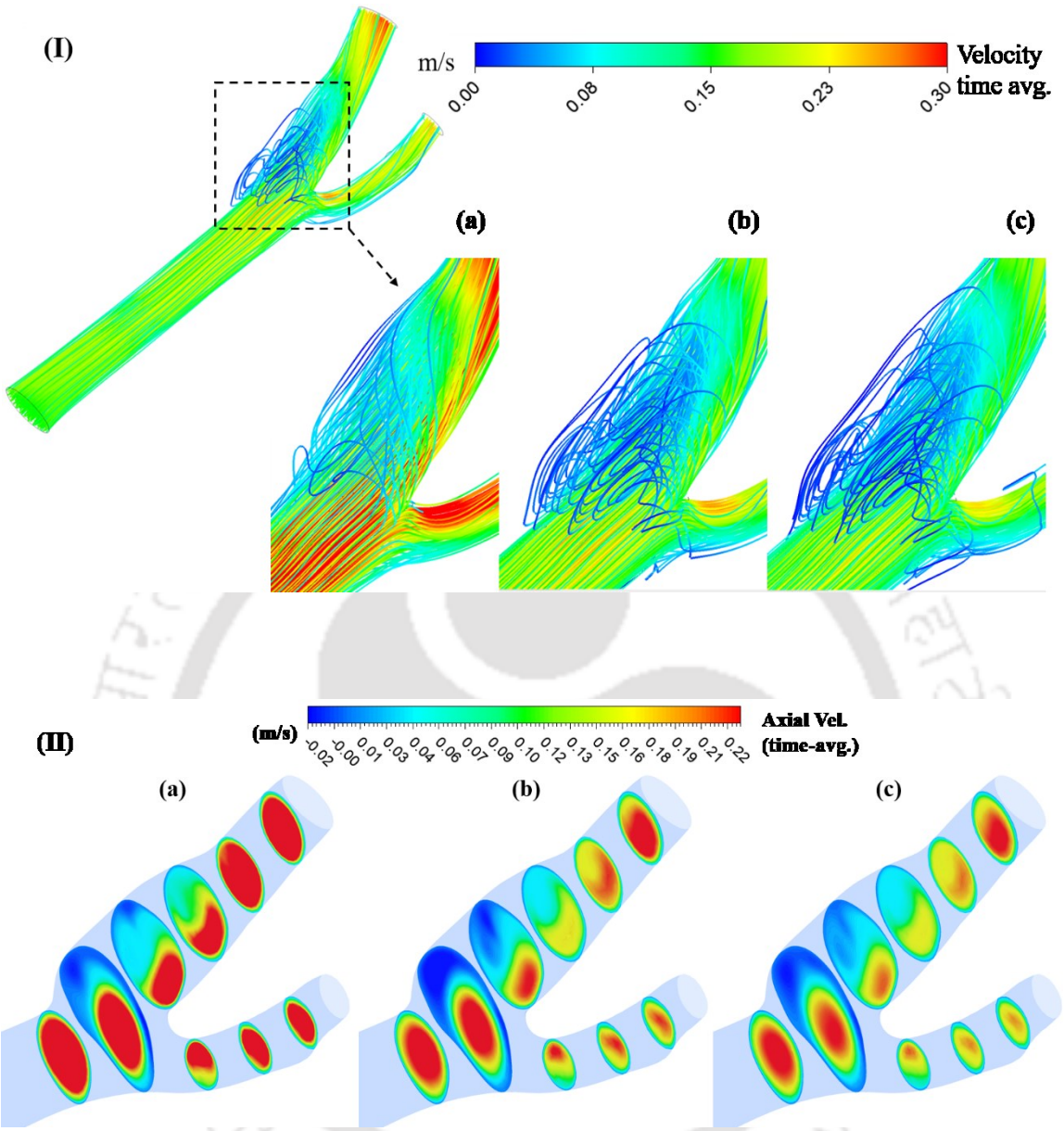

Figure 5.4 Time-averaged (I) velocity streamlines and (II) axial velocity contours at various inlet waveforms showing possible regions of recirculation in the patient-specific carotid artery sinus (a) waveform 1 (b) waveform 2 (c) waveform 3.

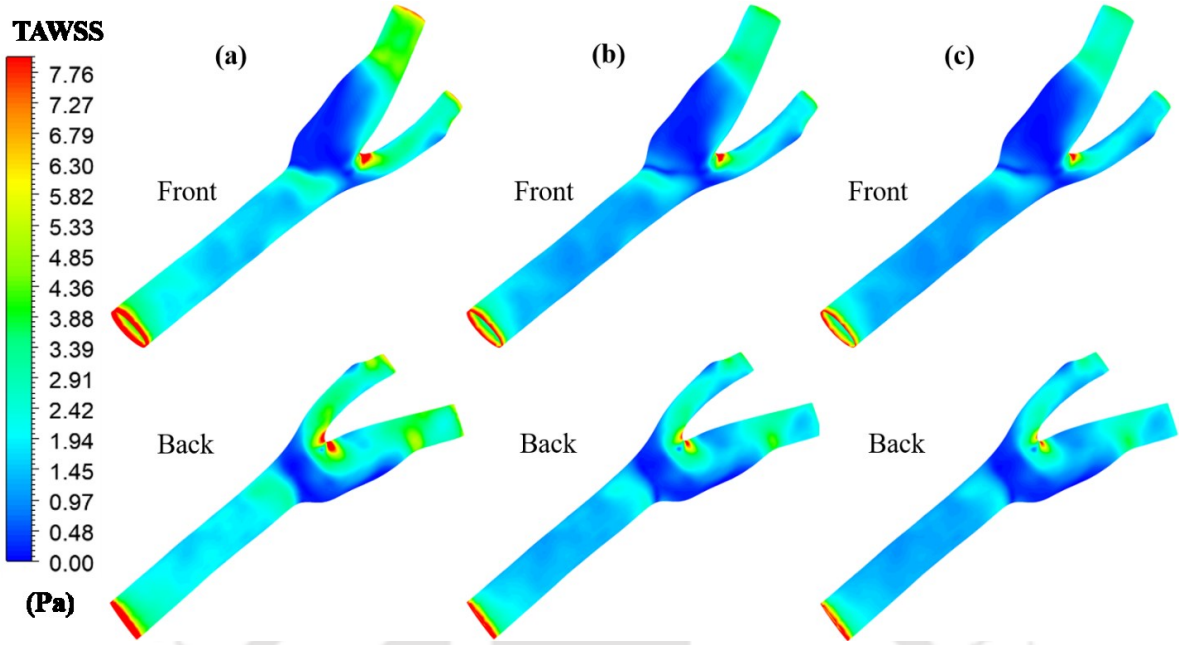

Figure 5.5 TAWSS at various inlet waveforms showing possible regions of atherosclerosis in the patient-specific carotid artery sinus (a) waveform 1 (b) waveform 2 (c) waveform 3.

Fig. 5.6 shows the OSI distribution on the carotid artery bifurcation walls for the three inlet waveforms. If the sign of WSS is not changing throughout the cardiac cycle, the value of WSS is zero. However, a change in sign of WSS during the cardiac cycle shows a non-zero value. The OSI value is maximum (0.5) when the WSS is changing direction by 180° in a cardiac cycle. For the three different inlet waveforms, similar distributions of OSI contours are observed with some minor differences. The OSI is very high in the sinus for all three waveforms. The difference is noticeable at the bifurcation and in the sinus region. The high frequency (waveform 1) of blood flow shows a smaller region having a high OSI value (denoted by red color) in the sinus region in comparison with that in low-frequency cases (waveform 2, 3). With an increase in frequency, the OSI values, and region occupied by high OSI decrease. For the lower frequency cases, larger regions of high OSI values are observed, which can be the probable sites of atherosclerosis formation.

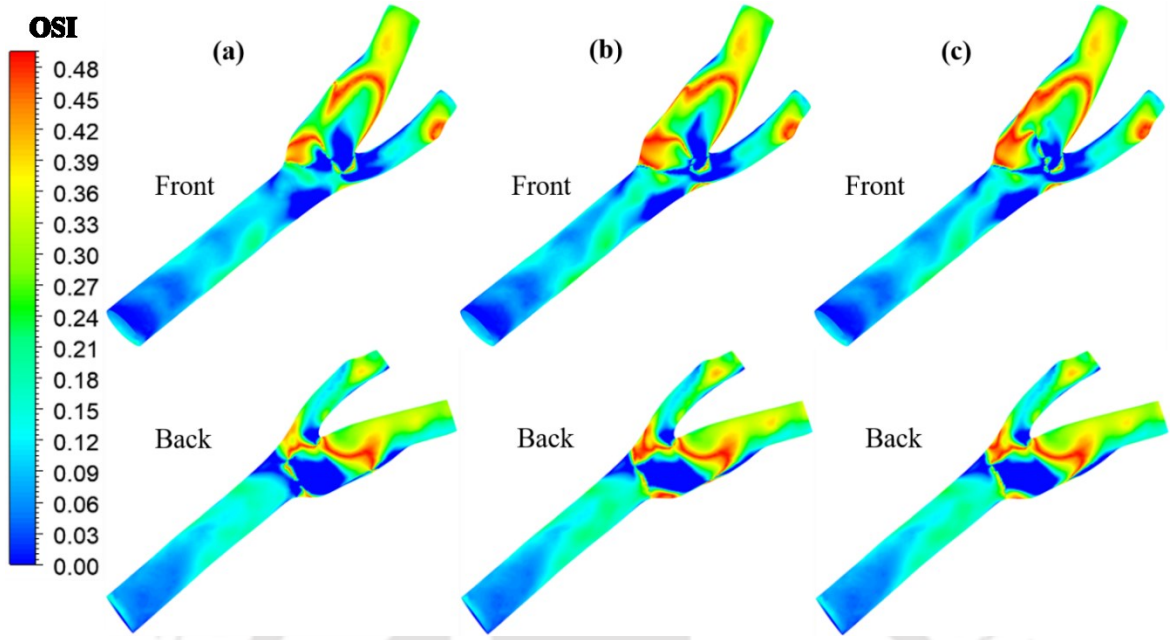

Figure 5.6 Numerical results analyses OSI at various inlet waveforms showing possible regions of atherosclerosis in the patient-specific carotid artery sinus (a) waveform 1 (b) waveform 2 (c) waveform 3.

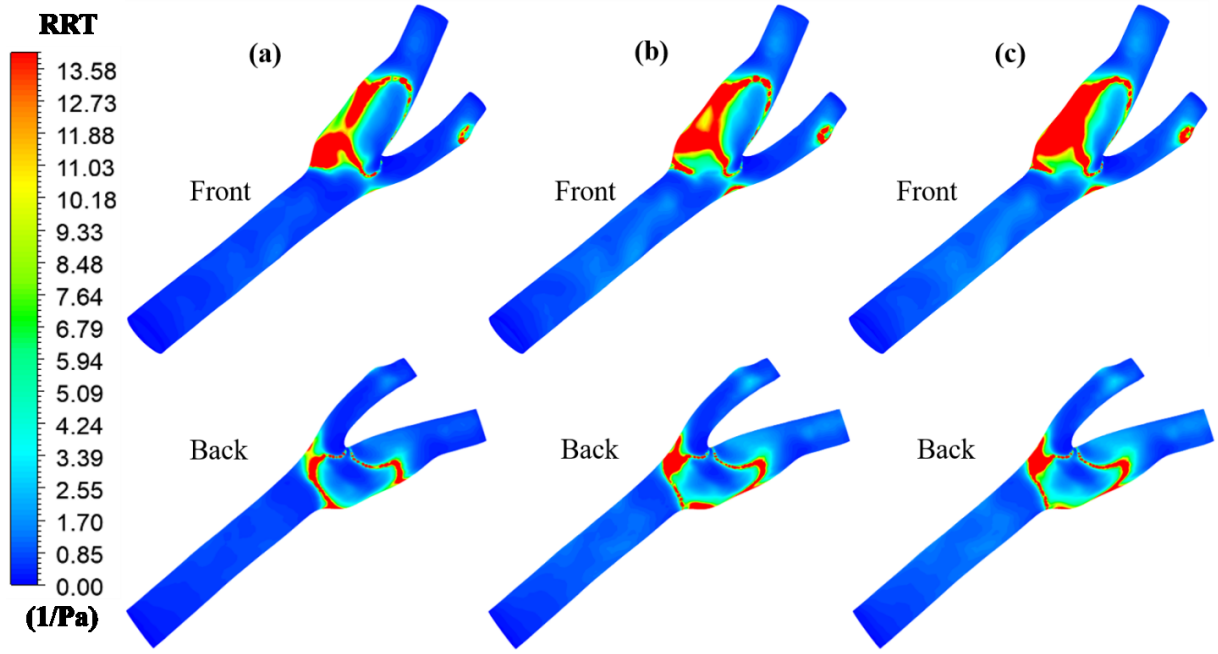

Figure 5.7 Numerical results analyses RRT at various inlet waveforms showing possible regions of atherosclerosis in the patient-specific carotid artery sinus (a) waveform 1 (b) waveform 2 (c) waveform 3.

The OSI can identify the probable regions of backflow, but it does not provide any information about the magnitude of WSS, which is an important parameter for atherosclerosis formation. The relative residence time is inversely proportional to TAWSS, and it is the robust indicator of atherosclerosis initiation and progression (Himburg et al., 2004). The RRT provides information about fluid particle adherence to the arterial wall, and higher RRT values mean higher adherence of fluid to arterial walls. Literature studies have shown that high OSI and RRT regions are observed in the carotid sinus, and it is the probable region of atherosclerosis formation (Gharahi et al., 2016; Ku et al., 1985; Mendieta et al., 2020). The knowledge of RRT distribution in the carotid artery bifurcation for varying pulse needs to be understood.

Figure 5.7 shows the distribution of RRT contours in a carotid artery bifurcation. The higher RRT regions are observed at an outer wall of bifurcation and sinus for all three inlet waveforms. The increase in the pulse rate shows a decrease in the size of the higher RRT region, as shown in Fig. 5.7(a). In contrast, the lower pulse rate shows an increase in the size of the higher RRT region (Fig. 5.7c). The higher pulse rate can be considered as a protective measure from the deposition of fatty material on the arterial walls and the stenosis formation.

Table 5.1 Quantitative comparison for various inlet waveforms using hemodynamic parameters.

Parameter	Waveform	Minimum	Maximum	Average
TAWSS	1	0.0121	25.96	2.617
	2	0.0173	18.67	1.970
	3	0.0066	16.72	1.724
OSI	1	0	00.49	0.161
	2	0	00.49	0.181
	3	0	00.49	0.198
RRT	1	0.0728	5795	3.942
	2	0.0568	17709	7.148
	3	0.0646	43362	12.128

Table 5.1 shows the quantitative comparison of hemodynamic parameters such as TAWSS, OSI, and RRT values for various inlet waveforms. It confirms the qualitative results shown earlier. The

value of TAWSS decreases with increasing pulse rate, and OSI, RRT value increases with lowering pulse rates. Higher pulse rates can be considered as a protective measure from stenosis.

At the carotid bifurcation, the flow is divided into the external and internal carotid arteries. As the flow streamlines turn at the bifurcation, the fluid particles experience a centrifugal force forcing them towards the inner wall of bifurcation in each daughter vessel. At the same time, a pressure gradient is generated across the inner wall and outer wall due to the difference in curvature, leading to the generation of secondary flow (Dean, 1927; Evegren et al., 2010; Pradhan and Guha, 2019). The secondary flow is present at the cross-sectional plane in the internal and external carotid arteries. As seen in Chapter 4, it is more significant in the sinus region in the internal carotid artery. To understand the evolution of secondary flow with location, the contours and vectors of secondary flow at various cross-sectional planes in the daughter branches are shown in Fig. 5.8.

The secondary flow is observed to have a significant value at the bifurcation, which decreases as the flow travels towards outlets. At the cross-sectional plane I, which is located at the bifurcation, the secondary velocity is observed to be more near the bottom wall from where the flow is directed towards the outer walls of ICA and ECA. The flow towards the ICA is relatively higher. Interestingly, the secondary velocity is significantly high in the near-wall regions. On entering the ICA, the secondary flow velocity is higher near the bottom wall, as seen on plane II. On moving further downstream, the gradient in the secondary velocity is observed to decrease, and the secondary flow becomes more uniform. The high-velocity region is shifted towards the outer wall. On moving downstream, the magnitude of secondary velocity reduces.

The three-dimensional flow can further be characterized using vorticity and helicity. Figure 5.9 shows the contours of streamwise vorticity and helicity on different cross-sectional planes in the daughter vessel. The streamwise vorticity in the daughter vessel is the component of vorticity parallel to the axis of the daughter vessel and characterizes the secondary vortices in the cross-sectional plane. The magnitudes of vorticity and helicity are the same in the two vortices, but the signs are different as the vortices are counter-rotating. The magnitude of vorticity is high in the boundary layer region near the wall and decreases away from it, as can be seen by red or blue colors on the wall. The magnitude of vorticity and helicity is high near the inner wall. The magnitude of vorticity increases just after the sinus region due to a reduction in cross-section and an increase in velocity.

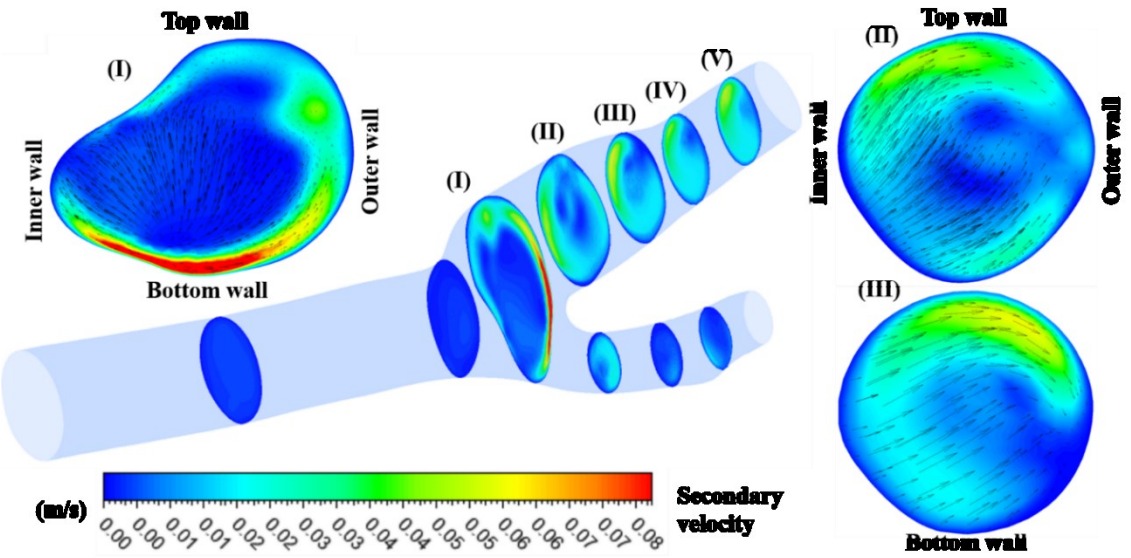

Figure 5.8 Time-averaged secondary flow superposed on secondary contours for waveform 1 in the patient-specific carotid artery bifurcation.

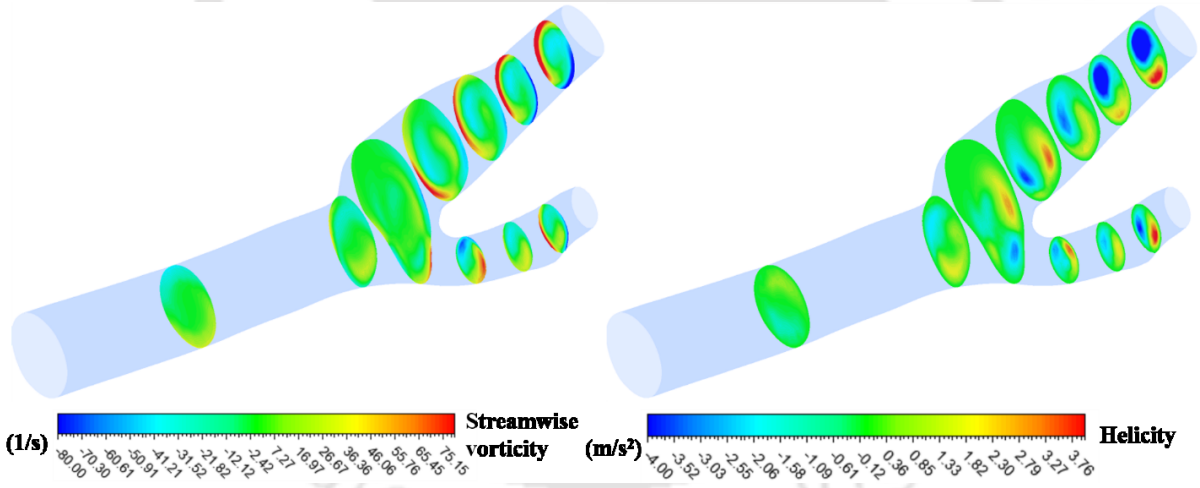

Figure 5.9 Contours of streamwise vorticity and helicity for waveform 1 in the patient-specific carotid artery bifurcation.

5.4 Conclusions

The pulsatile flow of blood in a patient-specific carotid artery bifurcation for non-Newtonian (Carreau model) fluid is studied. The effect of pulse rate variation on hemodynamics has been analyzed using hemodynamic parameters such as TAWSS, OSI, and RRT.

- The flow in a carotid sinus is very complex and near the outer wall of the sinus shows a backflow which leads to a decrease in WSS value.
- Inlet velocity waveform frequency has noticeable effects on TAWSS, OSI, RRT distribution at constant amplitude. The patterns are similar, but the region occupied by these parameters is distinguishable.
- Higher pulsatile frequency shows higher values of TAWSS and lower values of OSI and RRT.
- Lower pulsatile frequency waveform can be correlated with contributing factors for atherosclerosis initiation and progression.
- The higher secondary flow is observed at the bifurcation. Similarly, higher values of vorticity and helicity are observed just after the carotid sinus.

Chapter 6 Computational Investigations on Bubble Dynamics in Bifurcating Channels

In this Chapter, two-phase gas-liquid flow is modeled in planar, two-dimensional channels. The effect of bifurcation angle, capillary, and Reynolds number on bubble break up, flow behavior, and stresses on the wall is investigated.

6.1 Introduction

The flow of bubbles and droplets in confined geometries is a common phenomenon that occurs in a wide range of applications such as microfluidics (Anna, 2016; Link et al., 2004; Squires and Quake, 2005; Whitesides, 2006), medicine (Bull, 2005; Feng et al., 2018; Li et al., 2021) and food and cosmetics (Arzhavitina and Steckel, 2010; Eisner et al., 2005) amongst others. The flow of bubbles in microvessel

s may involve bubble formation (Du et al., 2016; Gupta et al., 2009), rupture (Sun et al., 2018; Wang et al., 2017), and coalescence (Khadiya et al., 2021; Liu et al., 2016). Various geometrical configurations have been employed to generate and split the bubbles, for example, T-shaped bifurcations (Fu et al., 2011; Garstecki et al., 2006; Link et al., 2004; Sun et al., 2018), Y-shaped bifurcations (Baroud et al., 2006; Manga, 1996; Wang et al., 2018), and combinations of both the configurations. The bubble splitting in the Y-shaped channel has an important role in a number of applications. In microfluidics, it is used to control the bubble size and occurrence of different splitting regimes during bubble propagation in a bifurcation. In medicine, understanding the transport of gas emboli in arterial bifurcations is necessary to avoid catastrophic bioeffects (Li et al., 2021). In gas embolotherapy, a potential cancer treatment, understanding the bubble splitting at a bifurcation plays a crucial role in effective treatment (Bull, 2005; Qamar et al., 2017). During surfactant therapy for acute respiratory distress syndrome (ARDS), understanding the splitting of the bubble at a bifurcation is important to devise better treatment strategies (Grotberg, 1994; Romanò et al., 2019; Zheng et al., 2006).

The bubble can be used as a drug carrier in a complex arterial network. Air embolism occurs due to intravascular bubbles that occlude the blood supply, which causes starvation of body organs. A recent study analyzed the lodging of bubbles in-vivo and in-vitro and found that lodging takes

place due to clot formation at the tail of the bubble, which reduces the lubrication film surrounding the bubble. Reduction in the lubricating film increases the friction and leads to bubble lodging (Li et al., 2021). In contrast, the gas bubbles can be used as a treatment strategy called gas embolotherapy to starve cancerous tumors. The understanding of bubble splitting dynamics at a bifurcation is necessary for effective treatment using gas embolotherapy. The bubble splitting behavior depends on gravity, surface tension, and inertia (Chen et al., 2014; Eshpuniyani et al., 2005).

Gas embolotherapy is a potential cancer treatment in which intra-arterial blood supply to cancer tumors is cut off using gas bubbles (Bull, 2007). In this treatment, the perfluorocarbon (PFC) microdroplets (~6 μm in diameter) are passed through the arteries and selectively vaporized at the desired tumor location using high-intensity ultrasound (Kripfgans, O. D., Fowlkes, J. B., Miller, D. L., Eldevik, O. P., & Carson, 2000; Kripfgans et al., 2005; Qamar et al., 2010). Due to ultrasound, these droplets get vaporized, and the bubble formation (~150 times volume expansion) takes place to occlude the blood flow covering the entire cross-section of the blood vessels (Kang, S. T., Huang, Y. L., & Yeh, 2014; Kang et al., 2014; Kripfgans et al., 2004). For effective treatment, a large number of these bubbles should pass through tumor affected vessels. The generated bubbles travel into smaller capillaries and eventually occlude the capillaries with a sausage or capsule shaped configuration (Samuel, S., Duprey, A., Fabiilli, M. L., Bull, J. L., & Brian Fowlkes, 2012). The capillaries are more likely to get damaged because of their fragile structure and thin vessel walls. Due to acoustic droplet vaporization (ADV) occurring in the capillaries, the expansion of droplets takes place with a higher wall velocity in the order of hundreds of meters per second (Kripfgans et al., 2004; Qamar et al., 2010; Wong et al., 2011). The bubble dynamics in capillaries leads to undesired bioeffects, such as endothelial damage and rupture of the capillaries (Bull, 2005; Wong and Bull, 2011). The potential embolotherapy has motivated researchers to investigate bubble transport in ideal bifurcation models to predict the bubble lodging and occlusion of the vessel (Calderón et al., 2006, 2005; Eshpuniyani et al., 2005).

In the past decade, a number of researchers have investigated various aspects of the gas embolotherapy process. Recently, it has been shown that tumor growth in mice having hepatocellular carcinoma (liver cancer) can be restricted employing gas embolotherapy techniques (Harmon et al., 2019). The multiphase flow at the bifurcation and control of ADV remains an

active topic of research for experimental (Fabiilli et al., 2009; Lo et al., 2007; Wong et al., 2011) and numerical work (Poornima and Vengadesan, 2012; Qamar et al., 2017; Ye and Bull, 2006, 2004), which analyzes the splitting behavior and lodging of bubbles in the capillaries. For a successful treatment, at least 78% of the blood supply to the tumor needs to be occluded (Di Segni, R., Young, A. T., Qian, Z., & Castaneda-Zuniga, 1997). Various factors such as blood flow rate, gravity, bubble size, and vessel geometry affect the splitting behavior of the bubble at the bifurcation. Different regimes and splitting behavior are observed at bifurcations. Faster flow rates and weaker gravitational effects result in even splitting in daughter vessels, whereas at lower flow rates, the splitting is uneven, depends on roll angle i.e. the angle made by horizontal plane with the mother vessel axis (Eshpuniyani et al., 2005).

In the case of severe COVID19, viral pneumonia may lead to acute respiratory distress syndrome (ARDS), in which the membrane between the alveoli and blood capillary breaks (Chastre and Fagon, 2002; Ruuskanen et al., 2011), leading to the leakage of fluid into the alveolar sac and restricting the expansion of sacs (Ghadiali and Gaver, 2008; Ware, L. B., Matthay, 2000; Wu et al., 2020). This severely compromises the gas exchange between blood capillaries and alveolar sacs, leading to oxygen deficiency in the body and may result in death (D'Angelo et al., 2008; Xu et al., 2020). In such cases, the patient is provided oxygen via mechanical ventilation (AMV), which pushes the air into the lungs (Amato et al., 1998).

During mechanical ventilation, the airways such as bronchioles are often filled with liquid, and the oxygen is not able to push through the airway as a continuous gas stream and breaks into smaller bubbles caused by Rayleigh Plateau instability. The size of these bubbles depends on the airflow rate, the surface tension of the pulmonary fluid, buoyancy effect, and fluid viscosity. Depending upon the bubble volume and size of the airway, the bubble may take a spherical or capsular shape. Studies on the hydrodynamics of long capsular bubbles in straight capillaries suggest that for a capsular bubble, the wall shear stress surrounding a spherical bubble increases along the axis and becomes maximum at the diametric plane and then decreases again (Kumari et al., 2018). For the long capsular bubble, the wall shear stress is observed to be higher near the front and back of the bubble and almost negligible in the middle. Further, as the curvature of the bubble changes along the axis, the pressure in the liquid film surrounding the bubble and on the wall also changes continuously in the axial direction. Thus, the flow of microbubbles through the liquid causes

additional stress and stress gradients on the airway walls (Chen et al., 2014; Munir and Xu, 2020). These stresses on the airway walls may enhance the pre-existing lung injury called ventilator-induced lung injury (VILI) (Bilek et al., 2003; D'Angelo et al., 2008; Dailey and Ghadiali, 2010; Kay et al., 2004; Zamankhan et al., 2018). This injury may include disruption of endothelial cells (innermost cell layer on the wall where exchange occurs) on the airway walls (Vlahakis and Hubmayr, 2005).

The stress caused by the motion of a bubble depends on the flow velocity, surface tension, viscosity, buoyancy effect, bubble diameter, and airway bifurcation diameter (Bilek et al., 2003; Yalcin et al., 2007). These parameters can be grouped in three non-dimensional numbers, namely capillary number $\frac{\mu U}{\sigma}$, Bond number $\frac{\Delta \rho g d^2}{\sigma}$, and Reynolds number $\frac{\rho U d}{\mu}$. The motion of a long capsular bubble in a fluid-filled vessel found that the film thickness surrounding the bubble and pressure drop vary with the capillary number (Ca) as $\sim Ca^{2/3}$ (Bretherton, 1961). Bubble propagation in rigid vessels has been extended to a fluid-filled flexible walled airway vessel for varying Reynolds and capillary numbers (Gaver et al., 1996; Heil, 2000). Later, the wall shear stress has been analyzed for oscillating microbubbles, and it is proposed that the dynamic behavior of normal stresses reduces the VILI (Smith and Gaver, 2008). Bilek et al. (2003) investigated the epithelial cell damage caused by surfactant imbalance during pulmonary airway reopening using a combination of experimental and computational investigations. The CFD simulations suggested that higher shear stress, pressure, shear stress gradient, and pressure gradient be potentially injurious to the epithelial cells. Correlating the simulation results with the experimental data, they suggested that the steep pressure gradients near the bubble front or nose are the most likely cause of cellular damage. A decrease in reopening velocity (velocity needed to open the occluded airways) and bronchiole radius increases the shear stresses on walls and leads to endothelial cell damage (Bilek et al., 2003; Yalcin et al., 2007). The magnitude of pressure gradient during reopening is found to be the major factor for cell damage (Kay et al., 2004).

The effect of inertia, gravity, and surface tension on microbubble splitting and hydrodynamic stresses has been investigated in past studies (Chen et al., 2014; Munir and Xu, 2020; Zheng et al., 2007). The effect of driving pressure and bifurcation angle on bubble splitting in a bifurcation found that the homogeneity of bubble splitting increased with driving pressure and decreased with increased bifurcation angle (Calderon et al., 2010). However, the droplet dynamics at a bifurcation

show a non-splitting behavior below the critical value of capillary number (Carlson et al., 2010). While, the shape of the bubble depends on weber number. Further, it was observed that vortices in the thin-film between the vessel wall and bubble interface are responsible for large shear forces, which cause endothelial cell injury (Qamar et al., 2017).

The addition of surfactant reduces the surface tension and the tendency of plug formation. Therefore, the surfactant can protect the airway endothelial cells near the walls from breakage. It was shown experimentally and theoretically that the addition of surfactant could protect lung airway linings from breakage (Tavana et al., 2011; Zheng et al., 2007). In an infinitely long gas bubble filled with a viscous surfactant solution, the Marangoni stresses are observed due to non-uniform surfactant adsorption across the interface surface (Stebe and Barthès-Biesel, 1995). However, with an increase in the Marangoni effect, the pressure and film thickness increases above the values predicted by Bretherton's correlation (Bretherton, 1961). Another computational study compared the pressure and shear stress gradients with and without surfactant and found that the addition of the surfactant decreases the higher pressure and shear stress gradients (Olgac and Muradoglu, 2013). A recent study observed a reduction in hydrodynamic forces by adding a surfactant, which reduces lung injury (Muradoglu et al., 2019). However, the bubble coalescences induce a high level of stress on the epithelial cells. These stress values are 300-600% higher than the precoalescence values, which are large enough to damage the cells (Romanò et al., 2019). In another study, simulations of the 3D non-Newtonian mucus breakage found that high surface tension increases the wall shear stress (WSS) and delays the rupture process (Hu et al., 2020). The WSS can be reduced by the smaller pressure difference and surface tension.

Most of the previous studies are limited to bubble propagation and splitting within straight (Fujioka et al., 2008; Gaver et al., 1996; Giavedoni and Saita, 1997; Romanò et al., 2019) and symmetric airway bifurcations (Bilek et al., 2003; Carlson et al., 2010; Chen et al., 2014; Deka et al., 2020). Munir and Xu (2020) recently analyzed the effect of asymmetric airway bifurcation on hydrodynamic stresses for the constant bubble size and bifurcation angle (Munir and Xu, 2020) computationally. They found higher hydrodynamics stresses for larger capillary number. The size of the mother vessel was 1 mm, and one daughter vessel was twice the size of the other.

For large ($L/d > 2$) and short bubbles ($L/d < 1.5$), the theoretical and experimental study of splitting dynamics of a gas bubble in a bifurcation has been studied in the past (Calderón et al., 2006;

Eshpuniyani et al., 2005; Valassis et al., 2012). Recently, the effect of symmetric bifurcation angle on bubble splitting has been analyzed and observed four stages of a splitting: the first stage of the squeezing process, the second stage of the squeezing process, fast pinch-off stage, and head forward process (Du et al., 2020; Ziyi et al., 2019). However, to the best of the author's knowledge, the splitting dynamics for asymmetric bifurcation are not well understood.

With the motivation of understanding bubble dynamics during gas embolotherapy and in pulmonary airways, CFD simulations in planar, two-dimensional bifurcations have been performed in two different geometries. The simulations are performed using blood as the liquid and perfluorocarbon (PFC) as the gas phase in geometry 1 and the effect of bifurcation angle on bubble splitting is investigated. In geometry 2, simulations are performed for gas-liquid flow, and the effect of Bond number, Capillary number, and geometric parameters on bubble propagation is analyzed.

6.2 Computational methodology

6.2.1 Governing equations and boundary conditions

The Volume of Fluid (VOF) method in which a single set of mass and momentum conservation equations are solved together with an advection equation for the volume fraction of one of the phases is used to model the two-phase flow (Hirt, C. W., Nichols, 1981). A finite volume-based commercial CFD code, ANSYS Fluent 19.2, is used to solve the governing equations and the appropriate boundary conditions (Fluent, 2019). The governing equations for the VOF formulation are:

Equation of Continuity:

$$\boldsymbol{\nabla}.\boldsymbol{u} = 0 \tag{6.1}$$

Equation of momentum conservation:

$$\rho\left(\frac{\partial \boldsymbol{u}}{\partial t} + (\boldsymbol{u}.\boldsymbol{\nabla})\boldsymbol{u}\right) = -\boldsymbol{\nabla}P + \boldsymbol{\nabla}.\boldsymbol{\tau} + \boldsymbol{f_s} + \rho g \tag{6.2}$$

The shear stress ($\boldsymbol{\tau}$) can be written as given by Eq. (7.3):

$$\boldsymbol{\tau} = \mu(\dot{\gamma})\,\boldsymbol{D} \tag{6.3}$$

Where, viscosity (μ) is constant for a Newtonian fluid and is a function of shear rate ($\dot{\gamma}$) for a non-Newtonian fluid. Strain rate tensor $\boldsymbol{D}$ and its magnitude $\dot{\gamma}$ are given by Eqs. (6.4) and (6.5), respectively:

$$\boldsymbol{D} = \frac{1}{2}(\nabla \boldsymbol{u} + \nabla \boldsymbol{u}^T) \tag{6.4}$$

$$\dot{\gamma} = \sqrt{\frac{1}{2}\boldsymbol{D}:\boldsymbol{D}} \tag{6.5}$$

An additional equation is solved for the volume fraction of one of the phases.

Volume fraction equation:

$$\frac{\partial \alpha_G}{\partial t} + \boldsymbol{u}.\nabla \alpha_G = 0, \tag{6.6}$$

The density (ρ) and viscosity (μ) in eqns. (6.1) and (6.2) are the average values of the two phases weighted by their volume fraction,

$$\rho = (1 - \alpha_G)\rho_L + \alpha_G \rho_G \tag{6.7}$$

$$\mu = (1 - \alpha_G)\mu_L + \alpha_G \mu_G \tag{6.8}$$

ρ_L, and μ_L are density and viscosity of liquid. While, α_G is gas volume fraction.

The body force term "$\boldsymbol{f_s}$" on RHS of equation of Eq. (6.2) includes the surface tension force, which is given by the continuum surface force (CSF) model (Brackbill et al., 1992), given by Eq. (6.9).

$$f_s = \sigma \kappa \delta(\boldsymbol{r} - \boldsymbol{r_{int}})\, \hat{\mathbf{n}} \tag{6.9}$$

Where, $\delta(\boldsymbol{r} - \boldsymbol{r_{int}})$ is the Dirac delta function which assumes the value of zero everywhere except at the interface. κ is given by equation (6.10).

$$\kappa = \nabla.\hat{\mathbf{n}} \tag{6.10}$$

$\hat{\mathbf{n}}$ is the unit vector normal to the interface and can be calculated using Eq. (6.11).

$$\hat{\mathbf{n}} = \frac{\nabla \alpha_G}{|\nabla \alpha_G|} \tag{6.11}$$

A fully-developed parabolic velocity profile is specified at the inlet. The volume fraction of the gas phase is specified to be zero at the inlet boundary. At the outlet boundary, a constant uniform pressure is specified. The walls are considered to be rigid, and a no-slip boundary condition is

specified on the wall. Initially, at time t = 0, the domain is filled with the liquid phase only, and a gas bubble of cylindrical shape is introduced at a distance *d* from the inlet boundary.

6.2.2 Numerical schemes

The simulations are performed in a transient manner using a non-iterative time advancement scheme. The QUICK scheme is used to discretize the convective term in the momentum equation. An explicit scheme is used to solve the VOF equation, and a piecewise-linear interface construction scheme is used to keep the interface sharp. A fractional step scheme is used for pressure-velocity coupling. The Green-Gauss node-based scheme, which helps in minimizing the spurious currents at the gas-liquid interface (Gupta et al., 2009), is used to calculate the gradients. The body force weighted scheme is used for pressure interpolation to compute the face pressure. A variable time step, based on a fixed Courant number of 0.25, is used. A typical value of the time step is 10^{-6} s or less.

6.2.3 Geometry

CFD simulations have been performed in geometries of two different dimensions. As shown in Fig. 6.1, the first geometry has the mother vessel of width 1 mm and daughter vessels of width d_1 = d_2= 0.78 mm each. The two bifurcation angles $(\alpha \text{ and } \beta)$ are varied, and the simulations are performed in symmetric as well as asymmetric bifurcations. The gravity is not considered in this case. The values of the bifurcation angles are given in Table 6.1.

The second geometry, shown in Fig. 6.2, has the mother vessel of width 1 mm and the two daughter vessels of width d_1 = 0.48 mm and d_2 = 0.96 mm. The bifurcation angles for the first and second daughter vessels are $\alpha = 13^{o}$ and $\beta = 65^{o}$, respectively. The gravity is acting in negative y direction. Both the geometries are considered a 2D planar and plotted in xy coordinate system. The depth of the vessel (z direction) is unit in dimension.

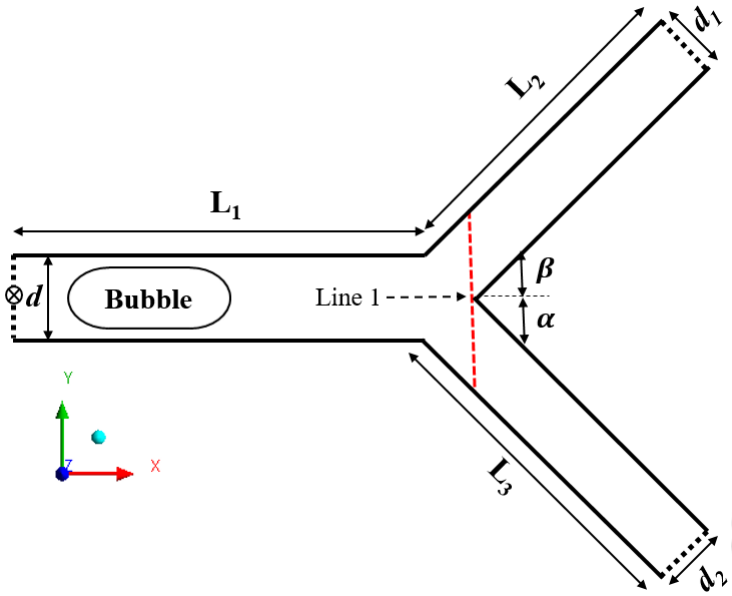

Figure 6.1. Schematic of the bifurcation geometry where: d = 1 mm; d_1, d_2 = *0.78 mm;* L_1, L_2, L_3 = *5d;* α, β are angle made by daughter vessels in-plane with mother vessel. The geometry lies in xy plane and origin is shown by cross symbol at the inlet of mother vessel. The vertical red dotted line is used to plot velocity profiles in the results. Gravity is not considered in this case.

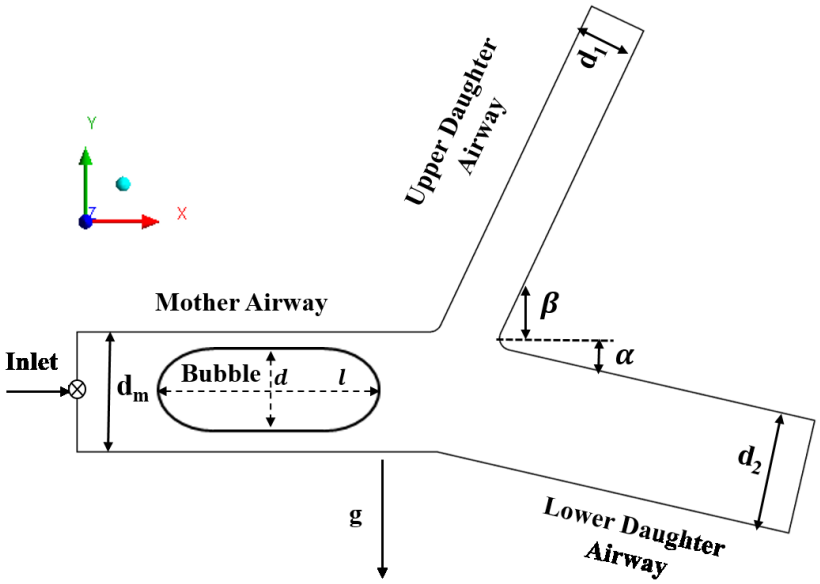

Figure 6.2. Schematic of the microbubble propagation in a 2D bifurcating airway. d_m, d_1 and d_2 are the mother vessel, upper daughter, and lower daughter vessel widths, respectively. The α = 13°, and β = 65° are bifurcation angles between the upper and lower daughter vessel in respect to the mother vessel. The *d* and *l* are the widths and length of the propagating bubble. The geometry lies in xy plane and origin is shown by cross symbol at the inlet of mother vessel.

6.2.4 Grid independence study

A structured mesh is used for the simulations. The implementation of surface tension modeling requires the mesh to have an aspect ratio close to one as far as possible. On the other hand, the mesh should be sufficiently refined to capture the thin film surrounding the gas bubble. Both the factors have been taken into account, and square elements are used everywhere except in the near-wall region where the mesh is refined such that at least five elements are present in the thin liquid film between wall and bubble (Gupta et al., 2009).

Considering the above guidelines, a mesh independence study is also conducted to evaluate the optimum and correct mesh size for further simulations in each geometry. Simulations are performed in the three meshes having elements 84000, 124000, and 18400 in geometry 1. The results are observed to be mesh independent in the two finer meshes and do not change with increasing mesh density for the two fine meshes. Therefore, the mesh consisting of 124000 elements is used for further simulations using geometry 1. Similarly, the final mesh used in geometry 2 consists of 117000 elements.

6.2.5 Validation

Liquid film thickness surrounding the bubble is a function of capillary number (Ca). Bretherton (1962) derived an expression, given by Eq. (6.12), to calculate the film thickness for the flow of long bubbles in a straight 2D rectangular channel at low values of Capillary numbers ($Ca < 0.01$). Later, this limitation was overcome, and a correlation was developed by (Aussillous and Quere, 2000), given by Eq. (6.13), for a wide range of *Ca* which was later derived from first principles (Klaseboer et al., 2014).

$$\frac{\delta}{R} = 1.34(Ca)^{\frac{2}{3}} \tag{6.12}$$

$$\frac{\delta}{R} = \frac{1.34(Ca)^{\frac{2}{3}}}{1+2.5(Ca)^{\frac{2}{3}}} \tag{6.13}$$

The bubble shape and film variation with the Ca is shown in Fig. 6.3(a). At low values of Ca, the Aussillous and Quére correlation reduce to Bretherton's expression. Therefore, the film thickness is compared with the Aussillous and Quére (Aussillous and Quere, 2000) correlation, as shown in Fig. 6.3(b). It may be noted that the Bretherton and Aussillous and Quére correlations have been developed considering very long bubbles in which a constant thickness film region exists.

However, such a region exists only for the lowest value of Ca in our case, and the bubble thickness changes continuously for the higher values of Ca. Film thickness is measured in the middle of the bubble. There is good agreement between the film thickness values obtained from CFD simulations and those using the correlation, with the maximum difference between the two being 15%.

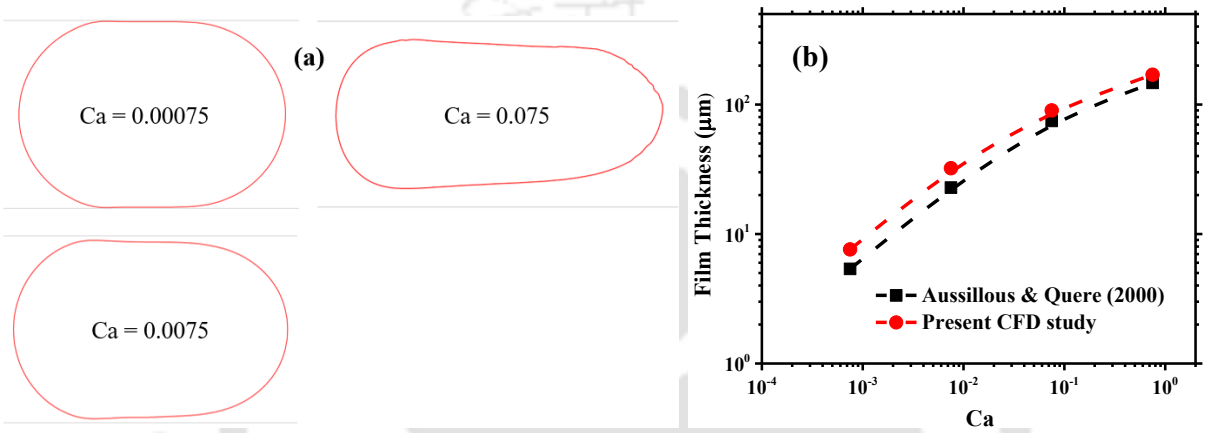

Figure 6.3. (a) Comparison of film thickness obtained with current CFD simulations and Aussillous and Quere(Aussillous and Quere, 2000) correlation (b) Variation of bubble shape and film thickness with change in capillary number.

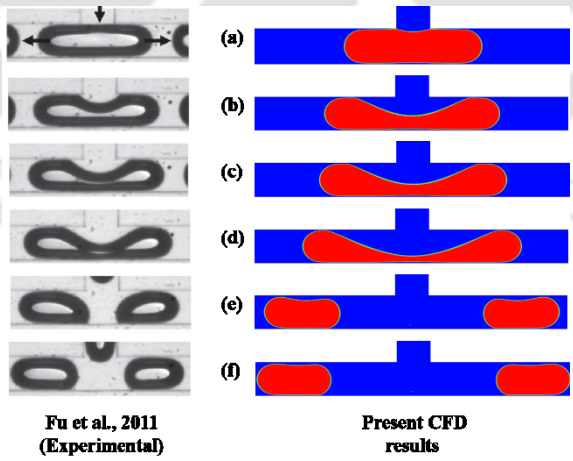

Figure 6.4. Comparison of snapshot of splitting bubbles with the experimental result from Fu et al. (2011) in a T junction, Ca = 0.016, l_b/d_m = 3.2.

Figure 6.3(a) shows the bubble shapes obtained from CFD simulations for the Ca values of 0.00075, 0.0075, and 0.075 in the mother vessel. There is a remarkable difference in the bubble shape for the three values of Capillary numbers. At the lowest Capillary number, the bubble is capsule shaped and has fore and aft symmetry. However, at the two higher values of Ca, the bubble is observed to become bullet shaped i.e. having a sharp nose. Similar effects of Capillary number on bubble shapes are observed in the literature for straight channel and symmetric bifurcation (Giavedoni and Saita, 1999; Khodaparast et al., 2015; Lac and Sherwood, 2009; Yao et al., 2019).

Figure 6.4 shows the comparison of bubble splitting with the experiments of Fu et al. (2011) in the T junction for water-glycerol mixture from literature at Ca = 0.0016 for bubble size l_b/d_m = 3.2 (Fu et al., 2011). The width and height of the square channel are each 400 μm, and the length is around 5 mm. The gas and liquid flow rates are 0.92 and 0.3 ml/min, respectively. In both cases, the process of bubble splitting is captured well qualitatively by the two-dimensional simulations. Once the bubble enters at the bifurcation, the part of the bubble at the T junction starts thinning, and a neck-like structure develops in both cases. Eventually, the bubble splits symmetrically.

6.3 Results and discussion

6.3.1 Effect of bifurcation angle on bubble splitting

A two-dimensional planar arterial model with mother vessel (d) and two daughter vessels (d_1 and d_2), as shown in Fig. 6.1, is used for modeling the bubble splitting. The width of the mother vessel is 1 mm, and that of daughter vessels is 0.78 mm each. The values of the bifurcation angles (α, β) are varied symmetrically $(\alpha = \beta)$ and asymmetrically $\alpha \neq \beta$), as shown in Table 6.1. The continuous phase is modeled as a primary phase (blood) with a viscosity of 0.0035 Pa.s and a density of 1060 kg/m^3. The secondary phase is a gas (PFC) with a viscosity of 2×10^{-5} Pa. s and a density of 12 kg/m^3 (Poornima and Vengadesan, 2012). The interfacial tension between PFC and blood is considered as 0.05 N/m. Gravity is assumed to be negligible and does not considered.

The splitting of the short bubble (L/d = 1.5) in the asymmetric bifurcation is studied. Reynolds number is considered to be Re = 10, 100 and respective capillary number is Ca = 0.00231, and 0.0231, respectively. Silations are initiated by patching the bubble at a distance of 1.5d from the inlet.

Table 6.1 Various bifurcation angles combinations used in the present study.

Sr. No.	Case	Angle
1	Symmetric	$\alpha = \beta$ =15°, 30°, 45°, 60°
2	Asymmetric	α = 15°, β = 30°
3		α = 15°, β = 45°
4		α = 15°, β = 60°
5		α = 30°, β = 45°
6		α = 30°, β = 60°
7		α = 45°, β = 60°

6.3.1.1 Symmetric bifurcation

The angle between the mother vessel and each daughter vessel ($\alpha = \beta$) is equal in the symmetric bifurcation. The effect of capillary number and bifurcation angle on bubble splitting has been analyzed and discussed.

Fig. 6.5 shows the process of bubble splitting in the symmetric bifurcation having $\alpha = \beta$ =45° for capillary number Ca = 0.0231 and Re = 100. At about 2.8 ms, the bubble tip or head enters into the bifurcation, and the bubble is squeezed at the bifurcation point between the wall and liquid entering from the mother vessel. As a result of the squeezing, the bubble extends in the lateral direction entering the two daughter vessels (4.9 ms), and a neck-like region develops at the bifurcation point. Finally, the bubble neck reaches a minimum, and the bubble breaks into two daughter bubbles (6.3 ms). After splitting, the daughter bubbles regain their shapes as they proceed towards the outlet (9 ms).

The effect of bifurcation angle on the dynamics of the bubble neck during the final stage of the breaking of the bubble is shown in Fig. 6.6. Throughout the rupture process, the shape of the bubble head does not change. It may be noted that the shape of the nose/front of a Taylor bubble develops independent of the shape of the bubble rear, for example (Bretherton, 1961; Klaseboer et al., 2014).

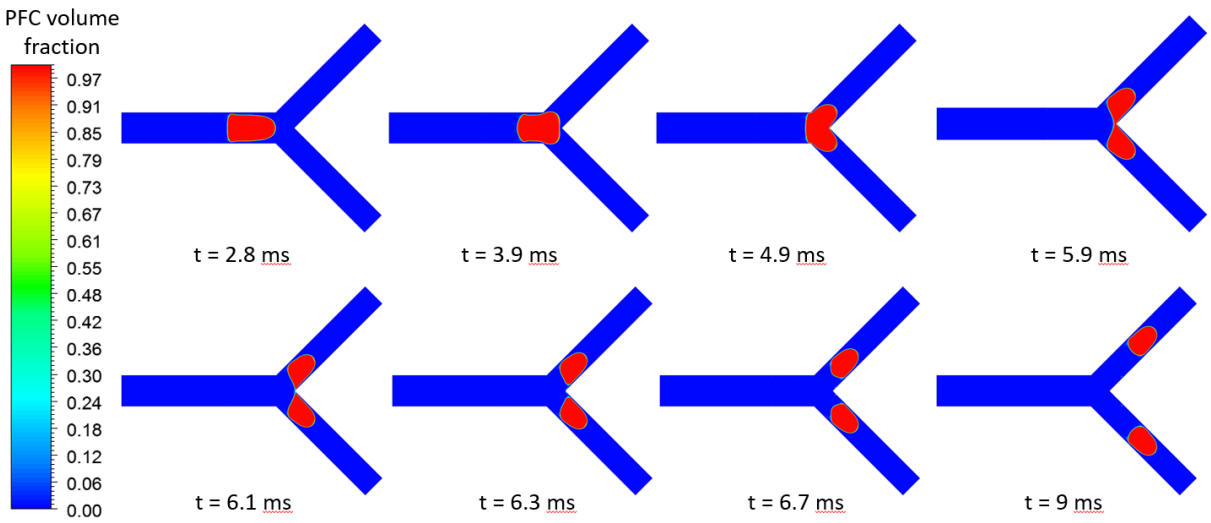

Figure 6.5. Volume fraction of PFC bubble passing through the symmetric bifurcation for bifurcation angle, $\alpha = \beta = 45°$ at Ca = 0.0231, and Re = 100.

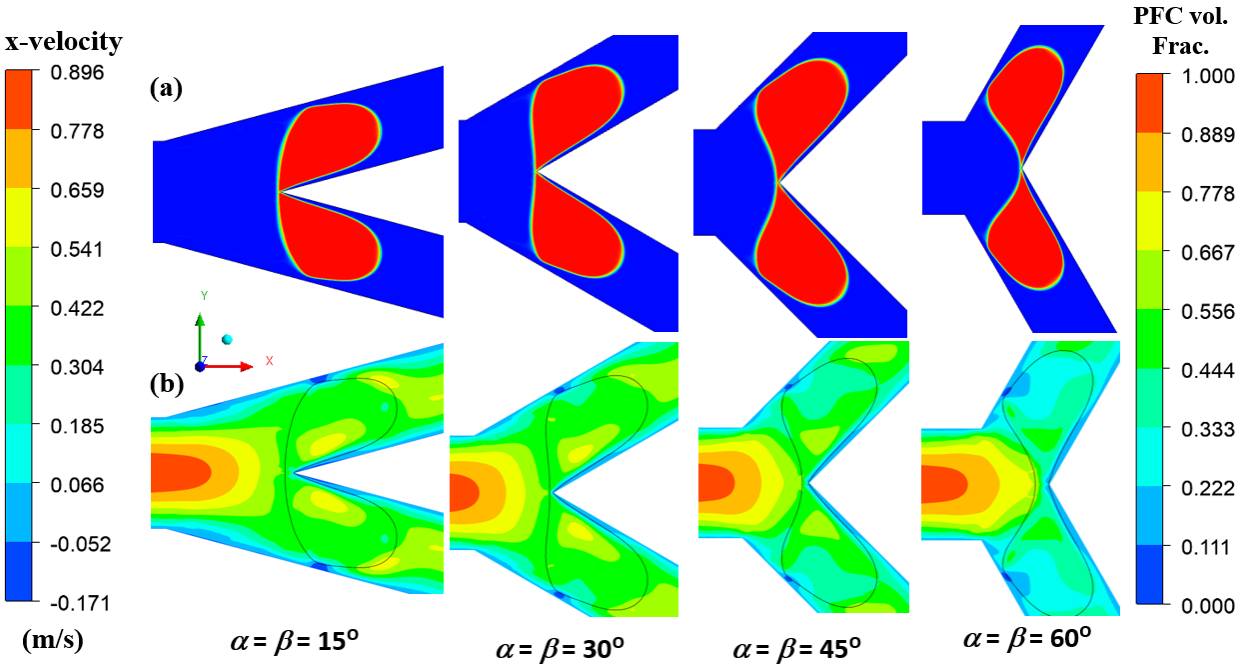

Figure 6.6 (a) Bubble shape and (b) distribution of *x*-component of velocity for different bifurcation angles in a symmetric bifurcation at Re = 100, Ca = 0.0231. Note that the x-direction is aligned with the axis of the mother vessel. The results are shown at a time instant when necking occurs in each case.

The width or thickness of the bubble decreases continuously and is highly deformed. It can be seen as time passes, the neck width gradually decreases to zero at the bifurcation, and then the bubble

gets pinched off. The bubble neck is slightly convex, as seen from the inlet, for lower bifurcation angle i. e. $\alpha = \beta = 15°$, but as the bifurcation angle increases, the neck of the bubble becomes almost flat at 30° and then concave for the two higher angles.

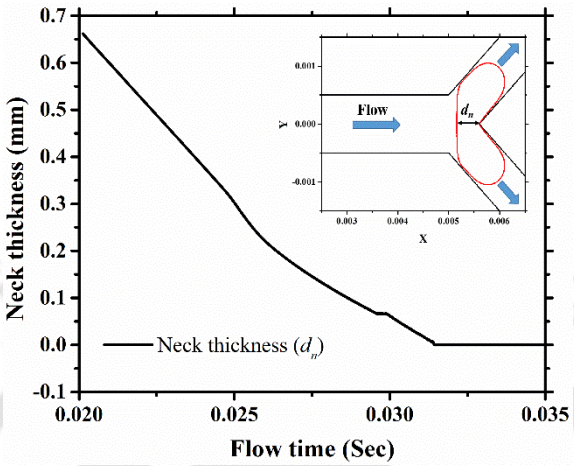

Figure 6.7 Variation of bubble neck thickness with time for $\alpha = \beta = 30°$ at Ca = 0.00231, and Re = 10.

The *x*-component of velocity is also shown in Fig. 6.6 for each case. The *x*-direction is aligned with the axis of the mother vessel. At the instant shown, the velocity profile is parabolic at the end of the mother vessel. As the liquid enters bifurcation, the cross-section area increases and the flow is turned towards the daughter vessel. Both factors contribute to the reduction of the x-component of velocity at the bifurcation. With an increase in the bifurcation angle, the x-component of velocity decreases at the bifurcation. In all the cases, a dark blue region indicating the reverse flow is observed at the thinnest region between the bubble and outer wall of the daughter vessel.

Figure 6.7 shows the variation of bubble neck thickness with time. At time 0.02 s, the bubble neck thickness is 0.6 mm i.e. the neck thickness before squeezing starts. As the bubble enters the daughter vessel, its neck thickness decreases linearly up to ~0.025 s, and a neck-type region develops. The slope of the curve changes, and the bubble neck thickness again decreases linearly until a bubble pinch-off occurs.

Figure 6.8 shows the contours of pressure at three different instants for three bifurcation angles at Re = 100 and Ca = 0.0231. The pressure inside the bubble is higher than that of the liquid surrounding it because of the Laplace pressure difference. The transverse pressure gradient in the mother vessel near the inlet region represents the presence of developing flow in the mother vessel.

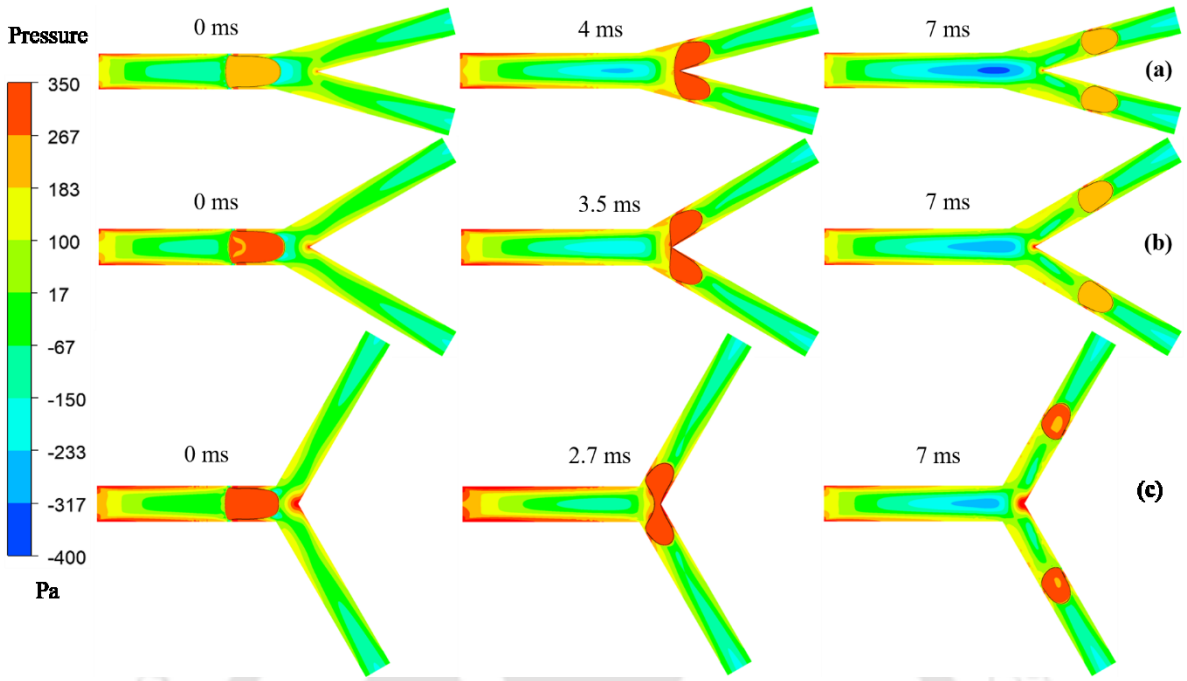

Figure 6.8. Pressure contours and bubble shape at various time instances during splitting process for Re = 100, Ca = 0.0231 (a) $\alpha = \beta = 15°$ (b) $\alpha = \beta = 30°$ (c) $\alpha = \beta = 60°$.

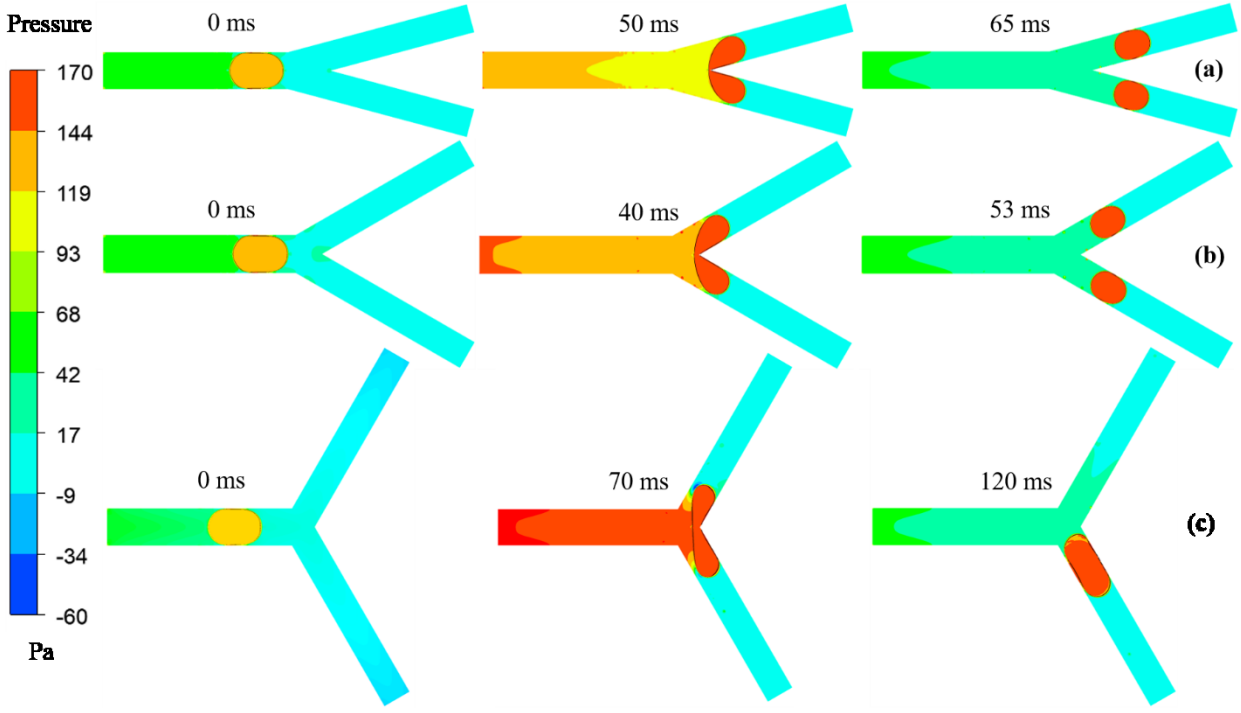

Figure 6.9. Pressure contours and bubble shape at various time instances during splitting process for Re = 10, Ca = 0.00231 (a) $\alpha = \beta = 15°$ (b) $\alpha = \beta = 30°$ (c) $\alpha = \beta = 60°$.

The carina or bifurcation point is the stagnation point, and therefore the pressure has a high value. The instant at which the bubble is at the bifurcation (at origin), the curvature of the bubble at the neck changes significantly, which explains the local variation of pressure near the interface.

Figure 6.9 shows the bubble shape and pressure contours at Re=10, Ca=0.00231 for various bifurcation angles. Due to relatively higher surface tension force than the cases shown in Fig. 6.8, the bubble shape is more rounded in the mother vessel. The film thickness surrounding the bubble is lower in this case, and it becomes challenging to capture the very thin film in the numerical simulations. In such cases, defining the contact angle as 0° helped as the contact lines is swept away even if it is developed. The bubble splits into equal size daughter bubbles at lower angles, but at a higher angle ($\alpha = \beta = 60°$), a non-splitting behavior is observed, and the bubble goes in one of the daughter vessels. As the bubble size is smaller in this case, the bubble does not obstruct the entire cross-section of the daughter vessels. The splitting with partial obstruction and splitting with complete obstruction is observed, and it depends on the Re and Ca values. Higher Re values show a splitting with complete obstruction. In comparison, lower Re values show a splitting with partial obstruction. The neck shape of the bubble during the pinch-off stage varies with bifurcation angle and flow rate.

Fig. 6.10 shows the splitting behavior of the PFC bubble at the carina of bifurcation for $\alpha = \beta = 15°$ at Re = 10. Initially, the bubble is close to the wall, separated by a thin film (δ) using Bretherton's correlation (Bretherton, 1961). The shape of the bubble starts to change at the bifurcation due to resistance to flow around the bubble, and the concave shape of the bubble takes place at the trailing end. After the bubble neck reaches a bifurcation, the thin film stretches, and the bubble splits into two equal-size daughter bubbles in a homogenous way, as shown in Fig. 6.10 (t_3). The x-component of velocity at the carina of the bifurcation is parabolic along line 1 at time instance t_1 and t_3, as shown in Fig. 6.10(a). The maximum velocity is skewed towards the inner wall of bifurcation. The volume of fluid method was used, which shows the velocities of gas and liquid depending on its position. During the pinch-off stage of bubble break up (t_2), the velocity profiles along line 1 are symmetric along both sides of the daughter vessel. The deviations of velocity is very small from steady-state (t_1 and t_3). Due to symmetry in the velocity profile during pinch-off, the bubble splits in a homogenous fashion. The symmetry in the velocity profile is observed for

the y-velocity component as well, as shown in Fig. 6.10(b). Once the bubble passes into the daughter vessels, the flow regains the steady state, as shown in Fig. 6.10(t_3).

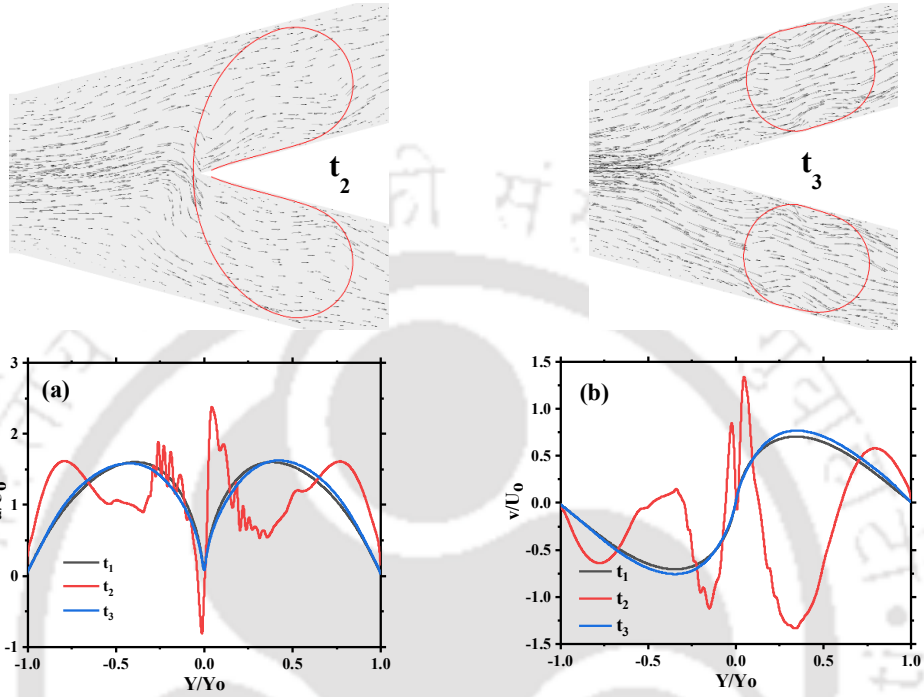

Figure 6.10 Splitting behavior of PFC bubble at carina of bifurcation for $\alpha = \beta = 15°$ (Re = 10 and Ca = 0.00231)) at different time instances, top: Bubble interface, bottom: (a) x-velocity and (b) y-velocity profiles along carina and the Y/Y_o shows the dimensionless distance along y direction.

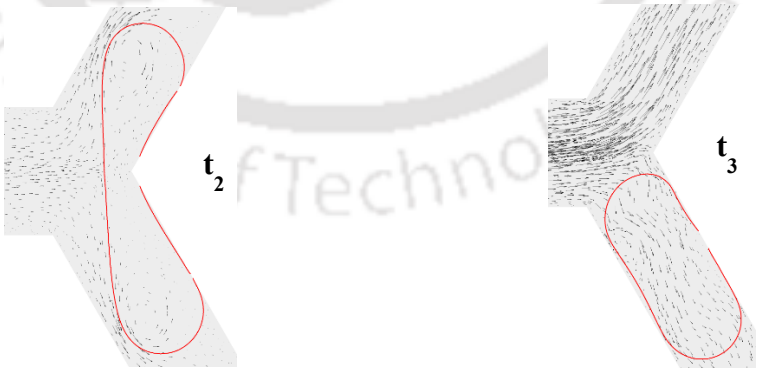

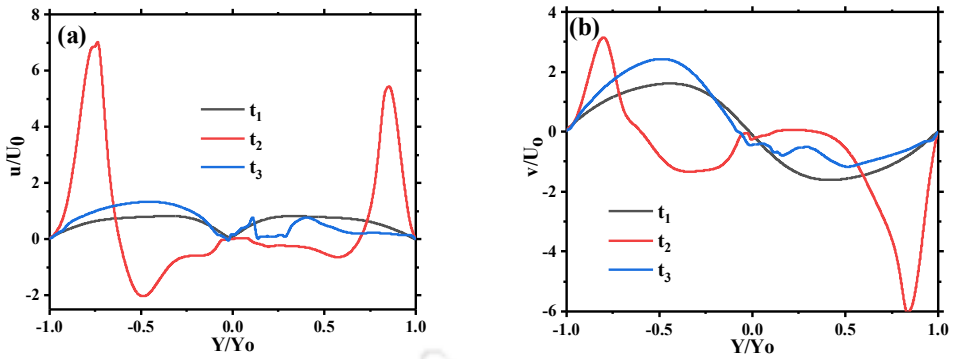

Figure 6.11 Splitting behavior of PFC bubble at carina of bifurcation for $\alpha = \beta = 60°$ (Re = 10 and Ca = 0.00231 at different time instances, top: Bubble interface, bottom: (a) x-velocity and (b) y-velocity profiles along carina.

For the larger bifurcation angle ($\alpha = \beta = 60°$), the bubble does not split and goes into the lower daughter vessel, as shown in Fig. 6.11(t_3). The bubble enters the bifurcation in the usual manner, as explained earlier, but the portion in the lower channel remains close to the vessel wall, while the portion in the upper channel separates and swings downward. This phenomenon of bubble behavior is called non-splitting behavior. At the lower Capillary number, the surface tension dominates over the inertial force, and the bubble reverses back into the lower vessel and completely passes through it. A similar kind of reversal splitting was observed for liquid droplets (Calderon et al., 2010; Carlson et al., 2010). Due to stronger capillary force, a larger curvature is observed at the bubble neck, resulting in a larger radius of the gas-liquid interface. As the perturbation grows, the bubble migrates into the lower daughter vessel. The stronger recirculations observed in the upper daughter vessel, which increases the pressure difference between the upper and lower daughter vessel. The velocity profiles at the carina of the bifurcation along line 1 reveal much about the non-splitting behavior. The bubble remains stable before reaching bifurcation. Once it reaches the bifurcation, the x-component of velocity shows a very high speed and high-velocity gradient between the two daughter vessels at the pinch-off stage, as shown in Fig. 6.11(a). The same phenomena observed for the y-velocity component and can be seen in Fig. 6.11(b). From the discussion of bubble splitting in symmetric bifurcation, it was observed that the homogenous splitting of the bubble is observed for higher Reynolds numbers at all bifurcation angles. Whereas, no splitting is observed at low Reynolds number (Re = 10) and high bifurcation angle ($\alpha = \beta = 60°$), and the bubble does not split and passes into the lower daughter vessel.

6.3.1.2 Asymmetric bifurcation

In this section, the effect of asymmetry in bifurcation angle ($\alpha \neq \beta$) on the bubble splitting for varying Reynolds numbers and capillary numbers from Re = 10, 100 and Ca = 0.0231, 0.00231, respectively, has been analyzed. The results are shown in the form of bubble interface at the final stage of bubble splitting and x and y velocity components along line 1 at bifurcation carina.

Figure 6.12 shows the bubble splitting dynamics at bifurcation for various asymmetric bifurcation angle combinations. The shape of the bubble and pressure contours are shown for various time instants at Re=100 and Ca=0.0231. As we can see, during the pinch-off stage, the bubble neck curvature is changing with a change in bifurcation angle. The neck shape is not symmetric with respect to the mother vessel due to asymmetry in the bifurcation angle. There is no gap between the channel wall and bubble during break up, which is called a splitting with complete obstruction. Just after the pinch-off, the bubble shape is not symmetric in the daughter vessel and skewed towards the outer wall. The skewness is more prominent in the higher angled vessel.

Figure 6.13 shows the pressure contours and bubble shape during splitting for various bifurcation angles at Re=10 and Ca=0.00231. As discussed in the symmetric case, the higher surface tension force generates more rounded bubbles. The non-splitting behavior of bubbles is observed for all the cases. The bubble goes into the lower angle vessel due to less resistance to flow.

Figure 6.14(a) shows the mass flow rate distributions at outlets of daughter vessels of asymmetric bifurcation angle case (α = 15°, β = 60°). Mass flow distribution is asymmetric due to varying bifurcation angles and the resistance to flow. The lower angle vessel (outlet 2) has a low resistance, as shown in Chapter 3 for single-phase flow in bifurcation. Due to less resistance to flow, a higher mass fraction drives into that vessel. During the non-splitting regime, the bubble pushes into a lower angle vessel and causes a change in mass flow distribution. There is a sudden increase in mass flow in higher angle vessels due to bubble pushes into the lower daughter vessel. Similarly, the neck thickness of the bubble decreases with time, as shown in Fig. 6.14(b). Due to non-splitting behavior, bubble travels into the lower vessel, and neck thickness suddenly drops to zero value.

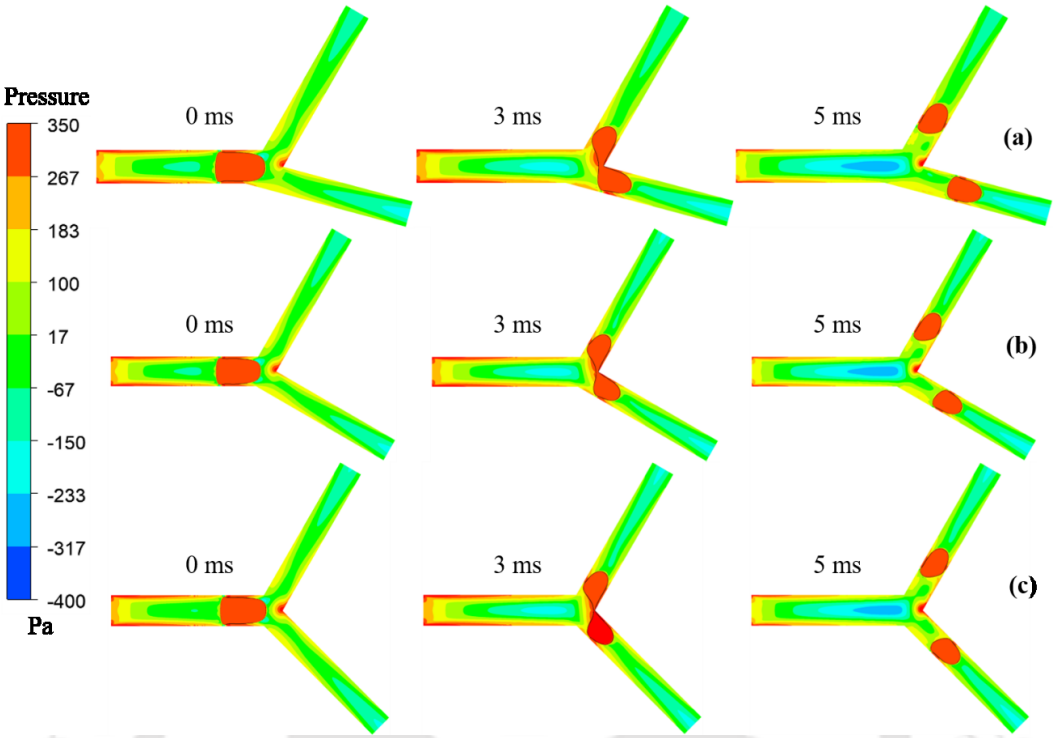

Figure 6.12 Pressure contours and bubble shape (black line) at various time instances during splitting process for Re = 100, Ca = 0.0231 (a) $\alpha = 15°$, $\beta = 60°$ (b) $\alpha = 30°$, $\beta = 60°$ (c) $\alpha = 45°$, $\beta = 60°$.

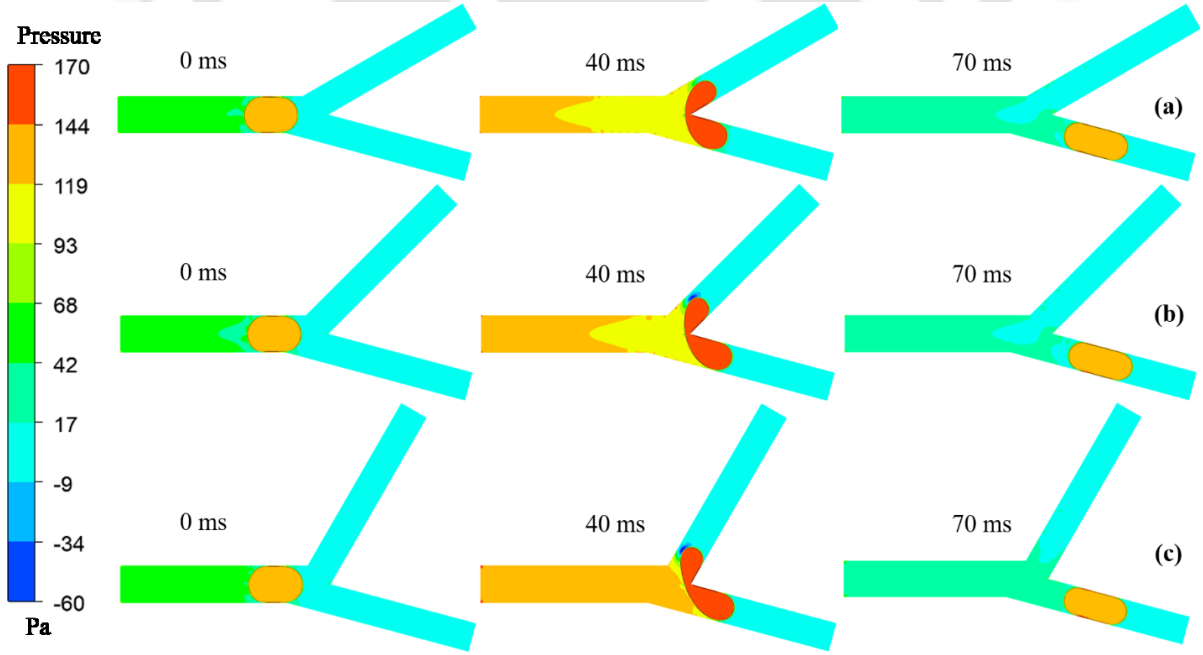

Figure 6.13. Pressure contours and bubble shape (black line) at various time instances during splitting process for Re = 10, Ca = 0.00231 (a) $\alpha = 15°$, $\beta = 30°$ (b) $\alpha = 15°$, $\beta = 45°$ (c) $\alpha = 15°$, $\beta = 60°$.

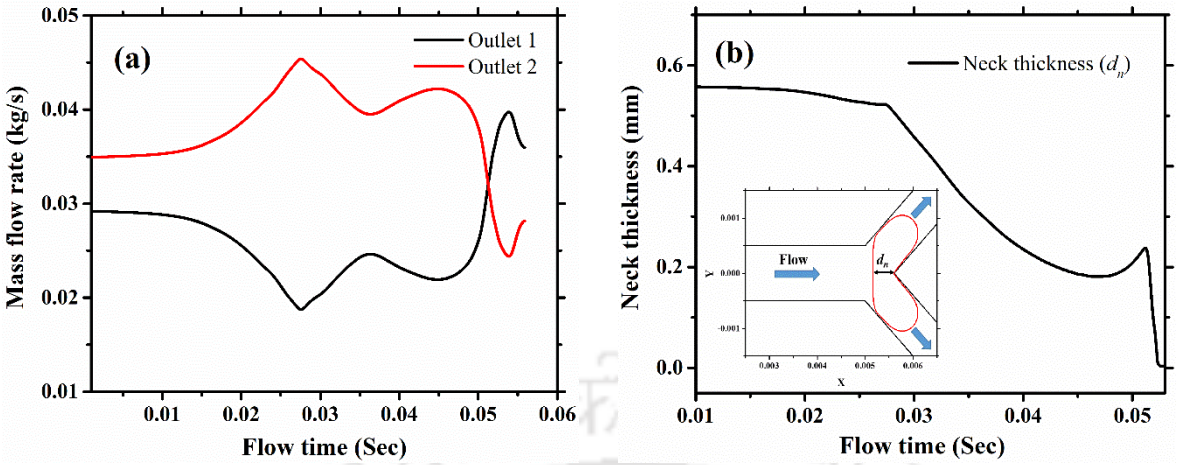

Figure 6.14. (a) Mass flow distribution at outlets of daughter vessels and (b) bubble neck thickness variation with time for asymmetric bifurcation $\alpha = 15°$, $\beta = 60°$ at Re = 10, and Ca = 0.00231.

Fig. 6.15 shows the PFC bubble splitting at bifurcation for Re = 100. It is found that the asymmetry in the bifurcation angle does not affect bubble splitting behavior. The homogenous splitting of the bubble takes place even after asymmetry in the bifurcation angle and flow velocities in a respective daughter vessel. As seen in Fig. 6.15(a), the axial velocities at line 1 are parabolic on both daughter vessels. Still, the axial velocity is higher in the lower angle vessels as compared with the larger angle vessel at time instances t_1 and t_3. The velocity is skewed at the bifurcation on both daughter vessels. During the pinch-off stage (t_2), the x – component of velocity on both daughter vessels is close to symmetric. Finally, the velocity gradient is not big enough to change the direction of the splitting bubble. The y – velocity component does not have a large velocity gradient, as shown in Fig. 6.15(b). Finally, the homogenous splitting occurs for the asymmetric case of bifurcation. As the bifurcation angle increases from $\alpha + \beta = 45°$ to 60° and 105°, it does not affect bubble splitting, as shown in Fig. 6.16.

The decrease in Reynolds number from 100 to 10 causes non-splitting behavior even for a small bifurcation angle ratio ($\beta/\alpha = 2$). As shown in Fig. 6.17 ($\alpha = 15°$, $\beta = 30°$), the bubble does not break into two daughter bubbles, and non-splitting behavior occurs, and the bubble passes into the lower daughter vessel. As seen from Fig. 6.17(a) the bubble goes into the lower daughter vessel due to large velocity gradients during the pinch-off stage (t_2). Fig. 6.17(b) shows a high-velocity gradient for the y – velocity component. The same splitting behavior occurs for a higher bifurcation angle (angle ratio $\beta/\alpha = 4$), as shown in Fig. 6.18.

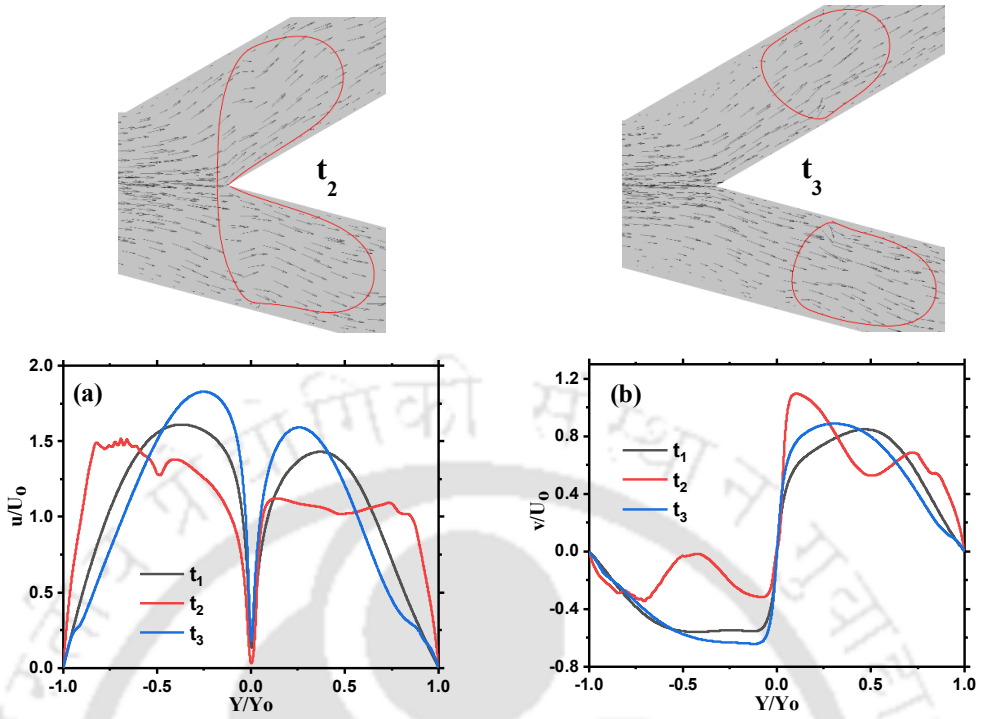

Figure 6.15. Splitting behavior of PFC bubble at carina of bifurcation for α = 15° β =30° (Re = 100, Ca = 0.0231) at different time instances, top: Bubble interface, bottom: (a) x-velocity and (b) y-velocity profiles along carina.

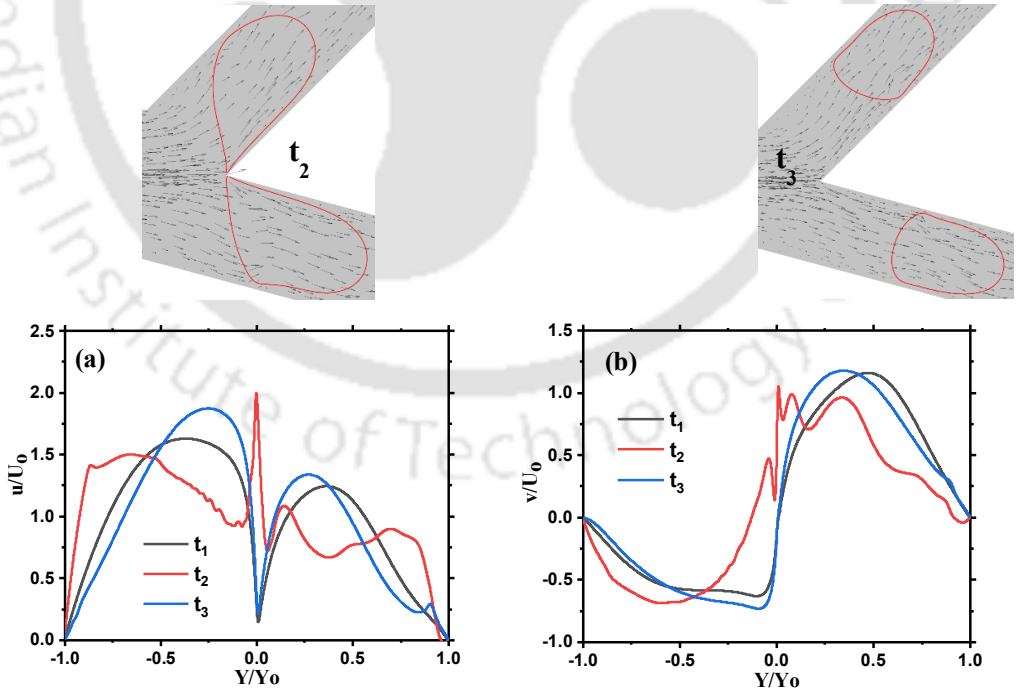

Figure 6.16. Splitting behavior of PFC bubble at carina of bifurcation for α = 15° β =45° (Re = 100, Ca = 0.0231) at different time instances, top: Bubble interface, bottom: (a) x-velocity and (b) y-velocity profiles along carina.

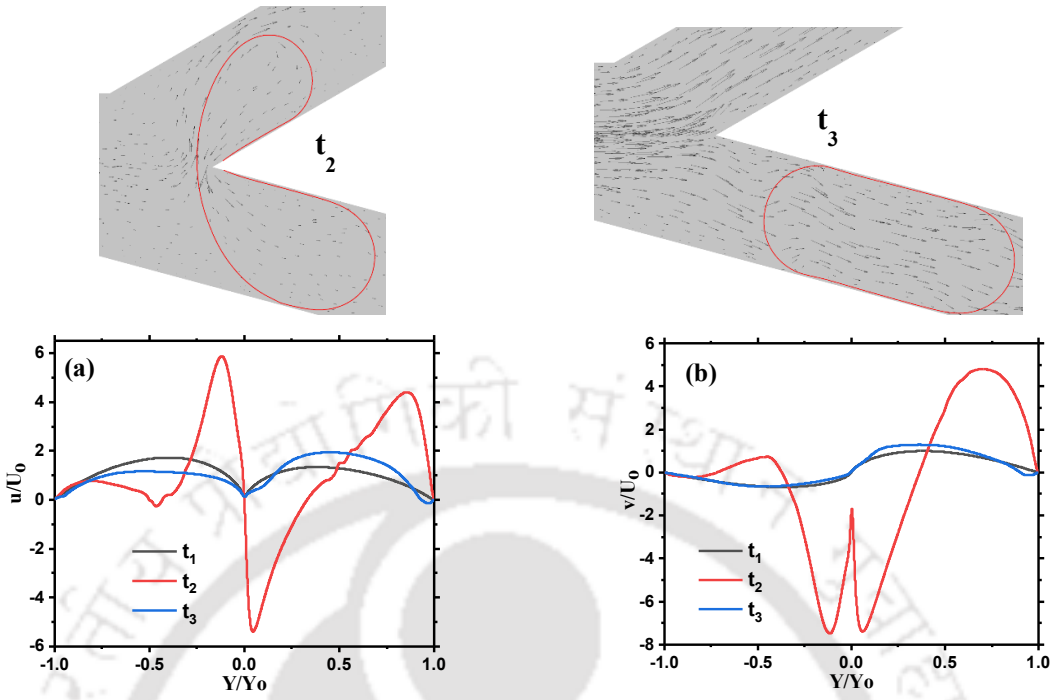

Figure 6.17. Splitting behavior of PFC bubble at carina of bifurcation for α = 15° β =30° (Re = 10, Ca = 0.00231) at different time instances, top: Bubble interface, bottom: (a) x-velocity and (b) y-velocity profiles along carina.

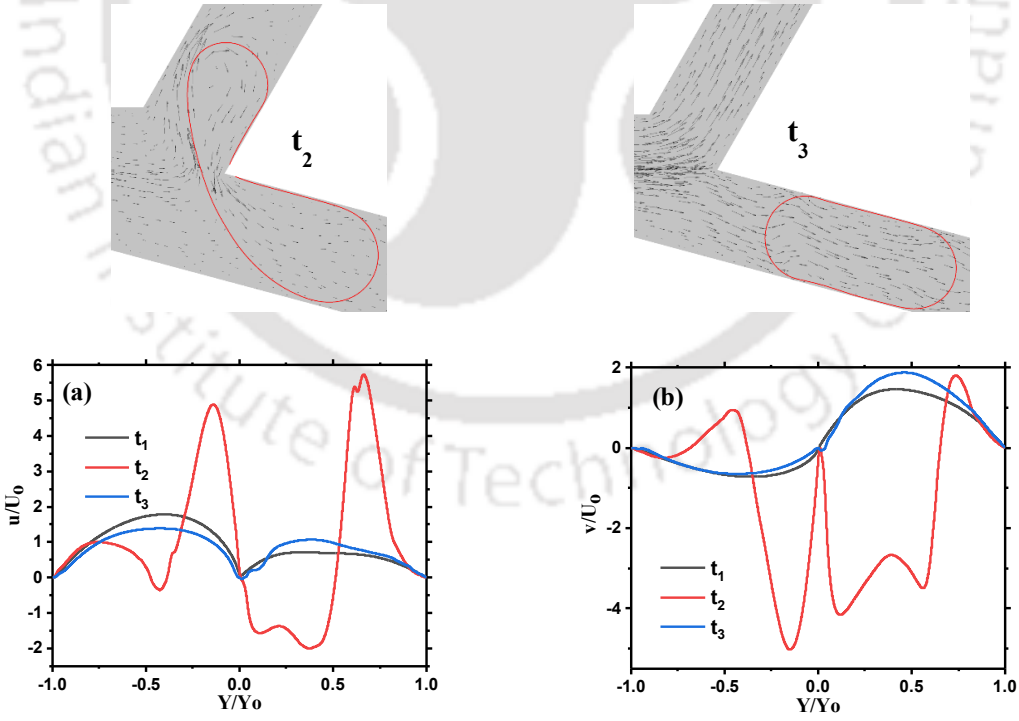

Figure 6.18. Splitting behavior of PFC bubble at carina of bifurcation for α = 15° β = 60° (Re = 10, Ca = 0.00231) at different time instances, top: Bubble interface, bottom: (a) x-velocity and (b) y-velocity profiles along carina.

6.3.2 Effect of flow parameters on bubble propagation in an airway bifurcation

The recent COVID19 outbreak has affected a significant portion of the world's population. It affects the respiratory system and compromises the oxygen supply to various body parts. Due to insufficient oxygen, the patient needs external oxygen via mechanical ventilation. The oxygen enters into small airways and may break the endothelial cells near a wall. In this section, the effect of various flow parameters on hydrodynamic stresses is explored.

The diameter of the trachea, the first-generation airway in the airway tree, is 18 mm, and that of the alveolus, the terminal of the airway tree, is 0.4 mm (Weibel, 1963). The diameters of the intermediate airways vary between these values. Yalcin et al. (2007) suggested that bronchioles of generation 10 to 19 are probable sites of cellular injury. CFD simulations are performed for the non-dimensional numbers *Re*, *Ca,* and *Bo* relevant to these airways.

A simplified two-dimensional model of a typical airway bifurcation has been considered, as shown in Fig. 6.2. The diameter of the airways decreases on branching following Murray's law relationship (Murray, 1926). Two different bifurcation geometries have been considered. The dimension of the lower daughter airway is twice that of the upper daughter airway for both geometries. The size of daughter vessels and bifurcation angles follow Murray's law (Murray, 1926) for the second geometry. The length of the vessels for each case is given in Table 6.2.

Initially, the airway bifurcation is filled with a liquid (mucus), and an air bubble is introduced in the mother vessel and its evolution at the bifurcation is investigated for a range of parameters given in Table 6.3. The shape of the air bubble depends on its volume and the diameter of the airway in which it is present. If the aspect ratio (l/d) of the air bubble is less than 1, the bubble is expected to be circular, whereas it assumes the shape of a long capsular bubble when the bubble aspect ratio is more than 1 (Kumari et al., 2019). Both possibilities have been considered by choosing two aspect ratios of the bubble 0.9 and 1.5.

A healthy human being normally breathes 12 times in a minute. The tidal volume under resting condition i.e. the volume inhaled in one breath, is about 500 ml. Assuming equal duration of inhalation and exhalation, the air flow rate is about 12 liters per minute. Chen et al. (2014) suggested the cross-sectional area of the airways between 10 to 19 generations of airways to be 8-1000 cm^2. A simple calculation suggests the flow velocity be in the range 0.002-0.25 m/s. The

mucus fluid viscosity is taken to be 0.047 Pa.s (Lai et al., 2009). In the lungs of a healthy human being, a surfactant is present, which resists the formation of liquid bridges and facilitates easy reopening if the liquid bridge is formed. Depending on the surfactant imbalance, the surface tension may vary widely. This results in a large variation in the non-dimensional parameters-capillary number (*Ca*), Bond number (*Bo*), and Reynolds number (*Re*). The following range of parameters has been considered:

$$Re = 2, 7.5 \times 10^{-4} \leq Ca \leq 0.075, 6.5 \times 10^{-2} \leq Bo \leq 0.6$$

The base case is considered for Re = 2, Ca = 0.075, and Bo = 0.14, which corresponds to the tenth generation airway reopening (Chen et al., 2014).

Table 6.2 Geometric parameters used for general and Murray's bifurcation in the CFD simulations.

Airway bifurcation	Width of vessels	Bifurcation angle (α and β)
Geometry 1	d_m = 1 mm, d_1 = 0.39 mm, d_2 = 0.78 mm,	$\alpha = \beta = 40^o$
Geometry 2	d_m = 1 mm, d_1 = 0.48 mm, d_2 = 0.96 mm, Length of mother and daughter vessels is 3 mm for each case	$\alpha = 65^o$, $\beta = 13^o$

Table 6.3. Hydrodynamic parameters used in the CFD simulations.

Hydrodynamic parameters studied	Values of flow parameters used in simulations
Bond number (Bo)	Bo = 0.06, 0.14, 0.6
Capillary number (Ca)	Ca = 0.00075, 0.0075, 0.075
Reynolds Number (Re)	Re = 2
Bubble size (l/d)	l/d = 0.9, 1.5

The airway bifurcation geometry has the mother vessel of width 1 mm and the two daughter vessels of widths d_1 = 0.48 mm and d_2 = 0.96 mm. The bifurcation angles for the first and second daughter vessels are $\alpha = 65^{o}$and $\beta = 13^{o}$, respectively. CFD simulations for the bubble motion in a bifurcating vessel are performed over a wide range of flow parameters, as given in Table 6.3. First, the typical motion of a bubble and its effect on the stress on the wall is analyzed for the base case (Re = 2, Ca = 0.075, Bo = 0.14). The physical properties of various liquid used in the present study is shown in Table 6.4.

Table 6.4. Physical properties of various fluids used in the present study.

Sr. No.	Ca or Bo	Viscosity (μ)	Density (ρ)	Surface tension (σ)
1	Ca=0.075 (Bo=0.14, Re=2)	0.04	1000	0.05
2	Ca=0.0075 (Bo=0.14, Re=2)	0.004	1000	0.05
3	Ca=0.00075 (Bo=0.14, Re=2)	0.001	1000	0.072
4	Bo=0.06 (Ca=0.075, Re=2)	0.032	440	0.072
5	Bo=0.14 (Ca=0.075, Re=2)	0.048	998	0.072
6	Bo=0.6 (Ca=0.075, Re=2)	0.1	4403	0.072

6.3.2.1 Typical bubble flow dynamics in a bifurcating channel

Figure 6.19(a) shows the evolution of the shape of the bubble in the bifurcating vessel for the base case (Re = 2, Ca = 0.075, Bo = 0.14). The bubble shape changes slightly as the bubble reaches the bifurcation region. The bubble does not split and goes into the lower daughter vessel. Note that gravity acts in the negative y-direction. In a symmetric channel for the same flow conditions, as shown in Fig. 6.19(b), the bubble breaks up into two unequal parts, and the bigger bubble goes in the upper vessel due to buoyancy. However, in the asymmetric geometry considered in this work, the lower daughter vessel is wider than the upper one. The flow resistance in a vessel increases with a decrease in the vessel width, and therefore the resistance to flow in the upper vessel having a smaller width is higher. Out of the two contrasting effects i.e. those of buoyancy and flow resistance, the effect of resistance is dominant, and the bubble moves in the lower vessel. The effect of buoyancy on the bubble shape can be seen when the bubble is at the bifurcation and is slightly pulled towards the upper vessel.

Fig. 6.20(a) shows the variation of the bubble velocity with time. The bubble velocity (U_B) in a bifurcation channel is calculated using Eq. (6.14).

$$U_B = \sqrt{{U_{B,x}}^2 + {U_{B,y}}^2}\ ;\ U_{B,x} = \frac{\int_V \alpha_G u_x dV}{\int_V \alpha_G dV}\ and\ U_{B,y} = \frac{\int_V \alpha_G u_y dV}{\int_V \alpha_G dV} \qquad (6.14)$$

u_x and u_y are x and y components of velocity, respectively. Once the bubble approaches the bifurcation (at 8 ms), its velocity starts decreasing with time and attains a minimum at about 13 ms when its nose has entered the daughter vessel, and then starts increasing and attains a steady value at about 20 ms when the entire bubble is in the daughter vessel. According to Kay et al. (2004), cell damage is best correlated against pressure gradient (Kay et al., 2004). Therefore, focus on the results for pressure gradients for different cases has been studied. Figure 6.20(b) shows the variation of dp/dx on the upper wall of the airway bifurcation at three time instants- the bubble is in the mother vessel (6 ms), the bubble is at the bifurcation (13 ms), and the bubble is in the daughter vessel (22 ms). A large variation in dp/dx can be seen at the location where the bubble is present. This variation is highest at the bifurcation. Therefore, the variation of dp/dx at the bifurcation is shown for the subsequent cases. The pressure gradient in the two-dimensional system has two components -dp/dx and dp/dy. Both the components are highest at the same location at the bifurcation. Therefore, the variation of dp/dx only is shown.

For comparison, the plots of pressure, pressure gradient, and wall shear stress along the upper and lower vessel airway walls at 13 ms are also shown in Fig. 6.21. The pressure is higher in the upper vessel than in the lower one in the region where the bubble is present. The difference between the two values corresponds to the capillary pressure difference across the bubble. In the region downstream of the bifurcation where only the liquid phase is present, the pressure has similar values in both the daughter vessels. The pressure peak in the lower vessel corresponds to the tip of the bubble. Note that the capillary pressure is inversely proportional to the bubble diameter and increases as the bubble diameter decreases. Similarly, the peak and trough in the pressure gradient plot correspond to the change in bubble diameter. The shear stress on the upper wall is higher than that on the lower wall in the bifurcation region. It is consistent with the past studies, which show that the smaller size of the daughter vessel has a higher pressure gradient (Yalcin et al., 2007).

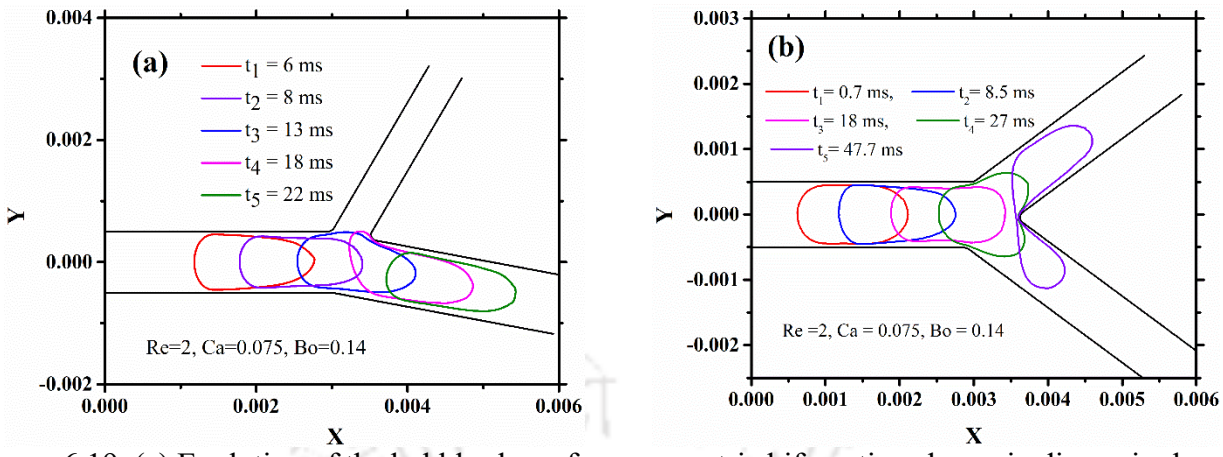

Figure 6.19. (a) Evolution of the bubble shape for asymmetric bifurcation shown in dimensionless X and Y coordinate system for base case (Re = 2, Ca = 0.075, Bo = 0.14). (b) The evolution of the bubble shape in a symmetric channel is also shown for comparison.

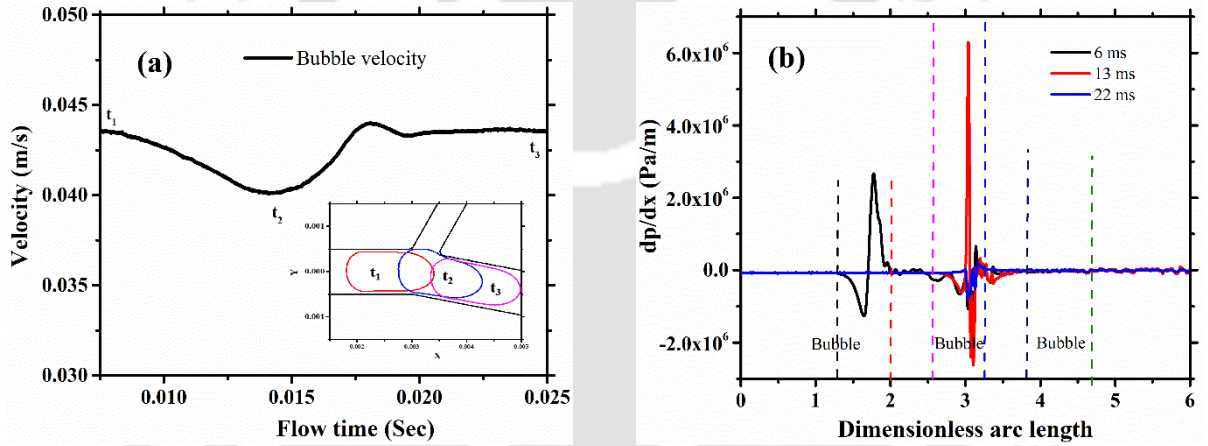

Figure 6.20. (a) Variation in bubble velocity with time at an airway bifurcation for the case shown in Fig. 3(a) (b) Pressure gradient on the upper wall at time instants t_1, t_3 and t_5 shown in Fig. 3(a).

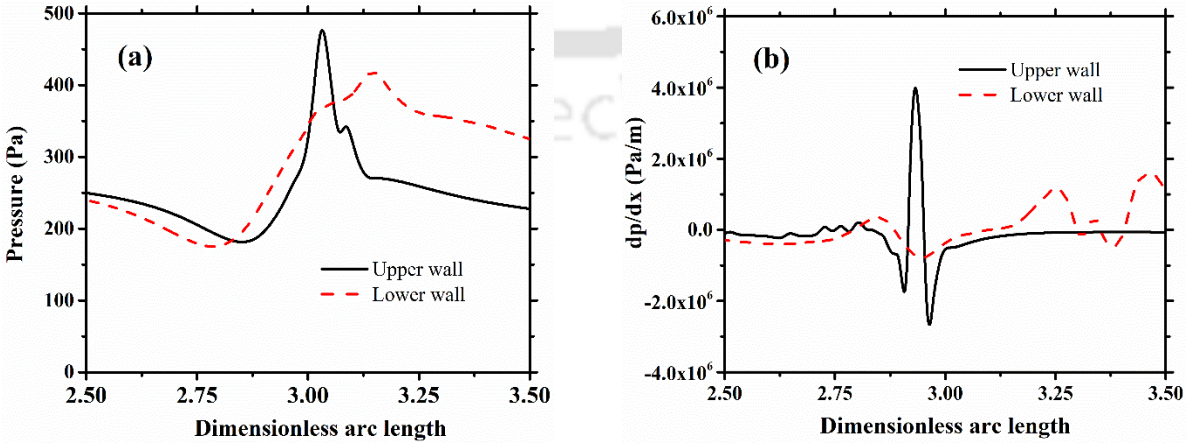

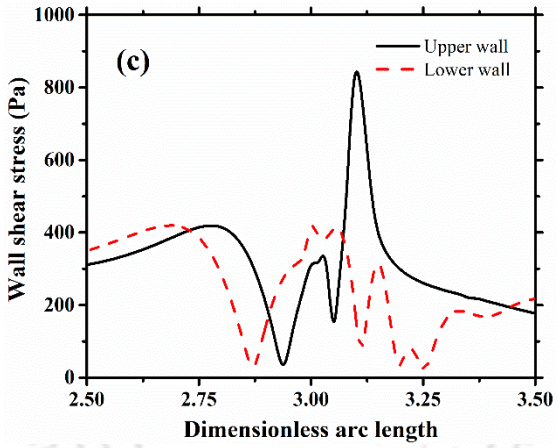

Figure 6.21 (a) Pressure (b) pressure gradient (c) wall shear stress at time instance t = 13 ms along the dimensionless arc length (ratio of length of polyline along walls to mother vessel width).

6.3.2.2 Effect of Bond number

In this section, the effect of Bond number (Bo) on the bubble shape and pressure gradient is discussed by varying Bo from 0.06 – 0.6 for Ca = 0.075 and Re = 2 for the base case geometry shown in Fig. 6.22. Figures 6.22 (a), (b), and (c) show the evolution of the bubble with time for Bo values of 0.06, 0.14, and 0.6, respectively. The presence of surfactants can change the value of surface tension and the value of the Bond number. Alternatively, a change in the value of acceleration due to gravity, which can occur due to the change in body position from vertical to horizontal (supine), can cause a change in the value of the Bond number. For all three values of *Bo*, the bubble does not bifurcate and enters the lower vessel. A minor difference among the three cases is that with an increase in the value of the Bond number, the fraction of the bubble protruding in the upper vessel before finally entering the lower vessel increases.

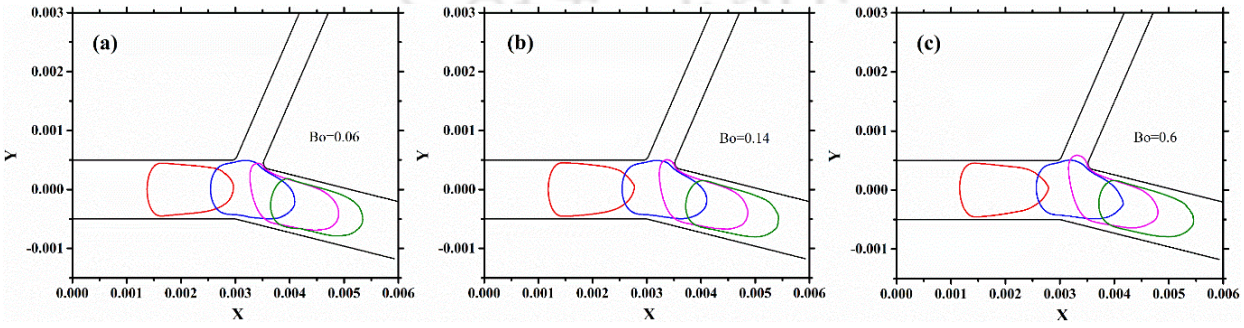

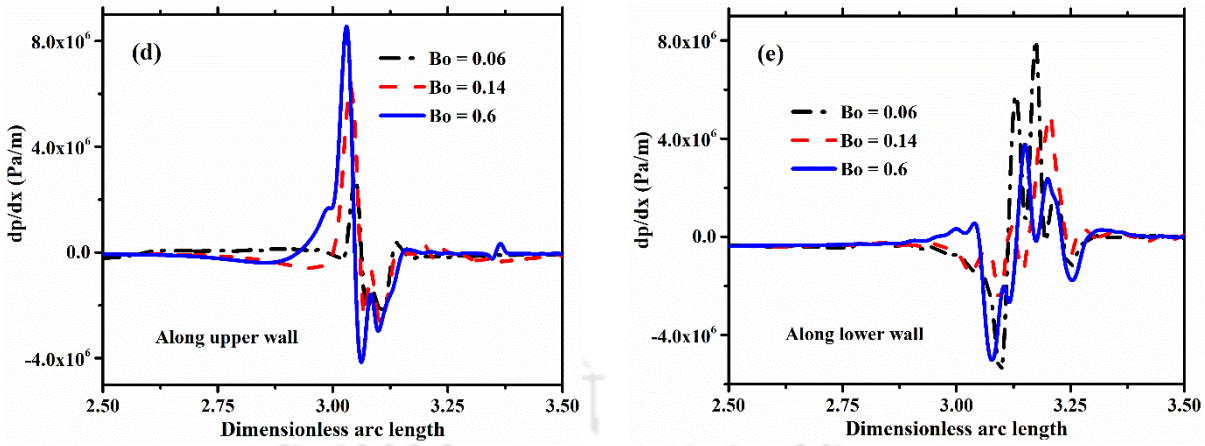

Figure 6.22. Bubble shape at various time instance for different bond number values (a) at Bo=0.06 (b) at Bo=0.14 (c) at Bo=0.6 and effect of Bond number (Bo) on pressure gradient for long bubble (l/d = 1.5) along (d) upper (e) lower daughter vessel wall at fix Ca = 0.075 and Re = 2 at time instant t_2 (blue bubble).

Figure 6.22 (d) and (e) show the pressure gradient on the inner walls of upper and lower daughter vessels when the bubble is at the bifurcation, respectively, for the three values of *Bo*. As observed for the base case, the large changes in the pressure gradient occur near the bubble. As the value of Bo increases, the maximum value of pressure gradient in the upper daughter airway also increases. Whereas, with an increase in the value of *Bo*, the pressure gradient in the lower daughter vessel decreases. These results are in agreement with the literature, where they studied the bubble flows in symmetric airway bifurcation (Chen et al., 2014). The pressure gradient in the mother vessel is very low for all values of *Bo*. In the daughter vessel, the pressure gradient suddenly increases due to a change in curvature of vessel wall and the presence of the bubble between arc length 2.80-3.25. The hydrodynamic stress increases with a decrease in the vessel width (Yalcin et al., 2007). In the present study, the pressure gradient in the upper daughter vessel is larger than lower daughter vessel even at low Bo.

6.3.2.3 Effect of capillary number and bubble size

Capillary number (Ca) is the ratio of viscous and surface tension forces and plays an important role in determining the hydrodynamics of bubble flow in straight (Aussillous and Quere, 2000; Bilek et al., 2003; Bretherton, 1961; Yalcin et al., 2007), and bifurcating vessels (Chen et al., 2014; Munir and Xu, 2020; Qamar et al., 2017). The effect of surface tension on pressure gradient along

the airway walls for three values of Ca (Ca = 0.00075, 0.0075, 0.075) for *Bo* = 0.14 and *Re* = 2 for two different bubbles having an aspect ratio of 1.5 and 0.9 have been analyzed.

Figure 6.23 shows the pressure gradient for the longer bubble (l/d = 1.5 in the mother vessel) for the three cases. The pressure gradient is shown on all three walls of the geometry. The nomenclature of the three walls is shown in Fig. 6.23(d). The film thickness (δ) between the bubble and channel wall decreases with a decrease in the value of *Ca* (Bretherton, 1961). The pressure inside the bubble is relatively uniform. The curvature of the bubble changes from the rear to the middle, becomes constant in the middle, and then again changes from the middle to the front or nose of the bubble. As a result, the gradient of the pressure in the liquid film changes from the rear of the bubble to the front of the bubble, as shown in Fig. 6.23 for the longer bubble.

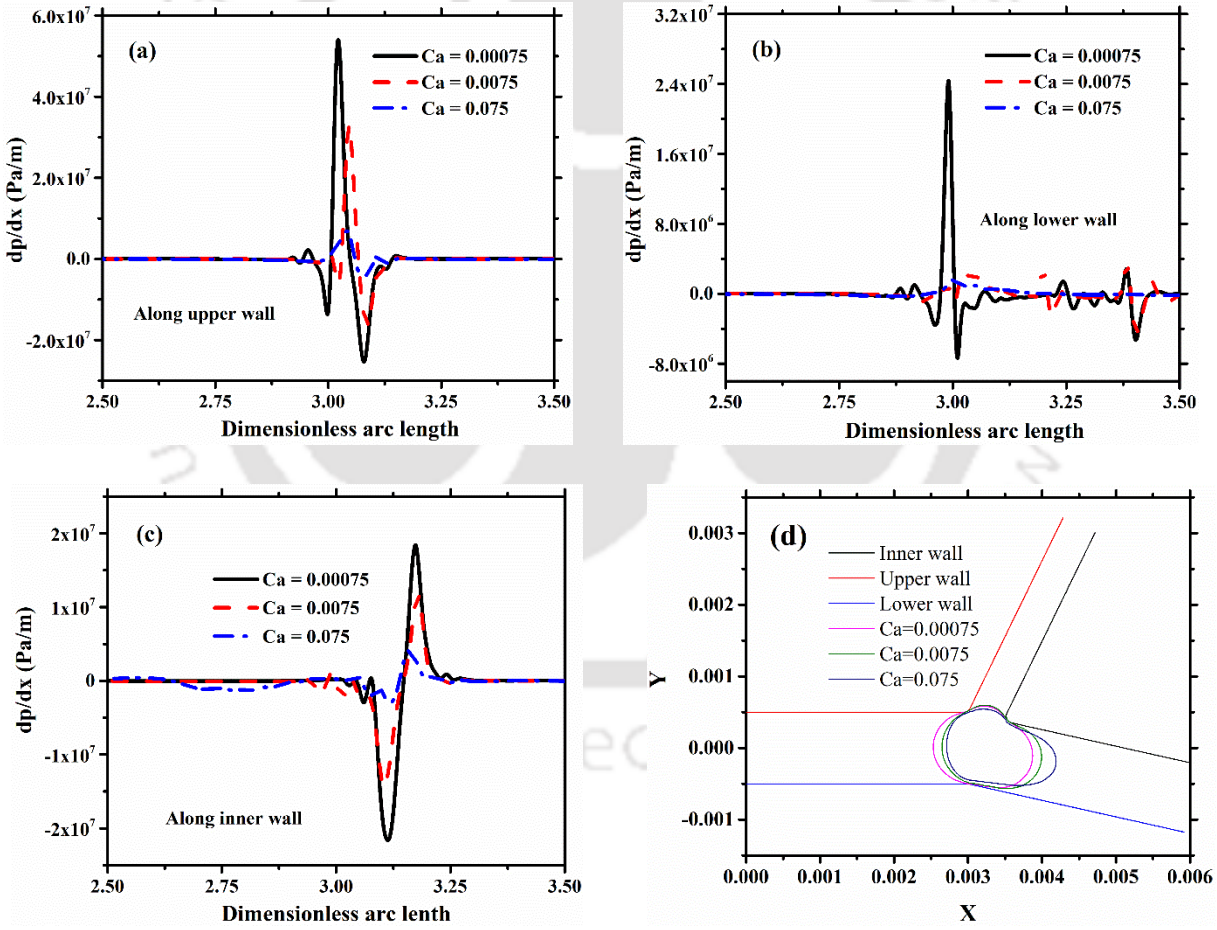

Figure 6.23. Effect of capillary number (Ca) on pressure gradient for long bubble (l/d = 1.5) along (a) Upper (b) lower (c) inner daughter vessel wall at fix Bo = 0.14 and Re = 2 when bubble is at bifurcation (d) variation of bubble shape for various Ca values at bifurcation junction.

The liquid film surrounding the bubble, as well as the bubble shape and its curvature, depends on the capillary number. Therefore, the pressure gradient also changes with the capillary number. The value of maximum and minimum (negative) pressure gradient on all the walls is observed to increase with a decrease in capillary number. This can be correlated with the thickness of the liquid film surrounding the bubble, whereby the thinner the liquid film, the higher the pressure gradient. The value of the pressure gradient within the upper daughter vessel (Fig. 6.23a) is higher than that within the lower daughter vessel (Fig. 6.23b). The reason behind this is that the hydrodynamic stresses are inversely proportional to airway radius (Gefen, 2010; Yalcin et al., 2007). The pressure gradients along the inner wall are comparatively lower than those along the upper walls, as shown in Fig. 6.23(c).

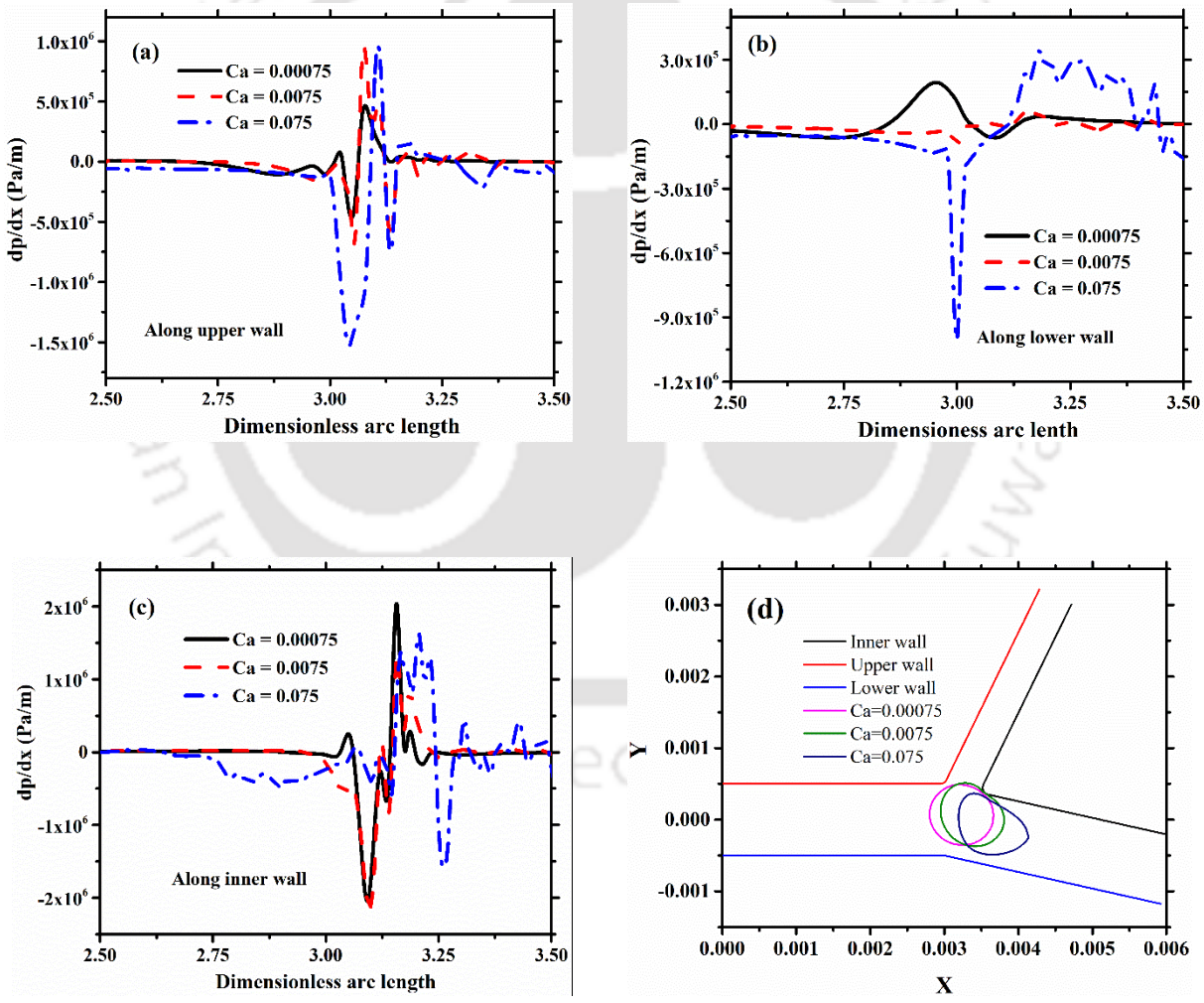

Figure 6.24. Effect of capillary number (Ca) on pressure gradient for short bubble (l/d = 0.9) along (a) Upper (b) lower (c) inner daughter vessel wall at fix Bo = 0.14 and Re = 2 when bubble is at bifurcation (d) variation of bubble shape for various Ca values at bifurcation junction.

Figure 6.24 shows the pressure gradient at various capillary numbers for the short bubble (l/d = 0.9 in the mother vessel). The shape of the bubble for three capillary numbers is also plotted in Fig. 6.24(d). For the lowest value of capillary number (Ca = 0.00075), surface tension is highest, and consequently, the bubble is observed to be spherical in shape. With an increase in the value of the capillary number, the bubble elongates and deviates from the spherical shape. Further, the effect of buoyancy is clearly observed on the location of a bubble for all three values of capillary numbers. The bubble is located slightly upward for all three cases. The values of the pressure gradient for the larger bubble are higher than those for the smaller bubble.

The maximum values of pressure gradient for smaller bubbles are significantly lower compared with that for the large bubbles along the three walls. Due to the small bubble size, the film thickness is much higher, which leads to lower pressure gradients along walls. However, the pressure gradients are higher for larger Ca along the upper (Fig. 6.24a) and lower walls (Fig. 6.24b) due to the negligible effect of surface tension on the vessel wall. The pressure gradient for the smaller bubble is highest along the inner wall (specifically at the bifurcation point), where the bubble squeezes due to obstruction by the bifurcation point and inertia of fluid. The film thickness becomes very less, and smaller Ca gives larger pressure gradients at the bifurcation point, as shown in Fig. 6.24(c).

6.3.2.4 Non-Newtonian Liquid

Airway mucus is a complex fluid. In the past studies the mucus has been numerically modeled using various non-Newtonian models such as the Bingham model (Mauroy et al., 2011; Zamankhan et al., 2018, 2012), Carreau model (Chatelin et al., 2017; Picchi et al., 2017), and power-law model (Cone, 2009; Dailey and Ghadiali, 2010; Paz et al., 2019, 2017; Rajendran and Banerjee, 2020; Ren et al., 2020). The mucus has been represented as a shear-thinning fluid for healthy and pulmonary disease patients at various physiological shear rates (Cone, 2009; Paz et al., 2019, 2017). In the present study, mucus is modeled as a non-Newtonian fluid using a power-law model, which follows a shear-thinning behavior. In shear-thinning fluid, viscosity is a function of shear rate and can be written as follow:

$$\mu(\dot{\gamma}) = k\dot{\gamma}^{n-1} \tag{6.15}$$

However, the value of apparent viscosity is limited between a certain range, and in the simulations, the minimum and maximum values of apparent viscosity are 0.001 and 0.047 Pa.s, respectively. *k* and *n* represent flow consistency and flow behavior index, respectively. The *k* and *n* have values of 5.2 and 0.15, respectively.

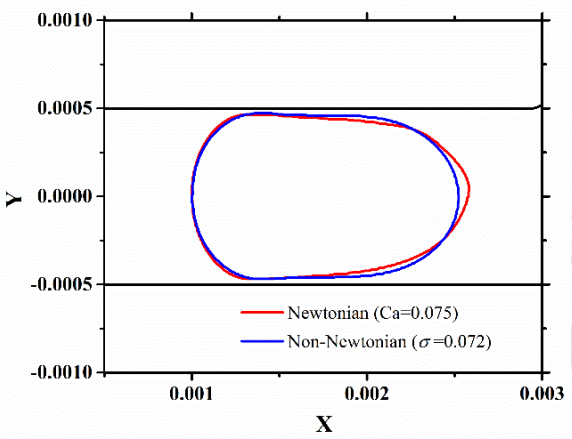

Figure 6.25. Comparison of bubble shape (l/d=1.5) in Newtonian and non-Newtonian liquid at the end of the mother vessel. The Y denotes a radial distance across vessel width.

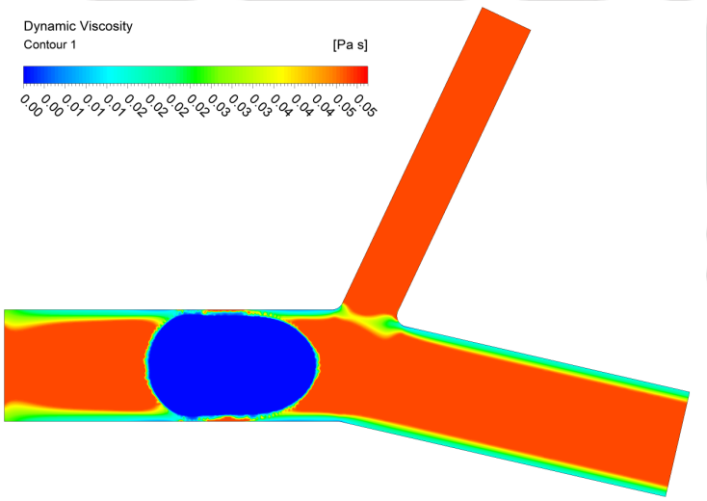

Figure 6.26. The viscosity variation for the shear-thinning fluid for surface tension value of 0.072 N/m and two-phase velocity of 0.1 m/s.

Figure 6.25 shows the comparison of the bubble shape in a Newtonian and a shear-thinning fluid when the bubbles are in the mother vessel. The capillary number for the Newtonian fluid is 0.075. For the non-Newtonian fluid, the (apparent) viscosity is not a constant. Figure 6.26 shows the

variation of viscosity for the shear-thinning fluid when the bubble is in the mother vessel. The viscosity of the liquid varies between 0.01 and 0.05 Pa.s. The liquid velocity at the inlet is 0.1 m/s, and therefore, the capillary number for the non-Newtonian fluid varies between 0.014 and 0.070, and the comparison between the two cases is qualitative. In the mother vessel and the lower daughter vessel, the viscosity is observed to be lower on the wall and higher in the center. It may be noted here that the shear rate is higher near the wall and decreases towards the center. For a shear-thinning fluid, the viscosity decreases with an increase in shear rate. The shear rate in the constant film thickness region surrounding a bubble is negligible. That is the reason the viscosity value to be high in this region. Figure 6.27 shows the pressure gradient along the upper, lower, and inner airway daughter walls for non-Newtonian and Newtonian fluids.

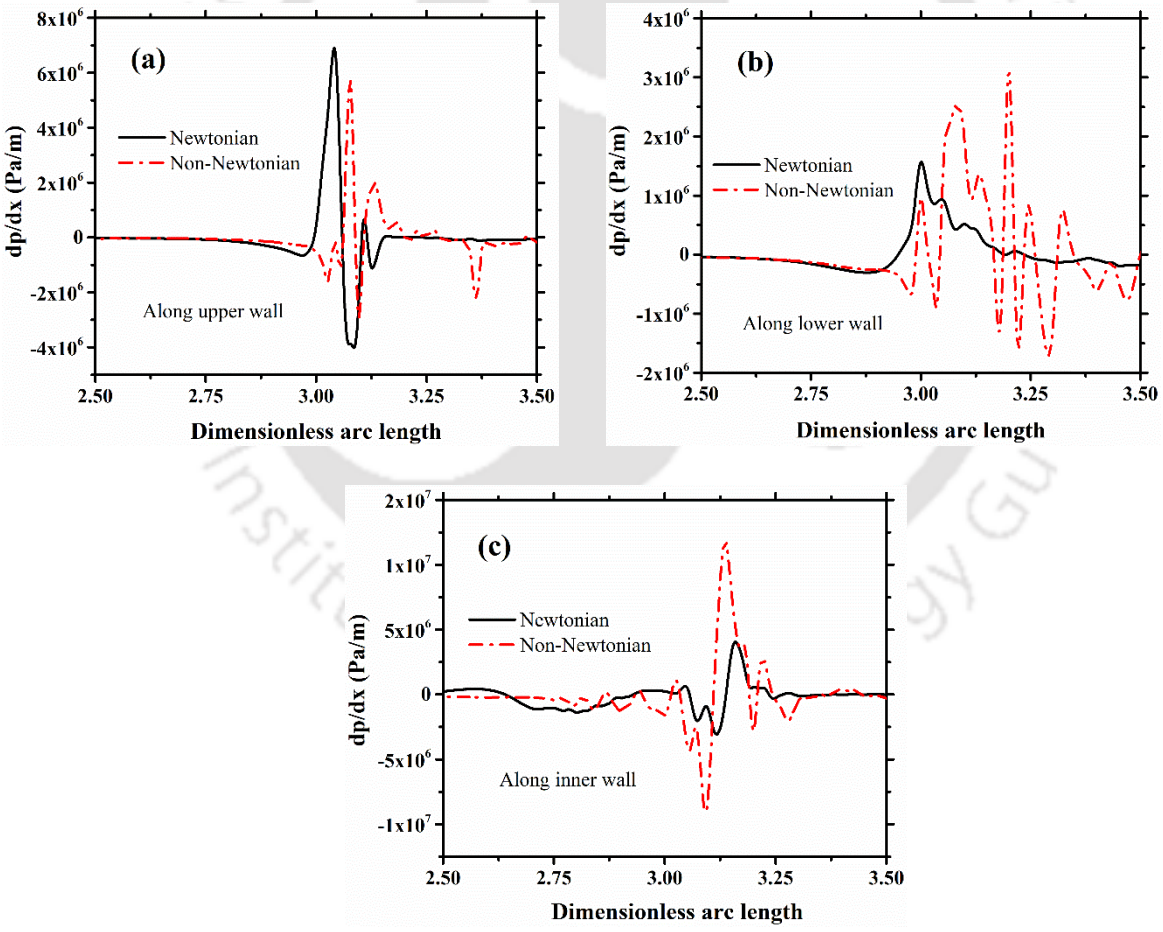

Figure 6.27. Comparison of Newtonian and non-Newtonian fluid on pressure gradient for long bubble (l/d = 1.5) along (a) upper (b) lower (c) inner daughter vessel walls.

6.3.2.5 Effect of geometric parameters

Figure 6.28 shows the comparison of bubble shapes at the bifurcation point for two different airway bifurcation geometries for long and short bubbles for Ca = 0.075 and Bo = 0.14 and 1.4. One (a) follows Murray's law, and the other (b) does not. It may be recalled the simulations in the previous sections are performed in geometry (a). The ratio of mother to daughter vessel size is smaller in geometry (a), whereas it is larger in geometry (b). As a result, the length of the bubble in the daughter vessel is more in geometry (b).

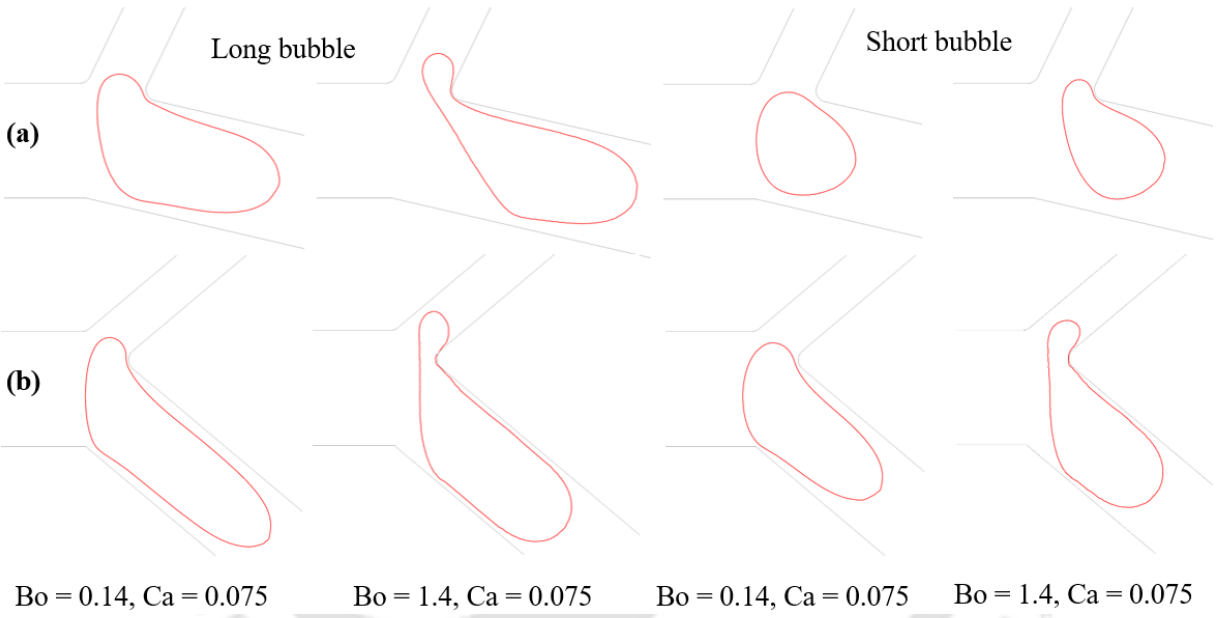

Figure 6.28. Comparison of long (l/d = 1.5) and short (l/d = 0.9) bubble shape at various Bond number values with fixed Ca = 0.075 (a) following Murray's dimensions for width of daughter vessels and bifurcation angle (b) without Murray's dimensions.

A longer bubble pulls more volume of bubble into upper daughter airway as compared to that in a short bubble. The volume of pulled bubble into upper daughter airways increases with Bo number due to an increase in the buoyancy force for both cases. The upper daughter vessel has more resistance to flow as compared to that of the lower daughter vessel due to more curvature and smaller vessel width. At the same time, the non-Murray's bifurcation (Fig. 6.28b) pushes more volume of bubble into the upper daughter airway vessel as compared to that in Murray's dimension (Fig. 6.28a). The pushed bubble and its larger volume cause hydrodynamic stresses on the airway

walls. The hydrodynamic stresses caused due to bubbles in the asymmetric airway bifurcation following Murray's law need to be addressed, which have been discussed further.

Figure 6.29 shows the pressure gradient along the upper and lower wall of vessels for the two geometries. The maximum value of pressure gradient is much higher in geometry (b) as compared with that in geometry (a). The resistance to flow in the daughter vessels is lower in geometry (a) as the size of the daughter vessels is bigger than in geometry (b). The value of dp/dx is also higher in geometry (b). The geometries in the airway follow Murray's law, and the change in the vessel widths is relatively gradual as considered in geometry (a).

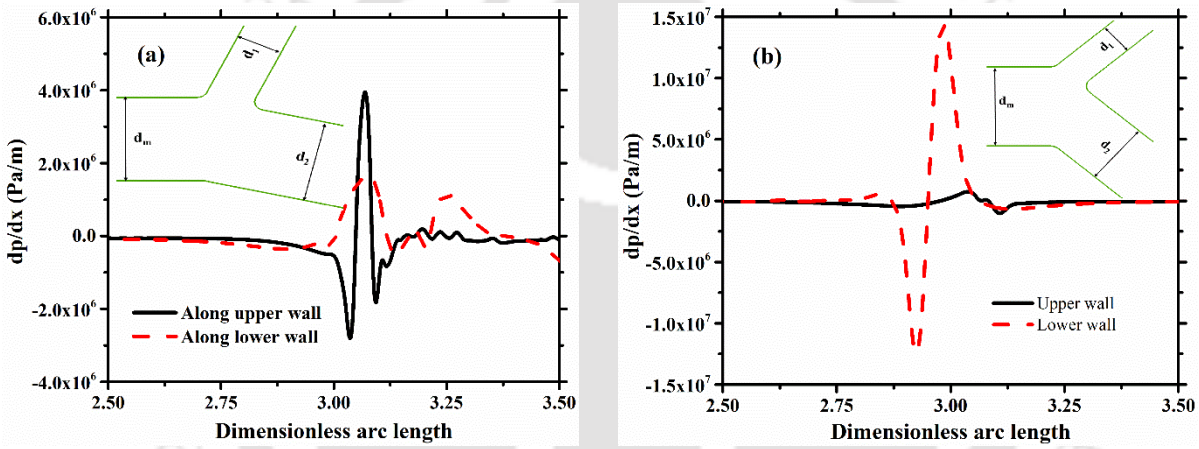

Figure 6.29. Pressure gradient along upper & lower walls at Bo = 0.14 and Ca = 0.075 for (a) Murray's dimensions (b) without Murray's dimensions using long bubble (l/d = 1.5).

There is a significant difference in the flow physics in geometry (a) and (b). Therefore, choosing the correct representation of the geometry is important when investigating the flow behavior in airways bifurcations. In this study, flow in planar two-dimensional bifurcations has been modeled. While this study gives a qualitative idea regarding the bubble flow at bifurcations, three-dimensional simulations are required in order to consider both the principal curvatures of the bubble.

6.4 Conclusions

In this chapter, two-dimensional numerical simulations of bubble dynamics in symmetric and asymmetric bifurcating vessel are performed for varying bifurcation angles. Simulations are

performed using blood and PFC as the gas and liquid phases, respectively. The effect of bifurcation angle on the bubble splitting dynamics is investigated.

- Depending of the bifurcation angles and capillary number, splitting and non-splitting behavior is observed.
- At a symmetric bifurcation, the bubble splits symmetrically at a higher value of the capillary number (Ca = 0.0231), where viscous force dominates over the surface tension force at a symmetric bifurcation.
- At the lower bifurcation angles ($\alpha = \beta < 60°$) and at the lower capillary number (Ca = 0.00231), splitting behavior is observed. But, for a higher bifurcation angle ($\alpha = \beta = 60°$), and lower capillary number (Ca = 0.00231) bubble does not split and goes into a lower daughter vessel.
- In asymmetric bifurcation angle case, at higher flow rates (Re=100) values, bubble splits almost symmetrically despite the asymmetry in the geometry. Whereas, at lower flow rates (Re=10) bubble does not split and goes into the lower daughter vessel for all asymmetric cases.

Further, the dynamics of the bubble in a planar, two-dimensional, asymmetric bifurcation is studied computationally for different values of Bond and capillary numbers in order to understand the effect of these parameters on wall shear stress.

- The bubble does not break up at the bifurcation for the parameters studied and goes into the lower daughter vessel. The stresses, both normal and shear and their gradients are observed to be high in the vicinity of the bubble.
- The pressure gradient, a parameter correlated with the cell damage, is observed to be the highest at the bifurcation. The pressure gradient is observed to increase with a decrease in capillary number.
- The bubble dynamics in the shear-thinning liquid is also studied. The apparent viscosity of the shear-thinning liquid is observed to be higher in the middle constant film thickness region of the bubble and is higher at the bubble ends.

Chapter 7 Experimental Investigations on the Bubble Dynamics in a Bifurcating Vessel

In this chapter, the dynamics of bubbles moving in a continuous liquid phase in a bifurcating channel are studied experimentally using flow visualization for three different Newtonian fluids. The effect of liquid flow rate and viscosity on bubble splitting is investigated.

7.1 Introduction

The flow of bubbles and droplets in confined geometries is a common phenomenon that occurs in a wide range of applications such as microfluidics (Anna, 2016; Link et al., 2004; Squires and Quake, 2005; Whitesides, 2006), medicine (Bull, 2005; Feng et al., 2018; Li et al., 2021) and food and cosmetics (Arzhavitina and Steckel, 2010; Eisner et al., 2005) amongst others. The flow of bubbles in microchannels may involve bubble formation (Du et al., 2016; Gupta et al., 2009), rupture (Sun et al., 2018; Wang et al., 2017), and coalescence (Khadiya et al., 2021; Liu et al., 2016). Various geometrical configurations have been employed to generate and split the bubbles, for example, T-shaped bifurcations (Fu et al., 2011; Garstecki et al., 2006; Link et al., 2004; Sun et al., 2018), Y-shaped bifurcations (Baroud et al., 2006; Manga, 1996; Wang et al., 2018), and combinations of both the configurations. The bubble splitting in the Y-shaped channel has an important role in a number of applications. In microfluidics, it is used to control the bubble size and occurrence of different splitting regimes during splitting. In medicine, an understanding of the transport of gas emboli in arterial bifurcations is necessary to avoid catastrophic bioeffects (Li et al., 2021). In gas embolotherapy, a potential cancer treatment, understanding of the bubble splitting at a bifurcation plays a key role for the effective treatment (Bull, 2005; Qamar et al., 2017). During surfactant therapy for acute respiratory distress syndrome (ARDS), understanding the splitting of the bubble at a bifurcation is important to devise better treatment strategies (Grotberg, 1994; Romanò et al., 2019; Zheng et al., 2006).

The bubble can be used as a drug carrier in a complex arterial network. Air embolism occurs due to intravascular bubbles that occlude the blood supply, which causes starvation of body organs. A recent study analyzed the lodging of bubbles in-vivo and in-vitro and found that lodging takes place due to clot formation at the tail of the bubble, which reduces the lubrication film surrounding the bubble. Reduction in the lubricating film increases the friction and leads to bubble lodging (Li

et al., 2021). Contrast, gas bubbles can be used as a treatment strategy called gas embolotherapy to starve cancerous tumors. The understanding of bubble splitting dynamics at a bifurcation is necessary for effective treatment using gas embolotherapy. The bubble splitting behavior depends on gravity, surface tension, and inertia (Chen et al., 2014; Eshpuniyani et al., 2005).

Bubble transport in straight capillaries has been widely studied, and relationships between film thickness as a function of capillary number has been developed (Aussillous and Quere, 2000; Bretherton, 1961; Klaseboer et al., 2014). In the literature, the bubble splitting and mechanisms responsible for the splitting have been studied numerically and experimentally in T-shaped bifurcations (Fu et al., 2011; Sun et al., 2019, 2018). The transition between splitting and the non-splitting mechanisms has been studied by varying the capillary number from 0.001 to 0.01. A power-law relationship between bubble neck thickness and the capillary number has been proposed (Fu et al., 2011). In a recent study of droplet splitting at a T junction, four different stages during the droplet splitting are identified: squeezing, transition, pinch-off, and thread rupture (Sun et al., 2018). Again, a power-law relationship is observed between droplet neck thickness and time during the squeezing regime. Similarly, several literature studies are available on the droplet or bubble splitting at a Y-shaped bifurcation. A droplet at a Y-shaped bifurcation is observed to show splitting as well as non-splitting behavior, and the occurrence of a particular behavior depends on the initial droplet length in the mother vessel and capillary number (Carlson et al., 2010). In a recent work on bubble splitting in a symmetric Y-shaped bifurcation, the authors identified three flow regimes: homogenous splitting, nonhomogeneous splitting, and non-splitting (Qamar et al., 2017).

In a recent experimental study, the droplet dynamics in an asymmetric bifurcation has been studied, and splitting ratio is observed to depend on the initial droplet length and droplet velocity (Wang et al., 2018). Furthermore, micro-particle image velocimetry was used to understand the splitting and non-splitting regimes using velocity vectors in the droplets (Wang et al., 2019). They proposed a critical neck thickness which determines the possibility of splitting and non-splitting regimes. The neck thickness varies with time during splitting by following a power-law during the squeezing stage, a linear relation during the transition stage, and an exponential decrease during the pinch-off stage (Ma et al., 2021). Fei et al. (2021) studied the effect of adding nanoparticles on the bubble dynamics. The nanoparticle addition had a negligible effect during squeezing but

extended the transition stage and accelerated the pinch-off stage (Fei et al., 2021). The addition of nanoparticles shows a rigid surface of the bubble and leads to a decrease in bubble tip curvature compared to conventional bubbles.

In summary, there are a number of studies on droplet splitting and droplet neck dynamics. However, there are only a few studies that investigate the bubble dynamics at a bifurcation. The primary difference between bubble and droplet splitting stems from the large difference in the viscosity of the two phases in the case of the bubble, and the nearly uniform pressure in the bubble when compared with that of a droplet. In some cases, the compressibility effect might also become important in the case of gas bubbles. In this chapter, the bubble dynamics in three Newtonian liquids of varying viscosities for various bubble lengths (l_b/d_m = 2-9) are investigated experimentally at a symmetric bifurcation. The effect of liquid flow rate at fixed gas flow rate on bubble size, splitting flow dynamics, and bubble neck dynamics is investigated.

7.2 Materials and methods

7.2.1 Fabrication of low-cost bifurcation model

A three-dimensional arterial model with mother vessel (d = *1mm)* and two daughter vessels (d_1 =d_2 = *0.78 mm*), as shown in Fig. 7.1(a), is used for experimental analysis of gas-liquid flow in the bifurcation. The value of the bifurcation angle is $\alpha = 90^{o}$. A schematic outlining the procedure of fabrication of the bifurcation models using low-cost 3D printing is shown in Fig. 7.1(b). A 3D solid CAD model (.stl file) of arterial bifurcation is prepared. The solid model is printed using a 3D printer (Ultimaker 3, Geldermalsen, Netherlands) with polylactic acid (PLA) as the filament material. The PDMS (1:10 ratio of reagent and base) is poured over the 3D printed model in a petri dish. The poured PDMS model is kept in a vacuum degasser for removing any small bubbles. Post degassing, the liquid PDMS-filled bifurcation model is kept for 24 hours to cure the PDMS at room temperature. The cured PDMS model is kept in dichloromethane (DCM) solution for around 1 hour in order to dissolve the PLA material. After complete degradation of PLA in DCM, the 3D printed model is replicated in the transparent PDMS slice.

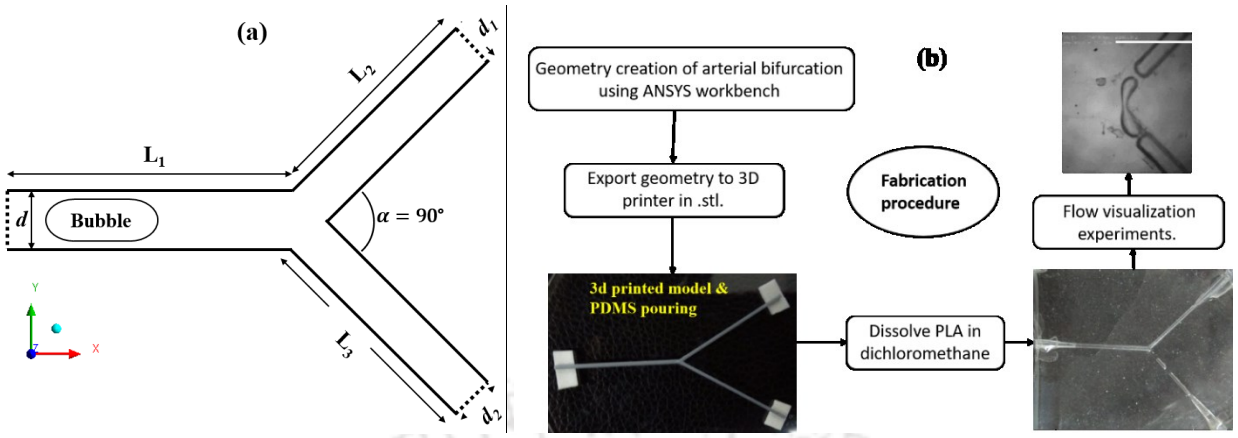

Figure 7.1. (a) Schematic of the bifurcation geometry where: d = 1 mm; d_1, d_2 = *0.78 mm;* L_1, L_2, L_3 = *5d;* α is the angle between daughter vessels (b) schematic diagram of fabrication of bifurcation models using 3D printing and PDMS curing.

7.2.2 Experimental setup

The schematic of the experimental setup is shown in Fig. 7.2. It consists of two syringe pumps (Hallmark, SPLF2, USA and New era pumps, NE-300, USA) to supply gas and liquid to the inlet of the test section at the desired flow rates. Bubbles are generated using a T junction (1 mm diameter) by varying the liquid flow rates, as shown in Fig. 7.2. The inside diameter of each syringe is 29.2 mm. Each syringe is connected to the bifurcation model using silicon tubing of diameter 1 mm. A high-speed camera is used to capture the splitting process of the bubble. The frame rate of the camera (Phantom; VEO 640, USA) is set to 2000 fps during experiments. A LED light source is used to illuminate the bifurcating channel. Images are recorded after the flow reaches a steady state. The images are analyzed using ImageJ (NIH, USA). All the experiments are carried out at room temperature and pressure.

7.2.3 Experimental conditions and material properties

In the present study, three different Newtonian liquids are used. The Newtonian liquids are deionized water, 50 wt. % ethylene glycol (EG), and 100 wt. % ethylene glycol (EG). The viscosities of these fluids are measured using a rheometer (Anton Paar, MCR 301, Austria), and surface tension is measured using a tensiometer (Kyowa, DY-300, Japan). The measured physical and flow parameters for the continuous phase are summarized in Table 7.1.

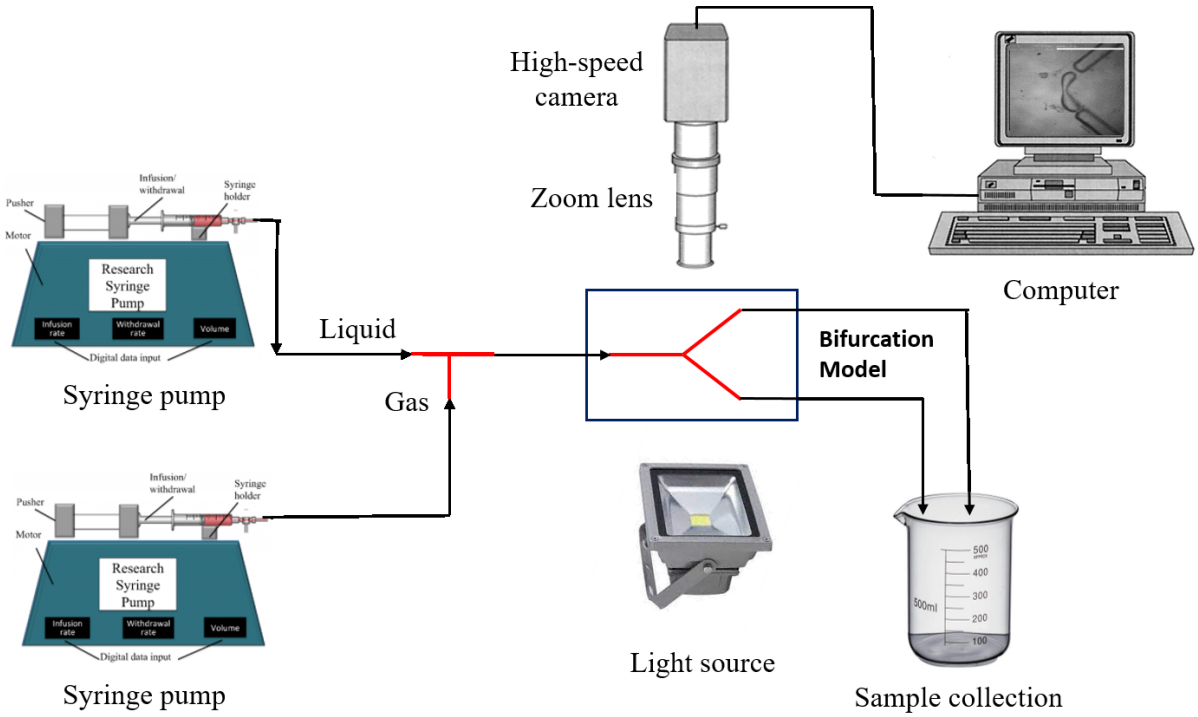

Figure 7.2. Schematic diagram of the experimental setup.

Table 7.1. Physical parameters of experimental solutions for a Newtonian fluid

Fluids	Density ρ (kg/m^3)	Surface tension σ (N/m)	Dynamic viscosity μ (Pa. s)
Water	998.2	0.0726	0.001
50 % EG	1055.0	0.0571	0.004
100% EG	1112.0	0.0462	0.016

7.3 Results and discussion

The experiments are performed using three different Newtonian liquids as the continuous phase and nitrogen as the gas phase. While the gas flow rate is constant (2 ml/min) in all the experiments, the liquid flow rate is varied from 0.4-4 ml/min, as outlined in Table 7.2. This allows the capillary number to vary in the range 0.0002-0.044, whilst the Reynolds number varies from 3.5 to 127 in

the experiments. It may be noted that the Reynolds and capillary numbers are defined with mixture velocity, the sum of gas and liquid flow rates per unit cross-sectional area, as the velocity scale.

Table 7.2 Flow parameters of experimental solutions for Newtonian fluid

Q_G (ml/min)	Q_L (ml/min)	Re (water)	Re (50% EG)	Re EG	Ca (water)	Ca (50% EG)	Ca EG
2	4.00	127	33.5	7.9	0.0012	0.0062	0.044
2	2.00	85	22.4	5.3	0.0005	0.0027	0.029
2	1.00	64	16.9	4.0	0.0004	0.0018	0.022
2	0.67	56	14.8	3.5	0.0002	0.0010	0.019

7.3.1 Bubble generation

Bubble generation occurs at a T-junction. With the change in the liquid flow rate, the length of the bubble in the mother vessel is observed to vary. Figure 7.3 shows the variation of bubble length with gas to liquid flow rate ratio for the three liquids.

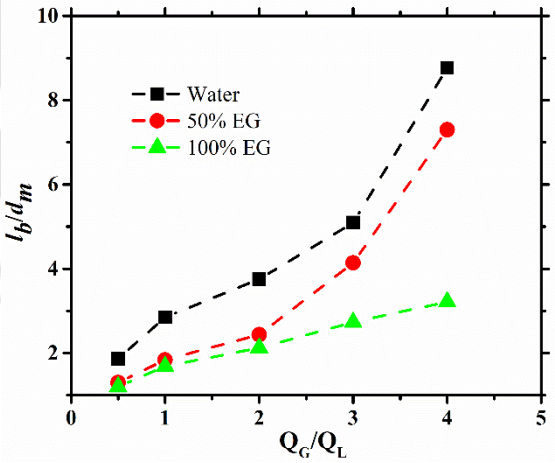

Figure 7.3. Variation of bubble lengths with the ratio of gas-liquid flow rates.

In all the cases, bubble size increases with an increase in the gas to liquid flow rate ratio. The bubble length follows a linear relation with the ratio of gas-liquid flow rates. At a particular flow rate ratio, the bubble length is observed to increase with a decrease in the viscosity of the

continuous phase. The comparison of water with EG illustrated that bubble length in EG is smaller than that of water at the same flow condition.

7.3.2 Bubble behavior at the bifurcation

As the bubble approaches the vessel bifurcation, both non-splitting and splitting regimes are observed in the experiments.

Non-splitting: As the name suggests, the bubble does not split at the bifurcation and passes into one of the daughter vessels. As the bubble enters into the bifurcation, the cross-sectional vessel area increases, and this allows the bubble to grow in the lateral direction. While it reaches bifurcation, it squeezes due to the inertia of the continuous phase and takes a kidney bean like shape, as shown in Fig. 7.4(a). However, the bubble does not split due to opposing surface tension force and randomly enters into one of the daughter vessels. The non-splitting behavior may occur due to smaller bubble size and higher surface tension force.

Splitting: In this type of flow behavior, the bubble takes a kidney beans like shape initially. Then the bubble starts thinning at the bifurcation, and its radius at the neck-like structure starts decreasing with time under the squeezing pressure. This process can be termed as necking. Due to the necking, the bubble length increases, and it starts to obstruct the liquid flow in the two daughter vessels. This obstruction can be either complete or partial, as shown in Figs. 7.4(b) and 7.4(c), respectively. In the case of partial splitting, the liquid passes through a film between the bubble and wall of the daughter vessel. As the area available for the liquid flow is small, the liquid velocity increases in order to satisfy mass conservation. As a result, the interface of the gas bubble experiences high shearing. Whereas in case of complete obstruction, pressure builds up in the liquid upstream of the gas bubble, which eventually causes the bubble to split. Thus, the shearing caused by the liquid film and pressure build-up contributes to the bubble splitting.

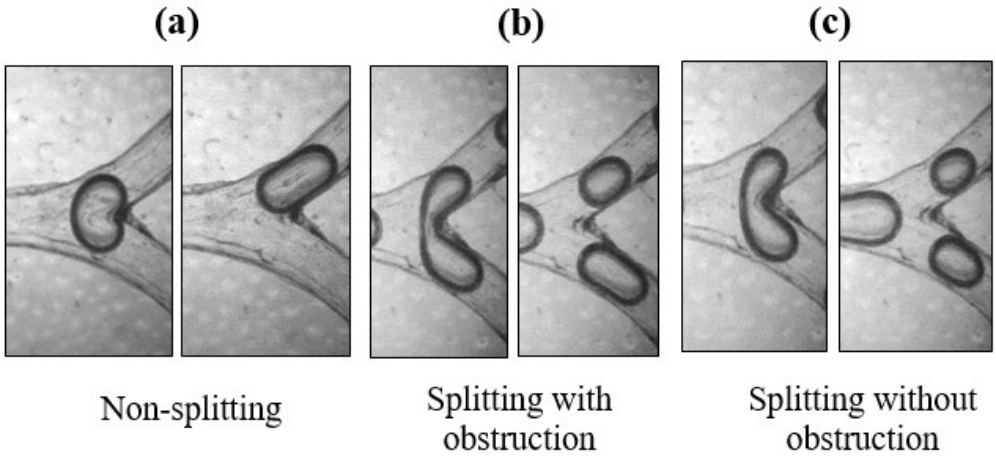

Figure 7.4. Various splitting regimes of air bubble in a bifurcating channel (a) Non-splitting (b) Splitting with partial obstruction (c) Splitting with permanent obstruction

The non-splitting behavior is observed for all cases of water. While splitting is observed for ethylene glycol solution except for the smaller bubbles. Figure 7.5 shows the snapshots of the non-splitting behavior at various time instants during the bubble flow at the bifurcation. It can be seen that a Taylor bubble shape is present in the mother vessel. While, once it reaches the bifurcation, the bubble tries to expand with the available area. After completely entering into the bifurcation the bubble head gets asymmetrically distributed into the two daughter vessels. The bubble does not break due to the dominance of surface tension force and gets pushed into one of the daughter vessels randomly, and a non-splitting regime is observed. In their study of droplet splitting in rectangular microchannels, Wang et al. (2018) identified a critical boundary for droplet break-up as $\frac{l_0}{w} = 0.5414Ca^{-0.21}$. They observed that the droplet break-up does not occur in cases when the capillary number or the bubble length is small. They suggested that the pressure build-up across the droplet, shearing caused by the viscous fluid cause the bubble deformation, whereas the interfacial tension opposes it. As the surface tension is high in the case of water, a neck region does not develop at all for the case shown in Fig. 7.5.

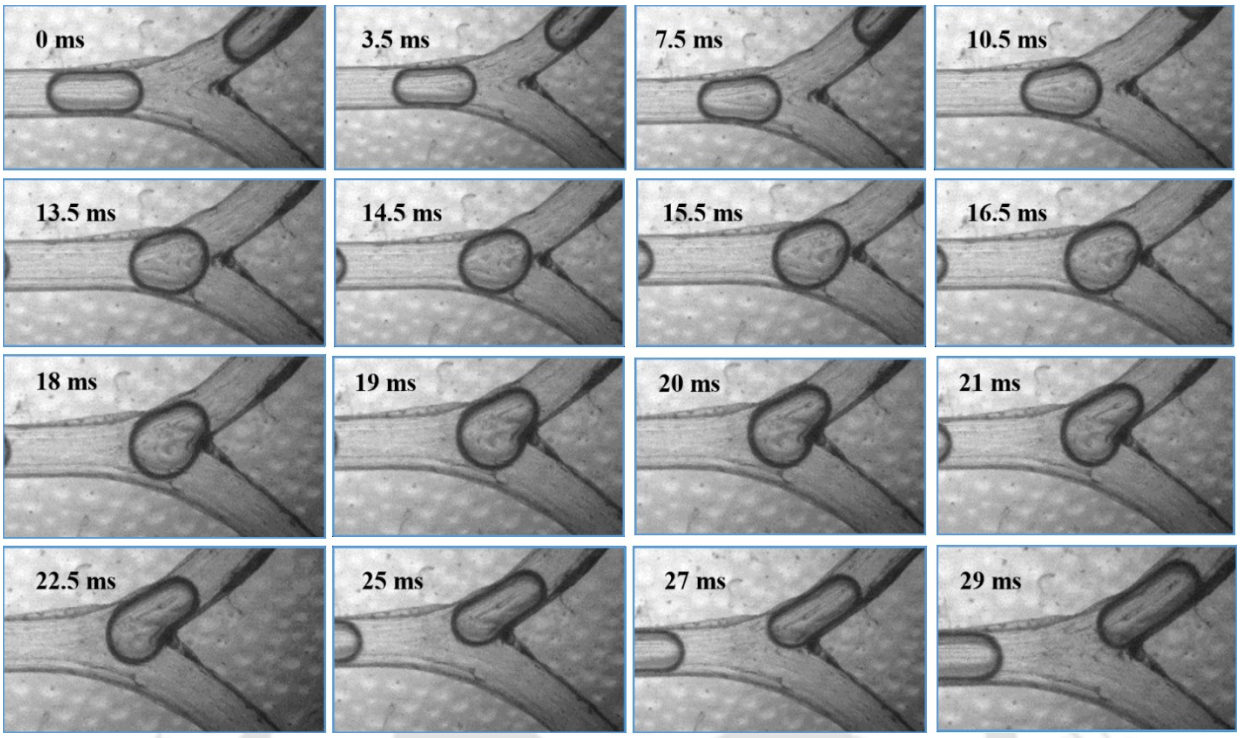

Figure 7.5. Variation of bubble shape for the non-spitting regime at various time instances during propagation in the bifurcation for air-water flow (Ca=0.0012, Re=127).

Figure 7.6 shows the snapshots for the splitting process during partial obstruction. Similar to the non-splitting regime, the radius of the bubble starts increasing as soon as it comes out of the mother vessel (0 ms). When the entire bubble is out of the mother vessel, it occupies almost the entire bifurcation region (7 ms). The bubble is now squeezed against the bifurcation point, and the necking process starts (16 ms). The radius of the neck keeps decreasing (16-32 ms), and the bubble breaks up into two daughter bubbles (34 ms). While the Laplace pressure ($\frac{\sigma}{R_1}+\frac{\sigma}{R_2}$) causes the bubble to assume a spherical or near-spherical shape, the inertia of the liquid (ρu^2) causes the squeezing of the neck region.

The splitting of the bubble can be divided into the following steps: squeezing (0-12 ms), transition (16-24 ms), and pinch-off (26-36 ms). During squeezing, the liquid phase acts to squeeze the bubble neck to thin it by allowing a very small amount of continuous phase from the film thickness. The neck thinning is the result of squeezing pressure force and viscous shear stress of the liquid phase. In contrast, the opposing surface tension force prevents the deformation of the bubble.

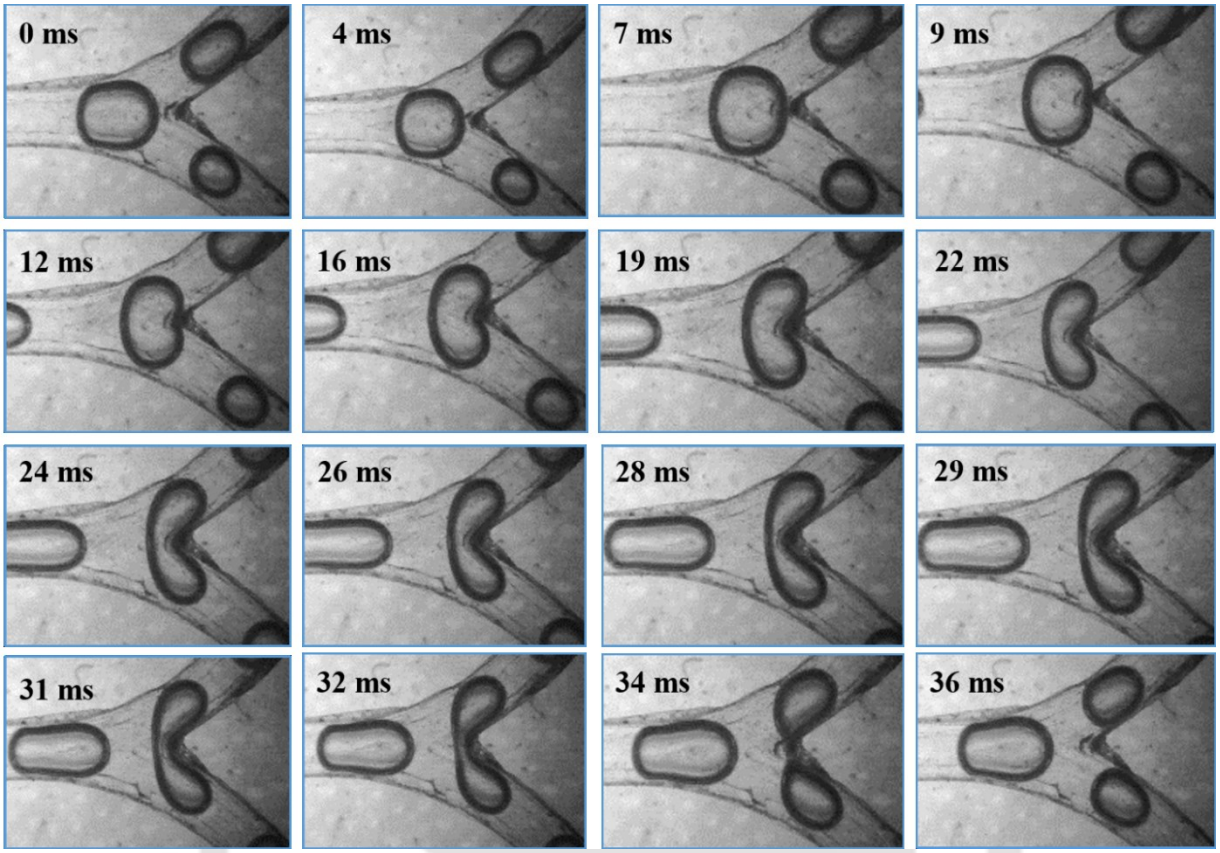

Figure 7.6. Variation of bubble shape for spitting regime at various time instances during propagation in the bifurcation for air-ethylene glycol (Ca=0.044, Re=7.9).

The transition stage observed similar behavior to the squeezing stage. During the transition stage, the thinning rate of the bubble slightly decreases with time. Similarly, a decrease in the neck thickness results in an increase in the gap between bubble head and channel wall. The curvature of the neck at the bifurcation increases, and the bubble leads to the pinch-off stage. The pinch-off stage is dominated by surface tension force. The curvature of the bubble neck starts to increase, and at a certain point the bubble splits under the action of inertial force. Carlson et al. (2010) and Wang et al. (2018) analyzed the neck rupture process using three-dimensional simulations and high-speed imaging experiments, respectively. They showed that beyond a critical value of neck thickness, the bubble gets pinched off. After the rupture of the bubble, the tail of the bubble recovers its curved shape due to surface tension force and travels into the respective daughter vessel.

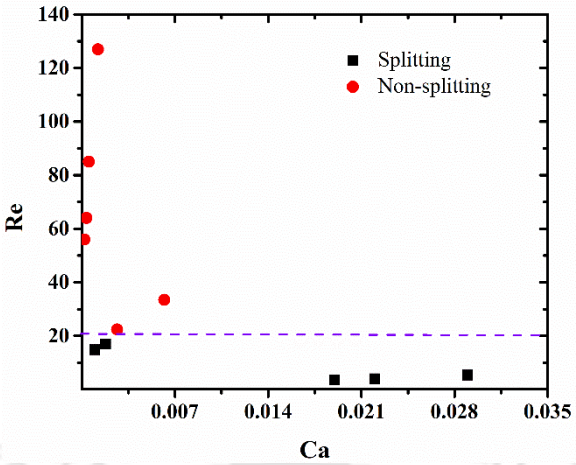

Figure 7.7. Splitting and non-splitting regime at various Re and Ca.

Bubble splitting and non-splitting depend on the relative importance of the surface tension force, inertial and viscous forces. The physical effects can be grouped in two non-dimensional parameters- Reynolds and capillary numbers. Fig. 7.7 shows the occurrences of splitting and non-splitting on a Ca-Re map. Two regimes can be identified. The bubble splits when the capillary number is greater than 0.001 and does not split when the capillary number is lower. The bubble dynamics is also observed to depend on bubble size and pressure driving the flow (Calderon et al., 2010; Eshpuniyani et al., 2005).

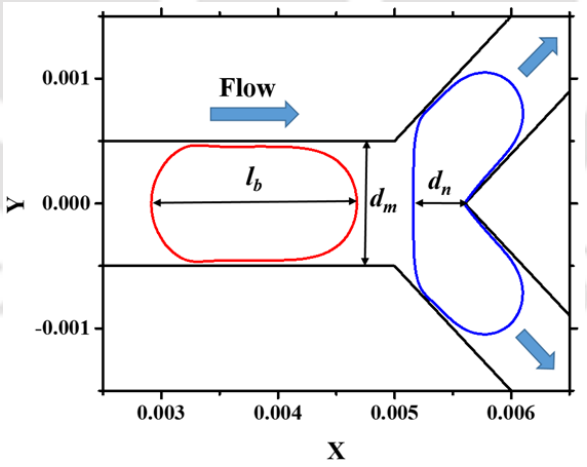

Figure 7.8. Definition of parameters during bubble splitting process in X and Y direction.

Figure 7.8 shows a schematic of a bubble in the mother vessel (red colour) and at the bifurcation (blue colour) and related nomenclature. d_m represents the diameter of the mother vessel, d_n is the bubble neck diameter, l_b is the length of the mother bubble, and $l_{b,d}$ is the length of daughter

bubbles. These parameters can be measured from images obtained by the high-speed camera. The uncertainties for the length of bubble and neck thickness is around ±2 pixels (0.05 mm).

Figure 7.9 (a) and (b) show the variation of the ratio between the length of daughter bubbles with the mother bubble as a function of Ca and Re, respectively. The difference in the lengths of the two daughter bubbles is much higher at low Ca values. A progression from lower to higher Ca values shows a transition from non-homogenous to homogenous splitting. It shows a transition from highly non-homogenous splitting to homogenous with an increase in Ca, and it is in agreement with the observation of (Calderón et al., 2005). However, the pattern is not very clear with the Reynolds number.

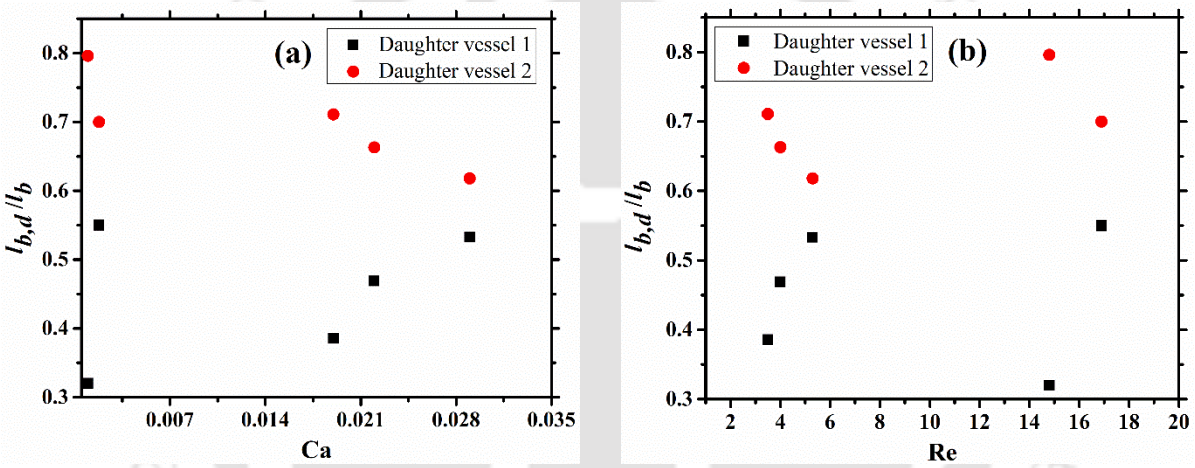

Figure 7.9 Dimensionless bubble length for various Ca and Re in both the daughter vessels.

The change in the neck diameter with time is also extracted from the images. Figure 7.10 shows the variation of the bubble dimension at the bifurcation during neck development and its thinning with time for three cases. It may be noted the term ‘neck’ should be used when the bubble diameter at the bifurcation is less than the bubble diameter elsewhere, which can typically be taken as the diameter of the mother vessel. In the case of red dots (Ca = 0.00098), neck development and neck thinning can be identified by the two lines of different slopes. The slopes change when the dimensionless neck thickness is ~1. A similar change in slope is also observed for the other two cases. During the neck thinning, the slope of the line i.e. rate of neck thinning, is almost the same for all three cases.

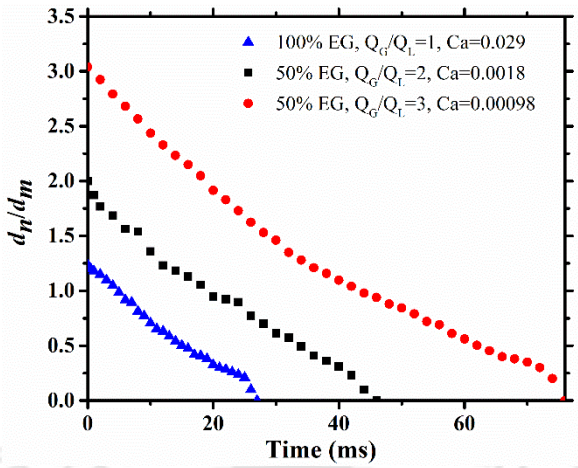

Figure 7.10. Evolution of bubble neck thickness over time at various gas/liquid flow rates and Ca.

Table 7.3. Splitting and non-splitting behavior at various gas and liquid flow rates.

Fluid	Q_G/Q_L	Breaking behavior
Water	0.5	Non-splitting
	1	Non-splitting
	2	Non-splitting
	3	Non-splitting
50% ethylene glycol	0.5	Non-splitting
	1	Non-splitting
	2	Splitting
	3	Splitting
Ethylene glycol	0.5	Non-splitting
	1	Splitting
	2	Splitting
	3	Splitting

7.3.3 Comparison with CFD

Two-dimensional CFD simulations are performed for $Q_G = Q_L = 2$ ml/min in order to compare the results in the two cases. The capillary number is 0.044, and the respective Re value is 7.9. The gas and liquid phases are nitrogen and ethylene glycol, respectively. The bubble shape and neck

thickness during the splitting process is compared with our experimental work, as shown in Fig. 7.11(a, b). While the bubble splits symmetrically in the CFD simulations, experimentally the size of the daughter bubbles can vary for different bubbles. This can be attributed to different factors such as downstream pressure in the two daughter vessels, geometric parameters such as channel roughness etc. The difference in the rate of neck thinning in CFD and experiments is because the CFD simulations are two-dimensional, whereas the bubble shape in the experiments is three-dimensional. As a result, the bubble curvature and surface tension are different in the two cases.

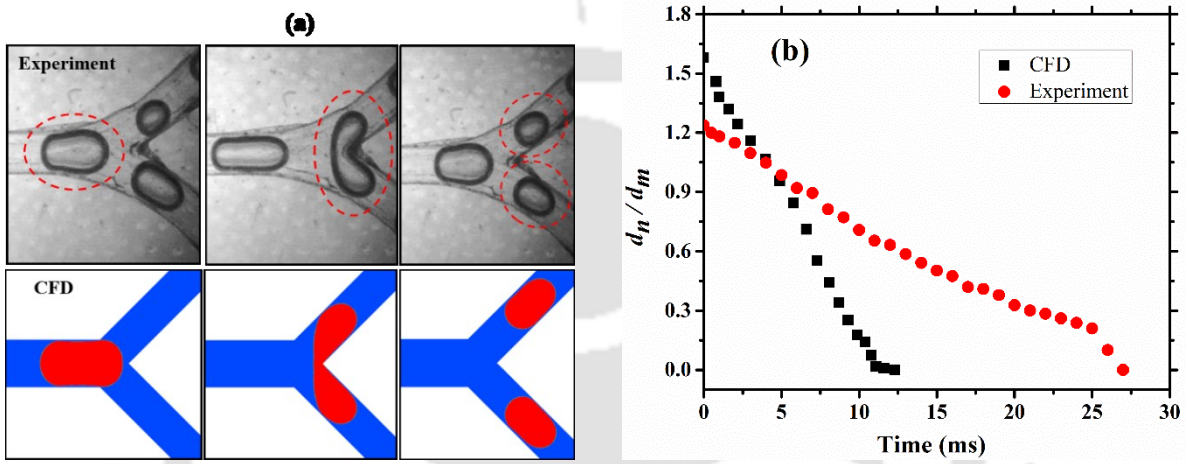

Figure 7.11. (a) Comparison of experimental and numerical results for (a) bubble splitting and (b) bubble neck thickness at $Q_G = Q_L = 2$ ml/min, Ca = 0.044, and Re = 7.9.

7.4 Conclusions

A bifurcating vessel using PDMS is developed employing a low-cost fabrication methodology. Flow visualization experiments are performed using three different liquids and nitrogen gas over a range of capillary (0.0002-0.044) and Reynolds numbers (3.5-127).

- The bubbles form at a T junction, and the length of the bubble increases with an increase in the ratio of gas to liquid flow rate for each fluid.
- Two regimes, splitting and non-splitting behavior is observed. Non-splitting behavior is observed at low capillary numbers and/or for shorter bubbles. Rate of neck thinning is observed to be constant.
- A comparison is made between the bubble splitting and neck thinning between the results obtained from experiments and planar, two-dimensional CFD simulations.

Chapter 8 Conclusions

8.1 Conclusions

In this thesis, the physics of laminar, single-phase liquid, and two-phase gas-liquid flow is studied in symmetric and asymmetric bifurcating vessels with a motivation for biomedical applications. The effect of geometric and flow parameters on flow behavior is investigated.

During single-phase flow at a bifurcation, while the flow distributes equally in the two daughter vessels in a symmetric bifurcation, the distribution is asymmetric in an asymmetric bifurcation and the flow rate is higher in the daughter vessel having a smaller bifurcation angle. When the flow is pulsatile, the flow distribution varies with time in a cardiac cycle in an asymmetric bifurcation.

The flow separates on the outer wall of the daughter vessel and a recirculation zone is observed at the outer wall of the daughter vessel near the bifurcation, and the wall shear stress is low on the outer wall. As the streamlines turn at the bifurcation, secondary flow is observed at the bifurcation, which gives rise to the helical motion of the fluid at the bifurcation. In an asymmetric bifurcation, WSS is observed to be lower on the lower angled wall near the bifurcation and higher away from the bifurcation. A comparison of the flow behavior by assuming the fluid to be Newtonian and shear-thinning suggests that the velocity field is similar during the systole in the two cases, whereas significant differences are observed when the shear rate is low e.g. during the period of diastole and in the flow separation region on the outer wall.

Time-dependent, three-dimensional CFD simulations are performed to model flow in an idealized carotid artery model. The simulations reveal the complex flow interaction between the separated flow caused by the bifurcation as well as flow expansion in the sinus. With an increase in the distance between the sinus and bifurcation point, an increase in backflow and reduction in the wall shear stress on the sinus wall is observed. An increase in carotid sinus size at a fixed location results in a reduction in asymmetric flow behavior in the sinus, and recirculation occurs near the outer as well as inner walls in bigger sinuses resulting in a decrease in WSS value on the sinus wall. Four different rheological models - Newtonian, Carreau, Herschel-Bulkley, and power law are used to model the rheology of blood. The flow behavior obtained from simulations shows no difference in flow pattern during peak systole and significant difference during diastole. The

difference is more prominent in the sinus region where the flow expands, and shear stress and rate of strain have low values.

Further, three-dimensional CFD simulations are performed to understand the effect of pulse rate variation in a patient-specific carotid artery bifurcation. The frequency of inlet velocity waveform has a noticeable effect on time-averaged wall shear stress (TAWSS), oscillatory shear index (OSI), and relative residence time (RRT) distribution on the bifurcation wall at a constant amplitude. Higher pulsatile frequency shows higher values of TAWSS and lower values of OSI and RRT. Lower pulsatile frequency waveform can be correlated with contributing factors for atherosclerosis initiation and progression. The higher secondary flow is observed at the bifurcation during the beginning of diastole. Similarly, higher values of vorticity and helicity are observed just after the carotid sinus.

Two-dimensional simulations of bubble dynamics in the symmetric and asymmetric bifurcating vessels are performed for varying bifurcation angles using blood and PFC are the liquid and gas phases, respectively. Depending on the bifurcation angle and capillary number, the splitting and non-splitting behavior of the bubble is observed. The bubble splits symmetrically at a symmetric bifurcation, at the higher value of the capillary number (Ca = 0.0231). At the lower bifurcation angles ($\alpha = \beta < 60°$) and at the lower capillary number (Ca = 0.00231) splitting behavior is observed. But, for a higher bifurcation angle ($\alpha = \beta = 60°$), and lower capillary number (Ca = 0.00231) the bubble does not split and goes into the lower daughter vessel. For the asymmetric bifurcation angle case, at higher capillary number the bubble splits almost symmetrically despite the asymmetry in the geometry. Whereas, at lower capillary number the bubble does not split and goes into the lower daughter vessel for all asymmetric cases.

Further, the dynamics of the bubble in a planar, two-dimensional, asymmetric bifurcation is studied computationally for different values of Bond and capillary numbers, in order to understand the effect of these parameters on wall shear stress using air and mucus as gas and liquid phases, respectively. For all the values of Bond and capillary number considered, the bubble does not split at the bifurcation and passes into the lower daughter vessel. The stresses, both normal and shear and their gradients are observed to be high in the vicinity of the bubble. The pressure gradient, a parameter correlated with the cell damage, is observed to be at its highest at the bifurcation. The pressure gradient is observed to increase with a decrease in capillary number. The bubble dynamics

in the shear-thinning liquid is also studied. The apparent viscosity of the shear-thinning liquid is observed to be higher in the middle constant film thickness region of the bubble and is higher at the bubble ends.

Further, an asymmetric bifurcating channel made of PDMS is fabricated using a 3D printed mold and flow visualization experiments are performed to understand the bubble dynamics in a symmetric bifurcation for three liquids of different viscosities. Gas and liquid phases are mixed at a T junction and the size of bubbles generated is observed to increase with an increase in the ratio of gas to liquid flow rate for each fluid specified in Table 7.1. Splitting with partial obstruction, splitting with complete obstruction, and non-splitting regimes have been observed. Non-splitting behavior is observed at low capillary numbers and/or for shorter bubbles. The rate of neck thinning is observed to be constant. A comparison is made between the bubble splitting and neck thinning for the results obtained from experimental measurements and planar, two-dimensional CFD simulations.

8.2 Recommendations for future work

This thesis makes a humble contribution to the knowledge of hemodynamics in arterial networks and its relation to atherosclerosis. Similarly, the present work understands bubble splitting and the effect of various hydrodynamic parameters on pressure gradient on walls of a vessel. Some of the recommendations for future work are:

- The idealized models used for single as well as two-phase studies in the present work have significant differences from patient-specific vascular pathways and airways. For a better understanding of the hemodynamics of air-mucus flow, simulations need to be performed in patient-specific geometries, in particular for Indian subjects for which such data is scarce.
- The walls of the artery are considered rigid in this work. However, arterial walls are flexible. It is advised to carry out the fluid-structure interaction studies incorporating the flexible nature of the walls.
- CFD simulations use a constant pressure boundary condition at the exits of both daughter vessels. In reality, the pressure downstream of the two daughter vessels is not necessarily the same, and should be taken into account.
- The deposition of the fat can be modeled by introducing solid particles from inlet and tracking the movement at bifurcations.

- The studies in this work are performed for a single bifurcation and may need to be extended to multiple bifurcations.
- CFD simulations of gas-liquid flow in this work are performed in a planar, two-dimensional geometry. However, in order to completely understand the physics of bubble splitting, it is important to model the flow in a three-dimensional computational domain, as shown by the comparison between the CFD and experiments.
- The bubble dynamics can be explored for other orientations such as out of plane mother vessels.
- The present work modeled the mucus fluid as Newtonian and non-Newtonian (power law model), but the mucus is a very complex material that may show viscoelastic behavior and non-zero yield stress value. This can be taken into account in future work.

References

Abugattas, C., Aguirre, A., Castillo, E., Cruchaga, M., 2020. Numerical study of bifurcation blood flows using three different non-Newtonian constitutive models. Appl. Math. Model. 88, 529–549. https://doi.org/10.1016/j.apm.2020.06.066

Amato, M.B.P., Valente Barbas, C.S., Medeiros, D.M., Magaldi, R.B., De Pinto Schettino, G., Lorenzi-Filho, G., Kairalla, R.A., Deheinzelin, D., Munoz, C., Oliveira, R., Takagaki, T.Y., Carvalho, C.R.R., 1998. Effect of a protective ventilation strategy on mortality in the acute respiratory distress syndrome. Pneumologie 52, 285. https://doi.org/10.1097/00132586-199810000-00009

Anand, S., Bradshaw, C., Prabhakaran, D., 2020. Prevention and management of CVD in LMICs: Why do ethnicity, culture, and context matter? BMC Med. 18, 1–5. https://doi.org/10.1186/s12916-019-1480-9

Anna, S.L., 2016. Droplets and Bubbles in Microfluidic Devices. Annu. Rev. Fluid Mech. 48, 285–309. https://doi.org/10.1146/annurev-fluid-122414-034425

Antiga, L., Piccinelli, M., Botti, L., Ene-Iordache, B., Remuzzi, A., Steinman, D.A., 2008. An image-based modeling framework for patient-specific computational hemodynamics. Med. Biol. Eng. Comput. 46, 1097–1112. https://doi.org/10.1007/s11517-008-0420-1

Apaydin, M., Cetinoglu, K., 2021. Carotid angle in young stroke. Clin. Imaging 70, 10–17. https://doi.org/10.1016/j.clinimag.2020.10.020

Araim, O., Chen, A., Sumpio, B., 2001. Hemodynamic forces: effects on atherosclerosis. New Surg. 1, 92–100.

Arjmandi-Tash, O., Razavi, S., Zanbouri, R., 2011. Possibility of Atherosclerosis in an arterial bifurcation model. BioImpacts 1, 219–224. https://doi.org/10.5681/bi.2011.0

Arzhavitina, A., Steckel, H., 2010. Foams for pharmaceutical and cosmetic application. Int. J. Pharm. 394, 1–17. https://doi.org/10.1016/j.ijpharm.2010.04.028

Aussillous, P., Quere, D., 2000. Quick deposition of a fluid on the wall of a tube. Phys. Fluids 12, 2367–2371. https://doi.org/10.1017/S0022112061000159

Baroud, C.N., Tsikata, S., Heil, M., 2006. The propagation of low-viscosity fingers into fluid-filled branching networks. J. Fluid Mech. 546, 285–294. https://doi.org/10.1017/S0022112005007287

Barth, T.J., Jaspersen, D.C., 1989. The design and application of upwind schemes on unstructured meshes, in: 27th Aerospace Sciences Meeting. p. Paper no.89-0366.

Bijari, P.B., Wasserman, B.A., Steinman, D.A., 2014. Carotid bifurcation geometry is an independent predictor of early wall thickening at the carotid bulb. Stroke 45, 473–478. https://doi.org/10.1161/STROKEAHA.113.003454

Bilek, A.M., Dee, K.C., Gaver, D.P., 2003. Mechanisms of surface-tension-induced epithelial cell damage in a model of pulmonary airway reopening. J. Appl. Physiol. 94, 770–783. https://doi.org/10.1152/japplphysiol.00764.2002

Bit, A., Ghagare, D., Rizvanov, A.A., Chattopadhyay, H., 2017. Assessment of Influences of Stenoses in Right Carotid Artery on Left Carotid Artery Using Wall Stress Marker. Biomed Res. Int. 2935195. https://doi.org/10.1155/2017/2935195

Brackbill, J.U., Kothe, D.B., Zemach, C., 1992. A continuum method for modeling surface tension. J. Comput. Phys. 100, 335–354. https://doi.org/10.1016/0021-9991(92)90240-Y

Bretherton, F.P., 1961. The motion of long bubbles in tubes. J. Fluid Mech. 10, 166–188. https://doi.org/10.1017/S0022112061000160

Bull, J.L., 2007. The application of microbubbles for targeted drug delivery. Expert Opin. Drug Deliv. 4, 475–493. https://doi.org/10.1517/17425247.4.5.475

Bull, J.L., 2005. Cardiovascular bubble dynamics. Crit. Rev. Biomed. Eng. 33, 299–346.

Calderon, A.J., Eshpuniyani, B., Fowlkes, J.B., Bull, J.L., 2010. A boundary element model of the transport of a semi-infinite bubble through a microvessel bifurcation. Phys. Fluids 22, 1–11. https://doi.org/10.1063/1.3442829

Calderón, A.J., Fowlkes, J.B., Bull, J.L., 2005. Bubble splitting in bifurcating tubes: A model study of cardiovascular gas emboli transport. J. Appl. Physiol. 99, 479–487. https://doi.org/10.1152/japplphysiol.00656.2004

Calderón, A.J., Heo, Y.S., Huh, D., Futai, N., Takayama, S., Fowlkes, J.B., Bull, J.L., 2006. Microfluidic model of bubble lodging in microvessel bifurcations. Appl. Phys. Lett. 89, 2004–2007. https://doi.org/10.1063/1.2402898

Carlson, A., Do-Quang, M., Amberg, G., 2010. Droplet dynamics in a bifurcating channel. Int. J. Multiph. Flow 36, 397–405. https://doi.org/10.1016/j.ijmultiphaseflow.2010.01.002

Caro, C.G., Fitz-Gerald, J.M., Schroter, R.C., 1971a. Atheroma and arterial wall shear. Observation, correlation and proposal of a shear dependent mass transfer mechanism for atherogenesis. Proc. R. Soc. London. Ser. B. Biol. Sci. 177, 109–159. https://doi.org/10.1098/rspb.1971.0019

Caro, C.G., Fitz-Gerald, J.M., Schroter, R.C., Caro, C.G., Fritz-Gerald, J.M., Schroter, R.C., 1971b. Atheroma and arterial wall shear. Observation, correlation and proposal of a shear dependent mass transfer mechanism for atherogenesis. Proc. R. Soc. London. Ser. B. Biol. Sci. 177, 109–159. https://doi.org/10.1098/rspb.1971.0019

Chaichana, T., Sun, Z., Jewkes, J., 2011. Computation of hemodynamics in the left coronary artery with variable angulations. J. Biomech. 44, 1869–1878. https://doi.org/10.1016/j.jbiomech.2011.04.033

Chandran, K.B., Yoganathan, A.P., Rittgers, S.E., Yoganathan, A.P., Rittgers, S.E., 2007. Biofluid mechanics The human circulation, Taylor and Francis Group. https://doi.org/10.1088/1751-8113/44/8/085201

Chastre, J., Fagon, J., 2002. State of the Art Ventilator-associated Pneumonia. Am J Respir Crit Care Med 165, 867–903. https://doi.org/10.1164/rccm.2105078

Chatelin, R., Anne-Archard, D., Murris-Espin, M., Thiriet, M., Poncet, P., 2017. Numerical and experimental investigation of mucociliary clearance breakdown in cystic fibrosis. J. Biomech. 53, 56–63. https://doi.org/10.1016/j.jbiomech.2016.12.026

Chen, J., Lu, X.Y., 2006. Numerical investigation of the non-Newtonian pulsatile blood flow in a bifurcation model with a non-planar branch. J. Biomech. 39, 818–832. https://doi.org/10.1016/j.jbiomech.2005.02.003

Chen, J., Lu, X.Y., 2004. Numerical investigation of the non-Newtonian blood flow in a

bifurcation model with a non-planar branch. J. Biomech. 37, 1899–1911. https://doi.org/10.1016/j.jbiomech.2004.02.030

Chen, X., Zielinski, R., Ghadiali, S.N., 2014. Computational analysis of microbubble flows in bifurcating airways: Role of gravity, inertia, and surface tension. J. Biomech. Eng. 136, 1–11. https://doi.org/10.1115/1.4028097

Cho, Y. I., Kensey, K.R., 1991. Effects of the non-Newtonian viscosity of blood on flows in a diseased arterial vessel. Part 1: steady flows. Biorheology 28, 241–262.

Cho, Y.I., Kensey, K.R., 1991. Effects of the non-Newtonian viscosity of blood on flows in a diseased arterial vessel. Part 1: steady flows. Biorheology 28, 241–262. https://doi.org/10.3233/BIR-1991-283-415

Choi, P.M.C., Singh, D., Trivedi, A., Qazi, E., George, D., Wong, J., Demchuk, A.M., Goyal, M., Hill, M.D., Menon, B.K., 2015. Carotid webs and novos AVC. Am. J. Neuroradiol. 36, 2134–2139. https://doi.org/10.3174/ajnr.A4431

Compagne, K.C.J., Dilba, K., Postema, E.J., Van Es, A.C.G.M., Emmer, B.J., Majoie, C.B.L.M., Van Zwam, W.H., Dippel, D.W.J., Wentzel, J.J., Van Der Lugt, A., Gijsen, F.J.H., 2019. Flow patterns in carotid webs: A patient-based computational fluid dynamics study. Am. J. Neuroradiol. 40, 703–708. https://doi.org/10.3174/ajnr.A6012

Cone, R.A., 2009. Barrier properties of mucus. Adv. Drug Deliv. Rev. 61, 75–85. https://doi.org/10.1016/j.addr.2008.09.008

Cox, C., Najjari, M.R., Plesniak, M.W., 2019. Three-dimensional vortical structures and wall shear stress in a curved artery model. Phys. Fluids 31. https://doi.org/10.1063/1.5124876

D'Angelo, E., Koutsoukou, A., Della Valle, P., Gentile, G., Pecchiari, M., 2008. Cytokine release, small airway injury, and parenchymal damage during mechanical ventilation in normal open-chest rats. J. Appl. Physiol. 104, 41–49. https://doi.org/10.1152/japplphysiol.00805.2007

Dailey, H.L., Ghadiali, S.N., 2010. Influence of power-law rheology on cell injury during microbubble flows. Biomech. Model. Mechanobiol. 9, 263–279. https://doi.org/10.1007/s10237-009-0175-0

Dean, W.R., 1928. The Stream-line Motion of Fluid in a Curved Pipe. London, Edinburgh, Dublin Philos. Mag. J. Sci. 5, 673–695.

Dean, W.R., 1927. Note on the motion of fluid in a curved pipe. London, Edinburgh, Dublin Philos. Mag. J. Sci. 4, 208–233.

Debakey, M.E., Lawrie, G.M., Glaeser, D.H., Sc, D., 1985. Patterns of Atherosclerosis and their surgical significance. Ann. Surg. 201.

Deka, D.K., Boruah, M.P., Pati, S., Randive, P.R., Mukherjee, P.P., 2020. Tuning the Splitting Behavior of Droplet in a Bifurcating Channel through Wettability-Capillarity Interaction. Langmuir 36, 10471–10489. https://doi.org/10.1021/acs.langmuir.0c01633

Di Segni, R., Young, A. T., Qian, Z., & Castaneda-Zuniga, W.R., 1997. Embolotherapy: agents, equipment, and techniques. Interv. Radiol. 3.

DiCarlo, A.L., Holdsworth, D.W., Poepping, T.L., 2019. Study of the effect of stenosis severity and non-Newtonian viscosity on multidirectional wall shear stress and flow disturbances in the carotid artery using particle image velocimetry. Med. Eng. Phys. 65, 8–23. https://doi.org/10.1016/j.medengphy.2018.12.023

Du, M., Qi, T., Fan, W., Chen, H., 2020. Numerical investigation of bubble breakup in a four-branched microchannel based on non-Newtonian pseudoplastic fluid. Asia-Pacific J. Chem. Eng. 15, 1–13. https://doi.org/10.1002/apj.2393

Du, W., Fu, T., Zhang, Q., Zhu, C., Ma, Y., Li, H.Z., 2016. Breakup dynamics for droplet formation in a flow-focusing device: Rupture position of viscoelastic thread from matrix. Chem. Eng. Sci. 153, 255–269. https://doi.org/10.1016/j.ces.2016.07.038

Eisner, M.D., Wildmoser, H., Windhab, E.J., 2005. Air cell microstructuring in a high viscous ice cream matrix. Colloids Surfaces A Physicochem. Eng. Asp. 263, 390–399. https://doi.org/10.1016/j.colsurfa.2004.12.017

Eshpuniyani, B., Fowlkes, J.B., Bull, J.L., 2005. A bench top experimental model of bubble transport in multiple arteriole bifurcations. Int. J. Heat Fluid Flow 26, 865–872. https://doi.org/10.1016/j.ijheatfluidflow.2005.10.002

Eustice, J., 1911. Experiments on stream-line motion in curved pipes. Proc. R. Soc. London. Ser. A, Contain. Pap. a Math. Phys. Character 85, 119–131.

Eustice, J., 1910. Flow of water in curved pipes. Proc. R. Soc. London. Ser. A, Contain. Pap. a Math. Phys. Character 84, 107–118.

Evegren, P., Fuchs, L., Revstedt, J., 2010. On the secondary flow through bifurcating pipes. Phys. Fluids 22. https://doi.org/10.1063/1.3484266

Fabiilli, M.L., Haworth, K.J., Fakhri, N.H., Kripfgans, O.D., Carson, P.L., Fowlkes, J.B., 2009. The role of inertial cavitation in acoustic droplet vaporization. IEEE Trans. Ultrason. Ferroelectr. Freq. Control 56, 1006–1017. https://doi.org/10.1109/TUFFC.2009.1132

Fei, Y., Zhu, C., Fu, T., Gao, X., Ma, Y., 2021. The breakup dynamics of bubbles stabilized by nanoparticles in a microfluidic Y-junction. Chem. Eng. Sci. 245, 116867. https://doi.org/10.1016/j.ces.2021.116867

Feng, Y., Qin, D., Zhang, J., Zhang, L., Bouakaz, A., Wan, M., 2018. Occlusion and rupture of ex vivo capillary bifurcation due to acoustic droplet vaporization. Appl. Phys. Lett. 112, 1–6. https://doi.org/10.1063/1.5025594

Fluent, A.N.S.Y.S., 2019. 19.2-Theory Guide.

Fu, T., Ma, Y., Funfschilling, D., Li, H.Z., 2011. Dynamics of bubble breakup in a microfluidic T-junction divergence. Chem. Eng. Sci. 66, 4184–4195. https://doi.org/10.1016/j.ces.2011.06.003

Fujioka, H., Takayama, S., Grotberg, J.B., 2008. Unsteady propagation of a liquid plug in a liquid-lined straight tube. Phys. Fluids 20. https://doi.org/10.1063/1.2938381

Gallo, D., Bijari, P.B., Morbiducci, U., Qiao, Y., Xie, Y., Etesami, M., Habets, D., Lakatta, E.G., Wasserman, B.A., Steinman, D.A., 2018. Segment-specific associations between local haemodynamic and imaging markers of early atherosclerosis at the carotid artery: An in vivo human study. J. R. Soc. Interface 15. https://doi.org/10.1098/rsif.2018.0352

Garstecki, P., Fuerstman, M.J., Stone, H.A., Whitesides, G.M., 2006. Formation of droplets and bubbles in a microfluidic T-junction - Scaling and mechanism of break-up. Lab Chip 6, 437–

446. https://doi.org/10.1039/b510841a

Gaver, D.P., Halpern, D., Jensen, O.E., Grotberg, J.B., 1996. The steady motion of a semi-infinite bubble through a flexible-walled channel. J. Fluid Mech. 319, 25–65. https://doi.org/10.1017/S0022112096007240

Gefen, A., 2010. Cellular and biomolecular mechanics and mechanobiology (Vol. 4). Springer Berlin Heidelberg.

Ghadiali, S.N., Gaver, D.P., 2008. Biomechanics of liquid-epithelium interactions in pulmonary airways. Respir. Physiol. Neurobiol. 163, 232–243. https://doi.org/10.1016/j.resp.2008.04.008

Gharahi, H., Zambrano, B.A., Zhu, D.C., DeMarco, J.K., Baek, S., 2016. Computational fluid dynamic simulation of human carotid artery bifurcation based on anatomy and volumetric blood flow rate measured with magnetic resonance imaging. Int. J. Adv. Eng. Sci. Appl. Math. 8, 46–60. https://doi.org/10.1007/s12572-016-0161-6

Giavedoni, M.D., Saita, F.A., 1999. The rear meniscus of a long bubble steadily displacing a Newtonian liquid in a capillary tube. Phys. Fluids 11, 786–794. https://doi.org/10.1063/1.869951

Giavedoni, M.D., Saita, F.A., 1997. The axisymmetric and plane cases of a gas phase steadily displacing a Newtonian liquid - A simultaneous solution of the governing equations. Phys. Fluids 9, 2420–2428. https://doi.org/10.1063/1.869360

Gibson, P.G., Qin, L., Puah, S.H., 2020. COVID-19 acute respiratory distress syndrome (ARDS): clinical features and differences from typical pre-COVID-19 ARDS. Med. J. Aust. 213, 54-56.e1. https://doi.org/10.5694/mja2.50674

Gijsen, F.J.H., Vosse, F.N. Van De, Janssen, J.D., 1999. The influence of the non-Newtonian properties of blood on the flow in large arteries : steady flow in a carotid bifurcation model. J. Biomech. 32, 601–608.

Glagov, S., Zarins, C., Giddens, D.P., Ku, D.N., 1988. Hemodynamics and atherosclerosis. Insights and perspectives gained from studies of human arteries. Arch. Pathol. Lab. Med. 112, 1018—1031.

Grabcad, 2019. GRABCAD COMMUNITY [WWW Document]. https://grabcad.com/library/carotid-bifurcation.

Gregg, S., Li, T.Y., France, M., Stephen, H., Paul, C.P., Amer, E., 2018a. Relationship between carotid artery atherosclerosis and bulb geometry. Int. J. Cardiovasc. Imaging 0, 0. https://doi.org/10.1007/s10554-018-1319-z

Gregg, S., Li, T.Y., Hétu, M.F., Pang, S.C., Ewart, P., Johri, A.M., 2018b. Relationship between carotid artery atherosclerosis and bulb geometry. Int. J. Cardiovasc. Imaging 34, 1081–1090. https://doi.org/10.1007/s10554-018-1319-z

Grotberg, J.B., 1994. Pulmonary flow and transport phenomena. Annu. Rev. Fluid Mech. 26, 529–571. https://doi.org/10.1146/annurev.fluid.26.1.529

Guha, A., Pradhan, K., 2017. Secondary motion in three-dimensional branching networks. Phys. Fluids 29. https://doi.org/10.1063/1.4984919

Guha, A., Pradhan, K., Halder, P.K., 2016. Finding order in complexity: A study of the fluid dynamics in a three-dimensional branching network. Phys. Fluids 28. https://doi.org/10.1063/1.4971315

Gupta, R., Fletcher, D.F., Haynes, B.S., 2009. On the CFD modelling of Taylor flow in microchannels. Chem. Eng. Sci. 64, 2941–2950. https://doi.org/10.1016/j.ces.2009.03.018

Hall, J.E., Guyton, A.C., 2011. Guyton and Hall textbook of medical physiology. Philadelphia, PA: Saunders Elsevier.

Harmon, J.S., Kabinejadian, F., Seda, R., Fabiilli, M.L., Kuruvilla, S., Kuo, C.C., Greve, J.M., Fowlkes, J.B., Bull, J.L., 2019. Minimally invasive gas embolization using acoustic droplet vaporization in a rodent model of hepatocellular carcinoma. Sci. Rep. 9, 1–11. https://doi.org/10.1038/s41598-019-47309-y

He, J., Kinouchi, Y., Yamaguchi, H., Miyamoto, H., 1995. Exercise-induced changes in R wave amplitude and heart rate in normal subjects. J. Electrocardiol. 28, 99–106. https://doi.org/10.1016/S0022-0736(05)80280-8

Heil, M., 2000. Finite Reynolds number effects in the propagation of an air finger into a liquid-

filled flexible-walled channel. J. Fluid Mech. 424, 21–44.

Himburg, H.A., Grzybowski, D.M., Hazel, A.L., LaMack, J.A., Li, X.M., Friedman, M.H., 2004. Spatial comparison between wall shear stress measures and porcine arterial endothelial permeability. Am. J. Physiol. - Hear. Circ. Physiol. 286, 1916–1922. https://doi.org/10.1152/ajpheart.00897.2003

Hirt, C. W., Nichols, B.D., 1981. Volume of Fluid (VOF) method for the dynamics of free boundaries. J. Comput. Phys. 39, 201–225. https://doi.org/10.1007/s40998-018-0069-1

Hu, Y., Romano, F., Grotberg, J.B., 2020. Effects of surface tension and yield stress on mucus plug rupture: A numerical study. J. Biomech. Eng. 142, 1–10. https://doi.org/10.1115/1.4045596

Huang, Q., Sun, J., Xu, C., 2021. Effects of waveform shape of pulsatile blood flow on hemodynamics in an artery bifurcation model. Proc. Inst. Mech. Eng. Part C J. Mech. Eng. Sci. 235, 428–440. https://doi.org/10.1177/0954406220911397

Huh, D., Fujioka, H., Tung, Y.C., Futai, N., Paine, R., Grotberg, J.B., Takayama, S., 2007. Acoustically detectable cellular-level lung injury induced by fluid mechanical stresses in microfluidic airway systems. Proc. Natl. Acad. Sci. U. S. A. 104, 18886–18891. https://doi.org/10.1073/pnas.0610868104

Huh, H.K., Ha, H., Lee, S.J., 2015. Effect of non-Newtonian viscosity on the fluid-dynamic characteristics in stenotic vessels. Exp. Fluids 56, 1–12. https://doi.org/10.1007/s00348-015-2037-0

Hussain, M.A., Kar, S., Puniyani, R.R., 1999. Relationship between power law coefficients and major blood constituents affecting the whole blood viscosity. J. Biosci. 24, 329–337. https://doi.org/10.1007/BF02941247

Johari, N.H., Hamady, M., Xu, X.Y., 2020. A computational study of the effect of stent design on local hemodynamic factors at the carotid artery bifurcation. Artery Res. 26, 161–169.

Johari, N.H., Wood, N.B., Cheng, Z., Torii, R., Oishi, M., Oshima, M., Xu, X.Y., 2019. Disturbed flow in a stenosed carotid artery bifurcation: Comparison of RANS-based transitional model and LES with experimental measurements. Int. J. Appl. Mech. 11, 1950032.

Joux, J., Chausson, N., Jeannin, S., Saint-Vil, M., Mejdoubi, M., Hennequin, J.L., Deschamps, L., Smadja, D., Olindo, S., 2014. Carotid-bulb atypical fibromuscular dysplasia in young afro-caribbean patients with stroke. Stroke 45, 3711–3713. https://doi.org/10.1161/STROKEAHA.114.007313

Kabinejadian, F., Cui, F., Su, B., Danpinid, A., Ho, P., Leo, H.L., 2015. Effects of a carotid covered stent with a novel membrane design on the blood flow regime and hemodynamic parameters distribution at the carotid artery bifurcation. Med. Biol. Eng. Comput. 53, 165–177. https://doi.org/10.1007/s11517-014-1222-2

Kang, S. T., Huang, Y. L., & Yeh, C.K., 2014. Characterization of acoustic droplet vaporization for control of bubble generation under flow conditions. Ultrasound Med. Biol. 40, 551–561.

Kang, S.T., Lin, Y.C., Yeh, C.K., 2014. Mechanical bioeffects of acoustic droplet vaporization in vessel-mimicking phantoms. Ultrason. Sonochem. 21, 1866–1874. https://doi.org/10.1016/j.ultsonch.2014.03.007

Kay, S.S., Bilek, A.M., Dee, K.C., Gaver, D.P., 2004. Pressure gradient, not exposure duration, determines the extent of epithelial cell damage in a model of pulmonary airway reopening. J. Appl. Physiol. 97, 269–276. https://doi.org/10.1152/japplphysiol.01288.2003

Keramati, H., Birgersson, E., Ho, J.P., Kim, S., Chua, K.J., Leo, H.L., 2020. The effect of the entry and re-entry size in the aortic dissection: a two-way fluid–structure interaction simulation. Biomech. Model. Mechanobiol. 19, 2643–2656. https://doi.org/10.1007/s10237-020-01361-0

Khadiya, S., Kumari, S., Gupta, R., 2021. Hydrodynamics of bubble coalescence in microchannels. Can. J. Chem. Eng. 99, 1199–1210. https://doi.org/10.1002/cjce.23918

Khodaparast, S., Magnini, M., Borhani, N., Thome, J.R., 2015. Dynamics of isolated confined air bubbles in liquid flows through circular microchannels: an experimental and numerical study. Microfluid. Nanofluidics 19, 209–234. https://doi.org/10.1007/s10404-015-1566-4

Klaseboer, E., Gupta, R., Manica, R., 2014. An extended Bretherton model for long Taylor bubbles at moderate capillary numbers. Phys. Fluids 26. https://doi.org/10.1063/1.4868257

Kripfgans, O. D., Fowlkes, J. B., Miller, D. L., Eldevik, O. P., & Carson, P.L., 2000. Acoustic

droplet vaporization for therapeutic and diagnostic applications. Ultrasound Med. Biol. 26, 1177–1189.

Kripfgans, O.D., Fabiilli, M.L., Carson, P.L., Fowlkes, J.B., 2004. On the acoustic vaporization of micrometer-sized droplets. J. Acoust. Soc. Am. 116, 272–281. https://doi.org/10.1121/1.1755236

Kripfgans, O.D., Orifici, C.M., Carson, P.L., Ives, K.A., Eldevik, O.P., Fowlkes, J.B., 2005. Acoustic droplet vaporization for temporal and spatial control of tissue occlusion: A kidney study. IEEE Trans. Ultrason. Ferroelectr. Freq. Control 52, 1101–1108. https://doi.org/10.1109/TUFFC.2005.1503996

Ku, D., Giddens, D., Zarins, C., Glagov, S., 1985. Pulsatile Flow and Atherosclerosis in the Human Carotid Bifurcation Positive Correlation between Plaque Location and Low and Oscillating Shear Stress. Arteriosclerosis 5.

Ku, D.N., 1997. Blood Flow in Arteries. Annu. Rev. Fluid Mech. 29, 399–434. https://doi.org/10.1146/annurev.fluid.29.1.399

Ku, D.N., Giddens, D.P., 1983. Pulsatile Flow in a Model Carotid Bifurcation. Arteriosclerosis 3.

Kuan, Y.H., Kabinejadian, F., Nguyen, V.T., Su, B., Yoganathan, A.P., Leo, H.L., 2015. Comparison of hinge microflow fields of bileaflet mechanical heart valves implanted in different sinus shape and downstream geometry. Comput. Methods Biomech. Biomed. Engin. 18, 1785–1796. https://doi.org/10.1080/10255842.2014.964220

Kumari, S., Kumar, N., Gupta, R., 2019. Flow and heat transfer in slug flow in microchannels: Effect of bubble volume. Int. J. Heat Mass Transf. 129, 812–826. https://doi.org/10.1016/j.ijheatmasstransfer.2018.10.010

Kumari, S., Kumar, N., Gupta, R., 2018. Effect of gas–liquid ratio on the wall shear stress in slug flow in capillary membranes. Asia-Pacific J. Chem. Eng. 13, e2258.

Lac, E., Sherwood, J.D., 2009. Motion of a drop along the centreline of a capillary in a pressure-driven flow. J. Fluid Mech. 640, 27–54. https://doi.org/10.1017/S0022112009991212

Lai, S.K., Wang, Y.Y., Wirtz, D., Hanes, J., 2009. Micro- and macrorheology of mucus. Adv.

Drug Deliv. Rev. 61, 86–100. https://doi.org/10.1016/j.addr.2008.09.012

Lee, S.W., Antiga, L., Spence, J.D., Steinman, D.A., 2008. Geometry of the carotid bifurcation predicts its exposure to disturbed flow. Stroke 39, 2341–2347. https://doi.org/10.1161/STROKEAHA.107.510644

Lee, S.W., Antiga, L., Steinman, D.A., 2009. Correlations among indicators of disturbed flow at the normal carotid bifurcation. J. Biomech. Eng. 131, 1–7. https://doi.org/10.1115/1.3127252

Li, Z., Li, G., Li, Y., Chen, Y., Li, J., Chen, H., 2021. Flow field around bubbles on formation of air embolism in small vessels. Proc. Natl. Acad. Sci. 118, e2025406118. https://doi.org/10.1073/pnas.2025406118

Li, Z.Y., Tan, F.P.P., Soloperto, G., Wood, N.B., Xu, X.Y., Gillard, J.H., 2015. Flow pattern analysis in a highly stenotic patient-specific carotid bifurcation model using a turbulence model. Comput. Methods Biomech. Biomed. Engin. 18, 1099–1107. https://doi.org/10.1080/10255842.2013.873033

Liepsch, D., Moravec, S., Rastogi, A.K., Vlachos, N.S., 1982. Measurement and calculations of laminar flow in a ninety degree bifurcation. J. Biomech. 15, 473–485.

Link, D.R., Anna, S.L., Weitz, D.A., Stone, H.A., 2004. Geometrically Mediated Breakup of Drops in Microfluidic Devices. Phys. Rev. Lett. 92, 4. https://doi.org/10.1103/PhysRevLett.92.054503

Liu, Z., Wang, X., Cao, R., Pang, Y., 2016. Droplet coalescence at microchannel intersection chambers with different shapes. Soft Matter 12, 5797–5807. https://doi.org/10.1039/c6sm01158f

Lo, A.H., Kripfgans, O.D., Carson, P.L., Rothman, E.D., Fowlkes, J.B., 2007. Acoustic droplet vaporization threshold: Effects of pulse duration and contrast agent. IEEE Trans. Ultrason. Ferroelectr. Freq. Control 54, 933–945. https://doi.org/10.1109/TUFFC.2007.339

Lu, Y., Lu, X., Zhuang, L., Wang, W., 2002. Breaking symmetry in non-planar bifurcations: Distribution of flow and wall shear stress. Biorheology 39, 431–436.

Ma, D., Liang, D., Zhu, C., Fu, T., Ma, Y., Yuan, X., Li, H.Z., 2021. The breakup dynamics and

mechanism of viscous droplets in Y-shaped microchannels. Chem. Eng. Sci. 231, 116300. https://doi.org/10.1016/j.ces.2020.116300

Malek, A.M., Alper, S.L., Izumo, S., 1999. Hemodynamic shear stress and its role in atherosclerosis. J. Am. Med. Assoc. 282, 2035–2042.

Malvè, M., García, A., Ohayon, J., Martínez, M.A., 2012. Unsteady blood flow and mass transfer of a human left coronary artery bifurcation: FSI vs. CFD. Int. Commun. Heat Mass Transf. 39, 745–751. https://doi.org/10.1016/j.icheatmasstransfer.2012.04.009

Manga, M., 1996. Dynamics of drops in branched tubes. J. Fluid Mech. 315, 105–117. https://doi.org/10.1017/S0022112096002352

Matsumoto, D., Fukudome, K., Wada, H., 2016. Two-dimensional fluid dynamics in a sharply bent channel: Laminar flow, separation bubble, and vortex dynamics. Phys. Fluids 28. https://doi.org/10.1063/1.4963864

Mauroy, B., Fausser, C., Pelca, D., Merckx, J., Flaud, P., 2011. Toward the modeling of mucus draining from the human lung: Role of the geometry of the airway tree. Phys. Biol. 8. https://doi.org/10.1088/1478-3975/8/5/056006

Mendieta, J.B., Fontanarosa, D., Wang, J., Paritala, P.K., Mcgahan, T., Lloyd, T., Li, Z., 2020. The importance of blood rheology in patient - specific computational fluid dynamics simulation of stenotic carotid arteries. Biomech. Model. Mechanobiol. 1–14. https://doi.org/10.1007/s10237-019-01282-7

Moradicheghamahi, J., Sadeghiseraji, J., Jahangiri, M., 2019a. Numerical solution of the Pulsatile, non-Newtonian and turbulent blood flow in a patient specific elastic carotid artery. Int. J. Mech. Sci. 150, 393–403. https://doi.org/10.1016/j.ijmecsci.2018.10.046

Moradicheghamahi, J., Sadeghiseraji, J., Jahangiri, M., 2019b. Numerical solution of the Pulsatile, non-Newtonian and turbulent blood flow in a patient specific elastic carotid artery. Int. J. Mech. Sci. 150, 393–403. https://doi.org/10.1016/j.ijmecsci.2018.10.046

Morbiducci, U., Kok, A.M., Kwak, B.R., Stone, P.H., Steinman, D.A., Wentzel, J.J., 2016. Atherosclerosis at arterial bifurcations: Evidence for the role of haemodynamics and geometry. Thromb. Haemost. 115, 484–492. https://doi.org/10.1160/TH15-07-0597

Munir, B., Xu, Y., 2020. Effects of gravity and surface tension on steady microbubble propagation in asymmetric bifurcating airways. Phys. Fluids 32. https://doi.org/10.1063/5.0012796

Muradoglu, M., Romanò, F., Fujioka, H., Grotberg, J.B., 2019. Effects of surfactant on propagation and rupture of a liquid plug in a tube. J. Fluid Mech. 872, 407–437. https://doi.org/10.1017/jfm.2019.333

Murray, C.D., 1926. The physiological principle of minimum work: I. The vascular system and the cost of blood volume. Proc. Natl. Acad. Sci. United States Am. 12, 207–214. https://doi.org/10.1085/jgp.14.4.445

Najjari, M.R., Cox, C., Plesniak, M.W., 2019. Formation and interaction of multiple secondary flow vortical structures in a curved pipe: Transient and oscillatory flows. J. Fluid Mech. 876, 481–526. https://doi.org/10.1017/jfm.2019.510

Nguyen, K.T., Clark, C.D., Chancellor, T.J., Papavassiliou, D. V., 2008. Carotid geometry effects on blood flow and on risk for vascular disease. J. Biomech. 41, 11–19. https://doi.org/10.1016/j.jbiomech.2007.08.012

Noh, S.M., Kang, H.G., 2019. Clinical significance of the internal carotid artery angle in ischemic stroke. Sci. Rep. 9, 1–5. https://doi.org/10.1038/s41598-018-37783-1

Olgac, U., Muradoglu, M., 2013. Computational modeling of unsteady surfactant-laden liquid plug propagation in neonatal airways. Phys. Fluids 25. https://doi.org/10.1063/1.4812589

Otero-Cacho, A., Aymerich, M., Flores-Arias, M.T., Abal, M., Álvarez, E., Pérez-Muñuzuri, V., Muñuzuri, A.P., 2018. Determination of hemodynamic risk for vascular disease in planar artery bifurcations. Sci. Rep. 8, 1–7. https://doi.org/10.1038/s41598-018-21126-1

Pauwels, P.R.A., Rabe, K.F., 2004. Burden and clinical features of chronic obstructive pulmonary disease (COPD). Lancet 364, 613–620. https://doi.org/10.1016/S0140-6736(04)16855-4

Paz, C., Suárez, E., Vence, J., 2017. CFD transient simulation of the cough clearance process using an Eulerian wall film model. Comput. Methods Biomech. Biomed. Engin. 20, 142–152. https://doi.org/10.1080/10255842.2016.1206532

Paz, C., Suárez, E., Vence, J., Cabarcos, A., 2019. Analysis of the volume of fluid (VOF) method

for the simulation of the mucus clearance process with CFD. Comput. Methods Biomech. Biomed. Engin. 22, 547–566. https://doi.org/10.1080/10255842.2019.1569637

Perktold, K., Hilbert, D., 1986. Numerical simulation of pulsatile flow in a carotid bifurcation model. J. Biomed. Eng. 8, 193–199. https://doi.org/10.1016/0141-5425(86)90083-X

Perktold, K., Peter, R.O., Resh, M., Langs, G., 1991. Pulsatile non-Newtonian blood flow in three-dimensional carotid bifurcation models : a numerical study of flow phenomena under different bifurcation angles. J. Biomed. Eng. 13, 507–515.

Perktold, K., Resch, M., 1990. Numerical flow studies in human carotid artery bifurcations : basic discussion of the geometric factor in atherogenesis. J. Biomed. Eng. 12, 111–123.

Phan, T.G., Beare, R.J., Jolley, D., Das, G., Ren, M., Wong, K., Chong, W., Sinnott, M.D., Hilton, J.E., Srikanth, V., 2012. Carotid artery anatomy and geometry as risk factors for carotid atherosclerotic disease. Stroke 43, 1596–1601. https://doi.org/10.1161/STROKEAHA.111.645499

Picchi, D., Poesio, P., Ullmann, A., Brauner, N., 2017. Characteristics of stratified flows of Newtonian/non-Newtonian shear-thinning fluids. Int. J. Multiph. Flow 97, 109–133. https://doi.org/10.1016/j.ijmultiphaseflow.2017.06.005

Poornima, J., Vengadesan, S., 2012. Numerical simulation of bubble transport in a bifurcating microchannel: A preliminary study. J. Biomech. Eng. 134, 1–10. https://doi.org/10.1115/1.4006975

Prabhakaran, D., Jeemon, P., Roy, A., 2016. Cardiovascular Diseases in India: Current Epidemiology and Future Directions. Circulation 133, 1605–1620. https://doi.org/10.1161/CIRCULATIONAHA.114.008729

Prabhakaran, D., Singh, K., Roth, G.A., Banerjee, A., Pagidipati, N.J., Huffman, M.D., 2018. Cardiovascular Diseases in India Compared With the United States. J. Am. Coll. Cardiol. 72, 79–95. https://doi.org/10.1016/j.jacc.2018.04.042

Pradhan, K., Guha, A., 2019. Fluid dynamics of oscillatory flow in three-dimensional branching networks. Phys. Fluids 31. https://doi.org/10.1063/1.5093724

Qamar, A., Warnez, M., Valassis, D.T., Guetzko, M.E., Bull, J.L., 2017. Small-bubble transport and splitting dynamics in a symmetric bifurcation. Comput. Methods Biomech. Biomed. Engin. 20, 1182–1194. https://doi.org/10.1080/10255842.2017.1340466

Qamar, A., Wong, Z.Z., Fowlkes, J.B., Bull, J.L., 2010. Dynamics of acoustic droplet vaporization in gas embolotherapy. Appl. Phys. Lett. 96, 1–4. https://doi.org/10.1063/1.3376763

Rajendran, R.R., Banerjee, A., 2020. Effect of Non-Newtonian Dynamics On the Clearance of Mucus From Bifurcating Lung Airway Models. J. Biomech. Eng. 143, 1–13. https://doi.org/10.1115/1.4048474

Ren, S., Li, W., Wang, L., Shi, Y., Cai, M., Hao, L., Luo, Zihao, Niu, J., Xu, W., Luo, Zujin, 2020. Numerical Analysis of Airway Mucus Clearance Effectiveness Using Assisted Coughing Techniques. Sci. Rep. 10, 1–10. https://doi.org/10.1038/s41598-020-58922-7

Rindt, C.C.M., Vosse, F.N. v. d., Steenhoven, A.A. v., Janssen, J.D., Reneman, R.S., 1987. A numerical and experimental analysis of the flow field in a two-dimensional model of the human carotid artery bifurcation. J. Biomech. 20, 499–509. https://doi.org/10.1016/0021-9290(87)90250-8

Ritman, E.L., Zamir, M., 2012. The Physics of Pulsatile Flow, Springer-Verlag, Wien, Austria.

Roberston, A., Owens, R., 2009. Rheology of blood in cardiovascular mathematics, Springer, Milano.

Romanò, F., Fujioka, H., Muradoglu, M., Grotberg, J.B., 2019. Liquid plug formation in an airway closure model. Phys. Rev. Fluids 4, 1–23. https://doi.org/10.1103/PhysRevFluids.4.093103

Ruuskanen, O., Lahti, E., Jennings, L.C., Murdoch, D.R., 2011. Viral pneumonia. Lancet 377, 1264–1275. https://doi.org/10.1016/S0140-6736(10)61459-6

Saho, T., Onishi, H., 2017. Quantitative analysis of effects of hemodynamic stress on temporal variations of cardiac phases in models of human carotid bulbs. Radiol. Phys. Technol. 10, 475–482. https://doi.org/10.1007/s12194-017-0421-6

Samuel, S., Duprey, A., Fabiilli, M. L., Bull, J. L., & Brian Fowlkes, J., 2012. In vivo microscopy of targeted vessel occlusion employing acoustic droplet vaporization. Microcirculation 19,

501–509.

Schulz, U.G.R., Rothwell, P.M., 2001. Sex differences in carotid bifurcation anatomy and the distribution of atherosclerotic plaque. Stroke 32, 1525–1531. https://doi.org/10.1161/01.STR.32.7.1525

Seetharaman, A., Keramati, H., Ramanathan, K., E Cove, M., Kim, S., Chua, K.J., Leo, H.L., 2021. Vortex dynamics of veno-arterial extracorporeal circulation: A computational fluid dynamics study. Phys. Fluids 33, 1–30. https://doi.org/10.1063/5.0050962

Sinnott, M., Cleary, P.W., Prakash, M., 2006. An investigation of pulsatile blood flow in a bifurcation artery using a grid-free method. Proc. Fifth Int. Conf. CFD Process Ind. 1–6.

Smith, B.J., Gaver, D.P., 2008. The pulsatile propagation of a finger of air within a fluid-occluded cylindrical tube. J. Fluid Mech. 601, 1–23. https://doi.org/10.1017/S0022112008000360

Soh, W.Y., Berger, S.A., 1984. Laminar entrance flow in a curved pipe. J. Fluid Mech. 148, 109–135.

Song, J., Kouidri, S., Bakir, F., 2021. Numerical study on flow topology and hemodynamics in tortuous coronary artery with symmetrical and asymmetrical stenosis. Biocybern. Biomed. Eng. 41, 142–155. https://doi.org/10.1016/j.bbe.2020.12.006

Soulis, J. V., Lampri, O.P., Fytanidis, D.K., Giannoglou, G.D., 2011. Relative residence time and oscillatory shear index of non-Newtonian flow models in aorta. 10th Int. Work. Biomed. Eng. BioEng 2011 4–7. https://doi.org/10.1109/IWBE.2011.6079011

Sousa, L.C., Castro, C.F., António, C.C., Santos, A., Santos, R., Castro, P., Azevedo, E., Tavares, J.M.R.S., 2014. Haemodynamic conditions of patient-specific carotid bifurcation based on ultrasound imaging. Comput. Methods Biomech. Biomed. Eng. Imaging Vis. https://doi.org/10.1080/21681163.2013.875486

Squires, T.M., Quake, S.R., 2005. Microfluidics: Fluid physics at the nanoliter scale. Rev. Mod. Phys. 77, 977. https://doi.org/10.12693/APhysPolA.133.1191

Stebe, K.J., Barthès-Biesel, D., 1995. Marangoni effects of adsorption—desorption controlled surfactants on the leading end of an infinitely long bubble in a capillary. J. Fluid Mech. 286,

25–48. https://doi.org/10.1017/S0022112095000632

Steinman, D.A., 2002. Image-based computational fluid dynamics modeling in realistic arterial geometries. Ann. Biomed. Eng. 30, 483–497. https://doi.org/10.1114/1.1467679

Sun, X., Zhu, C., Fu, T., Ma, Y., Li, H.Z., 2019. Breakup dynamics of elastic droplet and stretching of polymeric filament in a T-junction. Chem. Eng. Sci. 206, 212–223. https://doi.org/10.1016/j.ces.2019.05.030

Sun, X., Zhu, C., Fu, T., Ma, Y., Li, H.Z., 2018. Dynamics of droplet breakup and formation of satellite droplets in a microfluidic T-junction. Chem. Eng. Sci. 188, 158–169. https://doi.org/10.1016/j.ces.2018.05.027

Tabas, I., García-Cardeña, G., Owens, G.K., 2015. Recent insights into the cellular biology of atherosclerosis. J. Cell Biol. 209, 13–22. https://doi.org/10.1083/jcb.201412052

Tavana, H., Zamankhan, P., Christensen, P.J., Grotberg, J.B., Takayama, S., 2011. Epithelium damage and protection during reopening of occluded airways in a physiologic microfluidic pulmonary airway model. Biomed. Microdevices 13, 731–742. https://doi.org/10.1007/s10544-011-9543-5

Texon, M., 1957. A hemodynamic concept of atherosclerosis, with particular reference to coronary occlusion. Arch. Int. Med. 99, 418–427.

Thomas, J.B., Antiga, L., Che, S.L., Milner, J.S., Steinman, D.A.H., Spence, J.D., Rutt, B.K., Steinman, D.A., 2005a. Variation in the carotid bifurcation geometry of young versus older adults: Implications for geometric risk of atherosclerosis. Stroke 36, 2450–2456. https://doi.org/10.1161/01.STR.0000185679.62634.0a

Thomas, J.B., Antiga, L., Che, S.L., Milner, J.S., Steinman, D.A.H., Spence, J.D., Rutt, B.K., Steinman, D.A., 2005b. Variation in the carotid bifurcation geometry of young versus older adults: Implications for geometric risk of atherosclerosis. Stroke 36, 2450–2456. https://doi.org/10.1161/01.STR.0000185679.62634.0a

Valassis, D.T., Dodde, R.E., Esphuniyani, B., Fowlkes, J.B., Bull, J.L., 2012. Microbubble transport through a bifurcating vessel network with pulsatile flow. Biomed. Microdevices 14, 131–143. https://doi.org/10.1007/s10544-011-9591-x

Valencia, A.A., Guzmán, A.M., Finol, E.A., Amon, C.H., 2006. Blood flow dynamics in saccular aneurysm models of the basilar artery. J. Biomech. Eng. 128, 516–526. https://doi.org/10.1115/1.2205377

Vlahakis, N.E., Hubmayr, R.D., 2005. Cellular stress failure in ventilator-injured lungs. Am. J. Respir. Crit. Care Med. 171, 1328–1342. https://doi.org/10.1164/rccm.200408-1036SO

Wang, X., Liu, Z., Pang, Y., 2019. Breakup dynamics of droplets in an asymmetric bifurcation by MPIV and theoretical investigations. Chem. Eng. Sci. 197, 258–268. https://doi.org/10.1016/j.ces.2018.12.030

Wang, X., Liu, Z., Pang, Y., 2018. Droplet breakup in an asymmetric bifurcation with two angled branches. Chem. Eng. Sci. 188, 11–17. https://doi.org/10.1016/j.ces.2018.05.003

Wang, X., Zhu, C., Fu, T., Qiu, T., Ma, Y., 2017. Critical condition for bubble breakup in a microfluidic flow-focusing junction. Chem. Eng. Sci. 164, 178–187. https://doi.org/10.1016/j.ces.2017.01.066

Wang, Z., Wood, N.B., Xu, X.Y., 2015. A viscoelastic fluid–structure interaction model for carotid arteries under pulsatile flow. Int. j. numer. method. biomed. eng. 31, e02709.

Ware, L. B., Matthay, M.A., 2000. The acute respiratory distress syndrome. New England Journal of Medicine, 342(18), 1334-1349. New Enlgand J. Med. 342, 1334–1349.

Wei, L., Leo, H.L., Chen, Q., Li, Z., 2019. Structural and Hemodynamic Analyses of Different Stent Structures in Curved and Stenotic Coronary Artery. Front. Bioeng. Biotechnol. 7, 1–13. https://doi.org/10.3389/fbioe.2019.00366

Weibel, E.R., 1963. Morphometry of the human lung, Springer, Berlin, Heidelberg.

Wells, D.R., Archie, J.P., Kleinstreuer, C., 1996. Effect of carotid artery geometry on the magnitude and distribution of wall shear stress gradients. J. Vasc. Surg. 23, 667–678. https://doi.org/10.1016/S0741-5214(96)80048-6

Wells, R., Archie, P., Purpose, N.C., Surg, V., Engineering, A., Technology, A.E.A., Software, E., Archie, J.P., Bern, N., 1996. Effect of carotid artery geometry on the magnitude and distribution of wall shear stress gradients. J. Vasc. Surg. 23.

Whitesides, G.M., 2006. The origins and the future of microfluidics. Nature 442, 368–373. https://doi.org/10.1038/nature05058

WHO, 2019. World Health Organization, Geneva, Switzerland, accesed, Dec. 18, 2019, Geneva.

Williams, G.S., Hubbell, C.W., Fenkell, G.H., 1902. Experiments at Detroit, Mich., on the effect of curvature upon the flow of water in pipes. Trans. Am. Soc. Civ. Eng. 47, 1–196.

Womersley, J.R., 1955. Method for the calculation of velocity, rate of flow and viscous drag in arteries when the pressure gradient is known. J. Physiol. 127, 553–563.

Wong, Z.Z., Bull, J.L., 2011. Vascular bubbles and droplets for drug delivery. J. Drug Deliv. Sci. Technol. 21, 355–367. https://doi.org/10.1016/S1773-2247(11)50061-9

Wong, Z.Z., Kripfgans, O.D., Qamar, A., Fowlkes, J.B., Bull, J.L., 2011. Bubble evolution in acoustic droplet vaporization at physiological temperature via ultra-high speed imaging. Soft Matter 7, 4009–4016. https://doi.org/10.1039/c1sm00007a

Wootton, D.M., Ku, D.N., 1999. Fluid mechanics of vascular systems, diseases, and thrombosis. Annu. Rev. Biomed. Eng. 299–329. https://doi.org/10.1146/annurev.bioeng.1.1.299

Wu, C., Chen, X., Cai, Y., Xia, J., Zhou, Xing, Xu, S., Huang, H., Zhang, L., Zhou, Xia, Du, C., Zhang, Y., Song, J., Wang, S., Chao, Y., Yang, Z., Xu, J., Zhou, Xin, Chen, D., Xiong, W., Xu, L., Zhou, F., Jiang, J., Bai, C., Zheng, J., Song, Y., 2020. Risk Factors Associated with Acute Respiratory Distress Syndrome and Death in Patients with Coronavirus Disease 2019 Pneumonia in Wuhan, China. JAMA Intern. Med. 180, 934–943. https://doi.org/10.1001/jamainternmed.2020.0994

Xiang, J., Siddiqui, A.H., Meng, H., 2014. The effect of inlet waveforms on computational hemodynamics of patient-specific intracranial aneurysms. J. Biomech. 47, 3882–3890. https://doi.org/10.1016/j.jbiomech.2014.09.034

Xu, Z., Shi, L., Wang, Y., Zhang, J., Huang, L., Zhang, C., Liu, S., Zhao, P., Liu, H., Zhu, L., Tai, Y., Bai, C., Gao, T., Song, J., Xia, P., Dong, J., Zhao, J., Wang, F.S., 2020. Pathological findings of COVID-19 associated with acute respiratory distress syndrome. Lancet Respir. Med. 8, 420–422. https://doi.org/10.1016/S2213-2600(20)30076-X

Yalcin, H.C., Perry, S.F., Ghadiali, S.N., 2007. Influence of airway diameter and cell confluence on epithelial cell injury in an in vitro model of airway reopening. J. Appl. Physiol. 103, 1796–1807. https://doi.org/10.1152/japplphysiol.00164.2007

Yao, C., Zheng, J., Zhao, Y., Zhang, Q., Chen, G., 2019. Characteristics of gas-liquid Taylor flow with different liquid viscosities in a rectangular microchannel. Chem. Eng. J. 373, 437–445. https://doi.org/10.1016/j.cej.2019.05.051

Ye, T., Bull, J.L., 2006. Microbubble expansion in a flexible tube. J. Biomech. Eng. 128, 554–563. https://doi.org/10.1115/1.2206200

Ye, T., Bull, J.L., 2004. Direct numerical simulations of micro-bubble expansion in gas embolotherapy. J. Biomech. Eng. 126, 745–759. https://doi.org/10.1115/1.1824131

Yeow, S.L., Leo, H.L., 2016. Hemodynamic Study of Flow Remodeling Stent Graft for the Treatment of Highly Angulated Abdominal Aortic Aneurysm. Comput. Math. Methods Med. 2016. https://doi.org/10.1155/2016/3830123

Younis, H.F., Kaazempur-Mofrad, M.R., Chung, C., Chan, R.C., Kamm, R.D., 2003. Computational analysis of the effects of exercise on hemodynamics in the carotid bifurcation. Ann. Biomed. Eng. 31, 995–1006. https://doi.org/10.1114/1.1590661

Zamankhan, P., Helenbrook, B.T., Takayama, S., Grotberg, J.B., 2012. Steady motion of Bingham liquid plugs in two-dimensional channels. J. Fluid Mech. 705, 258–279. https://doi.org/10.1017/jfm.2011.438

Zamankhan, P., Takayama, S., Grotberg, J.B., 2018. Steady displacement of long gas bubbles in channels and tubes filled by a Bingham fluid. Phys. Rev. Fluids 3, 1–23. https://doi.org/10.1103/PhysRevFluids.3.013302

Zarins, C.K., Giddens, D.P., Bharadvaj, B.K., Sottiurai, V.S., Mabon, R.F., Glagov, S., 1983. Carotid bifurcation atherosclerosis. Quantitative correlation of plaque localization with flow velocity profiles and wall shear stress. Circ. Res. 53, 502–514. https://doi.org/10.1161/01.RES.53.4.502

Zhang, C., Xie, S., Li, S., Pu, F., Deng, X., Fan, Y., Li, D., 2012. Flow patterns and wall shear stress distribution in human internal carotid arteries: The geometric effect on the risk for

stenoses. J. Biomech. 45, 83–89. https://doi.org/10.1016/j.jbiomech.2011.10.001

Zhang, D., Dou, K., 2015. Coronary bifurcation intervention: What role do bifurcation angles play? J. Interv. Cardiol. 28, 236–248. https://doi.org/10.1111/joic.12203

Zheng, Y., Fujioka, H., Grotberg, J.B., 2007. Effects of gravity, inertia, and surfactant on steady plug propagation in a two-dimensional channel. Phys. Fluids 19. https://doi.org/10.1063/1.2762256

Zheng, Y., Fujioka, H., Grotberg, J.C., Grotberg, J.B., 2006. Effects of inertia and gravity on liquid plug splitting at a bifurcation. J. Biomech. Eng. 128, 707–716. https://doi.org/10.1115/1.2246235

Zhu, Y., Mirsadraee, S., Asimakopoulos, G., Gambaro, A., Rosendahl, U., Pepper, J., Xu, X.Y., 2021. Association of hemodynamic factors and progressive aortic dilatation following type A aortic dissection surgical repair. Sci. Rep. 11, 1–13. https://doi.org/10.1038/s41598-021-91079-5

Ziyi, X., Taotao, F., Chunying, Z., Shaokun, J., Youguang, M., Kai, W., Guangsheng, L., 2019. Dynamics of partially obstructed breakup of bubbles in microfluidic Y-junctions. Electrophoresis 40, 376–387. https://doi.org/10.1002/elps.201800330